

ISSN 2667-4211

ESKİŞEHİR TECHNICAL UNIVERSITY
JOURNAL OF SCIENCE AND TECHNOLOGY
A – Applied Sciences and Engineering

Volume **25** Number **1** - March - **2024**



Volume: 25 / Number: 1 / March - 2024

Eskiőehir Technical University Journal of Science and Technology A - Applied Sciences and Engineering (ESTUJST-A) is a peer-reviewed and refereed international journal published by Eskiőehir Technical University. Since 2000, it has been regularly published and distributed biannually and it has been published quarterly and only electronically since 2016.

The journal accepts only manuscripts written in English.

The journal issues are published electronically in **March, June, September, and December**.

Eskiőehir Technical University Journal of Science and Technology A - Applied Sciences and Engineering is an international peer-reviewed and refereed journal published by Eskiőehir Technical University.

The journal is dedicated to the dissemination of knowledge in applied sciences and engineering disciplines.

The journal aims to publish high quality, original international scientific research articles with specific contributions to the literature in the field of engineering and applied sciences. The journal publishes research papers in the fields of applied science and technology such as Physics, Biology, Mathematics, Statistics, Chemistry and Chemical Engineering, Environmental Sciences and Engineering, Civil Engineering, Earth and Atmospheric Sciences, Electrical and Electronical Engineering, Computer Science and Informatics, Materials Sciences and Engineering, Mechanical Engineering, Mining Engineering, Industrial Engineering, Aeronautics and Astronautics, Pharmaceutical Sciences.

The journal publishes original research articles and special issue articles. All articles are peer-reviewed and the articles that have been evaluated are ensured to meet with researchers as soon as possible.

Eskiőehir Technical University holds the copyright of all published material that appear in Eskiőehir Technical University Journal of Science and Technology A - Applied Sciences and Engineering.

"Anadolu Üniversitesi Bilim ve Teknoloji Dergisi A - Uygulamalı Bilimler ve Mühendislik (Anadolu University Journal of Science and Technology A - Applied Sciences and Engineering)" published within Anadolu University started to be published within Eskiőehir Technical University which was established due to statute law 7141, in 2018. Hence, the name of the journal is changed to " Eskiőehir Technical University Journal of Science and Technology A - Applied Sciences and Engineering (Eskiőehir Teknik Üniversitesi Bilim ve Teknoloji Dergisi A - Uygulamalı Bilimler ve Mühendislik)".

Indexed by **ULAKBIM TR Dizin**



Volume: 25 / Number: 1/ March - 2024

Owner / Publisher: Prof. Dr. Adnan ÖZCAN for Eskiőehir Technical University

EDITOR-IN-CHIEF

Prof. Dr. Semra KURAMA

Eskiőehir Technical University, Institute of Graduate Programs, 26470 Eskiőehir, TURKEY

Phone: +90 222 213 7470

e-mail: skurama@eskisehir.edu.tr

CO-EDITOR IN CHIEF

Assoc. Prof. Dr. Gülçin IŐIK

Eskiőehir Technical University, Institute of Graduate Programs, 26470 Eskiőehir, TURKEY

Phone: +90 222-213 7472

e-mail: gulciny@eskisehir.edu.tr

CO-EDITOR IN CHIEF

Assit. Prof. Dr. Hüseyin Ersin EROL

Eskiőehir Technical University, Institute of Graduate Programs, 26470 Eskiőehir, TURKEY

Phone: +90 222-213 7473

e-mail: heerol@eskisehir.edu.tr

CONTACT INFORMATION

Eskiőehir Technical University Journal of Science and Technology

Eskiőehir Technical University, Institute of Graduate Programs, 26470 Eskiőehir, TURKEY

Phone: +90 222 213 7485

e-mail : btada@eskisehir.edu.tr



Volume: 25 / Number: 1 / March - 2024

OWNER

Adnan ÖZCAN, **The Rector of Eskiőehir Technical University**

EDITORIAL BOARD

Semra KURAMA, **Editor in Chief**

Gülçin IŐIK, **Co-Editor in Chief**

Hüseyin Ersin EROL, **Co-Editor in Chief**

LANGUAGE EDITOR-ENGLISH

Burcu ERDOĞAN

İlker DEMİROĞLU

SECTION EDITORS

Sibel AKAR (Eskiőehir Osmangazi University, Turkey)
Ziya AKÇA (Eskiőehir Osmangazi University, Turkey)
İpek AKIN (İstanbul Teknik University, Turkey)
Sema AKYALÇIN (ESTU, Turkey)
Mehmet ALEGÖZ (ESTU, Turkey)
Suna AVCIOĞLU (Yıldız Teknik University, Turkey)
Uğur AVDAN (ESTU, Turkey)
Zehra YİĞİT AVDAN (ESTU, Turkey)
Ayşe H. BİLGE (Kadir Has University, Turkey)
Müjdat ÇAĞLAR (ESTU, Turkey)
Çağatay DENGİZ (Ortadoğu Teknik University, Turkey)
Rasime DEMİREL (ESTU, Turkey)
Elif Begüm ELÇİOĞLU (ESTU, Turkey)
Barış ERBAŐ (ESTU, Turkey)
Hüseyin Ersin EROL (ESTU, Turkey)
Metin GENÇTEN (Yıldız Teknik University, Turkey)
Ömer Neziğ GEREK (ESTU, Turkey)
Özer GÖK (ESTU, Turkey)
Cihan KALELİ (ESTU, Turkey)
Gordona KAPLAN (ESTU, Turkey)

T. Hikmet KARAKOÇ (ESTU, Turkey)
Elif KORUYUCU (ESTU, Turkey)
Semra KURAMA (ESTU, Turkey)
Hakan Ahmet NEFESLİOĞLU (ESTU, Turkey)
Anatoly NIKANOV (Saratov State Technical University, Slovenia)
Murad OMAROV (Kharkiv National University of Radio Electronics, Ukraine)
Mehmet İnanç ONUR (ESTU, Turkey)
Seyhan ÖNDER (Eskiőehir Osmangazi University, Turkey)
Zahide BAYER ÖZTÜRK (Nevőehir Hacı Bektaő Veli Univ., Turkey)
Emrah PEKKAN (ESTU, Turkey)
Najeeb REHMAN (Comsat University, Pakistan)
İsmail Hakkı SARPÜN (Akdeniz University, Turkey)
Aydn SİPAHİOĞLU (Eskiőehir Osmangazi University, Turkey)
İlkin YÜCEL ŐENGÜN (Ege University, Turkey)
Sevil ŐENTÜRK (ESTU, Turkey)
Gülsüm TOPATEŐ (Ankara Yıldırım Beyazıt University Turkey)
Önder TURAN (ESTU, Turkey)
Muammer TÜN (ESTU, Turkey)
Fatma TÜMSEK (Eskiőehir Osmangazi University, Turkey)
Berna ÜSTÜN (ESTU, Turkey)

Secretary/Typeset

Handan YİĞİT



ABOUT

Eskişehir Technical University Journal of Science and Technology A - Applied Sciences and Engineering (ESTUJST-A) is a peer-reviewed and refereed international journal published by Eskişehir Technical University. Since 2000, it has been regularly published and distributed biannually and it has been published quarterly and only electronically since 2016.

The journal accepts only manuscripts written in English.

The journal issues are published electronically in **MARCH, JUNE, SEPTEMBER, and DECEMBER.**

AIM AND SCOPE

Eskişehir Technical University Journal of Science and Technology A - Applied Sciences and Engineering is an international peer-reviewed and refereed journal published by Eskişehir Technical University.

The journal is dedicated to the dissemination of knowledge in applied sciences and engineering disciplines.

The journal aims to publish high quality, original international scientific research articles with specific contributions to the literature in the field of engineering and applied sciences. The journal publishes research papers in the fields of applied science and technology such as Physics, Biology, Mathematics, Statistics, Chemistry and Chemical Engineering, Environmental Sciences and Engineering, Civil Engineering, Earth and Atmospheric Sciences, Electrical and Electronical Engineering, Computer Science and Informatics, Materials Sciences and Engineering, Mechanical Engineering, Mining Engineering, Industrial Engineering, Aeronautics and Astronautics, Pharmaceutical Sciences.

The journal publishes original research articles and special issue articles. All articles are peer-reviewed and the articles that have been evaluated are ensured to meet with researchers as soon as possible.

PEER REVIEW PROCESS

Manuscripts are first reviewed by the editorial board in terms of its its journal's style rules scientific content, ethics and methodological approach. If found appropriate, the manuscript is then send to at least two renown referees by editor. The decision in line with the referees may be an acceptance, a rejection or an invitation to revise and resubmit. Confidential review reports from the referees will be kept in archive. All submission process manage through the online submission systems.

OPEN ACCESS POLICY

This journal provides immediate open access to its content on the principle that making research freely available to the public supports a greater global exchange of knowledge. Copyright notice and type of licence : **CC BY-NC-ND**.

PRICE POLICY

Eskişehir Technical University Journal of Science and Technology A - Journal of Applied Sciences and Engineering is an English, peer-reviewed, scientific, free of charge open-access-based journal. The author is not required to pay any publication fees or article processing charges (APCs) for peer-review administration and management, typesetting, and open-access. Articles also receive Digital Object Identifiers (DOIs) from the CrossRef organization to ensure they are always available.

ETHICAL RULES

You can reach the Ethical Rules in our journal in full detail from the link below:

<https://dergipark.org.tr/en/pub/estubtda/policy>

Ethical Principles and Publication Policy

Policy & Ethics

Assessment and Publication

As a peer-reviewed journal, it is our goal to advance scientific knowledge and understanding. We adhere to the guideline and ethical standards from the Committee on Publication Ethics (COPE) and the recommendations of ICMJE (International Committee of Medical Journal Editors) regarding all aspects of publication ethics and cases of research and publication misconduct to ensure that all publications represent accurate and original work and that our peer review process is structured without bias. We have outlined a set of ethical principles that must be followed by all authors, reviewers, and editors.

All manuscripts submitted to our journals are pre-evaluated in terms of their relevance to the scope of the journal, language, compliance with writing instructions, suitability for science, and originality, by taking into account the current legal requirements regarding copyright infringement and plagiarism. Manuscripts that are evaluated as insufficient or non-compliant with the instructions for authors may be rejected without peer review.

Editors and referees who are expert researchers in their fields assess scientific manuscripts submitted to our journals. A blind peer review policy is applied to the evaluation process. The Editor-in-Chief, if he/she sees necessary, may assign an Editor for the manuscript or may conduct the scientific assessment of the manuscript himself/herself. Editors may also assign referees for the scientific assessment of the manuscript and make their decisions based on reports by the referees. The Editor-in-Chief makes the final decision regarding the publishing of the manuscript.

Articles are accepted for publication by the Editor-in-Chief in accordance with the COPE (Committee on Publication Ethics). Authors can access this information online via the journals' websites (<https://publicationethics.org/>). Articles are accepted for publication on the understanding that they have not been published and are not going to be considered for publication elsewhere. Authors should certify that neither the manuscript nor its main contents have already been published or submitted for publication in another journal.

The journal adapts the COPE guidelines to satisfy the high-quality standards of ethics for authors, editors, and reviewers:

Duties of Editors-in-Chief and co-Editors

The crucial role of the journal Editor-in-Chief and co-Editors is to monitor and ensure the fairness, timeliness, thoroughness, and civility of the peer-review editorial process. The main responsibilities of Editors-in-Chief are as follows:

- Selecting manuscripts suitable for publication while rejecting unsuitable manuscripts,
- Ensuring a supply of high-quality manuscripts to the journal by identifying important,
- Increasing the journal's impact factor and maintaining the publishing schedule,
- Providing strategic input for the journal's development,

Duties of Editors

The main responsibilities of editors are as follows:

- An editor must evaluate the manuscript objectively for publication, judging each on its quality without considering the nationality, ethnicity, political beliefs, race, religion, gender, seniority, or institutional affiliation of the author(s). Editors should decline any assignment when there is a potential for conflict of interest.
- Editors must ensure the document(s) sent to the reviewers does not contain information of the author(s) and vice versa.
- Editors' decisions should be provided to the author(s) accompanied by the reviewers' comments and recommendations unless they contain offensive or libelous remarks.
- Editors should respect requests (if well reasoned and practicable) from author(s) that an individual should not review the submission.
- Editors and all staff members should guarantee the confidentiality of the submitted manuscript.
- Editors should have no conflict of interest with respect to articles they reject/accept. They must not have a conflict of interest with the author(s), funder(s), or reviewer(s) of the manuscript.
- Editors should strive to meet the needs of readers and authors and to constantly improve the journal.

Duties of Reviewers/Referees

The main responsibilities of reviewers/referees are as follows:

- Reviewers should keep all information regarding papers confidential and treat them as privileged information.
- Reviews should be conducted objectively, with no personal criticism of the author.
- Reviewers assist in the editorial decision process and as such should express their views clearly with supporting arguments.
- Reviewers should complete their reviews within a specified timeframe (maximum thirty-five (35) days). In the event that a reviewer feels it is not possible for him/her to complete the review of the manuscript within a stipulated time, then this information must be communicated to the editor so that the manuscript could be sent to another reviewer.
- Unpublished materials disclosed in a submitted manuscript must not be used in a reviewer's personal research without the written permission of the author. Information contained in an

unpublished manuscript will remain confidential and must not be used by the reviewer for personal gain.

- Reviewers should not review manuscripts in which they have conflicts of interest resulting from competitive, collaborative, or other relationships or connections with any of the authors, companies, or institutions connected to the papers.
- Reviewers should identify similar work in published manuscripts that has not been cited by the author. Reviewers should also notify the Editors of significant similarities and/or overlaps between the manuscript and any other published or unpublished material.

Duties of Authors

The main responsibilities of authors are as follows:

- The author(s) should affirm that the material has not been previously published and that they have not transferred elsewhere any rights to the article.
- The author(s) should ensure the originality of the work and that they have properly cited others' work in accordance with the reference format.
- The author(s) should not engage in plagiarism or in self-plagiarism.
- On clinical and experimental humans and animals, which require an ethical committee decision for research in all branches of science;

All kinds of research carried out with qualitative or quantitative approaches that require data collection from the participants by using survey, interview, focus group work, observation, experiment, interview techniques,

Use of humans and animals (including material/data) for experimental or other scientific purposes,

- Clinical studies on humans,
- Studies on animals,
- Retrospective studies in accordance with the law on the protection of personal data, (Ethics committee approval should have been obtained for each individual application, and this approval should be stated and documented in the article.)

Information about the permission (board name, date, and number) should be included in the "Method" section of the article and also on the first/last page.

During manuscript upload, the "Ethics Committee Approval" file should be uploaded to the system in addition to the manuscript file.

In addition, in case reports, it is necessary to include information on the signing of the informed consent/ informed consent form in the manuscript.

- The author(s) should suggest no personal information that might make the identity of the patient recognizable in any form of description, photograph, or pedigree. When photographs of the patient were essential and indispensable as scientific information, the author(s) have received consent in written form and have clearly stated as much.
- The author(s) should provide the editor with the data and details of the work if there are suspicions of data falsification or fabrication. Fraudulent data shall not be tolerated. Any manuscript with suspected fabricated or falsified data will not be accepted. A retraction will be made for any publication which is found to have included fabricated or falsified data.
- The author(s) should clarify everything that may cause a conflict of interests such as work, research expenses, consultant expenses, and intellectual property.
- The author(s) must follow the submission guidelines of the journal.
- The author(s) discover(s) a significant error and/or inaccuracy in the submitted manuscript at any time, then the error and/or inaccuracy must be reported to the editor.
- The author(s) should disclose in their manuscript any financial or other substantive conflicts of interest that might be construed to influence the results or interpretation of their manuscript.

All sources of financial support should be disclosed under the heading of “Acknowledgment” or “Contribution”.

- The corresponding author should ensure that all appropriate co-authors and no inappropriate co-authors are included in the paper and that all co-authors have seen and approved the final version of the paper and have agreed to its submission for publication. All those who have made significant contributions should be listed as co-authors. Others who have participated in certain substantive aspects of the research should be acknowledged or listed under the heading of “Author Contributions”.

Cancellations/Returns

Articles/manuscripts may be returned to the authors in order to increase the authenticity and/or reliability and to prevent ethical breaches, and even if articles have been accepted and/or published, they can be withdrawn from publication if necessary. The Editor-in-Chief of the journal has the right to return or withdraw an article/manuscript in the following situations:

- When the manuscript is not within the scope of the journal,
- When the scientific quality and/or content of the manuscript do not meet the standards of the journal and a referee review is not necessary,
- When there is proof of ruling out the findings obtained by the research, (When the article/manuscript is undergoing an assessment or publication process by another journal, congress, conference, etc.,)
- When the article/manuscript was not prepared in compliance with scientific publication ethics,
- When any other plagiarism is detected in the article/manuscript,
- When the authors do not perform the requested corrections within the requested time (maximum twenty-one (21) days),
- When the author does not submit the requested documents/materials/data etc. within the requested time,
- When the requested documents/materials/data etc. submitted by the author are missing for the second time,
- When the study includes outdated data,
- When the authors make changes that are not approved by the editor after the manuscript was submitted,
- When an author is added/removed, the order of the authors is changed, the corresponding author is changed, or the addresses of the authors are changed without the consent of the Editor-in-Chief,
- When a statement is not submitted indicating that approval of the ethics committee permission was obtained for the following (including retrospective studies):
- When human rights or animal rights are violated,

ETHICAL ISSUES

Plagiarism

The use of someone else’s ideas or words without a proper citation is considered plagiarism and will not be tolerated. Even if a citation is given, if quotation marks are not placed around words taken directly from other authors’ work, the author is still guilty of plagiarism. Reuse of the author’s own previously published words, with or without a citation, is regarded as self-plagiarism.

All manuscripts received are submitted to iThenticate®, which compares the content of the manuscript with a database of web pages and academic publications. Manuscripts are judged to be plagiarized or self-plagiarized, based on the iThenticate® report or any other source of information, will be rejected. Corrective actions are proposed when plagiarism and/or self-

plagiarism is detected after publication. Editors should analyze the article and decide whether a corrected article or retraction needs to be published.

Open-access theses are considered as published works and they are included in the similarity checks.

iThenticate® report should have a maximum of 11% from a single source, and a maximum of 25% in total.

Conflicts of Interest

Eskişehir Technical University Journal of Science and Technology A - Applied Sciences and Engineering should be informed of any significant conflict of interest of editors, authors, or reviewers to determine whether any action would be appropriate (e.g. an author's statement of conflict of interest for a published work, or disqualifying a referee).

Financial

The authors and reviewers of the article should inform the journal about the financial information that will bring financial gain or loss to any organization from the publication of the article.

*Research funds; funds, consulting fees for a staff member; If you have an interest, such as patent interests, you may have a conflict of interest that needs to be declared.

Other areas of interest

The editor or reviewer may disclose a conflict of interest that, if known, would be embarrassing (for example, an academic affiliation or rivalry, a close relationship or dislike, or a person who may be affected by the publication of the article).

Conflict of interest statement

Please note that a conflict of interest statement is required for all submitted manuscripts. If there is no conflict of interest, please state “There are no conflicts of interest to declare” in your manuscript under the heading “Conflicts of Interest” as the last section before your Acknowledgments.

AUTHOR GUIDELINES

All manuscripts must be submitted electronically.

You will be guided stepwise through the creation and uploading of the various files. There are no page charges. Papers are accepted for publication on the understanding that they have not been published and are not going to be considered for publication elsewhere. Authors should certify that neither the manuscript nor its main contents have already been published or submitted for publication in another journal. We ask a signed copyright to start the evaluation process. After a manuscript has been submitted, it is not possible for authors to be added or removed or for the order of authors to be changed. If authors do so, their submission will be cancelled.

Manuscripts may be rejected without peer review by the editor-in-chief if they do not comply with the instructions to authors or if they are beyond the scope of the journal. After a manuscript has been accepted for publication, i.e. after referee-recommended revisions are complete, the author will not be permitted to make any changes that constitute departures from the manuscript that was accepted by the editor. Before publication, the galley proofs are always sent to the authors for corrections. Mistakes or omissions that occur due to some negligence on our part during final printing will be rectified in an errata section in a later issue.

This does not include those errors left uncorrected by the author in the galley proof. The use of someone else's ideas or words in their original form or slightly changed without a proper citation is considered plagiarism and will not be tolerated. Even if a citation is given, if quotation marks are not placed around words taken directly from another author's work, the

author is still guilty of plagiarism. All manuscripts received are submitted to iThenticateR, a plagiarism checking system, which compares the content of the manuscript with a vast database of web pages and academic publications. In the received iThenticateR report; The similarity rate is expected to be below 25%. Articles higher than this rate will be rejected.

Uploading Articles to the Journal

Authors should prepare and upload 2 separate files while uploading articles to the journal. First, the Author names and institution information should be uploaded so that they can be seen, and then (using the additional file options) a separate file should be uploaded with the Author names and institution information completely closed. When uploading their files with closed author names, they will select the "Show to Referee" option, so that the file whose names are closed can be opened to the referees.

Preparation of Manuscript

Style and Format

Manuscripts should be **single column** by giving one-spaced with 2.5-cm margins on all sides of the page, in Times New Roman font (font size 11). Every page of the manuscript, including the title page, references, tables, etc., should be numbered. All copies of the manuscript should also have line numbers starting with 1 on each consecutive page.

Manuscripts must be upload as word document (*.doc, *.docx vb.). **Please avoid uploading texts in *.pdf format.**

Symbols, Units and Abbreviations

Standard abbreviations and units should be used; SI units are recommended. Abbreviations should be defined at first appearance, and their use in the title and abstract should be avoided. Generic names of chemicals should be used. Genus and species names should be typed in italic or, if this is not available, underlined.

Please refer to equations with capitalisation and unabbreviated (e.g., as given in Equation (1)).

Manuscript Content

Articles should be divided into logically ordered and numbered sections. Principal sections should be numbered consecutively with Arabic numerals (1. Introduction, 2. Formulation of problem, etc.) and subsections should be numbered 1.1., 1.2., etc. Do not number the Acknowledgements or References sections. The text of articles should be, if possible, divided into the following sections: Introduction, Materials and Methods (or Experimental), Results, Discussion, and Conclusion.

Title and contact information

The first page should contain the full title in sentence case (e.g., Hybrid feature selection for text classification), the full names (last names fully capitalised) and affiliations (in English) of all authors (Department, Faculty, University, City, Country, E-mail), and the contact e-mail address for the clearly identified corresponding author. The first page should contain the full title, abstract and keywords (both English and Turkish).

Abstract

The abstract should provide clear information about the research and the results obtained, and should not exceed 300 words. The abstract should not contain citations and must be written in Times New Roman font with font size 9.

Keywords

Please provide 3 to 5 keywords which can be used for indexing purposes.

Introduction

The motivation or purpose of your research should appear in the “Introduction”, where you state the questions you sought to answer, and then provide some of the historical basis for those questions.

Methods

Provide sufficient information to allow someone to repeat your work. A clear description of your experimental design, sampling procedures, and statistical procedures is especially important in papers describing field studies, simulations, or experiments. If you list a product (e.g., animal food, analytical device), supply the name and location of the manufacturer. Give the model number for equipment used.

Results

Results should be stated concisely and without interpretation.

Discussion

Focus on the rigorously supported aspects of your study. Carefully differentiate the results of your study from data obtained from other sources. Interpret your results, relate them to the results of previous research, and discuss the implications of your results or interpretations.

Conclusion

This should state clearly the main conclusions of the research and give a clear explanation of their importance and relevance. Summary illustrations may be included.

Acknowledgments

Acknowledgments of people, grants, funds, etc. should be placed in a separate section before the reference list. The names of funding organizations should be written in full.

Conflict of Interest Statement

The authors are obliged to present the conflict of interest statement at the end of the article after the acknowledgments section.

Author Contributions

All authors, author contributions and contribution rates should be clearly stated.

References

Writing Style; **AMA; References Writing format** should be used in the reference writing of our journal. If necessary, at this point, the reference writings of the articles published in our article can be examined.

Citations in the text should be identified by numbers in square brackets. The list of references at the end of the paper should be given in order of their first appearance in the text. All authors should be included in reference lists unless there are 10 or more, in which case only the first 10 should be given, followed by ‘et al.’. Do not use individual sets of square brackets for citation

numbers that appear together, e.g., [2,3,5–9], not [2], [3], [5]–[9]. Do not include personal communications, unpublished data, websites, or other unpublished materials as references, although such material may be inserted (in parentheses) in the text. In the case of publications in languages other than English, the published English title should be provided if one exists, with an annotation such as “(article in Turkish with an abstract in English)”. If the publication was not published with an English title, cite the original title only; do not provide a self-translation. References should be formatted as follows (please note the punctuation and capitalisation):

Journal articles

Journal titles should be abbreviated according to ISI Web of Science abbreviations.

Guyon I, Elisseeff A. An introduction to variable and feature selection. *J Mach Learn Res* 2003; 3: 1157-1182.

Izadpanahi S, Ozcinar C, Anbarjafari G, Demirel H. Resolution enhancement of video sequences by using discrete wavelet transform and illumination compensation. *Turk J Elec Eng & Comp Sci* 2012; 20: 1268-1276.

Books

Haupt RL, Haupt SE. *Practical Genetic Algorithms*. 2nd ed. New York, NY, USA: Wiley, 2004.
Kennedy J, Eberhart R. *Swarm Intelligence*. San Diego, CA, USA: Academic Press, 2001.

Chapters in books

Poore JH, Lin L, Eschbach R, Bauer T. Automated statistical testing for embedded systems. In: Zander J, Schieferdecker I, Mosterman PJ, editors. *Model-Based Testing for Embedded Systems*. Boca Raton, FL, USA: CRC Press, 2012. pp. 111-146.

Conference proceedings

Li RTH, Chung SH. Digital boundary controller for single-phase grid-connected CSI. In: *IEEE 2008 Power Electronics Specialists Conference*; 15–19 June 2008; Rhodes, Greece. New York, NY, USA: IEEE. pp. 4562-4568.

Theses

Boynukalin Z. *Emotion analysis of Turkish texts by using machine learning methods*. MSc, Middle East Technical University, Ankara, Turkey, 2012.

Tables and Figures

All illustrations (photographs, drawings, graphs, etc.), not including tables, must be labelled “Figure.” Figures must be submitted in the manuscript.

All tables and figures must have a caption and/or legend and be numbered (e.g., Table 1, Figure 2), unless there is only one table or figure, in which case it should be labelled “Table” or “Figure” with no numbering. Captions must be written in sentence case (e.g., Macroscopic appearance of the samples.). The font used in the figures should be Times New Roman. If symbols such as \times , μ , η , or v are used, they should be added using the Symbols menu of Word.

All tables and figures must be numbered consecutively as they are referred to in the text. Please refer to tables and figures with capitalisation and unabbreviated (e.g., “As shown in Figure 2...”, and not “Fig. 2” or “figure 2”).

The resolution of images should not be less than 118 pixels/cm when width is set to 16 cm. Images must be scanned at 1200 dpi resolution and submitted in jpeg or tiff format. Graphs and diagrams must be drawn with a line weight between 0.5 and 1 point. Graphs and diagrams with a line weight of less than 0.5 point or more than 1 point are not accepted. Scanned or photocopied graphs and diagrams are not accepted.

Figures that are charts, diagrams, or drawings must be submitted in a modifiable format, i.e. our graphics personnel should be able to modify them. Therefore, if the program with which the figure is drawn has a “save as” option, it must be saved as *.ai or *.pdf. If the “save as” option does not include these extensions, the figure must be copied and pasted into a blank Microsoft Word document as an editable object. It must not be pasted as an image file (tiff, jpeg, or eps) unless it is a photograph.

Tables and figures, including caption, title, column heads, and footnotes, must not exceed 16 × 20 cm and should be no smaller than 8 cm in width. For all tables, please use Word’s “Create Table” feature, with no tabbed text or tables created with spaces and drawn lines. Please do not duplicate information that is already presented in the figures.

Article Corrections and Uploading to the System

Authors should upload the desired edits for their articles without destroying or changing the Template file of the article, by selecting and specifying the relevant edits as Colored, and also submit the Clean version of the article in 2 separate files (using the Additional file option if necessary). * In case of submitting a corrected article, a separate File in Reply to the Referees must be prepared and the "Reply to the Referees" option in the Add additional file option should be checked and uploaded. If a separate file is not prepared in response to the referees, the Author will definitely be asked to upload the relevant file again and the evaluation will be in the pending phase.

CONTENTS

RESEARCH ARTICLE

EXPERIMENTAL AND NUMERICAL INVESTIGATION OF A DEFICIENT STORMWATER DRAINAGE SYSTEM <i>C. Yilmazer, A. O. Çelik</i>	1
RECOVERY OF BORON WASTES WITH INORGANIC ACID <i>E. Yoğurtcuoğlu</i>	14
AN APPLICATION FOR THE CALIBRATION OF THE TWO-PRESSURE HUMIDITY GENERATOR <i>C. Ekici</i>	27
DERIVATION OF EXPRESSION FOR PHOTOCURRENT DENSITY FOR NON-DESTRUCTIVE TESTING OF 3D PRINTING FILAMENT BY MEANS OF TERAHERTZ SPECTROSCOPY <i>I. Khoroshailo, N. Zaichenko, O. Zaichenko</i>	36
DETERMINATION OF THE PERFORMANCE OF LIGHT SHELVES FOR MORE EFFECTIVE BENEFIT FROM DAYLIGHT IN BUILDINGS <i>F. Meral, H.G. Demirkol</i>	44
THE CYTOTOXIC EFFECT OF BENZOIC ACID ON TEN DIFFERENT CANCER CELL LINES <i>H. Öztürkel Kabakaş, M. Sezer Kürkçü, K. A. Onat Taşdelen, B. Çöl</i>	66
PERFORMANCE EVALUATIONS OF THE MANTA RAY FORAGING OPTIMIZATION ALGORITHM IN REAL-WORLD CONSTRAINED OPTIMIZATION PROBLEMS <i>G. Yıldızdan</i>	78
NOVEL APPROACH FOR ONE-POT SELF-ASSEMBLED MONOLAYER PREPARATION OF GOLD TIPPED CdSe/CdS NANORODS <i>Z. Dikmen</i>	99
THE TRAVELING WAVE SOLUTIONS OF THE CONFORMABLE TIME-FRACTIONAL ZOOMERON EQUATION BY USING THE MODIFIED EXPONENTIAL FUNCTION METHOD <i>A. Alkan, T. Aktürk, H. Bulut</i>	108
SYNTHESIS OF ALUMINA FROM KAOLIN FOUND IN AJEBO, OGUN STATE, NIGERIA <i>H. E. Mgbemere, C. V. Oluigbo</i>	115
THE NOVEL CONFORMABLE METHODS TO SOLVE CONFORMABLE TIME- FRACTIONAL COUPLED JAULENT-MIODEK SYSTEM <i>Ö. Avit, H. Anaç</i>	123
EXACT TRAVELING WAVE SOLUTIONS FOR THE NON-LINEAR COUPLE DRINFEL'D-SOKOLOV-WILSON (DSW) DYNAMICAL SYSTEM USING EXTENDED JACOBI ELLIPTIC FUNCTION EXPANSION METHOD <i>N. Çelik</i>	141
MEMORY-BASED SELF-ORDERING FFT FOR EFFICIENT I/O SCHEDULING <i>Z. Kaya, E. Seke</i>	156



RESEARCH ARTICLE

EXPERIMENTAL AND NUMERICAL INVESTIGATION OF A DEFICIENT
STORMWATER DRAINAGE SYSTEM

Cem YILMAZER ^{1*} , Ahmet Ozan ÇELİK ² 

¹ Department of Civil Engineering, Faculty of Civil Engineering, Yıldız Technical University, Istanbul, Turkey

² Department of Civil Engineering, Faculty of Engineering, Eskişehir Technical University, Eskişehir, Turkey

ABSTRACT

In this paper, a deficient stormwater system was investigated with experimental and numerical methods. The main goal was to obtain an experimentally validated 3D computational fluid dynamics (CFD) model to identify the problems of the system and offer design solutions via numerical modeling. A scaled physical model of the structure was built for CFD validation. The validation was done via comparisons of point pressure statistics, discharge and water levels. Different mesh structures and turbulence closure methods were also tested for verification of the model. The validated model was then used to determine the cause of the problems in the structure. New geometries were tested numerically to suggest solutions to the detected problems. Empirical approaches and also regulations for the stormwater structures were also considered for comparison. Findings of this study suggest that a verified and validated CFD model is an effective tool to investigate special geometries for specific hydraulic structure problems where conventional approaches are insufficient.

Keywords: Stormwater drainage system, CFD, Hydraulic modelling, Validation

1. INTRODUCTION

Climate change, irregular urbanization and conurbation together with high intensity precipitations may cause extreme discharges which eventually need to be removed safely. In such cases, the existing stormwater drainage systems, if not effective enough, may be causing further problems. Although design and rehabilitation of such systems can be performed using experimental, empirical and theoretical approaches there are valuable results in the literature involving numerical modelling of stormwater drainage systems, some of which are reviewed below.

Saiyudthong and Guymer investigated joining pipes with different angles in a circular manhole under surcharge flow conditions reporting that increasing the angle between the pipes causes added momentum and decreases the energy loss coefficient in the manhole [1]. However, they were not able to obtain a good validation using experimental results. Zhao et al. simulated fully surcharged flow at a 90° combining sewer junction and found a good agreement between CFD and experiments for water depth, energy loss and velocity profiles [2]. Observing the flow inside a chute manhole, Sousa et al. focused on the effect of oxygen level on the flow characteristics as the hydraulic jump occurs. They measured velocity profiles, pressure at various locations and water levels for validation which lead to the conclusion that CFD can characterize water-air phase mixture reasonably well [3]. More recently, Beg et al. performed a CFD model study for both free surface flow and pressurized flow inside a manhole [4]. The numerical model was validated using 1:1 scaled experiments with different discharge combinations. However, they modeled a manhole with a simple geometry and this study did not include real flow cases or geometrical improvements.

*Corresponding Author: cem.yilmazer@yahoo.com

Received: 01.10.2022 Published: 28.03.2024

Although the literature has numerous examples of studies utilizing numerical methods, the ones listed so far do not involve detection of problems and/or providing solutions involving real cases using CFD tools. Studies involving more realistic cases are reviewed below.

Motlagh et al. investigated energy losses and flow behaviour in a more realistic model of a manhole with two inlet and one outlet pipe, reporting that increasing the height of the lateral inlet pipe causes energy loss coefficient to decrease as a result of decreasing eddy flow [5]. Chen et al. performed a CFD analysis for optimization of a municipal sewer system design aiming to optimize the design of an existing combined sewer system and the numerical model was validated using experimental results [6]. Isel et al. described a general method based on CFD to investigate discharge-water depth relationships for combined sewer overflow chambers, particularly for complex geometries. They reported problems with the validation due to sensors accuracy and complex geometry of the system [7]. Kaur, Laanearu and Annus in a case study analysed a pipe's performance between two manholes for design and storm discharges considering slurry flow. A three-phase CFD model was used, however without validation [8]. Beg, Carvalho and Leandro investigated an ideal manhole with CFD models testing three different chute manholes. This study resulted in the best design option based on hydraulic grade line and energy loss coefficient although the numerical model wasn't validated with experimental work [9].

Ozolcer and Dundar modeled flow with CFD in a half-bench manhole comparing three alternative manhole geometries for energy loss coefficients but they didn't validate the CFD model with experimental findings [10]. Beg, Carvalho and Leandro investigated a manhole with an integrated gully to the structure. CFD model was validated with 1:1 scaled experiments. They found that increasing the surcharge flow in the manhole decreased retention of stormwater in the gully and decreased the energy dissipation near the inlet [11]. Wang and Vasconcelos performed a CFD study for manhole cover displacement due to the release of entrapped air pocket inside the manhole considering rapid filling with stormwater as an operational problem [12]. Beg, Carvalho and Leandro more recently investigated numerically manhole structural mold shapes, small changes in inlet orientations and changes in the manhole to inlet pipe ratios for their effect on manhole head loss coefficient [13].

Literature suggests that CFD is a useful tool for many stormwater applications. However, the relevant studies in the literature, some of which have been given above either present unvalidated numerical models and/or use ideal systems not fully representing real cases. That is, the CFD method, proven to be very useful in hydraulics studies, seems to be not effectively used in providing solutions to the real hydraulic problems.

This study aims to address a practical concern in a given public stormwater drainage system, using the experimentally validated numerical models effectively to design new components/geometries in a stormwater system with known problems and also discuss shortcomings of the relevant regulations and empirical equations.

2. MATERIALS AND METHODS

2.1. The Investigated Structure

The drainage system investigated here is located in Eskisehir, Turkey and it involves a manhole and four integrated pipes (Figure 1). It was reported to the authors by the authorities that the manhole had conurbation related design and overflow problems. The main inlet pipe's diameter was changed from originally designed 1500 mm to 1200 mm to open space for a crossing heat pipeline. As a result, overflow and backflow occurred in the system. Subsequently, two additional pipes were integrated to the manhole as a solution. These pipes are 500 mm and 350 mm in diameters (Figure 1a, 1b) and are also believed to be causing backflow during extreme discharges.

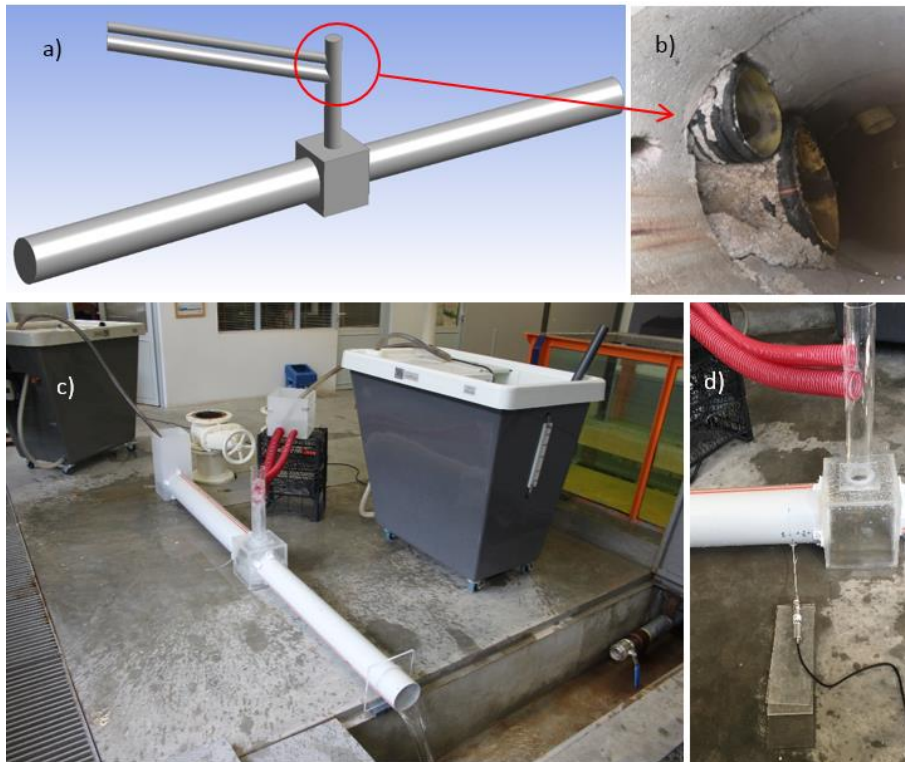


Figure 1. The manhole and four integrated pipes (a); integration of secondary corrugated pipes to the manhole in situ (b); the experimental set-up, general view (c); location of the pressure sensor (d)

2.2. The Physical Model

Experiments were performed at the Hydraulics Laboratory of the Eskişehir Technical University in Eskişehir, Turkey. The physical model was built with 1:10 geometric scale, to use the physical space in the current lab facilities effectively (Figure 1c, 1d). Froude dynamic similitude was used. Dimensions of the physical model are given in detail (Figure 2 and Tables 1, 2). For more about the experimental procedure please refer to Yilmazer [14].

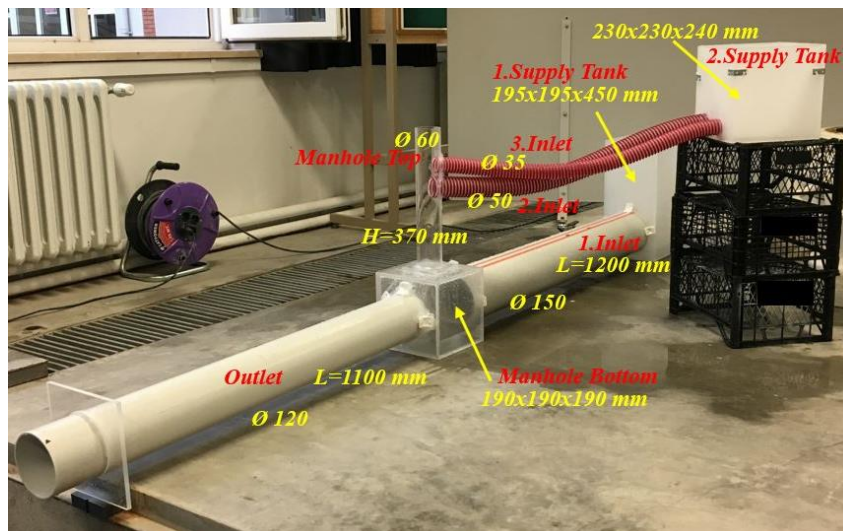


Figure 2. The experimental set-up with elements and dimensions

Table 1. The experimental set-up pipes dimensions

Pipes	Diameter (mm)	Length (mm)	Slope (mm/mm)
Inlet 1	150	1200	0.0037
Inlet 2	50	810	0.0158
Inlet 3	35	810	0.17
Outlet	120	1100	0.09
Manhole Top	60	370	---

Table 2. The experimental set-up elements dimensions

Elements	Width (mm)	Length (mm)	Height (mm)
1. Supply Tank	195	195	450
2. Supply Tank	230	230	240
Manhole Bottom	190	190	190

90 different discharge combinations were generated for observing the outlet discharges of the system to investigate the system’s performance (Table 3). For this, stabilized water levels in the manhole and the first supply tank were measured for all 90 combinations. Five of the combinations also included detailed pressure measurements at a fixed point at the bottom of the first main inlet pipe, 100 mm near the manhole (Figure 1d). This point was specifically selected to obtain pressure data to be used for CFD validation. Omega PX409-10WG USBH type pressure sensor was used for measuring pressure. The DC off-set of the pressure sensor was measured and recorded before and after each set of experiments and the obtained data was corrected accordingly [14].

Table 3. Outlet Discharge for two inlet discharge combinations (l/s)

Q ₁ \Q ₂	0.0	0.1	0.3	0.5	0.8	1.0	1.2	1.5	1.8	2.0
0.1	0.10	0.19	0.36	0.58	0.79	0.82	1.04	1.32	1.58	1.82
0.3	0.29	0.39	0.54	0.75	1.02	1.04	1.25	1.48	1.75	1.98
0.5	0.49	0.57	0.79	0.97	1.11	1.22	1.45	1.74	1.92	2.22
0.8	0.78	0.86	1.04	1.29	1.52	1.54	1.67	1.79	2.08	2.63
1.0	0.99	0.87	1.07	1.25	1.56	1.75	1.96	2.30	2.67	2.71
1.2	1.18	1.03	1.25	1.43	1.71	1.87	2.17	2.22	2.50	2.90
1.5	1.50	1.32	1.67	1.82	2.08	2.11	2.38	2.67	2.78	3.18
1.8	1.80	1.63	1.83	2.15	2.27	2.35	2.63	2.94	3.08	3.36
2.0	2.00	1.85	2.06	2.17	2.41	2.67	2.94	3.13	3.33	3.44
2.5	2.50	2.20	2.41	2.50	2.86	3.03	3.28	3.51	3.70	4.17

Second discharge (total of 2nd and 3rd inlets) was limited to 2.0 l/s after which overflow occurred. Normally, secondary pipe’s design discharges should be 4.93 and 1.39 l/s respectively according to Manning equation (with a total capacity of 6.32 l/s). But this value was observed to be around 2.0 l/s during the experiments which show that the integrated secondary corrugated pipe causes the backflow effect.

Another investigation was about the case when the secondary pipes’ discharge (Q₂) is more than main pipe’s discharge (Q₁). In this case, backflow effect was seen in the first supply tank. This is presumably due to high turbulence levels in the manhole. Outlet discharge was observed to be decreasing compared to the inlet discharge as a result of the accumulation and backflow in the tank. Particularly, the difference is much more apparent when Q₂ is dominant [14].

2.3. The Numerical Model

With a separate but parallel effort, a multi-phase CFD model was built using ANSYS-CFX solver. CFD is a flow simulation methodology based on discretized (second order, transient, implicit schemes-backward Euler-, using trilinear interpolation approach with turbulence -high resolution- closures given in Table 2, for details of the numerical schemes please refer to ANSYS C. 2010, ANSYS C. 2013 [15,16] equations of continuity and momentum. All models employed a convergence criteria of 10^{-4} for mass and momentum equations. For more detail about the CFD basics, model verification/validation and free-surface modeling please refer to Chen et al. [6], Isel et al. [7], Beg, Carvalho and Leandro [4] and Yilmazer [14].

2.3.1. Verification

First, drawings of 1:10 scaled storm water system (domain) were generated (Figure 1a) with dimensions identical to that of the experiments. For mesh independency study to choose optimum mesh sizes, CFD models with 6 different mesh configurations were compared with experimental results (1.0-2.0 l/s discharge combinations, representing the upper and lower limits of the whole experiment). The mesh structures were classified as coarse (2), medium (1) and fine (3) and summarized along with the element sizes in Table 4. Figure 3 shows the domain with mesh elements as well as the regions with refined mesh.

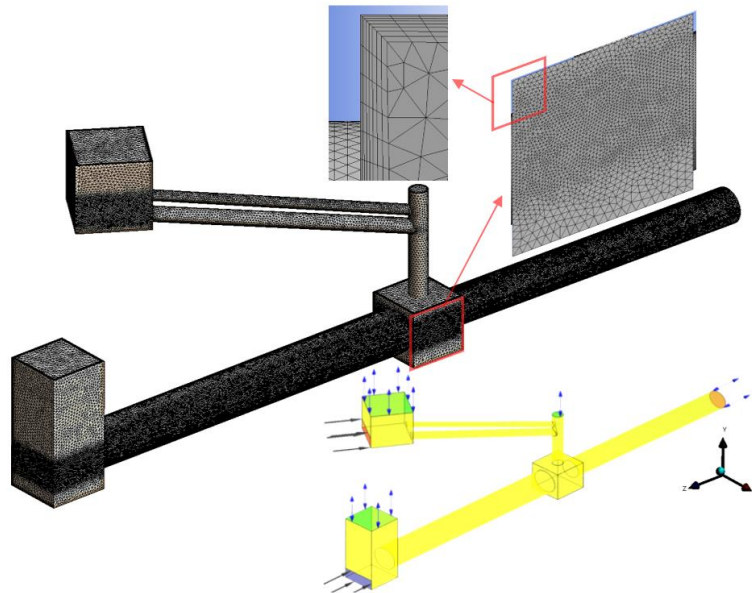


Figure 3. Meshed domain. Gravity force is considered in -Y direction. Bottom. Refinement and inflation as well as boundary conditions inside the domain are shown as insets

The mesh structure is assumed to be ideal if the skewness is less than 0.25 and orthogonality is close to 1.0. All fine mesh options have acceptable skewness and orthogonality (Table 4) [15]. Flow is subject to viscous effects near the walls where refinement of mesh size was performed. This was also applied where the free surface was anticipated to occur as shown in Figure 3. The coarse and medium mesh cases were unsatisfactory in terms of capturing gross flow parameters (Table 4). No detectable difference was observed in the free surface behaviour between options Fine 2 and 3. All three fine mesh options gave reliable results, but the Fine 2 option was accepted to be optimum by taking into consideration all relevant parameters, such as mesh skewness and run time (Table 4).

Time step, depended on Courant Number was defined as 0.1 seconds for an optimum solution which also matches the sampling frequency of the pressure sensor [14]. Regarding the relatively high Courant numbers in Table 4, the implicit transient code we utilize here does not require small Courant numbers for stability [16]. However, the optimized time step was chosen to reduce the RMS Courant number as much as possible. Mesh refining also helped obtain reasonable Courant numbers in the confined areas. This particularly helped resolve the unsteady behaviour of free fall.

Table 4. Mesh specifications for different mesh structures and comparisons of numerical model results with experimental model (EM) results. Bold columns indicate the chosen options

Parameters	EM	C1	C2	M	F1	F2	F3	k-ε	RNG	k-ω	SST
		For different mesh structures (Coarse: C; Medium: M; Fine: F)						For different turbulence models			
Element Number (x1000)	-	338.9	528.7	1022.1	3000.5	5994.8	7861.4	-	-	-	-
Node Number (x1000)	-	114.4	172.9	309.9	781.7	1448.3	1886.9	-	-	-	-
Skewness	-	0.272	0.254	0.224	0.208	0.209	0.205	-	-	-	-
Orthogonality Quality	-	0.850	0.866	0.882	0.886	0.881	0.885	-	-	-	-
RMS Courant Number	-	12.57	21.73	10.28	11.86	13.40	13.87	-	-	-	-
CPU Time (hour)	-	01:38	02:01	03:53	12:20	20:15	34:11	-	-	-	-
Averaged Pressure (Pa)	856	937	928	950	950	925	923	950	926	909	941
Q _{outlet} (l/s)	2.71	2.97	2.92	2.89	2.78	2.61	2.58	2.78	2.63	2.81	2.89
Averaged H _{Manhole} (mm)	139	110	123	129	131	137	125	131	115	119	144
H ₁ . Supply Tank (mm)	128	104	113	115	120	125	115	120	106	119	138

In addition to mesh independency, different Reynolds Averaged Navier Stokes (RANS) turbulence closure models for 1.0-2.0 l/s discharge combinations were also tested. These models are k-epsilon (k-ε), re-normalisation group k-epsilon (RNG k-ε), k-omega (k-ω), k-omega shear stress transport (k-ω SST). Table 4 shows the results and comparison with experimental results. k-epsilon turbulence model was selected as the best option due to better agreement with experimental results, particularly for outlet discharge.

Boundary conditions are defined in the flow domain as shown in Figure 3. Sand grain roughness was defined on wall type boundary according to material properties. Mass flow type inlets are on the front surface of the first and second supply tanks. Allowing air to enter and exit, tops of the tanks were defined as opening type boundary. Pressure outlet was defined (0 Pa gage) at the end of the outlet pipe allowing water and air to exit and air to enter the domain. Discharge combinations from the experiments and design discharges were specified for each CFD model. Inlet water levels (head) were determined from experimental results.

Entire domain in the initialization of all runs were defined as air and stabilized conditions were obtained via long transient runs rather than adapting conditions from a preliminary steady run. This was in an effort not to dictate the flow depths and obtain realistic flow behaviour.

Convergence criteria was applied as follows. Three momentum equations and two turbulence equations (k-epsilon) were converged near 10^{-4} . Continuity equation was converged around 0.005 because of

stormwater retention in the domain (i.e. inlet and outlet discharges aren't always equal). Volume of Fluid (VOF) method was to resolve free surface.

14 out of 90 combinations from experimental work were selected for CFD modeling. Water level at the first supply tank and manhole were also compared at stable conditions. In the numerical model, stable condition was assumed when the outlet discharge reached stable (non-trending) conditions after about 60 seconds of simulation time. The stable values from the time steps near the end of the simulations were averaged from discharge-time series at the outlet surface. The same procedure was followed for water levels and local pressure values (similar to the treatment of the experimental data).

2.3.2. Validation

Table 5 shows comparisons of local pressure values for five discharge combinations. Given the 1% or less error for the majority of the runs, the validation using the local pressure values is satisfactory. Table 3 also shows comparison of outlet discharges for 14 discharge combinations as a second validation. Big majority are within an error margin of 10% and less which is acceptable. Water levels in the manhole and the first supply tank were compared for the same 14 discharge combinations (Table 5) which gave lower error margins despite the high turbulence intensity near that region. Water levels in the first supply tank however were not matched very closely (error near 10%). This is presumably due to the deficiencies of the VOF method and/or air-water mix capabilities of RANS based transient simulation. Also both the free surface and boundedness requirements are believed to be causing the larger error margin in discharge compared to pressure.

Table 5. Comparisons between experimental (EM) and numerical modelling (NM) for each discharge combination (DC) along with the error (E)

DC (l/s)	EM (l/s)	NM (l/s)	E (%)	EM (mm)	NM (mm)	E (%)	EM (mm)	NM (mm)	E (%)	EM (Pa)	NM (Pa)	E (%)
Outlet Discharge comparison for each discharge combination			Water level comparisons in the manhole			Water level comparisons in the first supply tank			Average Pressure			
0.1-0.1	0.19	0.18	-5.3	65	62	-4.6	59	54	-8.5	760	765	0.7
0.1-2.0	1.82	1.74	-4.4	130	119	-8.5	106	98	-7.6	856	925	8.0
0.5-1.0	1.22	1.39	14.0	98	95	-3.1	96	97	1.0	-	-	-
0.5-1.5	1.74	1.79	2.9	116	115	-0.9	105	98	-6.7	-	-	-
1.0-1.0	1.75	1.88	7.4	108	104	-3.7	108	99	-8.3	-	-	-
1.0-2.0	2.71	2.61	-3.7	139	137	-1.4	128	125	-2.3	-	-	-
1.8-0.5	2.15	2.23	8.4	109	111	1.8	119	109	-8.4	-	-	-
1.8-1.8	3.08	3.09	0.3	138	138	0.0	139	130	-6.5	-	-	-
2.0-0.8	2.41	2.66	10.4	114	116	1.8	131	113	-13.7	871	862	-1.1
2.0-1.0	2.67	2.70	1.1	126	123	-2.4	131	119	-9.2	-	-	-
2.5-0.1	2.20	2.46	11.8	109	106	-2.8	135	123	-8.9	-	-	-
2.5-0.8	2.86	3.19	11.5	125	120	-4.0	140	127	-9.3	953	933	-2.1
2.5-1.0	3.03	3.31	9.2	129	126	-2.3	142	137	-3.5	974	968	-0.6
2.5-2.0	4.17	3.79	-9.1	157	151	-3.8	158	144	-8.9	-	-	-

3. RESULTS AND DISCUSSION

3.1. Investigation of the Original System

With the acceptable validation, the CFD model was subsequently used to investigate the performance of the system using design and maximum capacity discharges. Another goal here was to identify the systems problem once again using the numerical model.

First, the supply tanks were removed from the domain. Pipe's input discharge was determined according to Manning's equation as given in the regulations [17] to be 13.61 l/s. Outlet pipe's design discharge is 15.52 l/s. Secondary corrugated pipe's design discharges are 4.93 and 1.39 l/s. Outlet pipe's discharge capacity is high because of the high slope. Stormwater system should ideally deliver no more than 90% of the design capacity according to the regulations. 90% operating condition also represents the maximum filling conditions for this system. In the CFD model, both 100% and 90% usage were considered. Possible operational problems were: (i) possibilities of overflow through the manhole cover, (ii) outlet discharge being equal to total inlet discharge and (iii) exceeding water levels at 90% along the main pipes. The inlet boundary conditions were fixed to represent 90% fullness at initialization. Fair, Geyer and Okun [17] formed a diagram based on Manning's equation to help designers obtain gross flow parameters using the degree of fullness or vice versa at a given section, which was used here.

Next, the structure was tested numerically without adding secondary pipes to the manhole. It was observed in this case that the system didn't have overflow or backflow problems. The first supply tank was added to the system again in order to show the backflow effect (Figure 4). It is understood that the secondary pipes are the main cause of the backflow. Nevertheless, adding the secondary pipes was inevitable for the authorities because the accumulated stormwater must be discharged in that new area.

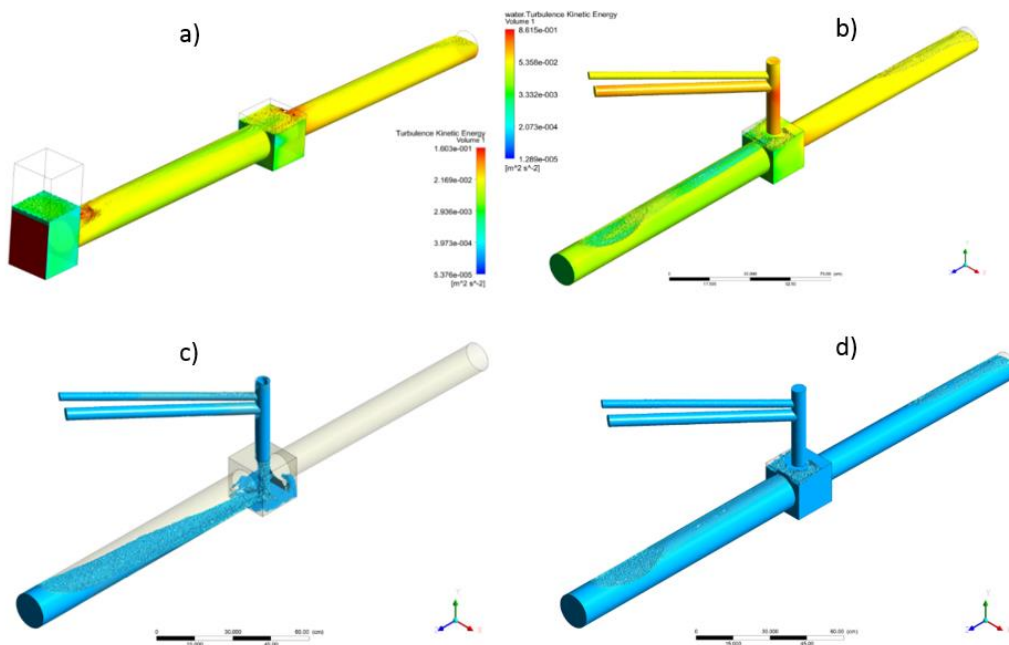


Figure 4. CFD model results: a) turbulence kinetic energy (TKE) without the manhole and secondary pipes, b) TKE with the manhole and secondary pipes (TKE parameter was used to colour the water volume fraction to help assess the level of mixing at a given domain), c) fast overflow in the manhole for 100% using conditions, d) the filled domain with storm water for 100% using conditions

The following results are for 100% using conditions. The outlet discharge reached 16.75 l/s within 2 seconds and became stable while it should be 15.51 l/s according to Manning’s equation. This result makes the standards in the regulation questionable for this particular storm water structure. CFD results also show the overflow discharge from the manhole to be 2.05 l/s while it should be “0” according to the regulations. This overflow shown in Figure 4 was also observed in the physical model tests.

3.2. Implications for Remedial Measures

In an effort to provide solution to the overflow and backflow problems, three new manhole geometries were designed and are shown in Figure 5. They were tested with full and 90% capacity discharges focusing on increasing manhole’s outlet discharge capacity and decreasing the turbulence level in the manhole. The latter is a measure of the water mix due to drop of water into the manhole.

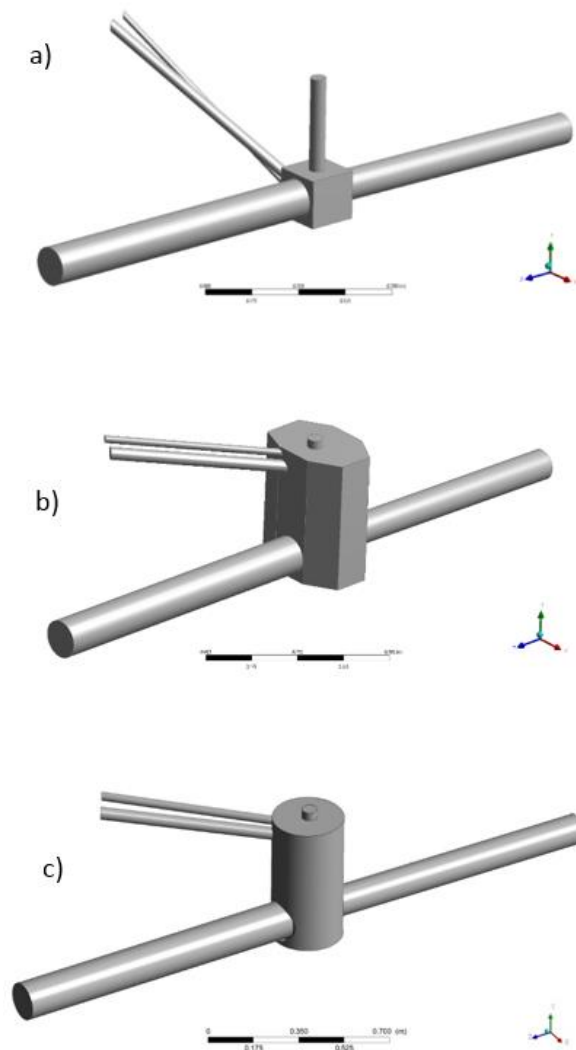


Figure 5. Three new geometry improvements: (a) alternative 1; (b) alternative 2; (c) alternative 3

In the first design, slopes of secondary corrugated pipes were directly integrated to the same manhole (Figure 5a). Although secondary pipe’s discharges were changed according to Manning equation (because the slope changed), overflow suddenly occurred in the manhole (Figure 6). In fact, the important one is original discharges, because they were obtained from a hydrological study. The first

alternative is found to be preventing the overflow. Water level is fixed at 225 mm in the manhole as shown in Figure 6b. Nevertheless, the new slopes of the secondary pipes exceed the acceptable levels in the regulations. High slopes also cause high velocity and turbulence in the manhole.

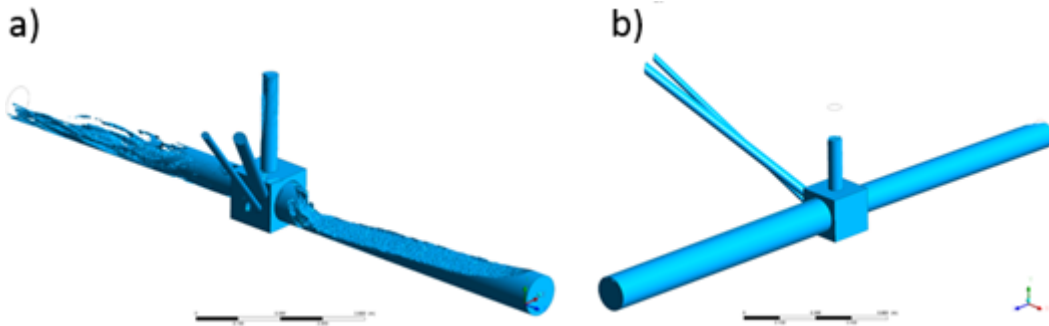


Figure 6. Alternative 1: Fast overflow for new discharges in the manhole (a) and operating condition with previous discharges (b)

Second design is intended to increase the manhole's volume for retention with the hexagonal geometry (Figure 5b, 525 mm high and 160 mm for each edge). Slopes and discharges remained the same for all pipes. Upper side of the manhole was kept the same as the original. Second alternative can easily discharge entered stormwater from the system as shown in Figure 7. This condition uses maximum discharges from Manning equation for all pipes (worst-case scenario). Although the sharp sides contribute to the mixing, the higher volume is then enough to decrease the mixing level. This alternative was also tested for normal operating conditions (also called minimum condition in the regulation, Figure 7b) and it is a potential solution although not economical.

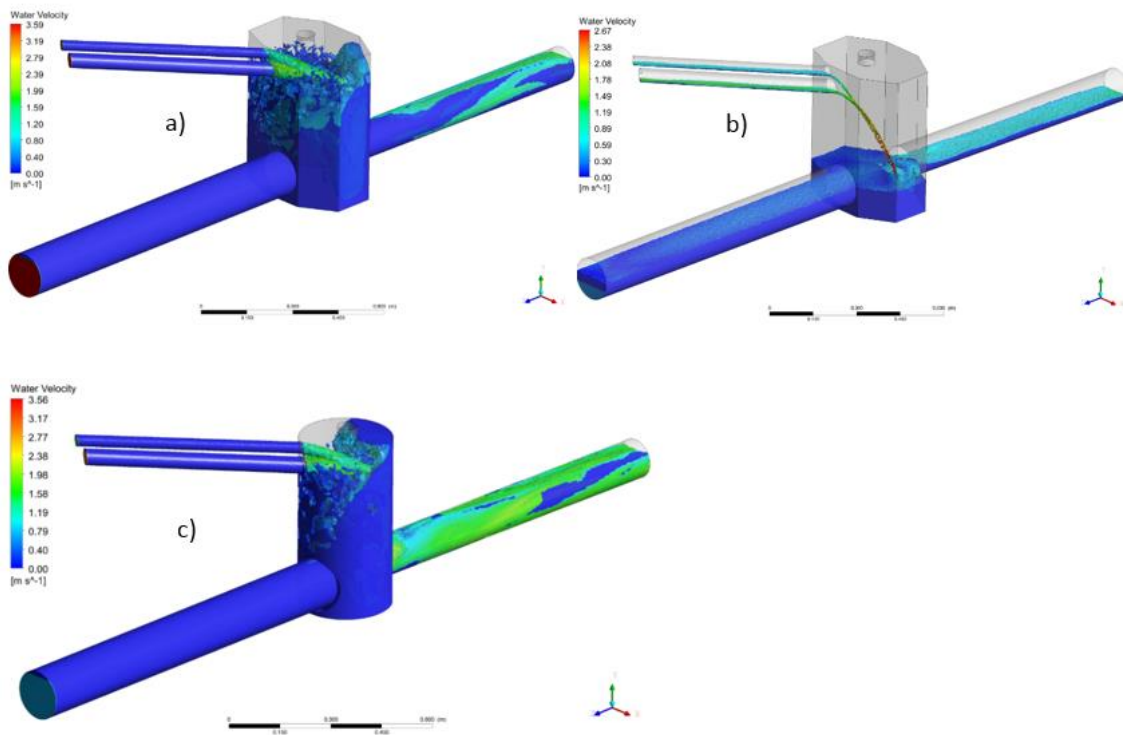


Figure 7. Alternative 2 in maximum operating condition (a); and in minimum operating condition (b); alternative 3 in maximum operating condition (c), all with water velocity rendering the volume fraction

Third design is a larger circular manhole (Figure 5c, 525 mm high and 280 mm in diameter). It is not only increasing the manhole's volume for retention using a simpler and more practical geometry, but also aiming to decrease the mixing level in the manhole. Figure 7c shows that third alternative easily discharges the storm water from the system in maximum operating conditions. Maximum water velocity profiles are almost the same with alternative two. Hence, it can be said that the circular and larger tank is a better solution.

All CFD models presented here indicate that the water levels in the pipes are below 90% even though the discharges are 90% of the operating conditions. Figure 8 shows the water levels in the pipes for alternatives 2 and 3.

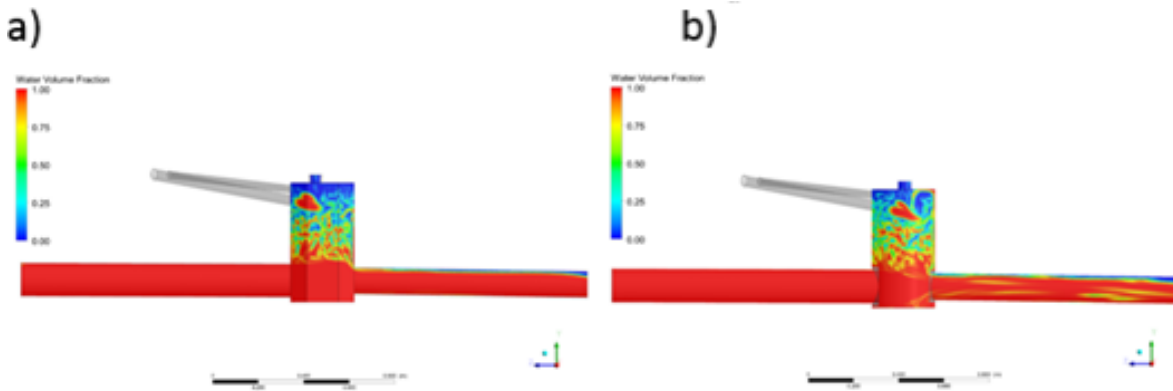


Figure 8. Water volume fraction for Alternative 2 (a) and Alternative 3 (b)

4. CONCLUSIONS

An existing and problematic stormwater drainage system was investigated using experimental and numerical modelling. Firstly, 1:10 scaled physical model was used to investigate the system experimentally. For the RANS based transient CFD models, mesh independency and comparison of turbulence models were performed. CFD model was successfully validated with experimental results in terms of pressure, outlet discharge and water levels. Overflow and backflow were observed in the system in both experiments and CFD models. High turbulence and mixing in the manhole as a result of secondary pipes is the cause of the backflow in the system. This is proved by observing that the outlet discharge is less than the total inlet discharges under design conditions. CFD model showed that outlet discharges and water levels are not always in agreement with the design values based on the regulations and Manning's equation. Therefore, conventional approaches fail to detect the problem and also are not useful in finding a solution. Three new manholes were designed and tested with the validated CFD model with alternative 3 selected to be the more suitable solution.

In light of the above discussion, with proper validation, CFD model is shown to be a powerful and effective tool for investigating, designing or rehabilitating stormwater drainage systems. Particularly, unconventional solutions to complex problems in such systems, where the empirical approaches fail to characterize, can be realized, tested and modified with less time and cost compared to experimental or field work.

ACKNOWLEDGEMENTS

Datasets for this research are included in this thesis: “Investigation of Stormwater Drainage Systems with Experimental and Numerical Methods”, (Yilmazer C. 2019). Also CFD model files or code that support the findings of this study are available from the corresponding author upon reasonable request. There is no funding source.

CONFLICT OF INTEREST

The authors stated that there are no conflicts of interest regarding the publication of this article.

AUTHORSHIP CONTRIBUTIONS

Cem Yilmazer: Experimental and numerical modeling, Methodology, Visualization, Writing – original draft. **Ahmet Ozan Çelik:** Supervision, Writing – review & editing.

REFERENCES

- [1] Saiyudthong C, Guymer I. Simulation of energy loss due to changes in pipe direction across a manhole. 10th National Conference on Civil Engineering 2005; 5-9.
- [2] Zhao CH, Zhu DZ, Rajaratnam N. Computational and experimental study of surcharged flow at a 90 combining sewer junction. J Hydraul Eng 2008; 134(6): 688-700.
- [3] Sousa V, Meireles I, Matos J, Almeida MC. Numerical modelling of air-water flow in a vertical drop manhole. 7th International Conference on Sewer Processes and Networks, 2013.
- [4] Beg NA, Carvalho RF, Lopes P, Leandro J, Melo N. Numerical investigation of the flow field inside a manhole-pipe drainage system. 6th International Symposium on Hydraulic Structures, 2016.
- [5] Motlagh YY, Nazemi AH, Sadraddini AA, Abbaspour A, Motlagh SY. Numerical investigation of the effects of combining sewer junction characteristics on the hydraulic parameters of flow in fully surcharged condition. Water Environ J 2013; 27(3): 301-316.
- [6] Chen Z, Han S, Zhou FY, Wang K. A CFD modeling approach for municipal sewer system design optimization to minimize emissions into receiving water body. Water Resour Manag 2013; 27: 2053-2069.
- [7] Isel S, Dufresne M, Bardiaux JB, Fischer M, Vazquez J. Computational fluid dynamics based assessment of discharge-water depth relationships for combined sewer overflows. Urban Water J 2014; 11(8): 631-640.
- [8] Kaur K, Laanearu J, Annus I. Numerical study of Tallinn storm-water system flooding conditions using CFD simulations of multi-phase flow in a large-scale inverted siphon. IOP Conf. Ser.: Mater. Sci. Eng. 2017; 251: 121-128.
- [9] Beg NA, Carvalho RF, Leandro J. Comparison of flow hydraulics in different manhole types. Proceedings of the 37th IAHR World Congress 2017; 6865: 4212-4221.

- [10] Özölçer IH, Dündar O. Determination of energy loss coefficient of rainwater and sewer manholes with CFD. *Fresenius Environ Bull* 2017; 26(7): 4716-4725.
- [11] Beg NA, Carvalho RF, Leandro J. Effect of surcharge on gully-manhole flow. *J. Hydro-Environ Res* 2018; 19: 224-236.
- [12] Wang J, Vasconcelos JG. Manhole cover displacement caused by the release of entrapped air pockets. *J Water Manag Model* 2018; 26(444): 1-6.
- [13] Beg NA, Carvalho RF, Leandro J. Effect of manhole molds and inlet alignment on the hydraulics of circular manhole at changing surcharge. *Urban Water J* 2019; 16(1): 33-44.
- [14] Yilmazer C. Investigation of Stormwater Drainage Systems with Experimental and Numerical Methods. MSc, Eskişehir Technical University, Eskişehir, Turkey, 2019.
- [15] Ansys Inc. ANSYS meshing user's guide. Canonsburg, PA, USA: 2010.
- [16] Ansys Inc. ANSYS CFX – Pre User's Guide, Release 15. Canonsburg, PA, USA: 2013.
- [17] Fair GM, Geyer JC, Okun DA. Elements of Water Supply and Wastewater Disposal. John Wiley & Sons 1971.



RESEARCH ARTICLE

RECOVERY OF BORON WASTES WITH INORGANIC ACID

Emine YOĞURTCUOĞLU^{1,*}

¹ Niğde Ömer Halisdemir University, Mining Engineering Department, 51240, Niğde, Turkey

ABSTRACT

Approximately 73-74% of boron mineral reserves all over the world are located in the Western Anatolian region of Turkey, in the provinces of Eskişehir, Kütahya, Balıkesir, and Bursa. The most intense minerals extracted from these fields are colemanite, ulexite, and tincal minerals, respectively. The general principle in the recovery of these minerals is to extract the raw ore and obtain it by size reduction processes of concentrates in high grade. In addition to concentrates, boric acid (H_3BO_3) production is also possible in Balıkesir and Kütahya. The production of this acid in question includes a series of processes from dissolution with sulfuric acid at high temperatures to crystallization. In this study, except for the aforementioned high concentrations, boron recovery from clay waste, which is high in boron content and is collected from plant waste ponds, is investigated. For this purpose, ulexite-colemanite-containing slime wastes of the Bigadiç (Balıkesir) Plant were dissolved in 7% solids at 60°C in different sulfuric acid concentrations (1-6% H_2SO_4) and were obtained with 83-97% B_2O_3 recovery. When the boron wastes are evaluated, issues such as the discovery and establishment of a new waste pond/dam will be solved, the valuable content in the wastes will be recovered, and the environmental problems of boron and other contents in clay will be eliminated. This article includes information about the characterization of the structure by considering the dissolution of boron and other compounds, as well as obtaining boric acid from inorganic acid and boron wastes.

Keywords: Boron waste, Colemanite, Ulexite, Inorganic acid, Sulfuric acid

1. INTRODUCTION

Boron (B), which is the first element of group 3A of the periodic table, is found in compounds with oxygen bonds due to oxygen affinity, although it is in the content of more than 150 minerals, with the properties indicated in Table 1. While the use of boron in Turkey dates back to ancient times, it is known that it was used in the production of tiles in Anatolia in the 1860s [1, 2].

Table 1. General properties of elemental boron [1, 2].

Properties	
Chemical symbol	B
Atomic number	5
Atomic weight	10.81-10.82
Melting point	2200°C
Boiling point	2250°C

The boron deposits located in Western Anatolia, the easternmost part of the Aegean Expansion Province, consist of two parts. The first part is the Izmir-Balıkesir Transfer Zone (IBTZ), which includes the Bigadiç, Sultançayır, and Kestelek basins, and the second part is the northern part of the Menderes Massif, where the Selendi and Emet basins are located. The Kırka boron deposit, located within the volcano-stratigraphic sequence, contains a completely different geological environment further east [3, 4].

*Corresponding Author: eyogurtcuoglu@ohu.edu.tr

Received:24.11.2022

Published: 28.03.2024

Borate deposits consist of three main groups: skarn (containing silicate and iron oxide), magnesium oxide (marine evaporitic sediment), and sodium-calcium borate hydrates (playa lake) group. Five formation steps are required for playa-lake volcano-sedimentary boron deposits. These occur as follows [3, 5] (Figure 1):

- The creation of a Playa-lake media,
- The enrichment of boron in this lake, which contains from andesite to rhyolite, and the deposition of either hydrothermal solutions or ash-fall sediments within the basin along the graben faults.
- Thermal resources near volcanism
- Conditions of an arid or semi-arid climate
- Alkaline pH conditions of lake water (varying between 8.5-11)

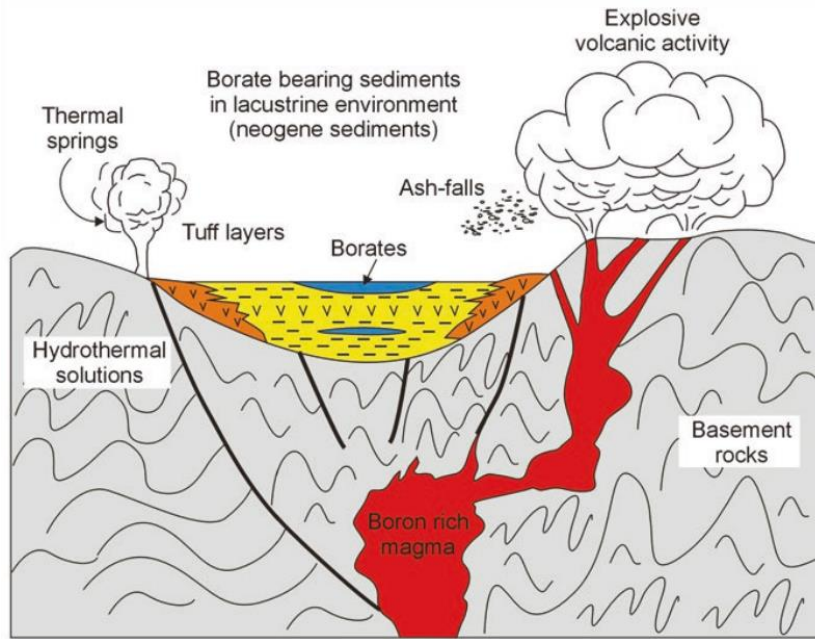


Figure 1. According to the generalized Playa lake sedimentation model, the formation of boron deposits in the Neogene basins in Western Anatolia [5]

Volcanics range from acid to base, where volcanic activities are very common, and pyroclastic rocks with sediments have been observed around the playa-lakes that form the borate deposits in Turkey [6].

Compared to the world, Western Anatolia has an important place with its reserves of around 73-74%. Colemanite (Kütahya-Emet, Balıkesir Bigadiç, Bursa Kestelek), ulexite (Balıkesir-Bigadiç), and tincal (Eskişehir-Kırka) minerals are the most abundant boron minerals in Turkey [6-10]. The densities of colemanite and ulexite minerals are 2.4 and 1.98 g/cm³, respectively [11]. The country rock minerals of boron ores are composed of carbonates and silicates, and the densities of these minerals are 2.6-2.7 g/cm³ [12]. The formulas and % B₂O₃ amounts of the commercially important boron minerals found extensively in Turkey are given in Table 2 [8, 10, 13, 14].

Table 2. Properties of some commercially important boron minerals [8, 13].

Mineral name	Formula	B ₂ O ₃ , %
Colemanite	Ca ₂ B ₆ O ₁₁ .5H ₂ O	50.8
Ulexite	NaCaB ₅ O ₉ .8H ₂ O	43.0
Tincal/Borax	Na ₂ B ₄ O ₇ .10H ₂ O	36.5
Pandermite	Ca ₄ B ₁₀ O ₁₉ .7H ₂ O	49.8
Propertite	NaCaB ₅ O ₉ .5H ₂ O	49.6

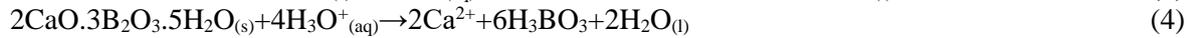
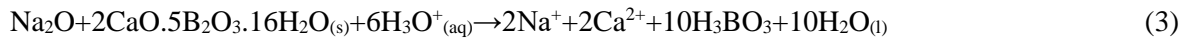
In general, the recovery principle of crude boron is based on physical recovery methods including size comminution and classification [15]. Some of the common names of crude boron products are known as tincal concentrate, ulexite concentrate, colemanite concentrate, ground colemanite. In addition, refined products are also known by names such as refined/calcined borax pentahydrate, refined/calcined borax decahydrate, boric acid, anhydrous boric acid, synthetic/calcined/refined colemanite, calcined tincal, calcined ulexite [7, 16]. Concentrated boron products are used in many industries such as glass-glass fiber, metallurgy-materials, agriculture, textile, cleaning, ceramics and medicine. In addition to these areas, refined boron products can also be used in many industries such as military, electronics, photography, cosmetics and aerospace [11].

Boric acid, which is one of the refined products, is obtained especially from the boric acid plants established in Emet (Kütahya) and Bandırma (Balıkesir) regions, especially with colemanite [17, 18]. Obtaining this acid from concentrated ores consists of a series of processes such as dissolving in sulfuric acid solutions at high temperatures (80-90°C), separation from impurities, filtration, cooling, evaporation, crystallization, and washing, and drying of crystals [19-21].

The two-stage separation of H₂SO₄, which is used for boric acid production, by dissolving into its ions in water is given below [20-24] (1-2):



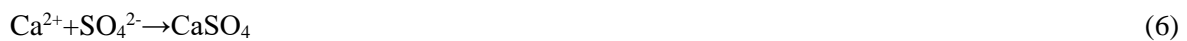
The equilibrium constant (2) for the second reaction is $K_a = 0.012$. It is suggested that the following reactions will occur when the minerals ulexite [22, 23] (3) and colemanite [24] (4) are added to this solution:



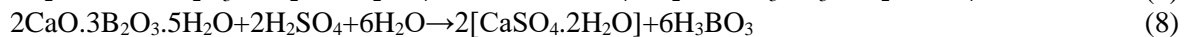
When Ca²⁺ concentrations reach a limiting value determined by the product of solubility (K_{sp}) (5);



The ion [SO₄²⁻] obtained by the 2nd reaction of sulfuric acid creates the following reaction (6).



Thus, a solid precipitate is obtained [21-24]. Finally, the dissolution reactions of sulfuric acid are as follows for boron minerals ulexite [22]; [23] (7) and colemanite minerals [8, 19, 20, 24-28] (8):



In Turkey, after the recovery of crude boron products, a large amount of high-grade B₂O₃-containing waste is collected in waste ponds/dams. While the amount of waste from these areas in 2001 was around 2 million tons [2], it is estimated that the 4 waste ponds in the Balıkesir/Bigadiç region recently exceeded this amount [20].

Recently, many different methods have been applied in the evaluation of boron wastes. Some of these evaluations can be made in the form of the recovery of boron contents in the waste, the use of all the contents, or other (except boron) contents in the waste in different sectors such as ceramics and building [2, 7, 29-31]. One of the most appropriate evaluations is the use of the remaining structures in appropriate industries after the recovery of boron from wastes. Therefore, this strategic mineral can be brought into the economy, and the remaining products such as clay can be used in other industries, as well as the environmental impact of waste can be eliminated [32].

In this context, in this study, ulexite-colemanite-containing wastes in the waste ponds of Etimaden Plant Balıkesir/Bigadiç Boron Operation Directorate between 1980-1995 have been evaluated. For this purpose, it was investigated whether the boron contents of these fine-grained processed wastes can be recovered from inorganic acids by dissolving them with sulfuric acid. Therefore, a preliminary evaluation will be carried out in order to reveal all the processes in the recyclability of this and other boron wastes. Thus, the study aims to make predictions about the industrial-scale recycling process.

2. MATERIALS AND METHODS

2.1. Characterization Studies

In the study, representative samples taken from Etimaden Bigadiç Boron Mining Directorate waste ponds, leaching process liquids and solid samples of waste were analyzed in Bigadiç Research laboratories.

In this context, chemical analyzes (using the melting method) for feed (main waste) sample and leaching wastes were carried out with the Rigaku ZSX Primus XRF (X-ray fluorescence) device.

For particle size distribution analysis, analyzes were carried out using the laser diffraction method with the Malvern Mastersizer 3000 device. Analyzes were obtained in an aqueous environment by taking the average of 3 samples.

Additionally, B₂O₃ analyzes were repeated using the titration method. LOI (loss on ignition) analyzes were carried out using the gravimetric method.

Experiments were carried out in the Sample Preparation Laboratory at the Central Research Laboratory of Niğde Ömer Halisdemir University (NOHU). Dissolution of the samples was done in a fume hood with a heated magnetic stirrer.

2.2. Reagents

The acid used during the experiments is Tekkim (Turkey) 95-98% H₂SO₄ (sulfuric acid). The acid solutions diluted with distilled water between 1-6.1% were adjusted to a 7% solids ratio, and then processes of dissolution were carried out.

2.3. Samples

For the experiments, the samples obtained from four waste ponds in Bigadiç (Balıkesir) depending on their quantity (around 60-65 kg in total) were dried. The dried sample (approximately 30 kg) was blended, divided in a way that it would be approximately 2 kg by coning and quartering method, and packaged. Experimental samples of about 100-120 g were obtained by re-dividing these packages.

The experiments were carried out under 60 minutes leaching time, 60°C leaching temperature, 7% solids ratio, 1500 rpm stirring speed, and approximately 1-2-3-4-6 H₂SO₄ concentration conditions. At the end of the experiment, the solution was filtered, and the solid part was washed several times and dried. Solid (secondary waste) and liquid samples were sent to the Etimaden Bigadiç plant analysis laboratory, and analyzed (Figure 2).

The feed sample (FS) in which the test was performed is the main waste sample with 11.43% B₂O₃ content. After the experiments, secondary waste samples were designated with the code "WS" and these samples were numbered 1-2-3-4-5 according to their acid concentrations (1-2-3-4-6%).



Figure 2. Leaching process (left image), filter and leaching liquid (medium image), and the resulting filter cake (right image)

The reason why the 7% solids ratio was chosen for the experiments is that mixing cannot be achieved at higher solid ratios due to the clay structure of the sample. The experiments were carried out in 2000 ml beakers. In experiments to be carried out with solid ratios lower than this solid ratio, the solid (waste) sample required for analysis cannot be obtained. In addition, it was thought that lower solid ratios could cause difficulties in the analysis and could harm the industrial-scale prediction of the study.

3. RESULTS & DISCUSSION

3.1. Particle Size Distribution

The particle size distribution of the test sample was analyzed by laser diffraction method since it was a slime-sized sample taken from the waste pond. Analysis results were determined as d_{90} = 81.9 μ m and d_{50} = 16.5 μ m in Figure 3.

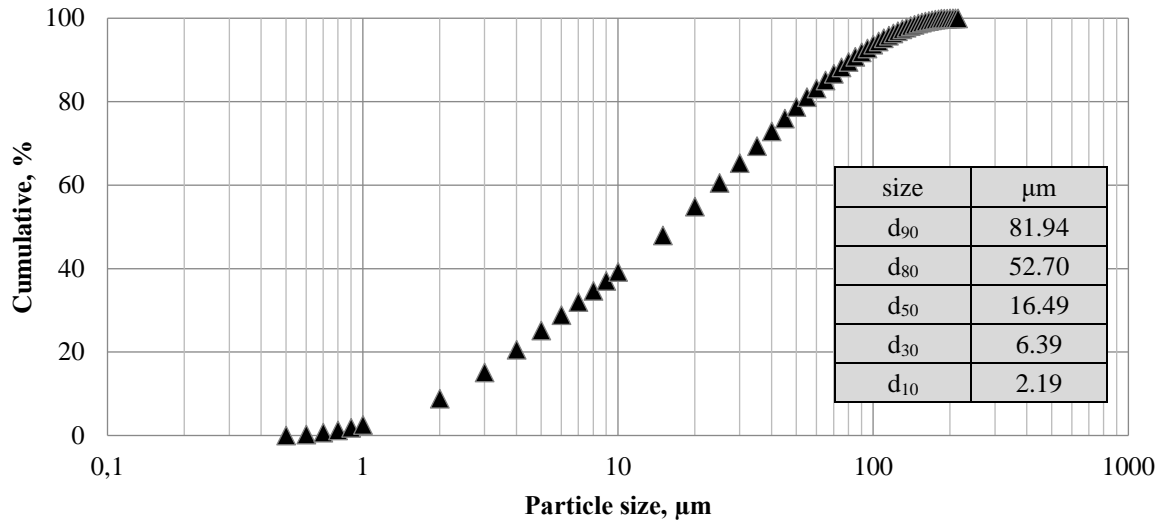


Figure 3. Particle size distribution of waste sample

3.2. Dissolution Results

Chemical analysis results of feed sample and leaching process waste samples are given in Figure 4-5 and dissolution results are given in Figure 6-7. Figure 2 shows the analysis results of Na_2O , Fe_2O_3 , SrO , and Al_2O_3 . Especially Na_2O (1-0.05%) and Al_2O_3 (4-1%) contents decreased as a result of the experiments. It indicates the presence of Na_2O ulexite mineral. The other two compounds did not change much.

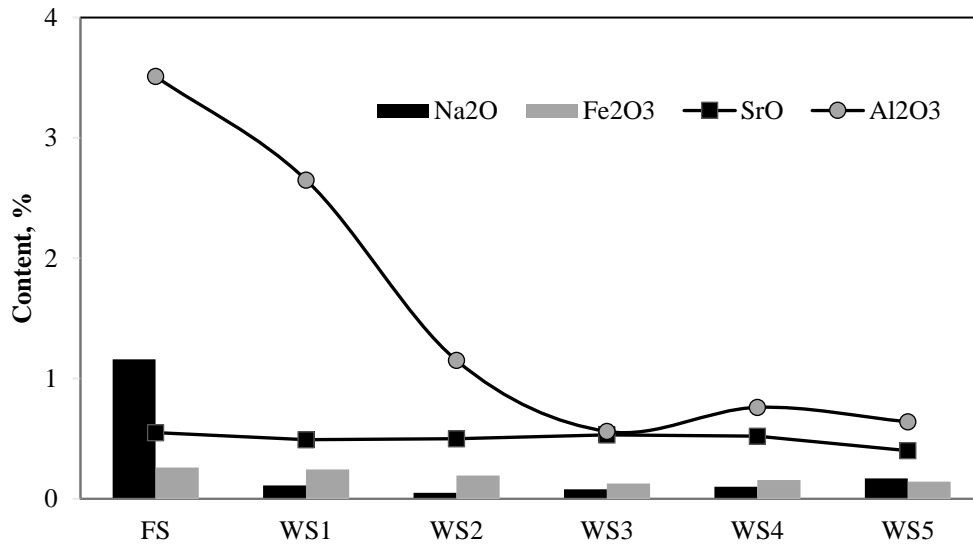


Figure 4. Chemical analyses result of feed and waste samples 1 (Na_2O , Fe_2O_3 , SrO , and Al_2O_3 , %)

In Figure 5, CaO , SO_3 , MgO , and SiO_2 analyses are observed. The increase in the amount of SO_3 is directly related to the sulfuric acid. It was determined that the CaO analysis values (around 16%) progressed steadily, the SiO_2 content increased towards WS3 and then decreased towards the same point

as in the feed sample. MgO, on the other hand, was observed to be too low to be detected in the WS3 experiment (24-1%) and then increased to around 4-8%. B₂O₃ is approximately 11.5% and changes to 0.5-1.8% at the end of leaching processes.

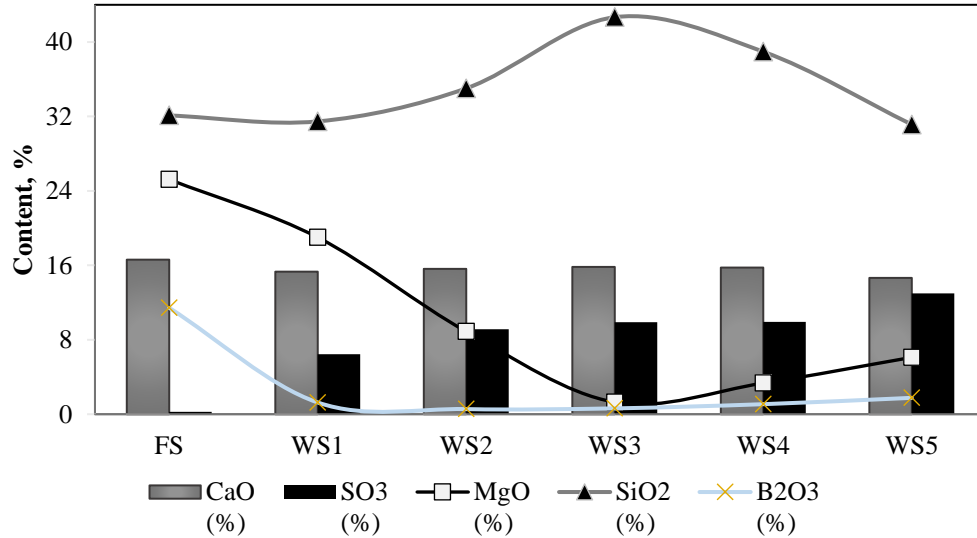


Figure 5. Chemical analyses result of feed and waste samples 2 (CaO, MgO, SO₃, SiO₂, and B₂O₃, %)

In Figure 6, CaO and SrO progressed to near solubility values up to WS4. In WS5, CaO increased more (44%), while SrO decreased in the opposite direction (19%). This situation of CaO is due to its precipitation in the form of CaSO₄, generally turning into gypsum in sulfuric acid dissolution processes. SO₃ increased due to the increase in sulfuric acid concentration. When compared to other compounds, the SiO₂ solubility varies between 5-18%, indicating that it is the least soluble compound.

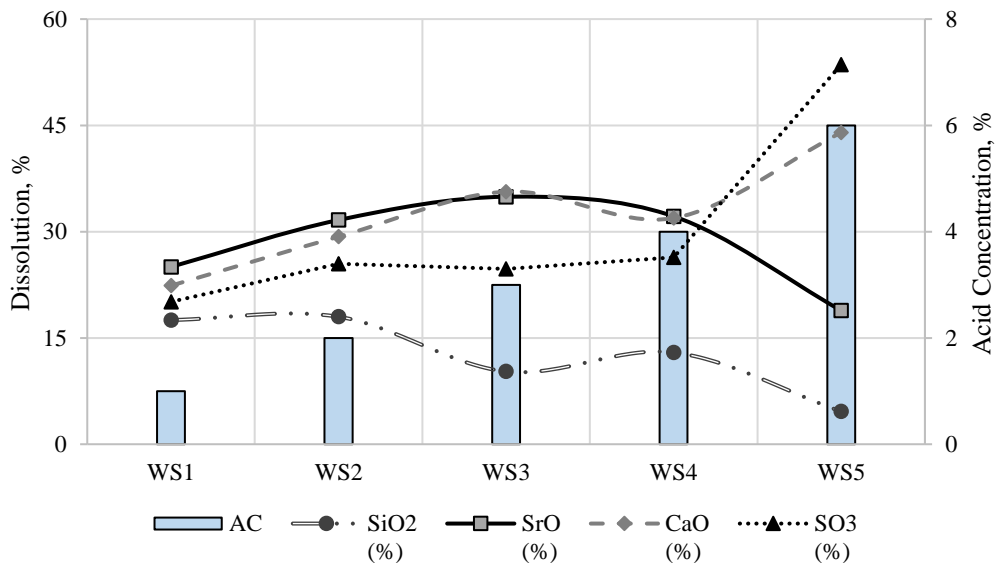


Figure 6. According to acid concentration (AC), %, dissolution of waste samples 1 (SiO₂, SrO, CaO, and SO₃, %).

Figure 7 examines the dissolution of the compounds found in 2. The solubility of Na₂O is in the range of about 84-97%, and while the acid concentration is the highest, the solubility is the lowest. Other compounds were particularly elevated in the WS3 experiment and then decreased to WS2 levels.

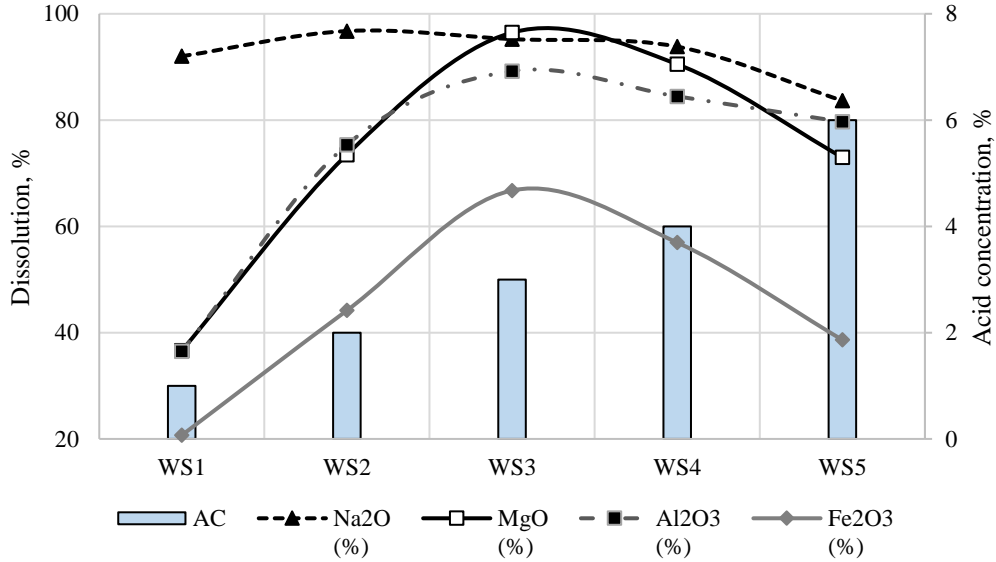


Figure 7. According to acid concentration (AC), %, dissolution of waste samples 2 (Na₂O, MgO, Al₂O₃, and Fe₂O₃, %)

3.3. Recovery Results of B₂O₃%

The %B₂O₃ recovery efficiencies were calculated with the solid waste and dissolved liquid analyses obtained as a result of the dissolution experiments in which different amounts of sulfuric acid were investigated and shown in Figure 8. These calculations are based on %B₂O₃ in solid (waste) analysis results and B (ppm) element in liquid concentrate analysis.

According to the acid leaching results, %B₂O₃ recovery yields were obtained with approximately 83-97%. Although these efficiencies tend to increase in general, it is observed that the recovery decreases in the experiment at the 6% concentration, where the amount of acid concentration is the highest. It is possible that this situation may be caused by reasons such as the reaction cannot occur after a certain acid concentration is exceeded, and the possibility of this inorganic acid reaction being reversible.

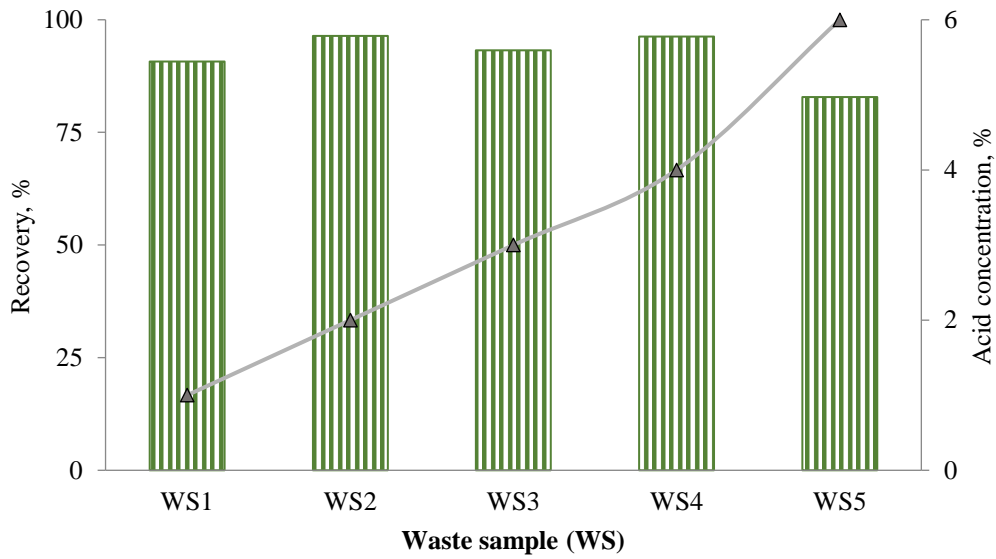


Figure 8. According to acid concentration (AC), %, % B_2O_3 Recoveries of waste samples

Similarly, when boron (38 ppm boron) from Qaron Lake waters was removed from the loaded resin using 10% sulfuric acid, boron elution efficiency was determined as 75.04% [33]. In different studies examining the solubility of colemanite [24] and ulexite [23], it was determined that the solubility decreased with the increase in acid concentration at a concentration of 0.5-2M sulfuric acid. The main reason for this can be explained as the increase in the formation of SO_4^{2-} ions per unit volume and the formation of solid $CaSO_4$ and $CaSO_4 \cdot 2H_2O$ in the environment as in Reaction 6 [23, 24, 34, 35]. After this stage, the final production of pure boric acid can be achieved from this solution, as in the Boric Acid Plants, after the purification stage, crystallization, and washing-drying processes [19-21].

Literature studies on Bigadiç sludge waste are generally on flotation studies, and positive results have been obtained in these studies [29, 36]. Some of the hydrometallurgical studies carried out are as follows:

As a result of a study in which a heap leaching experiment was performed with the same acid (4.7% H_2SO_4), the % B_2O_3 recovery efficiency was approximately 80% [20]. In the experiments investigated for these wastes, organic acids with citric acid at 8-12% solid ratios, 40-98°C temperatures, 20-66 minutes, and 0.15-0.45M acid concentrations, recoveries in the range of 60-95% were achieved [37, 38]. A result of approximately 90% was also possible in the studies conducted for the recovery of B_2O_3 with acetic acid (2-22% concentrations) from wastes [11].

In this study, the solid ratio in dissolution experiments is an important parameter when considering industrial dimensions. Because the more solids dissolve with less liquid, the lower the chemical consumption, the lower the water consumption. For this reason, the fact that the experiments were carried out at a rate of 7% can be seen as negative. However, boron wastes swell in aqueous media due to their dense clay content and mixing becomes a problem. Additionally, it is a remarkable output that the experiments reached over 90% B_2O_3 recovery efficiencies in a short time of 1 hour. These results are important in terms of their application both in Bigadiç wastes and in other boron plant wastes in Turkey. Thus, it will be possible to obtain boron from these wastes and to use the remaining content in different sectors and/or feed it back to the open pit.

The utilization of boron wastes will provide additional income by helping to obtain refined products such as boric acid from the wastes accumulated in the waste ponds/dams since the beginning of

production from their plants. In addition, it will be able to solve the location problem of ponds/dams and environmental issues related to boron and other content in wastes [20, 39, 40].

Consequently, for the success of this study on an industrial scale, pilot-sized, more applicable leaching tanks, and better mixing speeds are required. Therefore, by increasing the % solid ratio, it will be possible to achieve similar boric acid recoveries in which more solids can be processed with the same acid concentration (or near this value).

4. CONCLUSIONS

In this study, the high boron content (11.5% B₂O₃) in Bigadiç slime waste was dissolved with sulfuric acid, an inorganic acid. The boron minerals in this waste sample indicated the presence of ulexite and colemanite minerals due to their chemical content of sodium, calcium, and boron. The remaining part of the sample consisted of a dense clay structure.

The optimum condition of the leaching experiments was obtained from the experiment where the acid concentration was 2%, and the B₂O₃ leaching efficiency was determined as 96.38%. The reason for obtaining the lowest efficiency at 6.1% acid concentration was the increase in SO₄⁻² ions per unit volume. Therefore, solid CaSO₄ and CaSO₄·2H₂O were formed in the environment.

In conclusion, the study showed that Bigadiç and other boron plant wastes can be recycled. Correspondingly, it has been revealed that these valuable contents can be recovered, the remaining contents such as clay can be used in different areas, and the reusability of waste ponds and the search for space can be helped by eliminating their environmental impacts.

ACKNOWLEDGMENT

The author would like to thank the Bigadiç Boron Operations Directorate for all their contributions.

CONFLICT OF INTEREST

The author states that there are no conflicts of interest regarding the publication of this article.

REFERENCES

- [1] Kılınç E, Mordoğan H, Tanrıverdi M. Importance, Potential, Production and Economy of Boron Minerals (in Turkish). In: 4. Industrial Mineral Symposium. Izmir, Turkey; 2001:226–235.
- [2] Kilic AM, Kilic O, Andac I, Celik AG. Investigation of Possibilities on Usage of Low Grade Boron in Sectoral Areas (in Turkish). In: 4. Industrial Boron Symposium. Eskişehir, Turkey; 2009:35–42.
- [3] Helvacı C. Geological Features of Neogene Basins Hosting Borate Deposits: An Overview Of Deposits and Future Forecast, Turkey (in Turkish). Bulletin of the Mineral Research and Exploration 2015; 0(151). doi:10.19076/mta.75175.
- [4] Helvacı C. Geological Features of Neogene Basins Hosting Borate Deposits, West Anatolia, Turkey. In: 71st Geological Congress of Turkey; 2018:28–31.
- [5] Helvacı C. Chapter 11 Turkish Borate Deposits: Geological Setting, Genesis and Overview of the Deposits. In: Mineral Resources of Turkey, Modern Approaches in Solid Earth Sciences, 16;

2019:535–597.

- [6] Helvacı C. Turkish borate deposits : Geological setting, economic importance and boron policy (in Turkish). In: 5th Industrial Minerals Symp. İzmir, Turkey; 2004:11–27.
- [7] Guyaguler T. Türkiye Boron Potential (in Turkish). 4. Industrial Mineral Symposium 2001:18–19.
- [8] Bilal C. The reaction kinetics of colemanite with sulfuric acid (in Turkish). 2003.
- [9] Arslan V, Bayat O. Production of Boric Acid From Colemanite Ore by Oxalic Acid Leaching (in Turkish). Journal of Underground Resources/Yer Altı Kaynakları Dergisi 2016; (10):11–20.
- [10] Helvacı C. Borate deposits: An overview and future forecast with regard to mineral deposits. Journal of Boron 2017; 2(2):59–70.<https://dergipark.org.tr/boron/issue/31236/302668> Accessed.
- [11] Yoğurtcuoğlu E. Usage of acetic acid for boric acid production from boron wastes. Niğde Ömer Halisdemir University Journal of Engineering Sciences 2022; 11(3):819–825. doi:10.28948/ngmuh.
- [12] Gülsoy Ö, Ergün L, Can M, Mergen A, Ergül T, Aydın T. Alternative enrichment method for Bigadiç boron concentrator (in Turkish). In: 3. International Boron Symposium. Ankara, Türkiye; 2006:307–313.
- [13] Helvacı C. Mining, Dressing and Marketing problems of Borate Minerals (in Turkish). In: 3rd International Boron Symposium. Ankara, Türkiye; 2006:559–571.
- [14] Kipçak I, Özdemir M. Recovery of boron from the clay waste of boron industry by leaching. International Journal of Chemical Reactor Engineering 2012; 10(1). doi:10.1515/1542-6580.2468.
- [15] Şener S, Özbayoğlu G. Separation of ulexite from colemanite by calcination. Minerals Engineering 1995; 8(6):697–704. doi:10.1016/0892-6875(95)00030-T.
- [16] Elevli B, Yaman İ, Laratte B. Estimation of the Turkish Boron Exportation to Europe. Mining 2022; 2(2):155–169.
- [17] Evcin A, Ersoy B, Kavas T, Arsoy Z. Investigation on the Sinterability of Emet Boric Acid Factory Waste with Different Additives. 2015.
- [18] Boncukcuoglu R, Yilmaz MT, Kocakerim MM, Tosunoglu V. Utilization of borogypsum as set retarder in Portland cement production. Cement and Concrete Research 2002; 32(3):471–475. doi:10.1016/S0008-8846(01)00711-6.
- [19] Kalafatoğlu İE, Örs N, Özdemir SS. Dissolution behavior of Hisarcık colemanite with sulfuric acid (in Turkish). In: IV. National Chemical Engineering Congress. Istanbul, Turkey; 2000:263–268.
- [20] Yoğurtcuoğlu E, Dalgali O. Evaluation of Bigadiç Colemanite and Ulexite Slurry Wastes by Heap Leach (in Turkish). In: International Boron Symposium. Nevşehir, Türkiye; 2019:102–106.

- [21] Liu Y, Shi P, Mei X, Jiang M. Separation of boron and magnesium by stepwise crystallization of sulfuric acid leachate of high-magnesium borate minerals. *Hydrometallurgy* 2021; 204(March):105703. doi:10.1016/j.hydromet.2021.105703.
- [22] Tunç M, Yapıcı S, Kocakerim M, Yartasi A. The dissolution kinetics of ulexite in sulphuric acid solutions. *Chemical and Biochemical Engineering Quarterly* 2001; 15(4):175–180.
- [23] Gür A, Selçuk A. Studies on dissolution mechanism of ulexite in sulphuric acid. *Asian Journal of Chemistry* 2007; 19(5):3345–3352.
- [24] Gür A. Dissolution mechanism of colemanite in sulphuric acid solutions. *Korean Journal of Chemical Engineering* 2007; 24(4):588–591. doi:10.1007/s11814-007-0007-9.
- [25] Kuşçay Çelikoyan B, Bulutcu AN. Development of a new method for the boric acid production process from colemanite ore (in Turkish). *İTÜ Journal* 2010; 9(2):15–26.
- [26] İpeksever S, Yalçın A, Gönen M. Extraction of Boric Acid From Ulexite Mineral By Supercritical CO₂. In: 12. International Symp. on Supercritical Fluids. France; 2018:219–227.
- [27] Olufemi AS, Azeez MA, Olayebi OO. Process Intensification of Colemanite Leaching Using Sulfuric Acid in a Batch Process Intensification of Colemanite Leaching Using Sulfuric Acid in a Batch Reactor. *International Journal of Engineering Research and General Science* 2016; 4(November):149–160.
- [28] Bayca SU. Microwave radiation leaching of colemanite in sulfuric acid solutions. *Separation and Purification Technology* 2013; 105:24–32. doi:10.1016/j.seppur.2012.11.014.
- [29] Bentli İ, Özdemir O, Çelik MS, Ediz N. Boron Tailings and Evaluation Strategies (in Turkish). In: 1 st International Boron Symp.; 2002:250–255.
- [30] Oruç F, Sabah E, Erkan ZE. Evaluation Strategies of Boron Tailings according to Sector (in Turkish). In: II. International Boron Symposium; 2004:385–392.
- [31] Sabah E, Oruç F. Scientific Researches Conducted in Turkey for the Evaluation of Boron Wastes (in Turkish). II. Boron Workshop, 2004.
- [32] Baydır AT, Erdoğan Y. Dissolution Of The Rubidium From Eti Mine Kırka Boron Management Waste. *Afyon Kocatepe University Journal of Sciences and Engineering* 2013; 13(2):13–20. doi:10.5578/fmbd.6511.
- [33] Mahdy MA, El-Hussaini OM, A Wahab GM, El-Shahat MF. Extraction of Boric Acid from Bittern Solutions of Qaron Lake, Egypt by Ion Exchange. In: 2nd International Boron Symposium. Eskişehir, Turkey; 2004: 297-309.
- [34] Bulutcu AN, Ertekin CO, Kuskay Celikoyan MB. Impurity control in the production of boric acid from colemanite in the presence of propionic acid. *Chemical Engineering and Processing: Process Intensification* 2008; 47(12):2270–2274. doi:10.1016/j.cep.2007.12.012.
- [35] Taylan N, Gürbüz H, Bulutcu AN. Effects of ultrasound on the reaction step of boric acid production process from colemanite. *Ultrasonics Sonochemistry* 2007; 14(5):633–638. doi:10.1016/j.ultsonch.2006.11.001.

- [36] Göktepe F. Concentration Study of Bigadiç Boron Tailings by Flotation (in Turkish). In: 2nd International Boron Symposium. Eskişehir, Turkey; 2004:81–86.
- [37] Yoğurtcuoğlu E. The Production of Boric Acid With Citric Acid From Bigadic Bor Wastes (in Turkish). In: 1st International Conference on Environment, Technology and Management (ICETEM). Niğde, Türkiye; 2019:1054–1060.
- [38] Yoğurtcuoğlu E. The citric acid leaching of boron process wastes. *Canadian Metallurgical Quarterly* 2023; 62(4):773–790. doi:10.1080/00084433.2022.2131132.
- [39] Batar T, Bayca S, Solak O, Sayin E, Can E, Kahraman B. Effects of boron ore and its tailings to the ceramic wall tile structure (in Turkish). In: 6th International Industrial Minerals Symposium. İzmir, Turkey; 2007:328–333.
- [40] Sayin E, Batar T, Solak O, Yamik A, Tufan MB. Use of tincal ore and boron tailings in ceramic paste and water insulating monitor (in Turkish). In: 6th International Industrial Minerals Symposium. İzmir, Turkey; 2007:428–437.



RESEARCH ARTICLE

AN APPLICATION FOR THE CALIBRATION OF THE TWO-PRESSURE HUMIDITY
GENERATOR

Can EKİCİ * 

Gebze Calibration Laboratory, Turkish Standards Institution, Kocaeli, Türkiye

ABSTRACT

Two-pressure humidity generator (2-PHG) has capability to produce environments of known humidity with the “two pressure” method that is proven by NIST. The 2-PHG is supplied with known humidity values, the values can be used for instrument calibration, verification and such as other processes. The set point values can be entered from the device’s front panel by an operator. 2-PHG calculates the relative humidity from the pressure and temperature measurements with the formula. The computer controls the ratios on the formula to generate a known humidity value. 2-PHG has to have traceability for using on calibration processes of other devices; 2-PHG must be calibrated. This study represents an application of the 2-PHG calibration by using the guides and articles in the literature about the device. Calibration of the 2-PHG contains examination of the each parameter of the formula that was given for humidity calculation. Four temperature and two pressure probes that are saturation temperature probe, pre-saturation temperature probe, expansion valve temperature probe, chamber temperature probe, low pressure probe, high pressure probe help 2-PHG to calculate the formula. Calibration of the 2-PHG, also, contains the calibration of the temperature probes and the pressure probes. This study expresses an application of the calibration of a 2-PHG which is located in Turkish Standard Institution Gebze Calibration Laboratories and the uncertainty calculation of this application can be seen on this paper. Each uncertainty parameter of the formula and uncertainty parameters of the probes that are affected to the total uncertainty were calculated. For different temperatures and different relative humidities, the measurement uncertainty of this application was given on this paper. This study can be used as a supplementary document in the calibrations of the 2-PGH and in the new studies.

Keywords: Calibration, Humidity, Metrology, Two-pressure humidity generator

1. INTRODUCTION

Two pressure humidity generators are highly accurate for instrument calibrations, evaluations and verifications. The “two pressure” principle has been proven by NIST [1].

The two pressure humidity generator is supplied with continuous humidity values. An operator can input the set point values from the device's front panel. The two pressure humidity generator determines the relative humidity from pressure and temperature measurements by utilizing a formula. Operation of the humidity generator is based on the two-pressure method of producing known atmospheres of relative humidity and assumes that the water vapour pressure remains a fraction of the total pressure, known as Dalton's Law of Partial Pressure [1].

Saturating air with water vapor at a specific pressure and temperature is part of the two-pressure approach.

The saturated gas is isothermally lowered to chamber pressure as it passes through an expansion valve. If the temperature of the gas is held constant during pressure reduction, the humidity, at chamber pressure, may then be approximated as the ratio of two absolute pressures [2]. The following formula [1] can be used to determine relative humidity.

*Corresponding Author: canekici@gmail.com

Received: 28.02.2023

Published: 28.03.2024

$$\%RH = (P_{\text{chamber}} / P_{\text{saturation}}) * 100 \quad (1)$$

In this paper, calibration steps of the two humidity generator are given for an application in the Turkish Standard Institution. The uncertainty formulas were obtained from the publications of the "two pressure humidity generator." The uncertainty estimate for this application may be viewed in this paper. This study expresses an application of the calibration of a two pressure humidity generator that is placed in Turkish Standard Institution Gebze Calibration Laboratories. Each uncertainty parameter of the formula and uncertainty parameters of the probes that are affected to the total uncertainty were calculated. This document provides the measurement uncertainty for this application for various temperatures and relative humidities. Because there are few instances in the literature about the calibration of two-pressure humidity generators and their uncertainty calculations, this work may be helpful for future researches.

Equation 2 is used to compute relative humidities from pressure and temperature values [1]:

$$\% RH = P_c/P_s * e_s/e_c * F_s/F_c * 100 \quad (2)$$

The pressure ratio P_c/P_s is controlled by the computer, and the enhancement factor ratio is used to produce the known humidity, f_s/f_c , and the effective saturation level, e_s/e_c . Produced humidity is directly dependent on the measurement of pressures and temperatures and it does not rely on any other device for the measurement of water vapour content. Precision humidity generation is determined by the accuracy of the pressure measurements and it is dependent on the accuracy and uniformity of temperature inside the chamber [3].

Figure 1 shows the two-pressure humidity generator.



Figure 1. The two-pressure humidity generator

2. PROCEDURES FOR THE CALIBRATION OF THE TWO-PRESSURE HUMIDITY GENERATOR

Two pressure gauges with capacities of 50 psi and 150 psi are included in the device. A reference pressure calibrator with traceability was used to measure low (15 psi), medium (30 psi), and high (50 psi) pressure points for low pressure probes with 50 psi capacities, and low (50 psi), medium (100 psi,

and high (150 psi) pressure points for high pressure probes with 150 psi capacities. The pressure values and the actual temperature values were entered to the system through the program and the new coefficients for the device were calculated and recorded to the system. After then the creation of the coefficients on the device, two pressure probes were calibrated by the reference pressure calibrator which has got traceability. Euramet’s comprehensive calibration procedure was followed in the pressure calibration and the calibration was made with comparison method [4].

For the two pressure humidity generators to calculate the relative humidity, four temperature probes—saturation temperature probe, pre-saturation temperature probe, expansion valve temperature probe, chamber temperature probe— and two pressure probes— low pressure probe, and high pressure probe— are used. First, the device's four temperature probes were measured at the temperatures on 0 °C (low), 35 °C (middle), and 70 °C (high) in a liquid bath. Next, the temperature coefficients were calculated and saved to the device's software. Following the determination of the temperature coefficients, the temperature probes were calibrated using a liquid bath, a high-accuracy SPRT, and water at its triple point. The same technique was used to calibrate the chamber temperature probe.

Temperature homogeneity and stability tests have been made with reference devices for the cabinet’s chamber. A temperature probe was placed in the centre of the cabinet during the stability testing, and after the balance state, temperature measurements were taken at 5-minute intervals, with twenty-one values being recorded for each temperature point. Table 2 shows the temperatures stabilities.

Expanded uncertainty, which in this case is defined as measurement uncertainty multiplied by the expansion coefficient $k=2$, offers %95 reliability, is given in the tables.

3. RESULTS

The calibration of the chamber temperature probe in the water bath was carried out using the comparison method at various temperatures and the water's triple phase point. Table 1 contains the values and deviations.

Table 1. Reference temperature values, chamber temperature probe’s temperature values and deviations

Reference Temperature (°C)	Reading from the Chamber Temperature Probe (°C)	Deviation (°C)
-10,078	-10,02	0,056
-0,010	-0,0074	0,0026
10,234	10,23	-0,004
20,189	20,18	-0,009
30,177	30,17	-0,007
40,173	40,17	-0,003
50,250	50,26	0,010
60,231	60,24	0,009
70,243	70,24	-0,003

The uncertainty analysis of the chamber temperature must take into account a number of factors.

Measurement uncertainty includes the effects of the resolution, self-heating and the reference standard [5].

The standard deviation of the difference between the reference standard and chamber temperature is the uncertainty component of the chamber temperature due to measurement, $u(M)$ [5].

The resolution of the device's temperature indicator is 0,01 °C. The uncertainty component of temperature resolution is [5]:

$$u(R) = 0,01/2\sqrt{3} = 0,0029 \text{ } ^\circ\text{C} \quad (3)$$

The temperature probe was calibrated in the water bath, but it uses in air. There is the possibility of some self-heating because of that. The self-heating, with temperature measurements is estimated to be +0,05% of reading [5],

$$u(SH) = 0,05\% * T_c / \sqrt{3} = 0,00029 * T_c \quad (4)$$

The uncertainty component of the reference standard was found as $u(T_{ref}) = 0,004 \text{ } ^\circ\text{C}$ with calculations.

The combined uncertainty of the chamber temperature can be found by the following formula.

$$u_c^2(T_c) = u^2(M) + u^2(R) + u^2(SH) + u^2(T_{ref}) \quad (5)$$

Utilizing a coverage factor $k=2$, the expanded uncertainty is $U = k * u_c(T_c)$.

Uncertainty components of the chamber temperature are seen in Table 2.

Table 2. Uncertainty components of the chamber temperature inside the cabinet

Component	Temperature (°C)								
	-10	- 0	10	20	30	40	50	60	70
u (M)					0,018				
u (R)					0,0029				
u (SH)	-0,0029	0	0,0029	0,0058	0,0087	0,0116	0,0145	0,0174	0,0203
u (T _{ref})					0,004				
u _c (T _c)	0,0189	0,0187	0,0189	0,0195	0,0206	0,0220	0,0236	0,0255	0,0276
U (T _c)	0,03778	0,03733	0,03778	0,03909	0,04119	0,04395	0,04727	0,05104	0,05515
stability	0,05	0,0004	0,02	0,00	0,02	0,02	0,00	0,00	0,00

Chamber temperature uniformity has a direct effect on relative humidity gradients within the test chamber. The thermometers were then carefully placed at various locations within the test chamber [6].

The maximum measurement deviation is determined by noting the maximum and minimum readings from the set of probes at the same point in time, then taking half the difference of these values.

$$MaxDev = \pm 0.5(MaxReading - MinReading) \quad (6)$$

Then uniformity can be calculated by the following formula.

$$Uniformity^2 = MaxDev^2 + u^2(T_{ref}) \quad (7)$$

$u(T_{ref})$ is the uncertainty of the reference temperature standard. The maximum deviation and the uniformity of the test chamber temperature are given in Table 3.

Table 3. Temperature maximum deviation and temperature uniformity in the chamber

	0 °C	35 °C	70 °C
Max. deviation	0,400	0,078	0,390
Uniformity	± 0,400	± 0,078	± 0,390

Relative Humidity in a two-pressure humidity generator is determined from the measurements of temperature and pressure and is expressed by the equation below [7].

$$RH = P_c/P_s * e_s/e_c * F_s/F_c * 100 \quad (8)$$

Total uncertainty of the relative humidity is the quantitative combination of the uncertainty component of the pressure ratio, the vapour pressure ratio's uncertainty component, the uncertainty contribution from the enhancement factor and from saturator efficiency [7].

When pressure is greater than 50 psia, the uncertainty contribution from the pressure can be calculated from the formulas that are below [7].

$$u(P_c) = \pm \{ \pm \partial P_c / P_s \} * 100 \quad (9)$$

$$u(P_s) = \pm \{ (P_c) / (P_s \pm \partial P_s) - (P_c / P_s) \} * 100 \quad (10)$$

For saturation pressures below 50 psia, a different measurement scheme is employed. When pressure is lower than 50 psia, the uncertainty component of the pressure can be calculated as the formula below [7].

$$u(P_c) = \pm \{ (P_c + \partial P_c) / (P_s + \partial P_c) - (P_c / P_s) \} * 100 \quad (11)$$

Uncertainty due to pressure hysteresis is given equation below [7].

$$u(H) = \pm 0,058 * (1 - P_c / P_s) \quad (12)$$

Uncertainty contribution from the pressure measurement resolution can be found by the equations below [7].

$$u(R_{pc}) = \pm (resolution / P_s) * 100 \quad (13)$$

$$u(R_{ps}) = \pm \{ (P_c) / (P_s + resolution / P_s) - (P_c / P_s) \} * 100 \quad (14)$$

Total uncertainty effect from the pressure ratio P_c/P_s can be found by the formula below.

$$u_c^2(P_c/P_s) = u^2(P_c) + u^2(P_s) + u^2(R_{pc}) + u^2(R_{ps}) + u^2(H) \quad (15)$$

Standard uncertainty components of RH due to pressure at various saturation pressures are seen in Table 4.

While the actual measurement accuracy of the two temperature probes is of little concern, the ability of the chamber and saturation temperature probes to indicate the same measured value at the same temperature is important, and is termed the inter-comparison uncertainty [7]. The RH uncertainty due to temperature inter-comparison, $u(T_i)$, is then written as

$$u(T_i) = \pm \{ (E_{[T_s+\partial T_s]}) / (E_{[T_c]}) - 1 \} * RH \quad (16)$$

Table 4. Standard Uncertainty Components of RH due to pressure at Various Saturation Pressures

Source	Term	$P_s < 50 \text{ psi}$					$P_s > 50 \text{ psi}$						
		15,5	20	25	35	45	50	50	65	75	100	125	150
Measurement	$u(P_c)$	0,003	0,014	0,017	0,017	0,015	0,015	0,021	0,016	0,014	0,010	0,008	0,007
Measurement	$u(P_s)$	0,020	0,015	0,012	0,009	0,007	0,006	0,015	0,009	0,007	0,004	0,002	0,002
Resolution	$u(R_{pc})$	0,004	0,003	0,002	0,002	0,001	0,001	0,001	0,001	0,001	0,001	0,000	0,000
Resolution	$u(R_{ps})$	0,004	0,002	0,001	0,001	0,000	0,000	0,001	0,001	0,000	0,000	0,000	0,000
Hysteresis	$u(H)$	0,045	0,050	0,044	0,023	0,133	0,180	0,060	0,031	0,067	0,026	0,030	0,034
combined	$u_c(P_c/P_s)$	0,050	0,054	0,049	0,030	0,134	0,181	0,065	0,036	0,068	0,028	0,032	0,035

The standard deviation of the difference between the saturation and chamber temperatures over the stated temperature range is ∂T_s .

The uncertainty components of the temperature indicator resolution that is affect to the total uncertainty of the relative humidity are given below.

$$u(R_{T_c}) = \pm \{ (E_{T_s}/E_{T_c+0.0029}) - 1 \} * RH \quad (17)$$

$$u(R_{T_s}) = \pm \{ (E_{T_s+0.0029}/E_{T_c}) - 1 \} * RH \quad (18)$$

Standard uncertainty components of RH due to temperature at various temperatures are given in Table 5.

Table 5. Standard Uncertainty Components of RH due to Temperature at Various Temperatures

Source	Term	Temperature (°C)								
		-10	0	10	20	30	40	50	60	70
T_s-T_c Intercomparison	$u(T_i)/RH$	0,00157	0,00204	0,00188	0,00174	0,00161	0,00149	0,00139	0,00130	0,00121
T_s Resolution	$u(R_{T_s})/RH$	0,00016	0,00024	0,00019	0,00018	0,00017	0,00015	0,00014	0,00013	0,00013
T_c Resolution	$u(R_{T_c})/RH$	0,00016	0,00024	0,00019	0,00018	0,00017	0,00015	0,00014	0,00013	0,00013
Self-Heating	$u(SH)/RH$	0,00016	0,00000	0,00019	0,00036	0,00050	0,00062	0,00072	0,00080	0,00087
Combined uncertainty	$u(E_s/E_c)/RH$	0,00159	0,00207	0,00191	0,00179	0,00170	0,00163	0,00158	0,00153	0,00150

Uncertainty of the enhancement factor equation which is affecting to the relative humidity is below and given in Table 6.

$$u(F_s/F_c) = \pm 0,00088 * (100-RH) \quad (19)$$

Uncertainty due to saturator efficiency can be calculated as formula below [7].

$$u(SE) = 0,143 * RH \quad (20)$$

The combined standard uncertainty, $u_c(RH)$, is obtained by statistical combination of the standard uncertainty components of pressure ratio, vapor pressure ratio, enhancement factor ratio, and saturator efficiency. The combined uncertainty formula is then the sum of the variances

$$u^2(RH) = u^2(P_c/P_s) + u^2(e_s/e_c) + u^2(F_s/F_c) + u^2(SE) \quad (21)$$

Expanded uncertainty of RH with coverage factor k=2 is seen in Table 7.

Table 6. Standard Uncertainty Components of RH due to Enhancement Factor

Source	Term	<i>P_s < 50 psi</i>					<i>P_s > 50 psi</i>			
		15,5	20	30	40	50	50	100	150	
		%RH	%RH	%RH	%RH	%RH	%RH	%RH	%RH	
Combined uncertainty	<i>u(F_s/F_c)</i>	0,005	0,023	0,045	0,056	0,062	0,062	0,075	0,079	

Table 7. Expanded Uncertainty of RH with coverage factor k=2

Saturation Temperature	<i>P_s < 50 psi</i>					<i>P_s > 50 psi</i>			
	15,5	20	30	40	50	50	100	150	
	%RH	%RH	%RH	%RH	%RH	%RH	%RH	%RH	
-10 °C	±0,419	±0,336	±0,242	±0,249	±0,403	±0,219	±0,183	±0,178	
0 °C	±0,488	±0,388	±0,274	±0,267	±0,410	±0,233	±0,195	±0,180	
10 °C	±0,464	±0,369	±0,263	±0,260	±0,407	±0,228	±0,190	±0,179	
20 °C	±0,447	±0,357	±0,255	±0,256	±0,406	±0,225	±0,188	±0,179	
30 °C	±0,434	±0,347	±0,249	±0,252	±0,404	±0,222	±0,186	±0,178	
40 °C	±0,424	±0,340	±0,244	±0,250	±0,403	±0,220	±0,184	±0,178	
50 °C	±0,417	±0,334	±0,241	±0,248	±0,403	±0,219	±0,183	±0,178	
60 °C	±0,411	±0,330	±0,238	±0,247	±0,402	±0,218	±0,182	±0,178	
70 °C	±0,406	±0,326	±0,236	±0,245	±0,402	±0,217	±0,181	±0,178	

4. CONCLUSIONS

Humidity is a computational value. The "two pressure humidity generator" is the one of the most precise way for producing humidity. Utilizing a mathematical equation, the two-pressure humidity generator determines the relative humidity from pressure and temperature measurements. The ratios in the equation are controlled by the computer to produce a known level of humidity.

Two-pressure humidity generators are generally used in metrology institutes, advanced calibration laboratories, meteorological laboratories and military areas that require precise measurements. The relative humidity value obtained by calculation from this device can remain stable for a long time with high accuracy, and fluctuations are less during the measurements. Although the cost is higher than other systems, related devices are preferred for such reasons. These types of devices, which are not usually found in country inventories, provide traceability to secondary level calibration laboratories in countries. The two-pressure humidity generator in the Turkish Standards Institute provides traceability to many different sectors in a wide area in Turkey. Many secondary level calibration laboratories' reference humidity instruments are calibrated by the two-pressure humidity generator in the Turkish Standards Institute. In this sense, the Turkish Standards Institute calibrates its own double-pressure humidity generator with the method described in this publication, in order to reduce dependency on external

institutions. During the calibration, thermometers and pressure calibrators with international traceability are used.

This study provided an application for calibrating two-pressure humidity generators. The calibration data for the two-pressure humidity generators, which are located in the calibration laboratory of the Turkish Standard Institution, were provided in this application. Temperature calibration, temperature uniformity analysis, relative humidity calibration of the device was processed by using the literature. Measurement uncertainties were calculated step by step. The components of each parameter which is affecting to the total uncertainty of the relative humidity are examined and calculated.

Calibration results were given for various points in this study by tables. Hygrometers and other humidity measuring devices can now be calibrated using a "two pressure humidity generator."

This compact study is provided to the literature. This study can be a supplementary document for the metrology researchers who are studying on the relative humidity calibration and temperature calibration. Also, this study can be used for the new studies about the calibration of the "two pressure humidity generator" as a document.

NOMENCLATURE

% RH: relative humidity

P_c : Chamber Pressure

P_s : Saturation Pressure

e_s : Saturation Vapor Pressure at Saturation Temperature

e_c : Saturation Vapor Pressure at Chamber Temperature

F_s : Enhancement Factor at Saturation Temperature and Pressure,

F_c : Enhancement Factor at Chamber Temperature and Pressure,

$u(M)$: RH uncertainty due to self-heating of the chamber temperature probe

$u(R)$: RH uncertainty due to self-heating of the chamber temperature probe

$u(SH)$: RH uncertainty due to self-heating of the chamber temperature probe

$u(T_{ref})$: The uncertainty of the reference temperature standard

$uc(T_c)$: Combined uncertainty of the chamber temperature

$u(P_c)$: Uncertainty in chamber pressure measurement

$u(P_s)$: Uncertainty in saturation pressure measurement

$u(H)$: Uncertainty component due to hysteresis

$u(R_{pc})$: Uncertainty due to chamber pressure measurement resolution

$u(R_{ps})$: Uncertainty due to saturation pressure measurement resolution

$u_c(P_c/P_s)$: Uncertainty in the Pressure Ratio P_c/P_s

$u(T_i)$: The RH uncertainty due to temperature intercomparison,

$u(R_{Tc})$: Uncertainty due to chamber temperature resolution,

$u(R_{Ts})$: Uncertainty due to saturation temperature resolution,

$u(F_s/F_c)$: Uncertainty in the Enhancement Factor Ratio

$u(SE)$: Uncertainty due to Saturator Efficiency

$u(RH)$: Total uncertainty in relative humidity

ACKNOWLEDGEMENTS

Thanks to the Turkish Standard Institution for facilities.

CONFLICT OF INTEREST

The author stated that there are no conflicts of interest regarding the publication of this article.

REFERENCES

- [1] Series 2500 Benchtop Two-Pressure Humidity Generator Operation and Maintenance Manual. Thunder Scientific Corporation, 2003.
- [2] El-Din E, Mekawy M, Ali K. Realization of humidity standard facility using two-pressure humidity generator and humidity chamber. *Metrol. Meas. Syst.*, 2009; 16(2), 323-327.
- [3] Model 2500 Benchtop / Mobile “Two-Pressure” Humidity Generator Brochure. Thunder Scientific Corporation, 2003.
- [4] Guidelines on the Calibration of Electromechanical and Mechanical Manometers. EURAMET/cg-17/v.4.1, 2022.
- [5] Hardy B. Chamber Temperature Uncertainty Analysis of the Thunder Scientific Model 2500 Two Pressure Humidity Generator. Thunder Scientific Corporation, 1998.
- [6] Hardy B. Chamber Temperature Uniformity Analysis of the Thunder Scientific Model 2500 Two-Pressure Humidity. Thunder Scientific Corporation, 1998.
- [7] Hardy B. Relative Humidity Uncertainty Analysis of the Thunder Scientific Model 2500 Two-Pressure Humidity. Thunder Scientific Corporation, 1998.



RESEARCH ARTICLE

DERIVATION OF EXPRESSION FOR PHOTOCURRENT DENSITY FOR NON-DESTRUCTIVE TESTING OF 3D PRINTING FILAMENT BY MEANS OF TERAHERTZ SPECTROSCOPY

Iurii KHOROSHAILO ¹ , Nataliia ZAICHENKO ² , Olga ZAICHENKO ^{1,*} 

¹ Department of Design and Operation of Electronic Devices, Faculty of Automatics and Computerized Technologies, Kharkiv National University of Radioelectronics, Kharkiv, Ukraine

² Department of Microelectronics, Electronic Devices and Appliances, Faculty of Electronic and Biomedical Engineering, Kharkiv National University of Radioelectronics, Kharkiv, Ukraine

This report presents a revised expression for the photocurrent density in terahertz spectroscopy, which is a non-destructive testing technique of particular interest to the authors in the context of 3D printed parts. 3D printing, also known as additive manufacturing, involves creating three-dimensional objects based on computer-aided design (CAD) models. The process entails depositing, joining, or solidifying material under computer control, layer by layer.

Defects in 3D printing, such as weak infill, gaps in thin walls, inconsistent extrusion, layer separation, and bed drop, can lead to low printing quality and render some printed parts unfit and unsafe for use. Moreover, the ability to tamper with internal layers without altering the exterior could result in the production of maliciously defective parts without detection. Therefore, it is crucial to test 3D printed details and filaments at each stage of processing using non-destructive methods.

A comprehensive review of the relevant literature indicates the potential for enhancing measurement accuracy through various improvements in terahertz spectrometer models. The mathematical model for the photocurrent involves a convolution integral of the current density and the laser radiation pulse that irradiates the surface of the material under study. The expression within the integral incorporates parameters such as the duration of the optical pulse, carrier lifetime, and momentum relaxation time. By evaluating the integral, the result can be obtained as two terms, each being a product of an exponent and a complementary error function with the same parameters mentioned earlier.

The calculation involves several steps, including a change of variables during integration. Verification using Maple software demonstrates agreement with analytical calculations and suggests a pathway for further refinement of the expression for the photocurrent density. The Maple program influenced the results by means of repeating same calculation with aid of computer and allowing to compare if analytical results are same and true, also it could be use for simulation and example calculation, for results graphical representation.

The connection between the obtained mathematical expression and its relation to 3D printing (additive manufacturing) exists. The explanation is in that the 3D printer uses filament, filament has defects, defectoscopy of filament in the terahertz domain have models and methods. The research of defectoscopy models and methods is helpful to increase accuracy of measurement of filament defect parameters and account on it and improve the quality of 3D printed details.

Keywords: 3D-filament, Testing, Terahertz, Spectroscopy, Model

1. INTRODUCTION

This report focuses on non-destructive testing methods for evaluating the quality of filaments used in 3D printing. 3D printing, or additive manufacturing, involves constructing three-dimensional objects from CAD models using various processes that deposit, join, or solidify material under computer

control, layer by layer. Filaments for 3D printing are thermoplastic polymers that melt when heated and are extruded through a nozzle to create the desired object.

Defects in 3D printing, such as weak infill, gaps in thin walls, inconsistent extrusion, layer separation, splitting, and bed drop, can result in substandard print quality and render printed parts unsuitable and unsafe for use. Additionally, the ability to manipulate internal layers without affecting the external appearance raises concerns about the potential production of maliciously defective parts without detection. Therefore, it is essential to test both the 3D printed details and the 3D printing filament at every stage of the process, preferably using non-destructive methods.

Several non-destructive testing methods exist, including radiography, ultrasound, and others. Mechanical tests and light microscopy, although standardized, are mostly performed offline, meaning they are time-consuming and destructive. Recent developments have aimed to bring testing closer to the manufacturing process through in-line and on-line measurements, such as the pressure filter test, ultrasonic testing, and spectroscopic monitoring, particularly in the near-infrared (NIR) frequency range. However, each method is limited to specific applications. The pressure filter test lacks reliability with higher additive concentrations and is unsuitable for fibrous materials. Ultrasonic testing is only suitable for low spatial resolution applications, while NIR offers high resolution but is primarily useful for near-surface analysis or thin samples due to its decreasing penetration depth with increasing frequency.

In the following sections, we will demonstrate that terahertz time-domain spectroscopy (THz TDS) in the frequency range between 100 GHz and a few THz holds promise as a non-destructive testing technique for polymeric compounds. THz TDS combines the advantages of high penetration depth, similar to microwaves, with submillimeter spatial resolution. It enables the extraction of frequency-dependent refractive index and absorption coefficient by capturing phase and amplitude information of the propagated electromagnetic wave.

Among the various non-destructive testing methods for polymers, terahertz spectroscopy was chosen due to its wide spectral coverage in the terahertz region, high dynamic range, ability to detect both amplitude and phase, picosecond time resolution, and potential use as a terahertz pump source.

After early work [5,7] there was rapid development of THz TDS. The modern publications are mainly about application so still there are many interesting aspects in the theory.

Terahertz Time Domain Spectroscopy (THz-TDS) has witnessed a surge in popularity in recent decades owing to its broad frequency range and high signal-to-noise ratio. Researchers have devoted substantial efforts to various aspects of this field, encompassing the development of spectroscopy for acquiring high-resolution signals and extracting crucial information from both gas molecules and biological samples.

The study [11] focuses on leveraging the potent THz-TDS technique for quantitative information extraction. The investigation highlights the estimation of spectroscopy sensitivity by measuring sample concentrations. There was demonstrated this approach through a physical model applied to solid and gas samples. Despite the prevalent use of convolutional mathematical models for enhanced precision, limited attention has been given to measuring uncertainties in the parameters derived from these models.

In this research, the author delves into visualizing uncertainties in the optical parameters of a lactose sample, extracted through the Lorentz model of electronic dispersion. This visualization is achieved by numerically evaluating the Hessian matrix, representing second-order partial derivatives of the function at optimized parameters. Subsequently, standard deviations are computed by extracting the diagonal elements of the inverse of the Hessian matrix. These uncertainties are depicted through error bars on the real and imaginary parts of the refractive index of the lactose sample [11].

Simultaneous compensation of lateral and temporal walk-offs between the fundamental wave and the second harmonic wave plays a pivotal role in our homemade air plasma system, resulting in a notable threefold enhancement in THz conversion efficiency. Furthermore, we optimize the efficiency of second harmonic generation for THz radiation. The incorporation of a dual-wavelength half-waveplate contributes to achieving a high THz conversion efficiency exceeding 0.06% at an 800 nm excitation in a dry air environment. This corresponds to an overall enhancement factor of 6.

In the detection phase, there was experimentally explored electro-optic sampling and air-biased coherent detection. Leveraging our air plasma system, we successfully identify two characteristic peaks (4.85 and 5.8 THz) in the rust sample. This underscores the effectiveness of our approach in both enhancing THz conversion efficiency and enabling precise detection of characteristic features in materials [12].

Terahertz time-domain spectroscopy (THz-TDS) has emerged as a potent and versatile tool across various scientific domains, including imaging, material characterization, and layer thickness measurements. Despite its significant success in research settings, the widespread commercialization of this technology has been impeded by the high cost and cumbersome nature of most systems. The primary contributors to the size and expense of these systems are the laser and the optical delay unit (ODU).

In response to these challenges, the efforts was dedicated to the development of THz-TDS systems centered around compact monolithic mode-locked laser diodes (MLLDs). The ultra-high repetition rate (UHRR) of the MLLD is advantageous, enabling the use of shorter ODUs, thereby reducing the overall size and cost of our systems. However, achieving the necessary precision in the ODU to obtain accurate terahertz time-domain signals remains a critical consideration.

To address this challenge, the interferometric extension was introduced and enhanced for UHRR-THz-TDS systems. This extension is characterized by its affordability, compact design, and ease of integration. In this article, we detail the system setup, the extension itself, and the algorithmic procedure for reconstructing the delay axis based on the interferometric reference signal. Our evaluation, based on a dataset comprising 10,000 signal traces, reveals a low standard deviation of the measured terahertz phase at 1.6 THz, as low as 3 mrad.

Additionally, the remaining peak-to-peak jitter of only 20 fs and a record-high peak signal-to-noise ratio of 133 dB at 100 GHz after averaging. The method outlined in this paper not only simplifies the construction of THz-TDS systems but also reduces bulk and cost. Consequently, it facilitates the transition of terahertz technologies from laboratory settings to practical field applications [13].

The critical literature review show versatility of research direction, its relevance. At the same time it forced us to go back to the beginning in order to go through the evolution of scientific thought through personal experience.

The objective of this study is to validate the accuracy of the mathematical calculations in the model THz of [1-3], as they form the foundation for further research in this field.

2. DERIVATION OF EXPRESSION FOR PHOTOCURRENT DENSITY

The photocurrent density in the emitter corresponds to the convolution of the temporal shapes of the exiting optical pulse and of the impulse current response of the photo switch

$$j_{em}(t) = P_{opt}(t) \otimes [n_{em}(t)q\nu_{em}(t)], \quad (1)$$

where \otimes denotes convolution product, $P_{opt}(t)$ is the optical power, are respectively, the charge, density and the velocity of photocarriers on emitting antenna. The current density $n_{em}(t)qv_{em}(t)$ represents the impulse response of the photo switch, i.e. response to a delta Dirac optical excitation. We make the assumption that the temporal profile of the optical pulse is Gaussian. Moreover, to get a simple expression for the current, the free-carrier relaxation in both emitting and receiving photo switches is assumed to be governed by a single exponential decay law [3].

We suppose here that the switch is uniformly illuminated and that the bias field E_{DC} is constant over the whole illuminated region. We get the expression of the photocurrent density in the emitter [1, p.64]

$$I_{pc}(t) \approx \mu_e E_{DC} I_{opt}^0 \int_0^{+\infty} e^{-(t-t')/\tau_p^2 - t'/\tau_c} \left[1 - e^{-t'/\tau_s} \right] dt' = I_1 + I_2 \quad (2)$$

where μ_e is electron mobility, $\mu_e = e\tau_s / m$, m is effective mass of carrier,

E_{DC} is the DC bias field, I_{opt}^0 is magnitude of optic pulse, τ_p is optic pulse duration, τ_c is carrier life time, τ_s is momentum relaxation time, I_1 is first term, $I_1 = \mu_e E_{DC} I_{opt}^0 \int_0^{+\infty} e^{-(t-t')/\tau_p^2 - t'/\tau_c} dt'$,

I_2 is second term, $I_2 = -\mu_e E_{DC} I_{opt}^0 \int_0^{+\infty} e^{-(t-t')/\tau_p^2 - t'/\tau_c} e^{-t'/\tau_s} dt'$.

The expression under the integral sign is product of three exponents and subjected to a transformation in order to obtain the result of integration.

The transformation includes such steps as variable and the lower limit of integration changing.

Let's consider integral first term in (2)

$$\int_0^{\infty} e^{-(t-t')/\tau_p^2 - t'/\tau_c} dt' = I_1 \quad (3)$$

Let's in expression (3) denote

$$x = \frac{1}{\tau_p}, \quad y = \frac{1}{\tau_c}, \quad (4)$$

And get such expression

$$\int_0^{\infty} \exp\left(- (t-t')^2 x^2 - t'y\right) dt' = I_1, \quad (5)$$

by definition of complimentary error function

$$erfc(\zeta) = \frac{2}{\sqrt{\pi}} \int_{\zeta}^{\infty} e^{-b^2} db, \quad (6)$$

As it is known [2, p.322] there is substitution for variable changing

$$t \cdot x + \frac{y}{2x} = b, \quad (7)$$

After differentiation (7)

$$db = dt, \quad (8)$$

We get after substitution (7), (8) into (6)

$$\int_0^{\infty} \exp\left(-tx + \frac{y}{2x}\right)^2 dt = \frac{1}{x} \operatorname{erfc}\left(tx + \frac{y}{2x}\right) \frac{\sqrt{\pi}}{2}, \quad (9)$$

From expression (7) squaring

$$b^2 = \left(tx + \frac{y}{2x}\right)^2 = t^2x^2 + 2tx \frac{y}{2x} + \frac{y^2}{4x^2} = t^2x^2 + ty + \frac{y^2}{4x^2}, \quad (10)$$

After transfer of terms

$$t^2x^2 + ty = -b^2 + \frac{y^2}{4x^2}, \quad (11)$$

$$\int_0^{\infty} \exp\left(-t^2x^2 - ty\right) dt = \int_0^{\infty} \exp\left(-b^2 + \frac{y^2}{4x^2}\right) dt = \frac{\exp\left(\frac{y^2}{4x^2}\right)}{x} \operatorname{erfc}\left(\frac{y}{2x} + xt\right) \frac{\sqrt{\pi}}{2}, \quad (12)$$

Expression (12) differs from expression (9) by multiplicand $\exp\left(\frac{y^2}{4x^2}\right)$.

Finally add and subtract t/τ_c and group second and third term and change terms order in first bracket they in second degree

$$\begin{aligned} -(t-t')^2 x^2 - t'y &= -(t-t')^2 x^2 - t'y + ty - ty = \\ &= -(t-t')^2 x^2 - (t-t')y - ty \end{aligned} \quad (13)$$

Denote $a = ty$

$$-(t-t')^2 x^2 - t'y = -(t-t')^2 x^2 - (t-t')y - a, \quad (14)$$

Consider auxiliary expression

$$-t^2x^2 - ty + a, \tag{15}$$

Substitute (14) in integral gives

$$\int_0^\infty \exp(-t^2x^2 - ty + a)dt = \frac{\sqrt{\pi} \cdot \exp\left(a + \frac{y^2}{4x^2}\right) \operatorname{erfc}\left(xt + \frac{y}{2x}\right)}{2x}, \tag{16}$$

In expression (16) as compare to (12) appears second summand in exponent argument

As to second integral I_2 by analogue with exception

$$y = \frac{1}{\tau_{cs}}, \frac{1}{\tau_{cs}} = \frac{1}{\tau_c} + \frac{1}{\tau_s}, \tag{17}$$

From back substitution of expression (4) into expression (15) we get expression what we sought

$$J(t) = \tau_p \frac{\sqrt{\pi}}{2} \mu_e E_{DC} I_{opt}^0 \left\{ \exp\left(\frac{\tau_p^2}{4\tau_c^2} - \frac{t}{\tau_c}\right) \operatorname{erfc}\left(\frac{\tau_p}{2\tau_c} - \frac{t}{\tau_p}\right) - \exp\left(\frac{\tau_p^2}{4\tau_{cs}^2} - \frac{t}{\tau_{cs}}\right) \operatorname{erfc}\left(\frac{\tau_p}{2\tau_{cs}} - \frac{t}{\tau_p}\right) \right\} \tag{18}$$

To verify expression (18) derived analytically was used software Maple and result from Maple is coincided with expression (18) so proof result rightness.

And now compare expression with known expression [1-3].

An approximation of the physics of these emitters, where the generated photo-current an incident optical, femtosecond pulse is given by [1, p.64]

$$I(t) = \frac{\sqrt{\pi}}{2} \mu_e E_{DC} I_{opt}^0 \left\{ \exp\left(\frac{\tau_p^2}{4\tau_c^2} - \frac{t}{\tau_c}\right) \operatorname{erfc}\left(\frac{\tau_p}{2\tau_c} - \frac{t}{\tau_p}\right) - \exp\left(\frac{\tau_p^2}{4\tau_{cs}^2} - \frac{t}{\tau_{cs}}\right) \operatorname{erfc}\left(\frac{\tau_p}{2\tau_{cs}} - \frac{t}{\tau_p}\right) \right\} \tag{19}$$

Expression (18) differs from expression (19) by multiplicand $\frac{1}{x} = \tau_p$.

Only in expression (15) we consider auxiliary expression $-t^2x^2 - ty + a$ instead of $-(t-t')^2 x^2 - (t-t')y - a$.

Let's use Maple and get correct solution. It is after substitution (4)

$$\begin{aligned}
 I_1 &= -\frac{\sqrt{\pi}}{2} \mu_e E_{DC} I_{opt}^0 \frac{\sqrt{\pi} \exp\left(-x^2 t^2 + \frac{(4tx^2 - y)^2}{4x^2}\right) \operatorname{erf}\left(-xt' + \frac{2tx^2 - y}{2x}\right)}{2x} = \\
 &= \frac{1}{2} \tau_p \frac{\sqrt{\pi}}{2} \mu_e E_{DC} I_{opt}^0 \sqrt{\pi} \exp\left(-\frac{t^2}{\tau_p^2} + \frac{\left(\frac{4t}{\tau_p^2} - \frac{1}{\tau_c}\right)^2}{4 \frac{1}{\tau_p^2}}\right) \operatorname{erf}\left(-\frac{t'}{\tau_p} + \frac{\frac{2t}{\tau_p^2} - \frac{1}{\tau_c}}{2 \frac{1}{\tau_p^2}}\right) =
 \end{aligned}
 \tag{20}$$

$$= \frac{1}{2} \tau_p \frac{\sqrt{\pi}}{2} \mu_e E_{DC} I_{opt}^0 \sqrt{\pi} \exp\left(-\frac{t^2}{\tau_p^2} + \frac{4t}{\tau_p^2} - \frac{2}{\tau_c} + \left(\frac{\tau_p}{\tau_c}\right)^2 \frac{1}{4t}\right) \operatorname{erf}\left(-\frac{t'}{\tau_p} + t - \frac{\tau_p^2}{2\tau_c}\right).$$

The problem of each research is in contradiction. This research results have its own contradiction between known formula (19) and derived by us formula (18). The two formula differ by multiplicand τ_p . Next step was to check by means automated calculation with Mapple software to be sure that our result without error. And our results was confirmed with the aid of Maple software.

3. CONCLUSION

The subject of this report is a derivation of expression for photocurrent density in terahertz spectroscopy. The mathematical model of the photocurrent is a convolution of the laser radiation pulse irradiating the surface of the material under test and the current density, which in turn is the product of the carrier concentration, charge, and velocity. The result of calculation partially coincide with known result but could be improved if instead of taking tabular integral pay attention to the conditions of a particular task. There was revised expression for photocurrent density and was received more correct result due to using of Maple.

The issue in every research lies in contradictions. This study's findings exhibit a contradiction between the established formula (19) and the formula we derived (18). The discrepancy between the two lies in the multiplicand. To ensure the accuracy of our results, the subsequent step involved verifying them through automated calculations using Maple software. The confirmation of our results came through the validation process with Maple software, reassuring the absence of errors.

CONFLICT OF INTEREST

The authors stated that there are no conflicts of interest regarding the publication of this article.

AUTHORSHIP CONTRIBUTIONS

Iurii Khoroshailo: Supervision. Nataliia Zaichenko: Experimental and numerical modeling, Methodology, Visualization, Writing – original draft, Olga Zaichenko: Writing – review & editing.

REFERENCES

- [1] Lee YS. Principles of terahertz science and technology. Springer Science & Business Media, 2009, 337.
- [2] Klokko N, Gorecki J, Wilkinson JS, Apostolopoulos V. Artificial neural networks for material parameter extraction in terahertz time-domain spectroscopy *Optics Express* 2022; 30(9): 15583-15595.
- [3] Duvillaret L, Gare F, Roux JF, Coutaz JL. Analytical modeling and optimization of terahertz time-domain spectroscopy experiments, using photoswitches as antennas. *IEEE Journal of Selected Topics in Quantum Electronics* 2001; 7(4): 615-623.
- [4] Gradshtein IS, Ryzhik IM. Tables of integrals, sums, series and products. Fizmatgiz, 1963, 1108.
- [5] Arjavalingham G, Theophilou N, Pastol Y, Kopcsay GV, Angelopoulos M. Anisotropic conductivity in stretch-oriented polymers measured with coherent microwave transient spectroscopy. *The Journal of chemical physics*, 1990, 93(1), 6-9.
- [6] Nuss MC, Goossen KW, Gordon JP, Mankiewich PM, O'malley ML, Bhushan M. Terahertz time-domain measurement of the conductivity and superconducting band gap in niobium. *Journal of Applied Physics*, 1991, 70(4), 2238-2241.
- [7] Van Exter M, Grischkowsky DR. Characterization of an optoelectronic terahertz beam system. *IEEE Transactions on Microwave Theory and Techniques*, 1990, 38(11), 1684-1691.
- [8] Withayachumnankul W, Fischer BM, Lin H, Abbott D. Uncertainty in terahertz time-domain spectroscopy measurement. *JOSA B*, 2008, 25(6), 1059-1072.
- [9] Jepsen PU, Jacobsen RH, Keiding SR. Generation and detection of terahertz pulses from biased semiconductor antennas. *JOSA B*, 1996, 13(11), 2424-2436.
- [10] Piao ZS, Tani M, Sakai K. Carrier dynamics and THz radiation in biased semiconductor structures. In *Terahertz Spectroscopy and Applications*, 1999, 3617, 49-56.
- [11] Raj A. Quantitative analysis of optical parameters using THz-TDS. Master Thesis Report, University Jean Monnet, 2023, 47.
- [12] Li E, Yang J, Zhang K, Li H, Xu Y, Su F, Fang G. (2023). Systematic Study of Two-color Air Plasma Broadband THz-TDS. *IEEE Transactions on Terahertz Science and Technology*, 2023, 13(5), 476-484.
- [13] Cherniak V, Kubiczek T, Kolpatzeck K, Balzer JC. Laser diode based THz-TDS system with 133 dB peak signal-to-noise ratio at 100 GHz. *Scientific Reports*, 2023, 13(1), 13476.



RESEARCH ARTICLE

DETERMINATION OF THE PERFORMANCE OF LIGHT SHELVES FOR MORE
EFFECTIVE BENEFIT FROM DAYLIGHT IN BUILDINGS

Furkan MERAL^{1*} , Hatice Günseli DEMİRKOL² 

¹ Architecture, Faculty of Architecture and Design, Eskişehir Technical University, Eskişehir, Turkey

² Architecture, Faculty of Architecture and Design, Eskişehir Technical University, Eskişehir, Turkey

ABSTRACT

Studies on the efficient use of daylight in sustainable architectural design and energy conservation are increasing. Indoor lighting methods include daylighting, artificial, and integrated lighting. Basic priorities in lighting are such as “effective use of daylight”, “uniform illumination in space”, “glare control”, “visual connection with the external environment” and “daylight harvesting.” Advanced contemporary systems include light shelves and light tubes. Light shelves consist of horizontal or slightly angled elements that can be applied to the inner and outer surfaces of the window openings, usually at eye level, to block the daylight or to reflect it to the ceiling, integrated with the facade, or added later. In this research, light shelves, which is one of the advanced daylighting methods, are emphasized. Daylight analysis method was carried out with the help of a physical model and computer simulation techniques using DiaLux software. To effectively utilize the daylight factor in the internal volume through light shelf, certain parameters such as the height and angle of the light shelf, date and time, and direction of the room's opening, play a crucial role. In daylight analyzes, these parameters were subjected to experimental testing both in physical models and through computer simulations. As a result of the comparison of the obtained data, alternatives that will provide the opportunity to benefit from daylight in the most effective way have been identified. The results obtained have unique value and widespread impact in terms of sustainable architecture and energy saving. The study's originality lies in its specific measurements of the latitude in which it is located, as it is the first time the study is conducted under Eskişehir's conditions. In addition, the examination of the advantages and disadvantages of the light shelf in specific combinations is another original side of the project.

Keywords: Light shelf, Daylight, Efficiency, Illumination, Reflection, Architecture

1. INTRODUCTION

Architectural design has undergone a significant transformation in recent years, owing to the escalating concerns surrounding energy efficiency and environmental sustainability. While technological advancements have brought about improvements in artificial lighting, the quality of illumination provided by daylight remains unparalleled [1]. Daylight is favored by users for the numerous psychological and physiological benefits it offers, including enhanced productivity, well-being, and energy savings. To leverage the advantages of daylight, architects and lighting designers are developing efficient systems for optimal utilization of daylight, leading to improved lighting quality, energy efficiency, and a more sustainable built environment [2]. The integration of daylighting strategies in building design is a fundamental aspect of architectural lighting. This technique is typically accomplished through the installation of windows or skylights, which enable the effective use of daylight while providing a visual connection to the external environment. Critical considerations in daylighting design include the achievement of uniform illumination, the minimization of discomfort glare, and the provision of sufficient light to interior spaces that lack adequate daylight. Advancements in daylighting technology, such as reflective or directional systems, are being developed to illuminate closed volumes that are inaccessible to daylight or have never been exposed to it. Yener suggests that,

*Corresponding Author: furkanmeral321@gmail.com

Received: 07.03.2023

Published: 28.03.2024

as many states, it is of great importance to illuminate buildings with daylight in terms of sustainable architecture and energy saving. In this sense, the effective use of daylight and the designs aimed at reducing lighting energy consumption are among the priority issues of today's architecture. Moreover, light shelves are recognized as a sustainable design strategy for achieving Leed Point System accreditation, specifically in the "internal quality: daylight and landscape" category. These systems effectively redirect daylight deeper into the building, promoting energy efficiency and reducing the need for artificial lighting [3]. According to Kılıç Demircan and Gültekin, parameters that are effective in the process of energy-effective building design; are the location of the building, building intervals, orientation of the building, building form, building shell, natural ventilation order [4]. In addition, they argued that by using these parameters, it is possible to design buildings effectively through passive and active systems.

Architectural design professionals who focus on the interplay of natural light and building form, often rely on the LEED-NC (version 2.2) Indoor Environmental Quality section's daylight and views credits 8.1 and 8.2 for a performance metric. These credits are crucial in determining the effectiveness of a building's daylighting design. The primary objective of daylighting in architecture is to maximize the effective use of natural light while providing homogeneous lighting in the space and controlling discomfort glares to the eye. Furthermore, daylighting design should provide visual relationships with the external environment. Architects employ various systems to illuminate closed volumes that cannot receive sufficient daylight or have never been exposed to natural light. These systems include those that reflect, direct, or carry daylight to the desired spaces [5]. Adequate and homogeneous daylighting is primarily related to window dimensions. As stated in Neufert, the status of the windows, sizes, and type in the room, affects the influx of daylight. In DIN 5034 standards, suitable window sizes are identified for living and study rooms. According to the aforementioned standards, the ratio of window width to wall width was recommended for maximum 55%. Considering the room area, 1/8-1/10 of this area is recommended to leave a window area. In case of high room height (2.5-3,50m), the window area (Figure 1) was deemed appropriate by less than 30% of the room area [6]. According to Reinhart, in the realm of architectural design, the LEED reference guide is a vital resource for implementing sustainable strategies. One critical aspect of sustainable design is daylighting, which involves the use of natural light to illuminate interior spaces. However, the guide notes that glare control is a common challenge in daylighting strategies and suggests the use of shading devices to mitigate this issue. Beside that, the guide does not provide detailed guidance on how to effectively employ such solar control devices, nor does it present any metrics for measuring their effectiveness [7].

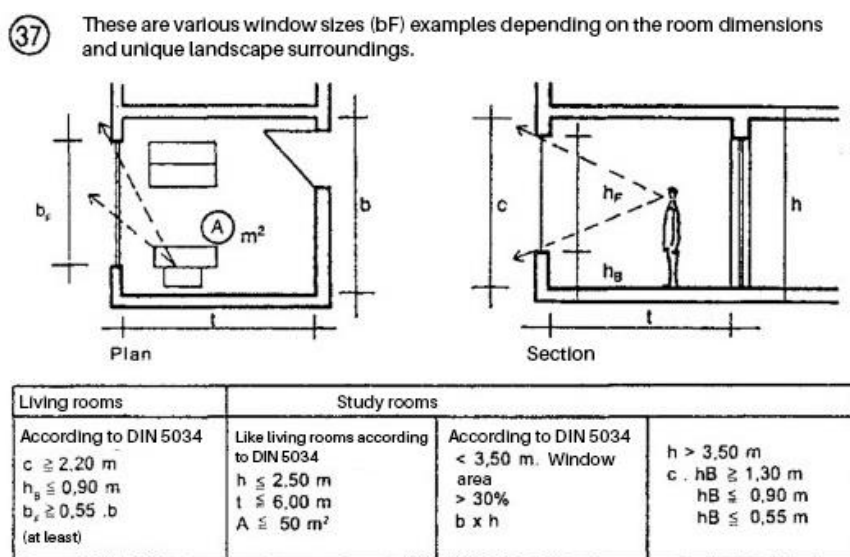


Figure 1. DIN5034 Window openings and room sizes are foreseen for different room dimensions [6].

According to Fabi, Andersen, Corgnati and Olesen; factors that influence occupant behavior can be categorized into five groups: physical environmental, contextual, psychological, physiological, and social factors. Physical environmental factors, such as temperature, air velocity, noise, illumination, and odor, play a crucial role in driving behavior and have a direct impact on energy consumption. Windows can help regulate these factors by providing natural light, ventilation, and views to the outside environment [8].

Contextual factors, such as the insulation of buildings, orientation of facades, heating system type, thermostat type, and more, can indirectly influence occupant behavior. Windows can play a significant role in regulating these factors and help create a comfortable indoor environment. Psychological factors, such as thermal comfort, visual comfort, acoustical comfort, health, safety, and other expectations related to indoor environmental quality, can also impact occupant behavior. Windows can provide natural light and views to the outside environment, which can promote positive behavior. Physiological factors, such as age, gender, health situation, clothing, activity level, and intake of food and beverages, play a significant role in determining the physiological condition of the occupant. Windows can promote a healthy indoor environment and positively influence occupant behavior. Social factors refer to the interaction between occupants, which can significantly influence behavior. Windows can create a sense of community and promote positive social interactions among occupants [8].

According to Erel [9], the windows have no characteristics to reach the depths of the room to the same extent. In order to deliver the light, the windows must be equipped with auxiliary optical elements. This requirement leads to;

- Reduction of daytime use of artificial lighting or reduce to zero if possible and save electrical energy,
- Increasing interest in energy-active buildings as part of the sustainable architectural movement and designers' focus on the designs and solutions of such buildings,
- Providing enough daylight for insertion and distribution to spaces in order to change user needs,
- To be able to benefit from daylight and components in the most efficient way.

Erel suggests that in traditional architecture, daylighting systems rely on windows that have roof openings and reflective light shelves incorporated into them. With the development of technology, new materials and techniques have emerged. These new materials and technologies are called developed daylighting systems (Figure 2) which are used in traditional daylighting systems [10].

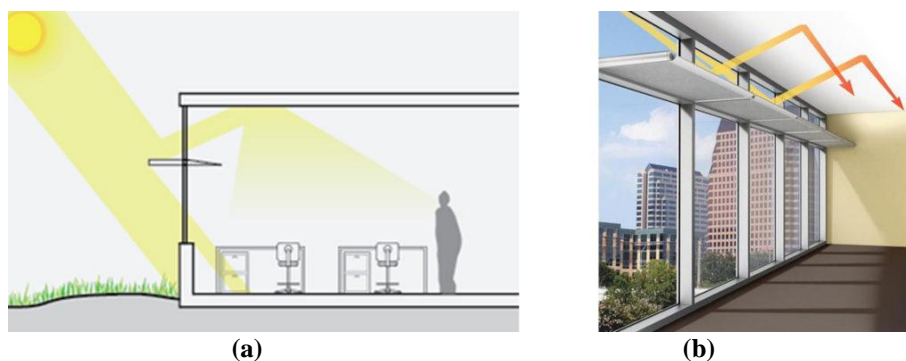


Figure 2. Access to the interior of light through light shelves [10]. (a): section, (b): 3d image

In the realm of advanced daylighting systems, the light shelf plays a vital role in optimizing daylight distribution within a space. This architectural feature is typically a horizontally or sloping placed curtain within a window, designed to reflect incoming daylight onto the ceiling and back of the room. The result is a well-lit space that maximizes the use of daylight, providing a comfortable and energy-efficient environment. As a result, it is stated that the expected benefit depends on the characteristics of the

reflective surface and the careful planning by Warrier and Raphael. Variables to determine the performance of a light shelf include the height, width, angle, and material of the shelf; appropriate variable control is required to maximize the performance of the light shelf. Warrier and Raphael, as a result of their model simulation study [11], they achieved an increase of approximately 21% in lighting using horizontal light shelves made of aluminum or glass mirror material. Their study comprises two segments. The initial segment is experimental and entails measurements on a scaled prototype. Regrettably, due to practical constraints, a full-scale prototype was unfeasible to construct. Moreover, the number of configurations that can be experimentally tested is restricted. Therefore, theoretical simulations were integrated into the experiments. The latter segment of the study conducted simulations through Radiance lighting simulation software. The conducted experiments have demonstrated that horizontal light shelves composed of aluminum or glass mirror can lead to an approximate 21% increase in illuminance. Additionally, by rotating the external light shelf, a nearly threefold increase in illuminance can be accomplished. Glass mirror is a superior material for a rotatable shelf when compared to aluminum. Using simulations, it has been determined that the majority of standard architectural spaces can benefit from such light shelves. The use of materials and software is assessed based on achieving maximum efficiency as a percentage. The results are not evaluated in terms of disadvantages, but the maximum efficiency is considered as the focal point of the project. However, if the shelves are planned to be mobile according to the arrival of sunlight, they stated that the lighting could be achieved three time efficient in the lighting.

Barker posits that within educational institutions and classrooms, a plethora of procedures can be executed seamlessly, with the ocular well-being of both staff and students being of paramount importance. However, it is stated that optimal illumination levels not only enhance the learning experience but also promote physical health and productivity among individuals by using light shelves in schools (Figure 3) [12].



Figure 3. Light shelf example at Roy Lee Walker Elementary School [13]

In their study by Kurtay and Esen, the light shelf settlements and yields for 30° and 45° latitudes, including Turkey, were investigated for different heights in a standard office unit. In the calculations, better results were obtained in the internal light shelf settlements in 30° and 45° latitudes under the specified conditions and appropriate shelf sizes were determined accordingly [14].

In the study of Meresi, the lighting performances of the light shelves placed in 6 different ways in a room environment of 7 x 7 meters were examined at different angles. As a result of the study, the shelves located at a height of 2.00 m from the floor, 0.80m (out of the building), 0.20m (internal) width, are operated between 10° and 20°; it has been revealed that it has achieved the best performance both in improving the distribution of daylight and protecting it from glaring [15].

After conducting a thorough literature review, it has become evident that the use of light shelves is imperative for effective daylighting in Turkey. The implementation of such studies is crucial for spreading awareness and promoting the use of light shelves in architecture. This research puts emphasis on the use of light shelves and aims to measure their effectiveness through computer simulation models and physical models. Through this research, lighting levels within a space have been determined. The light shelves, which utilize reflection values and have been recommended, were placed at varying angles of 0°, 10°, and 20°. By comparing the data obtained, alternative approaches were identified and suggestions were made to maximize the benefits of daylight. The most efficient light shelf was determined by testing various parameters. These findings hold significant value in terms of sustainable architecture and energy conservation. This study is particularly noteworthy as it is the first of its kind in Eskişehir, and includes specific measurements of the latitude.

2. EXPERIMENTAL METHOD AND THEORETICAL METHOD

The method of daylight analysis made with a physical model and computer simulation techniques. Furthermore, it explains the process of obtaining the constant parameters that were maintained throughout the experiments.

2.1. Site Surveying and Location Analysis

Architects require assistance to assess the daylighting performance of their buildings. Sky simulators are experimental tools that, when used with physical models, allow for a tangible and intuitive method of approaching the issue. According to Michel and Scartezzini, standard artificial skies and their measurement technology have their limitations. They cannot accurately evaluate the building's performance under a non-standard sky luminance distribution (CIE sky models). Therefore, alternative systems that can reflect, direct or transport daylight are being developed to illuminate enclosed spaces that cannot receive adequate daylight or have never been exposed to it [16]. In this study, in order to evaluate the performance of the building correctly, in the computer simulation measurements, Eskişehir's sky values were taken from Dialux Evo. The values were obtained based on the dates and times of the physical model measurements.

Analyzing the effectiveness of daylighting can be accomplished through experimental measurements and computer modeling. Experimental measurements may be derived from either field measurements or scaled model tests. Chen Y., Liu, Pei, Cao, Chen Q. and Jiang say computer modeling has become an increasingly popular method for analyzing daylighting performance. This method allows architects and designers to simulate various lighting scenarios and make informed decisions based on the results [17].

In order to determine the performance of light shelves, it is necessary to determine the geography and climatic conditions. This study was conducted under the conditions of Eskişehir, which is located in 30° and 45° latitude in the temperate climate zone. In the days when the sky above Eskişehir was devoid of clouds, experimental studies were carried out measurements on the physical model with the help of

Luxmeter. Also, measurements made by computer modeling were analyzed and compared with the results of the physical model.

The computer simulation design of the building was measured according to the sky state of Eskişehir, which is located at 30° East longitude and 39° North latitude. The measurements were compared to the physical model, which was also evaluated in Eskişehir. All computer simulation measurements were conducted under the assumption of an open sky. The measurement location was determined to be the living room of a real house with a window opening of the same living room. The hall has a width of 420cm, a length of 667cm, and a height of 280cm. The dimensions of the window opening are 90cm in height, 140cm in width, and 180cm in length (Figure 4).

According to Selkowitz, Indoor and outdoor model testing are similar to mathematical or graphical daylighting design procedures. However, outdoor testing allows for evaluation under various sky conditions and unique environmental factors, while indoor testing is limited to artificial light sources. The main drawback of outdoor testing is the constantly changing nature of the sky, but it can be mitigated by conducting tests at different times of the day [18]. Furthermore, it is worth noting that the scaled model experiments conducted may not fully align with reality as the reflection values of the materials utilized may not be entirely compatible with the actual environment. To address this issue, the present study aimed to assess the efficacy of the light shelf in improving daylighting performance and compare the results with those obtained from computer simulations. The focus was on determining whether the light shelf height played a significant role in enhancing the daylighting performance of the space.

Among the many available software tools, there are some popular options such as Matlab, Ecotect, Dialux, Velux, Energy Plus, Radiance and Climate Studio. These programs are capable of measuring lighting systems in a computer environment [19]. Among these softwares, Dialux shows the light measurements made in a two-dimensional environment with the colors, isohips, and measurement points. This program is particularly suitable for this study as it provides point data information, which is essential for accurate comparison of computer simulation measurements with scaled model measurements.

Luxmeter was used in measurements with the physical model (Figure 5). DIALux evo software was used in computer simulation measurements. For the open and closed sky, the DIALUX program uses Krochmann's Zenit formula and can calculate the multiplier of the sunlight. When calculating daylight in the program, the daylight environment is added from the guide section. To achieve the correct sky condition in Dialux software, the software takes into account specific date and time information, as well as properties of the sky type DIALux evo software lets input the geographical location (latitude, longitude) and time data of a place to calculate this information for any direction. Additionally, it can be selected the geographical location and time period data for many cities worldwide from the software's library. [20].

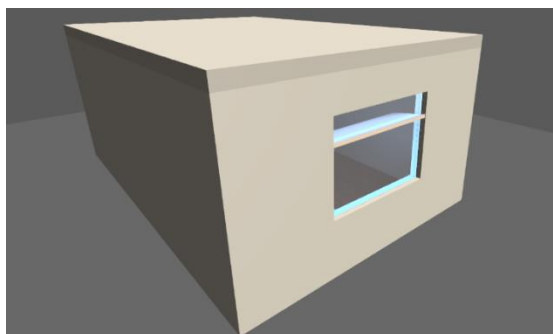


Figure 4. Assessing daylight performance with computer simulation model made in Dialux software.

2.2. Determination of Light Shelf Height with the Help of the Physical Model

To ensure the effectiveness of the light shelf, it is essential that it provides maximum daylight to the innermost areas of the room possible. In this way, the occurrence of shadowy areas in the depths of the room is avoided, and uniform illumination is achieved throughout the space. The height, which is one of the variables in this regard, is one of the parameters that affect light shelf efficiency the most. In this experiment, the optimal height value for this parameter was determined based on the physical model and then compared with the height value obtained through computer simulation measurements to determine its effectiveness. The model's data is compared within its own regions (Table 2-7). The impact of light shelf height on daylighting has been analyzed by comparing different heights of light shelf in specific areas of the model. The daylight analysis with the physical model was based on proportional and comparative results so the reflection values of the physical model's materials were ignored. The results obtained from the computer simulation showed similar proportional results as the physical model. The model was prepared at a scale of 1/10, with a width of 42cm, a length of 66.7cm, and a thickness of 5mm using MDF material (Figure 4). As a result of the physical model's 1/10 rate, the same rate of depth as real room sizes was formed. In this way, how much light shelf height affects the yield has been observed in a close way.

The effect of daylight on the ceiling in order to examine the performance of the light shelf in the deep areas of the room was measured with the help of the physical model and DiWU LX-1010B model Luxmeter (Figure 5). Measurements made with the help of a model and lux metre were compared with the measurements made in the computer environment and provided. Based on these proportional measurements, it is predicted that the light shelf will provide the maximum illumination performance on the ceiling when placed at a height of 185 cm.



Figure 5. (a): Daylight measurement with the physical model. (b): The value obtained from the luxmeter.

In this experiment, light leaks were prevented by using black tape. The photometer sensor of the lux meter is attached to the ceiling and the display is on the outside. (Figure 5, 6). The measured light shelf's heights are indicated by height signs as shown in the photograph (Figure 6). In order to test different openings and shapes, all components of the model are capable of staying intact during both installation and transportation (Figure 6).

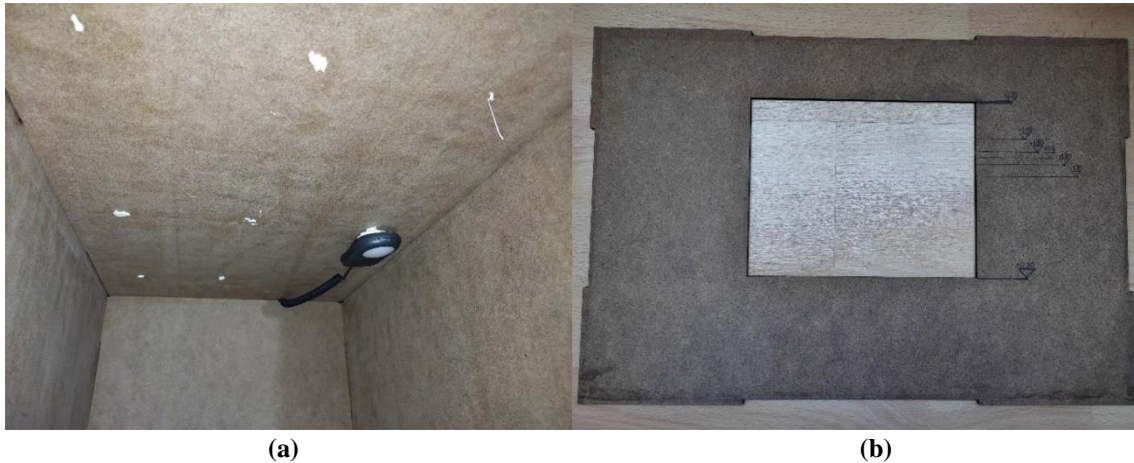


Figure 6. (a): Inside the model. (b): Measurement areas and height signs of the light shelf.

2.3. Determining the Light Reflection Values of the Materials Used

In order to determine the performance of the light shelf and provide the closest values to the reality, should be determined the reflection values of the materials situated in the room and on the light shelf. The computer simulation measurement results were measured in lx. The specified reflection values were applied in Dialux software for computer simulation measurements are made. In the study, the contribution of light shelf performance to the uniformity of illuminance in the room was examined based on the specified parameters. The factors that the user can change (furnitures) in the room will not make a great change in these comparative measurements so the models don't contain these factors. The reflection values of the laminated door and window profiles are the same reflection value of the wall, so that the model doesn't contain laminated door and window profiles.

Light reflection values of the materials found in the study (ρ): Laminated door 0.7, wall 0.7, composite light shelf 0.8, aluminum window profile 0.75. The reflection factor values were determined depending on the surface colors of the ceiling, wall. According to the table below, the ceiling reflection value was determined as 0.7 (Table 1).

Table 1. Reflection Values of Materials [21]

Average Reflection Factor of the Ceiling	Average Reflection Factor of the Wall
0.80 ρ shiny white	0.70 ρ light colored
0.70 ρ light white	0.50 ρ dark colored
0.50 ρ dirty white	0.30 ρ darker colored

2.4. Size and Settlement of the Light Shelf

Ruck suggests that light shelves can be installed both on the outer and inner sides of the window in a light shelf application. To determine the appropriate width of light shelves, it is recommended to use a measurement that is at least equal to the window height, or at least 60 cm or more. Placing the light shelf inside of the window is more efficient to reflect the daylight to the deepest points of the volume, no matter what angle of light comes [22]. In this study, the same opinion was reached and the use of light shelf was made in the room. The width of the light shelf is considered to be 60 cm.

3. RESULTS AND DISCUSSIONS

In this part of the study, certain parameters are kept constant. While each measurement is made in computer simulation measurements, only one of the parameters is variable. In this way, the combination that provides optimum efficiency was found by using the most suitable parameters step-by-step. Measurements have been visualized in a work plane. The "work plane" is a flat surface positioned at a certain height from the ground, where daylight measurements are taken and displayed. The figures that represent the daylight measurements on this surface are referred to as the visualized work plane.

3.1. Determining the Light Reflection Value of the Light Shelf

The fact that the daylight reaches deep areas and provides uniform lighting is an indicator showing the efficient use of the light shelf. In the study, which is visualized with isohips, color and point lx values below, was calculated with the help of the Dialux software.

The light shelf height was 185 cm, the direction of the opening was east and the light shelf slope was 0 degrees. It was measured in open sky values of Eskişehir (30° East longitude and 39° North latitude) on 01/08/2021 at 12:00. Daylight measurement is on 80 cm work plane height.

In the Dialux software, the models generated on a plane are merged into lines by grouping the points that have similar light levels. The reflection value of the reflective shelf is very important for reflecting the light to the depth of the room and providing homogeneous illumination to the room. The Dialux software comes equipped with a library of medium-dark colored wood, composite material, and wood. As evident from the modeling, the reflective value of these materials results in different outcomes.

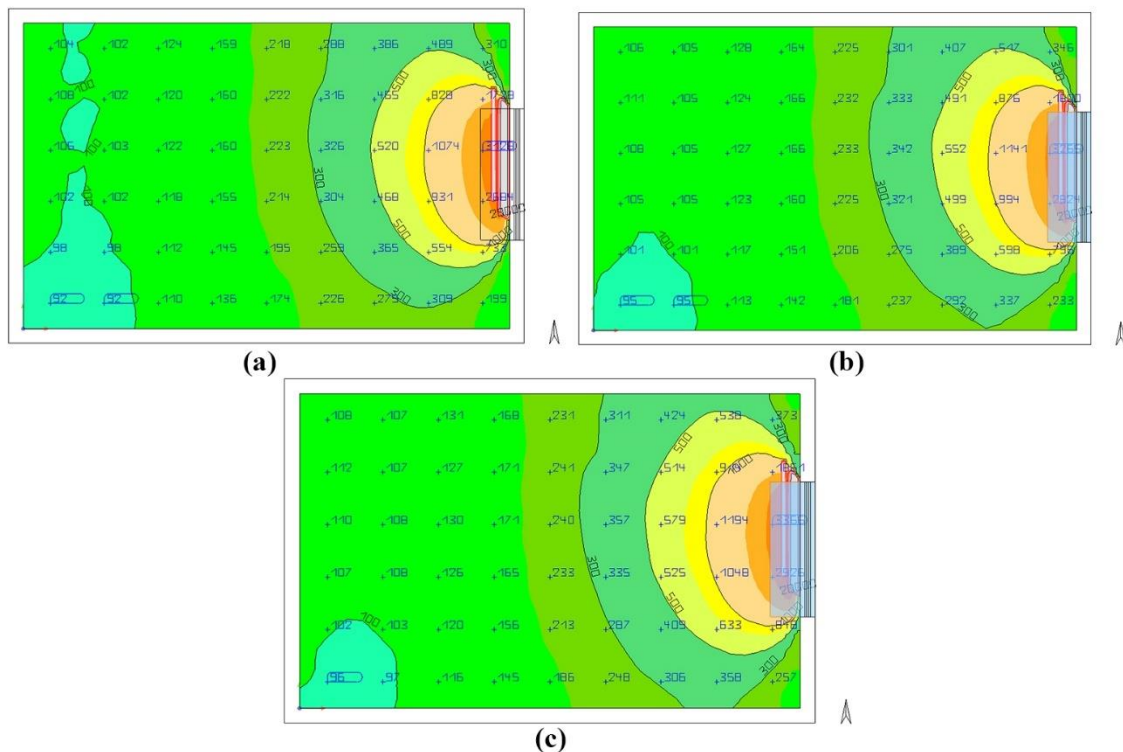


Figure 7. Comparison of light shelf reflection values (a): Reflection value of the light shelf on DiaLux software in default wooden material settings (0.15 ρ). (b): Reflection value of the wooden light shelf (0.50 ρ). (c): Reflection value of the composite light shelf material (0.80 ρ).

The reflection value of the composite light shelf material is high because it undergoes processes such as varnishing. As a result of these computer simulation measurements, it has been observed that the performance of the light shelf with 0.8 ρ reflection value in terms of reflecting the light to the deep areas of the room and providing homogeneous illumination in the room was more effective (Figure 7).

3.2. Comparison of the Direction of the Opening

To determine the facade where the light shelf performs better in buildings, it's essential to take lighting measurements of the light shelf while the room openings face different directions. These measurements, which are calculated by Dialux software, are visualized (Figure 8) and compared. At the bottom and right of each image, there is a north arrow. The arrows are indicating the southern and east directions of the opening by showing the north and west directions.

According to Ruck: The performance of light shelves in the east and west direction is not good; It is stated that the light shelf is efficient in the south direction in the northern hemisphere (north in the southern hemisphere) and in climates where sunny days are intensely [22]. To obtain the maximum yield of the light shelf, the orientation parameter was kept constant in the southern direction during investigation of the combination.

The light shelf height was 185 cm, the direction of the opening was east and the light shelf slope was 0 degrees. It was measured in open sky values of Eskişehir (30° East longitude 39,90° North latitude) on 01/08/2021 at 12:00. Daylight measurement is in 80 cm working plane height. The light shelf reflection value was 0.8 ρ as determined by previous computer simulation measurement.

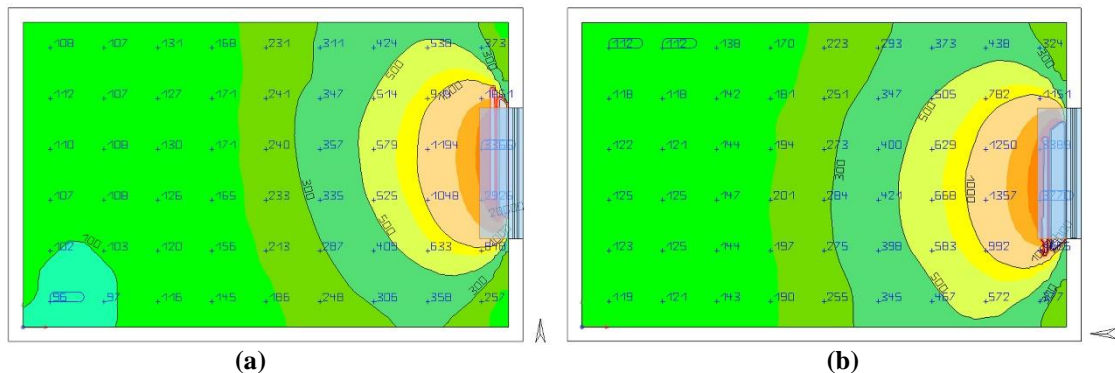


Figure 8. Daylight measurements made in different directions of room's opening (a): East direction. (b): South direction.

As a result of these measurements, the dark area was not found in the depths of the room where the light shelf in the south was used and the light scattered in the room was more homogeneous. Therefore, it was concluded that the light shelf in the southern direction would be more effective (Figure 8).

3.3. Comparison of Light Shelf Height in the East Direction

In order to ensure the most efficient use of the light shelf, the height of the light shelf should be optimum value. In the following study, the optimum height was calculated with the help of the DiaLux software and visualized with isohips, color and point in lx values (Figure 9). The use of the light shelf in the south is the most efficient compared to other directions, but this section (3.1.) was performed by assuming the opening of the room in the east direction. Because the comparison conducted in the east direction has demonstrated the substantial impact of efficient utilization.

In the following comparison (Figure 9), the opening of the room was in the east direction and the slope of the light shelf was 0 degrees. At 12:00 on 01/08/2021, in Eskişehir (30° East longitude 39.90° North latitude), the open sky values were measured during daylight measurements taken at a working plane height of 80 cm. The reflection value of the light shelf was 0.15 ρ .

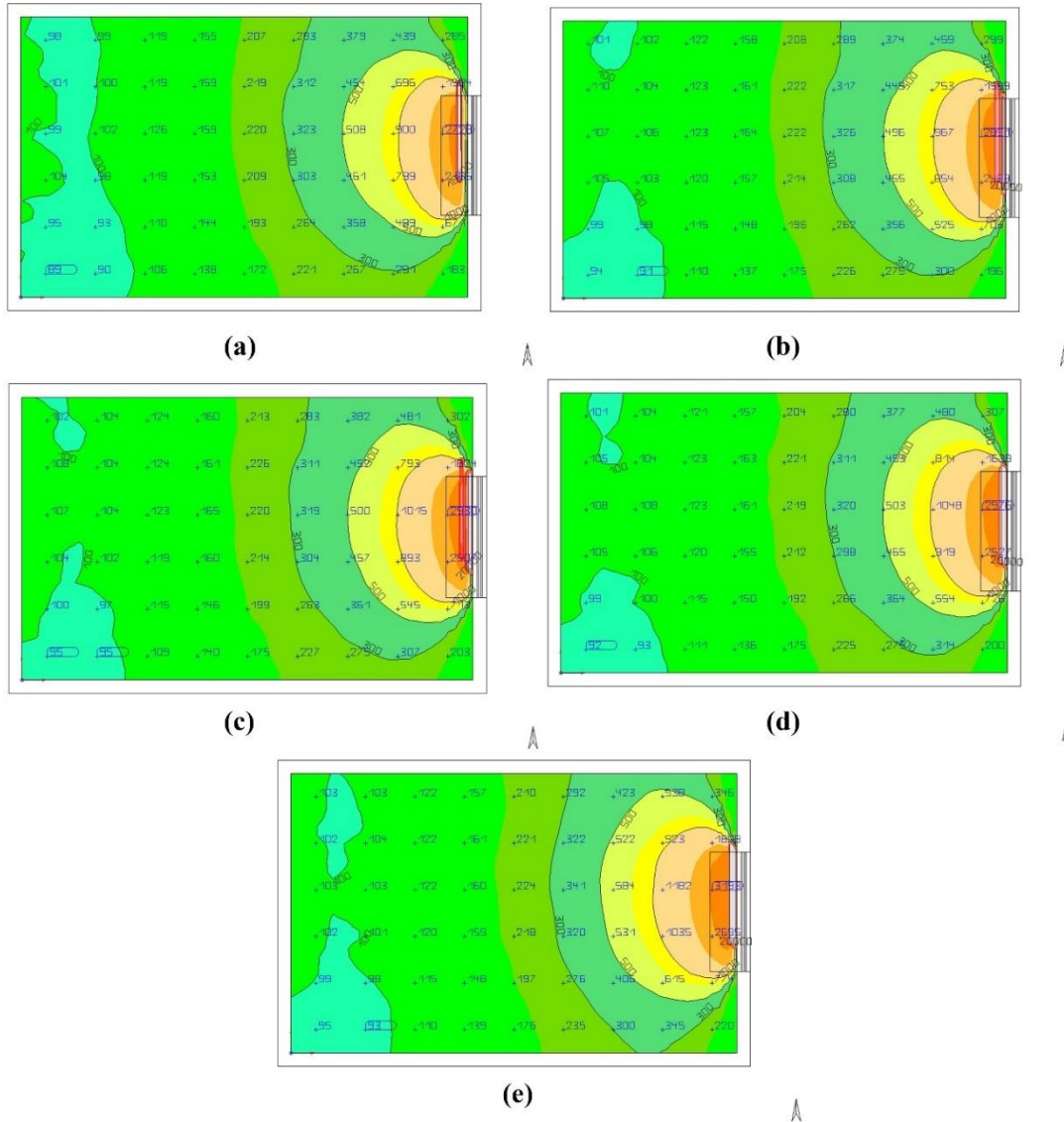


Figure 9. Light shelf height comparison. (a): Light shelf on 170 cm height. (b): Light shelf on 180 cm height. (c): Light shelf on 185 cm height. (d): Light shelf on 190 cm height. (e): Light shelf on 200 cm height.

According to Ruck: The recommended height for light shelves is 2 meters. As the height of the shelf decreases from the ground, the reflection power and daylight amount scattered on the ceiling increases. For this reason, when the light shelves system is intended to implement, it is stated that the ceiling height should be 3 meters [22]. As a result of the measurements, it was observed that the light shelves of 180, 185 and 190 cm height positively affect the performance. Moreover, the study determined that the optimal height for the light shelf was 185 cm in a space with a height of 280 cm. The efficiency was highest at this height, and the most appropriate height ratio was approximately 2/3, which corresponds to a ratio of 185/280 cm.

Ruck suggested a light shelf with a height of 2 meters for a volume of 3 meters. The ideal light shelf ratio was 2/3, and in a space with a height of 280 cm, the light shelf's optimal height was around 185 cm. When this height is tried on the southern facade and on the eastern facade, it was seen that the height of 185 cm was the most suitable height for this room and followed the Ruck's 2/3 ratio proposal [22].

3.4. Determination of Light Shelf's Slope

To maximize the performance of the light shelf, it is advisable to install it on the inside. Figure 10 illustrates the effect of the light shelf slope on the visuals generated using dialux software and light calculations, as well as the efficient utilization of the light shelf in Eskişehir conditions.

In order to examine the penetrative effects of measurements, the orientation of the room was in the east direction. It was measured in open sky values of Eskişehir (30° East longitude 39,90° North latitude) were measured on 01/08/2021, at 12:00. Daylight measurement is on 80 cm working plane height. The light shelf reflection value was 0.8 ρ and the height was 185 cm.

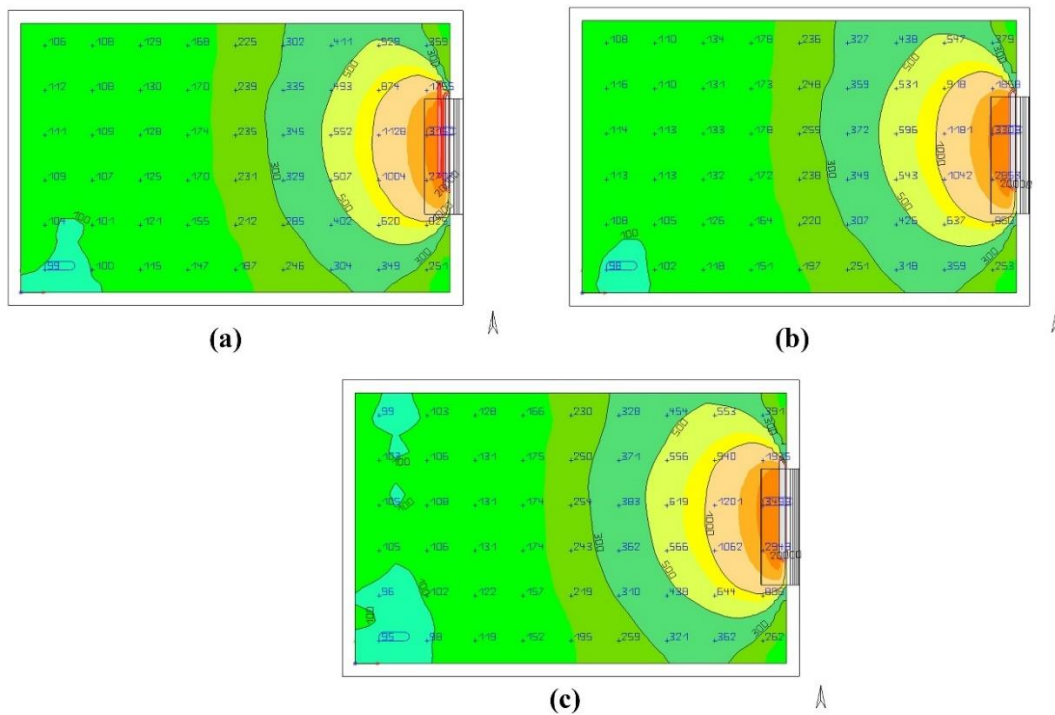


Figure 10. Light shelf slope comparison. (a): Light shelf's slope is 0°. (b): Light shelf's slope is 10°. (c): Light shelf's slope is 20°.

According to Costanzo: The rates are also stated for the most effective use of blinds and roller blinds systems. When the ratio between the wall and window area increases over 40% and 60%, the degree of surface of the plates plays a major role. In this case, the appropriate slope angle is recommended as between 10° to 20° [23].

As shown in the measurements, the performance of the light shelf which has a slope of 10° (Figure 10), was more efficient in reflecting the light to the depths of the room and providing homogeneous light in the room.

3.5. Comparison of Computer Simulation and Physical Model Daylight Analysis

In order to examine the performance of the light shelf in the deeper parts of the room, the effect of daylight on the ceiling (Figure 12-17) was analyzed by comparing both the model (Table 2-7) and computer simulation analyzes. The model measurements were based on results obtained in open sky conditions. The columns in the tables correspond to the specific areas indicated in the image below (Figure 11).

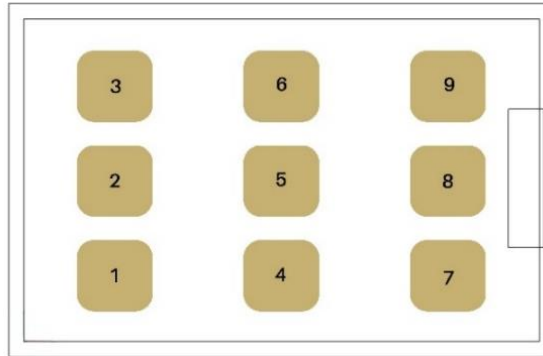


Figure 11. The areas are numbered on the ceiling.

3.5.1. Results of measurements dated 01/08/2021 in lx

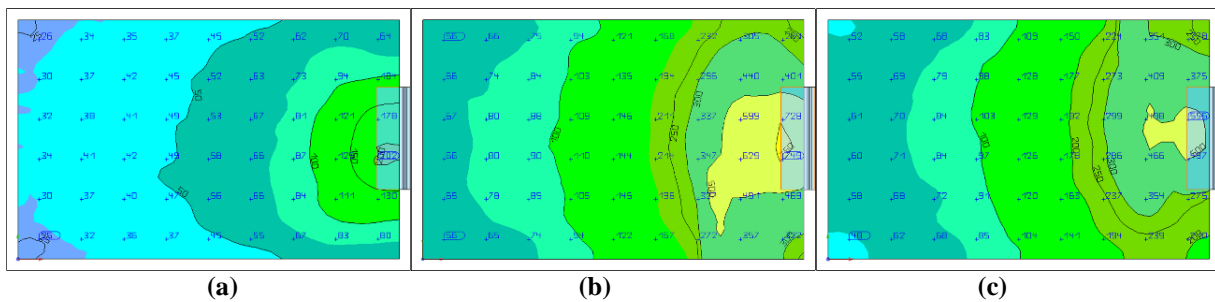


Figure 12. Images of computer simulation measurements, hours respectively: (a): 09:00. (b): 12:00. (c) 15:00.

Table 2. Results of physical model measurements dated 01/08/2021 in lx

Hours / Areas	1	2	3	4	5	6	7	8	9
09.00	40 lx	43 lx	45 lx	58 lx	68 lx	55 lx	115 lx	291 lx	98 lx
12.00	81 lx	85 lx	79 lx	155 lx	148 lx	136 lx	480 lx	648 lx	450 lx
15.00	72 lx	75 lx	72 lx	125 lx	132 lx	135 lx	361 lx	513 lx	413 lx

3.5.2. Results of measurements dated 15/08/2021 in lx

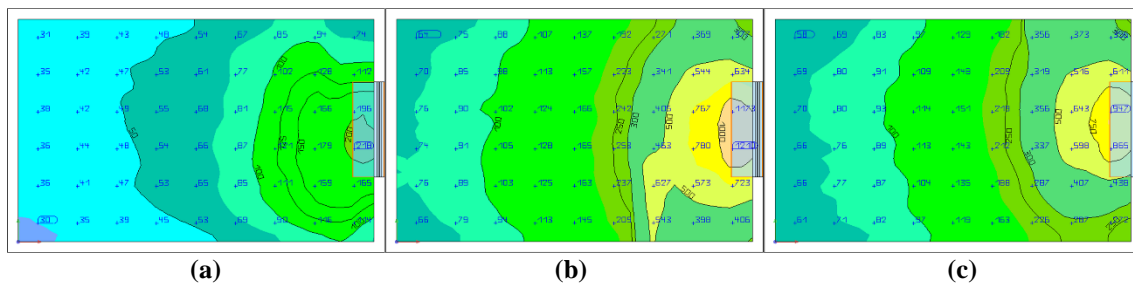


Figure 13. Images of computed measures, hours respectively. (a): 09:00. (b): 12:00. (c) 15:00.

Table 3. Results of physical model measurements dated 15/08/2021 in lx

Hours / Areas	1	2	3	4	5	6	7	8	9
09.00	46 lx	51 lx	43 lx	67 lx	71 lx	63 lx	163 lx	182 lx	133 lx
12.00	93 lx	98 lx	89 lx	177 lx	183 lx	172 lx	613 lx	820 lx	598 lx
15.00	82 lx	95 lx	83 lx	139 lx	158 lx	152 lx	413 lx	655 lx	523 lx

3.5.3. Results of measurements dated 01/09/2021 in lx

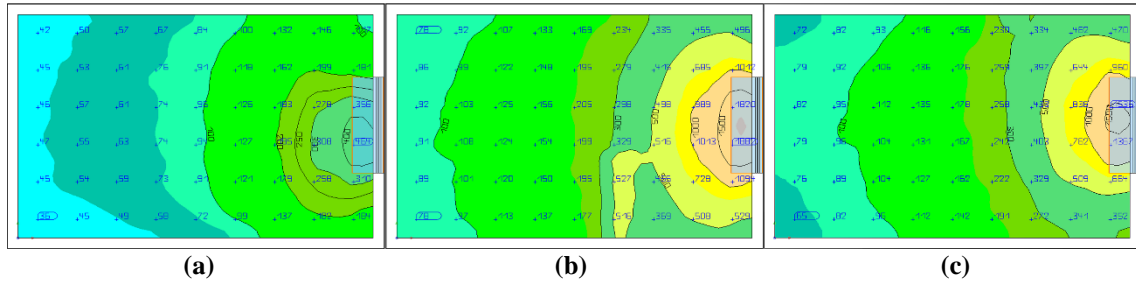


Figure 14. Images of computed measures, hours respectively. (a): 09:00. (b): 12:00. (c) 15:00.

Table 4. Results of physical model measurements dated 01/09/2021 in lx

Hours / Areas	1	2	3	4	5	6	7	8	9
09.00	58 lx	59 lx	55 lx	101 lx	123 lx	98 lx	289 lx	320 lx	203 lx
12.00	106 lx	116 lx	107 lx	215 lx	270 lx	202 lx	768 lx	1208 lx	712 lx
15.00	93 lx	98 lx	91 lx	152 lx	154 lx	163 lx	420 lx	730 lx	615 lx

3.5.4. Results of measurements dated 15/09/2021 in lx

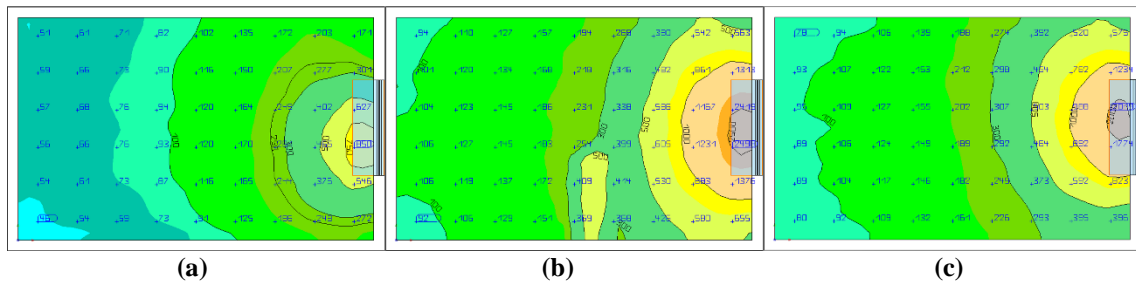


Figure 15. Images of computed measures, hours respectively. (a): 09:00. (b): 12:00. (c) 15:00.

Table 5. Results of physical model measurements dated 15/09/2021 in lx

Hours / Areas	1	2	3	4	5	6	7	8	9
09.00	58 lx	61 lx	57 lx	123 lx	129 lx	103 lx	412 lx	432 lx	245 lx
12.00	132 lx	129 lx	135 lx	352 lx	331 lx	312 lx	935 lx	1276 lx	928 lx
15.00	112 lx	135 lx	122 lx	194 lx	235 lx	202 lx	694 lx	1325 lx	945 lx

3.5.5. Results of measurements dated 01/10/2021 in lx

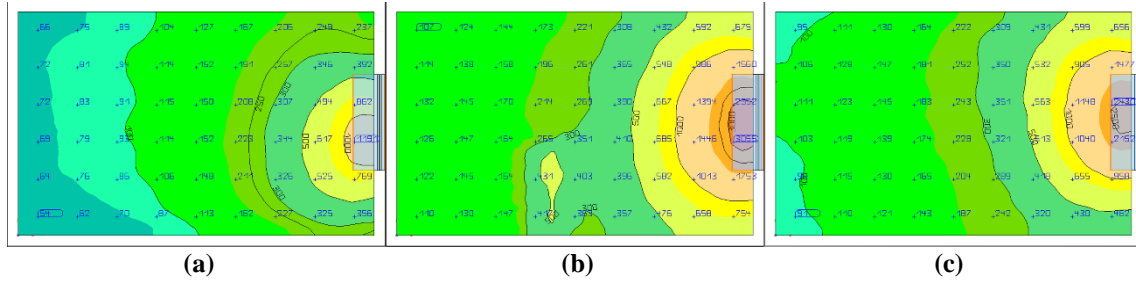


Figure 16. Images of computed measures, hours respectively. (a): 09:00. (b): 12:00. (c): 15:00.

Table 6. Results of physical model measurements dated 01/10/2021 in lx

Hours / Areas	1	2	3	4	5	6	7	8	9
09.00	81 lx	96 lx	68 lx	163 lx	187 lx	149 lx	557 lx	698 lx	361 lx
12.00	152 lx	159 lx	147 lx	423 lx	436 lx	278 lx	1188 lx	1565 lx	1147 lx
15.00	126 lx	146 lx	132 lx	215 lx	265 lx	271 lx	687 lx	1328 lx	1154 lx

3.5.6. Results of measurements dated 15/10/2021 in lx

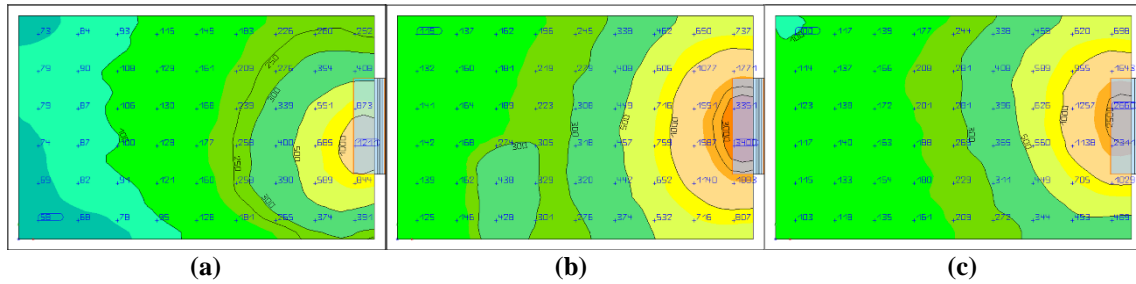


Figure 17. Images of computed measures, hours respectively. (a): 09:00. (b): 12:00. (c): 15:00.

Table 7. Results of physical model measurements dated 15/10/2021 in lx

Hours / Areas	1	2	3	4	5	6	7	8	9
09.00	89 lx	95 lx	85 lx	184 lx	196 lx	172 lx	614 lx	706 lx	425 lx
12.00	152 lx	159 lx	145 lx	256 lx	278 lx	200 lx	752 lx	1103 lx	856 lx
15.00	136 lx	145 lx	132 lx	226 lx	294 lx	268 lx	759 lx	1056 lx	1125 lx

In the following comparison (Table 8) where the room opening faced the east direction and the light shelf had a slope of 0 degrees. Open sky values were measured in Eskişehir (30° East longitude 39.90° North latitude) on 01/08/2021 at 12:00. Daylight measurement is on the ceiling with the help of the lux meter.

Table 8. Results of physical model measurements dated on 01/08/2021 in lx

Heights / Areas	1	2	3
170	236 lx	335 lx	245 lx
180	289 lx	365 lx	270 lx
185	335 lx	423 lx	350 lx
190	315 lx	410 lx	330 lx
200	180 lx	220 lx	170 lx

During this phase of the study, the measurements obtained from the physical model were compared with each other. Moreover, computer simulations were conducted under the same conditions and their outcomes were compared with the physical model results. This approach was taken to examine the consistency of the simulation results with the physical model. The findings were found to be proportional to each other, which enhances the accuracy of the research. Table 8 includes measurements that examine how the height of the light shelf affects the illumination of daylight. As part of this study, light measurements were taken on the ceiling in 1, 2, and 3 areas (Figure 11). A similar study was also illustrated (Figure 9). The results of both studies indicate that the most efficient height is 185 cm at a volume of 280 cm.

3.6. Investigation of Situations in Which the Light Shelf is Advantage-Disadvantage

The primary purpose of light shelves is to allow light to penetrate deeper into the interior of a space, illuminating even the darker areas while ensuring uniform illumination throughout the space. However; The height of the light shelf, the light reflection value of the light shelf (ρ), the angle of the light shelf, the direction of the opening in the room, the daylight in Eskişehir conditions according to different date and different hours are examined in different combinations. During the use of the light shelf with maximum efficiency in Eskişehir's conditions, certain combinations were found to have a negative impact on specific dates and hours. Rather than using a specific lx value as a criterion, the advantages and disadvantages have been evaluated through a comparison of scenarios where light shelves are used versus scenarios where they are not used. If the light shelf has improved the room's illumination, it is considered an advantage, but if it hasn't, it is considered a disadvantage.

The computer simulation measurements (Figure 18) compare the quality of illumination in the room on October 15th at 12:00, with and without light shelves installed, for a window opening on the southern facade. With the light shelf; The homogeneous lighting in the room is provided and the positive impact is seen in reflecting the light in front of the window onto the ceiling. In addition, it is seen that daylight is reflected in the deep areas of the room successfully.

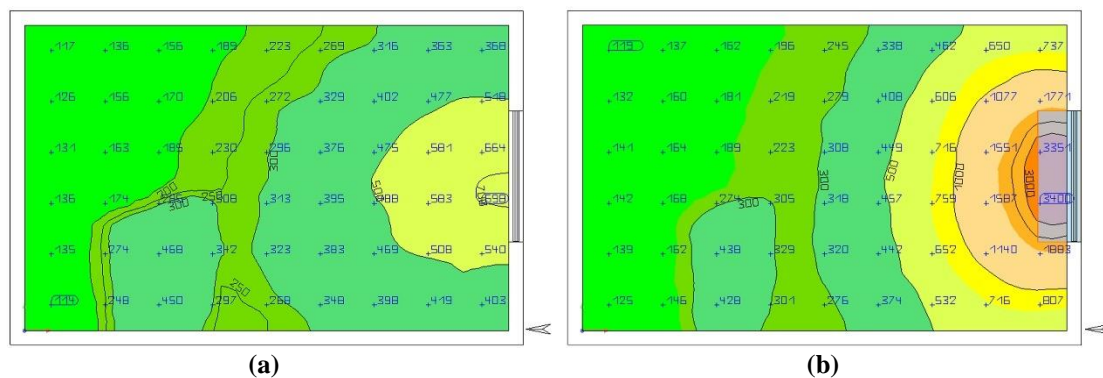


Figure 18. Comparison of no light shelf and with light shelf measurements (a): Without light shelf. (b): With light shelf.

The computer simulation measurements (Figure 19) compare the quality of illumination in the room on October 15th at 15:00, with and without light shelves installed, for a window opening on the southern facade. With the light shelf; The homogeneous lighting in the room is provided and the positive impact is seen in reflecting the light in front of the window onto the ceiling. However, deficiencies have been observed in terms of the transmission of light to the deeper parts of the room.

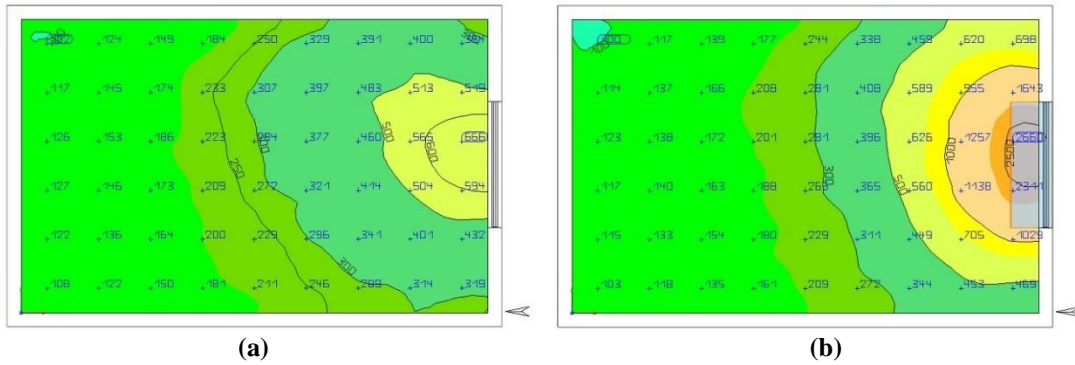


Figure 19. Comparison of no light shelf and with light shelf measurements (a): Without light shelf. (b): With light shelf

The computer simulation measurements (Figure 20) compare the quality of illumination in the room on October 15th at 12:00, with and without light shelves installed, for a window opening on the southern facade. In this comparison daylight measurement is on a 80 cm working plane height. The homogeneous lighting in the room is provided with light shelf. In addition, it is seen that daylight is reflected in the deep areas of the room successfully.

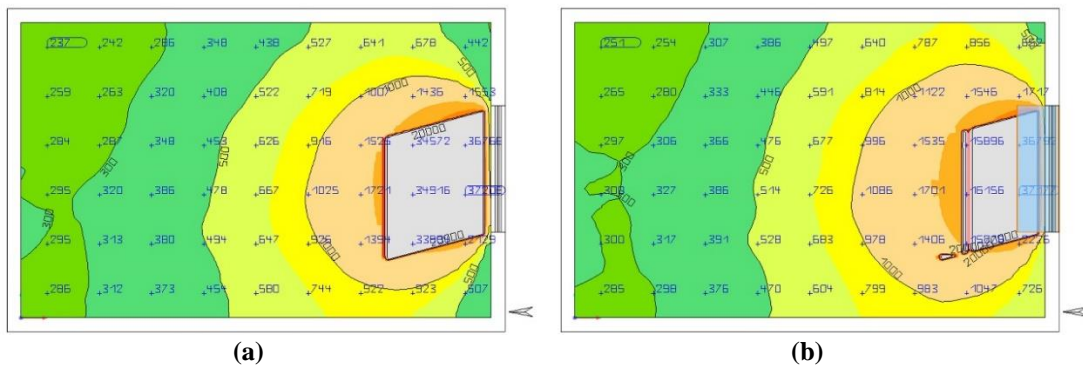


Figure 20. Comparison of no light shelf and with light shelf measurements (a): Without light shelf. (b): With light shelf.

The computer simulation measurements (Figure 21) compare the quality of illumination in the room on October 15th at 12:00, with and without light shelves installed, for a window opening on the southern facade. In this comparison daylight measurement is on a 80 cm working plane height. There was no positive impact on scattering daylight to the room. It was found that it had a negative impact on reflecting daylight to the deep areas of the room.

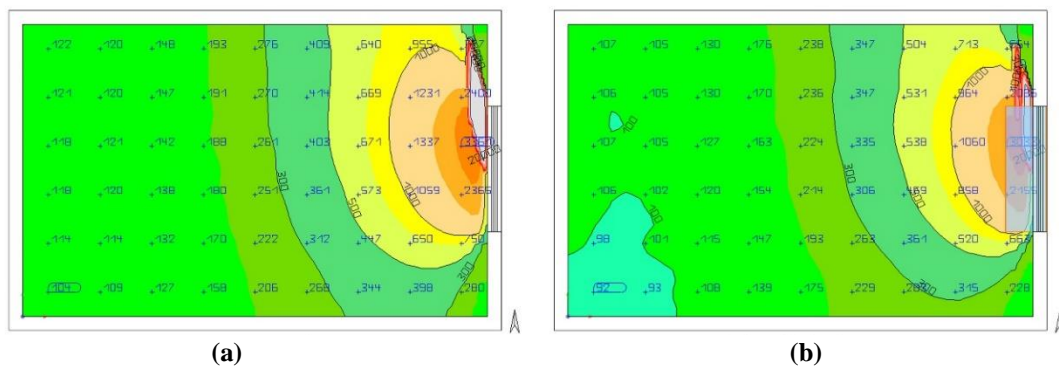


Figure 21. Comparison of no light shelf and with light shelf measurements (a): Without light shelf. (b): With light shelf.

The computer simulation measurements (Figure 22) compare the quality of illumination in the room on October 15th at 15:00, with and without light shelves installed, for a window opening on the southern facade. In this comparison daylight measurement is on a 80 cm working plane height. The homogeneous lighting in the room is provided. It has been observed that the light shelf has only partially succeeded in reflecting light to the deeper parts of the room.

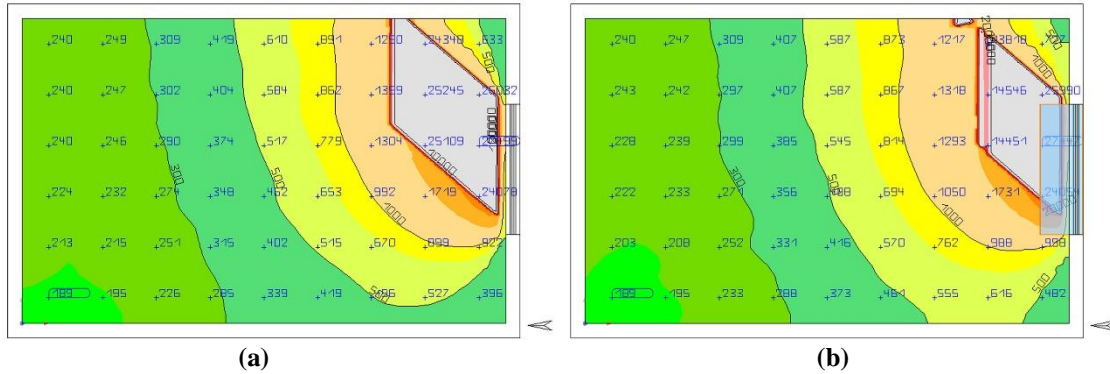


Figure 22. Comparison of no light shelf and with light shelf measurements (a): Without light shelf. (b): With light shelf.

The computer simulation measurements (Figure 23) compare the quality of illumination in the room on October 15th at 15:00, with and without light shelves installed, for a window opening on the eastern facade. In this comparison daylight measurement is on a 80 cm working plane height. Light shelf has not positive impact on scattering the daylight to the room is provided. It was found that it had a negative impact on reflecting daylight to the deep areas of the room.

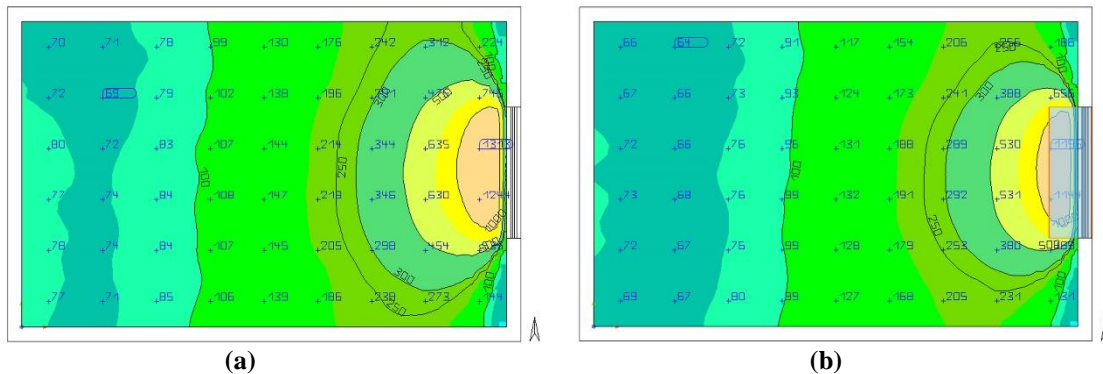


Figure 23. Comparison of no light shelf and with light shelf measurements (a): Without light shelf. (b): With light shelf.

4. EVALUATION AND CONCLUSION

The research and observations conducted indicate that increasing the reflection value of the light shelf has a positive effect on the even distribution of daylight in Eskişehir's conditions. However, the measurements revealed that excessive daylight reflecting from the light shelf can result in discomfort in certain situations that may not occur otherwise.

As a result of the research and observations, it was concluded that the light shelf application is more appropriate and efficient to use the daylight for buildings on the southern facade.

As stated in the figure below, the measurements made in A, B, C, D, E, and F areas (Figure 24) are compared with the help of a graphic (Figure 25). The measurements taken at 12:00 under the open sky

conditions in Eskişehir, comparing the performance of a light shelf with a 0° slope and a light shelf with a 0.15 ρ reflection value (Figure 25). The study examines the lighting performance at different heights of the light shelf in the deepest points of the room, with lx values recorded on the ceiling. In this way, the effect of light shelf height in deep regions has been observed more accurately. The graph shows that the most efficient lighting is achieved at a light shelf height of 185cm, as per the obtained data.



Figure 24. Areas compared in the graph (Figure 25)

Through experimental methods, the most efficient height for the light shelf to reflect daylight into the deeper areas of the room was determined to be 185 cm (Figure 25). This finding was further confirmed by computer simulation measurements. The research showed that light shelves placed at a height corresponding to $2/3$ of the room height provided accurate data, which was confirmed through experimentation and measurements in Eskişehir's conditions. The impact of light shelf height on efficient use was found to be more clearly visible than the case where the window is facing east.

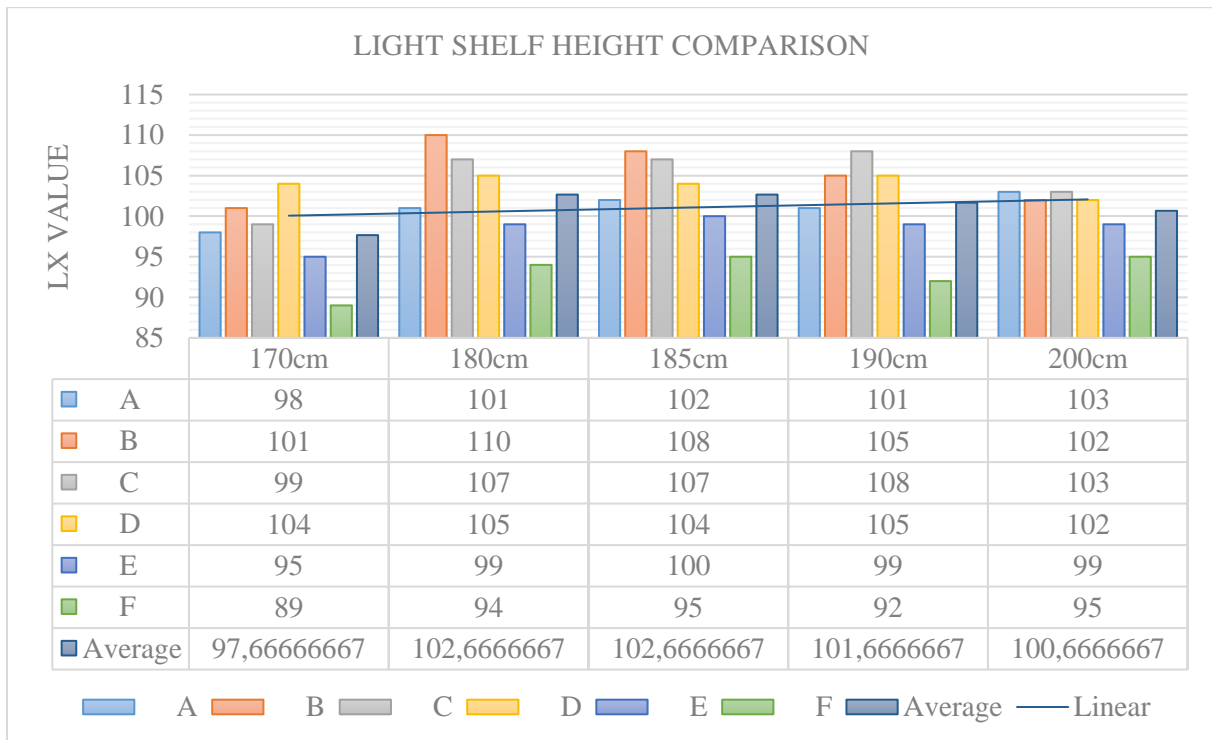


Figure 25. Light shelf height comparison with computer simulation techniques

As a result of computer simulation measurements in determining the light shelf slope, there was no significant difference in the use of the light shelf in the south direction compared to east. The application of a 10° slope for the light shelf in the east direction has enabled us to obtain the most effective comparisons in reflecting daylight to the deeper areas of the room. Based on the data obtained from the experiment's measurements and evaluations, the research determined that the light shelf with a width of 60 cm and a height of 185 cm should be placed facing south for the maximum benefit.

Experimental measurements were conducted using both computer simulation and physical models to analyze the impact of daylight on the ceiling and evaluate the light shelf's performance in reflecting daylight to the deeper areas of the room. In the measurements made with the physical model, in the open sky results are taken as basis. After conducting model and computer simulation measurements, it was observed that the outcomes did not completely coincide with each other. However, they displayed a certain level of similarity in terms of proportion. These measurements on the ceiling were measured and the maximum daylight on the ceiling was obtained with the same parameters to reflect the maximum daylight to the depths of the room.

Upon examining the scenarios where the light shelf could be advantageous or disadvantageous, it was discovered that in Eskişehir conditions, the light shelf may not always have a positive impact, even during the dates and hours where it was most efficient. However, at these dates and hours where the light shelf is seen inefficient, the light shelf may become more efficient than the reflective variables at the base of the room. In the room where the study was conducted, it was assumed that there were no objects present. However, in a room with reflective objects like carpet rugs that absorb light, the light shelf may enhance efficiency by reflecting the light towards the ceiling in the disadvantageous scenario.

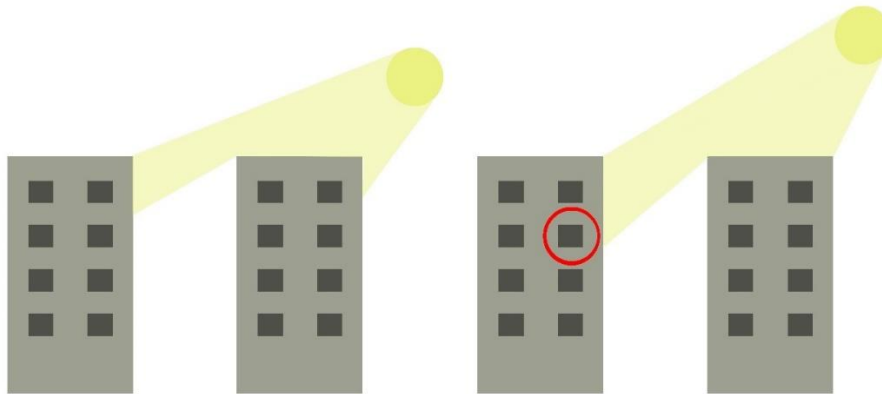


Figure 25. Apartment samples benefiting from daylight according to the angle of the sun rays.

Based on these findings, it is recommended to use a light shelf with the parameters that were found to be most effective under Eskişehir conditions. Especially in buildings that cannot take the horizontal daylight into the room (Figure 25), it is concluded that the use of the light shelf on the southern facade is the most appropriate use by preventing the daylight in front of the window and reflect to the ceiling when the daylight enters the room with a steeper angle.

ACKNOWLEDGEMENTS

This article has been prepared from the research project titled "Determination of the Performance of Light Shelves for More Effective Benefit from Daylight in Buildings" scope of TUBITAK's "2209/A University Students' Domestic Research Projects Support Program", which was completed in the architecture program, ESTÜ Faculty of Architecture and Design.

In the article, national and international research and publication ethics are complied with. Ethics Committee permission was not required in the study.

We would like to thank TÜBİTAK for their support of this research project and thank Doç. Dr. Hatice Günseli Demirkol for giving consultancy. Also, we would like to thank Eskişehir Technical University for its support and for the 3rd prize within the scope of the EsTekFest-2022 Technology Festival.

CONFLICT OF INTEREST

The authors stated that there are no conflicts of interest regarding the publication of this article.

AUTHORSHIP CONTRIBUTIONS

The manuscript was written by Furkan Meral, who took on the role of corresponding author. Meanwhile, Doç. Dr. Hatice Günseli Demirkol provided consultancy during both the research project and manuscript writing stages. Therefore, both authors made equal contributions.

REFERENCES

- [1] Kontadakis A, Tsangrassoulis A, Doulos L, Zerefos S. Review of Light Shelf Designs for Daylit Environments, MPDI Sustainability. Basel, Switzerland, 2017; 10-71.
- [2] Rashid M, Zimring C. A Review of the Empirical Literature on the Relationships Between Indoor Environment and Stress in Health Care and Office Settings. Sage Publications, 2008; 151-190.
- [3] Yener A K. Methods of Use of Daylight in Buildings, Contemporary Techniques, VIII. National Installation Engineering Congress. İzmir Tepekule Congress and Exhibition Center, 2007; 231.
- [4] Kılıç Demircan R, Gültekin A B. Investigation of Passive and Active Solar Systems in Buildings. TÜBAV Bilim Dergisi, 2017; 10 (1), 36-51.
- [5] US Green Building Council. 2006. LEED-NC (Leadership in Energy and Environmental Design). Version 2.2. www.usgbc.org/LEED/ Access Date 20th December, 2023; 10:40.
- [6] İstanbul, Türkiye: Beta. Neuferd E. Çağla Özaslan (Ed.) Lighting Lighting Glass, Building Design Information, 2009; 35, 166.
- [7] Reinhart C F, Mardaljevic J, Rogers Z. Dynamic Daylight Performance Metrics for Sustainable Building Design. LEUKOS, 2006; 7-31.
- [8] Fabi V, Andersen R V, Corgnati S, Olesen B W. Occupants' window opening behaviour: A literature review of factors influencing occupant behaviour and models, The International Journal of Building Science and its Applications, 2012; 188-198.
- [9] Erel B. A Research on New Technologies Developed in Daylighting, Master Thesis. Istanbul Technical University, Institute of Science and Technology, İstanbul, 2004; 4-5.
- [10] GKS Dergisi, Sun Control: Sun Reflector and Shelves, <https://gksdergisi.com/gunes-kontrolu-gunes-kirici-ve-raflari/>. Publication date 18th March, 2018. Access date 2nd February, 2022; 00:22.

- [11] Warriar A G, Raphael B. Performance evaluation of light shelves, *Energy and Buildings* 2017; 140, 19–27.
- [12] Barker L L. *Communication in the classroom*. Prentice Hall Inc: Englewoods Cliffs. 1982; 55-72.
- [13] Lighting Research Center, *Guide for Daylighting Schools*. 850 West Morgan Street Raleigh, NC 27603 2004; 9-10
- [14] Kurtay C, Esen O. *Journal of the Faculty of Engineering and Architecture of Gazi University*, 2019; 34:2, 835-843.
- [15] Meresi A. Evaluating daylight performance of light shelves combined with external blinds in south-facing classrooms in Athens. *Energy and Buildings*, 2016; 116, 190-205.
- [16] Michel L, Scartezzini J. Implementing the partial daylight factor method under a scanning sky simulator. *Solar Energy*, 2002; 473-492.
- [17] Chen Y, Liu J, Pei J, Cao X, Chen Q and Jiang J. Experimental and simulation study on the performance of daylighting in an industrial building and its energy saving potential. *Energy and Buildings*, 2014; 184-191.
- [18] Selkowitz S. *A Hemispherical Sky Simulator For Daylighting Model Studies*. Lawrence Berkeley National Laboratory, 1981.
- [19] Ahmad A, Kumar A, Prakash O, Aman A. Daylight availability assessment and the application of energy simulation software – A literature review, *Materials Science for Energy Technologies*, 2020; 679-689.
- [20] Işık U. *The Assessment of Relationship Between Lighting Design Programs and Rendering Plugins*, Master Thesis. Yıldız Technical University, Institute of Science and Technology, İstanbul, 2009; 69.
- [21] Pelsan, reflection values of materials, <https://www.pelsan.com.tr/tr-TR/aydinlatma-hesaplari/26124>. Publication date 24th December, 2016. Access Date 25th August, 2021; 10:40.
- [22] Ruck N, vd. Christoffersen J. (Ed.) S. *Daylight in Buildings, a source book on daylighting systems and components*, International Energy Agency Energy Conservation in Buildings and Community Systems Programme. USA: ECBCS Annex. 2000; 2-20,4-26.
- [23] Costanzo V, Evola G, Marletta L. A review of daylighting strategies in schools: state of the art and expected future trends *Buildings MDPI*. 2017; 7-41.



RESEARCH ARTICLE

THE CYTOTOXIC EFFECT OF BENZOIC ACID ON TEN DIFFERENT CANCER CELL LINES

Hatice ÖZTÜRKEL KABAKAŞ¹ , Merve SEZER KÜRKCÜ^{2,3} ,
Kadriye Aslıhan ONAT TAŞDELEN¹ , Bekir ÇÖL^{3,4,*} 

¹ Muğla Sıtkı Koçman University, Graduate School of Natural and Applied Sciences, Biology Program, Muğla, Türkiye

² Muğla Sıtkı Koçman University, Research Laboratories Center (ALM), Proteogenome Laboratory Muğla, Türkiye

³ Muğla Sıtkı Koçman University, Biotechnology Research Center, Muğla, Türkiye

⁴ Muğla Sıtkı Koçman University, Science Faculty, Department of Biology, Muğla, Türkiye

ABSTRACT

Cancer, having numerous types, is among the most dangerous and complex chronic diseases in the world affecting the wellbeing of humans, society and economy. The exploration and reassessment of effective chemicals, compounds, and natural products as potential agents for alleviating the adverse effects of cancer and its related symptoms continue on a global scale. This process involves an initial evaluation of the cytotoxic activities of potential drug candidates or treatment regimens on diverse cancer cell types in an ex vivo context. Benzoic acid (BA), an aromatic carboxylic acid that is widely available and used in the food industry, is one of the phenolic acids that may bear considerable anti-cancer potential. It is useful to find out the comparable effect of BA on various cancer types. Therefore, in this study, we tested the cytotoxicity of BA using MTT assay, on a number of ten different cancer cell lines and one normal cell type, namely prostate cancer (PC3), cervical cancer (HeLa), liver cancer (HUH7), colon cancer (CaCO2, HT29, SW48), bone cancer (MG63 and A673), pharyngeal cancer (2A3), lung cancer (CRM612) and kidney epithelial control cell line (Phoenix), respectively. IC₅₀ (µg/ml) values after 48 and 72-hour exposure to BA were found to differ between 85.54±3.17 to 670.6±43.26, while the IC values for the control cell line Phoenix were 410.54±32.29 and 231.16±25.25, respectively. Taking into account of statistical evaluation of the IC₅₀ values for BA on 11 cell types, we suggest that the molecular and omics approaches can be implemented in more details in order to find cellular and biochemical targets of BA as well as elucidating molecular mode of action, especially starting with the cancer cell lines of MG63, CRM612 and A673, in which the IC₅₀ levels are relatively the lowest compared to those of the control cell line.

Keywords: Benzoic acid, Cytotoxic effect, Anticancer, MTT

1. INTRODUCTION

Cancer represents a cluster of diseases arising from genetic anomalies, including the loss of function in tumor suppressor genes, gene mutations, gene deletions in chromosomes and epigenetic changes in gene expression [1]. Transcriptional epigenetic modifications play an important role in the onset and progression of cancer pathogenesis [2]. Various factors, such as the rise in unhealthy eating habits, smoking, and aging of the population, contribute to the transformation of normal cells into cancerous ones [3].

The treatment process in cancer patients is related to the size of the tumor, the age of the patient, the presence of metastases, the susceptibility to chemotherapy, and the feasibility of surgical intervention [4]. The side effects associated with chemotherapy, radiotherapy, and commonly used surgical methods in cancer treatment, coupled with the development of chemotherapy resistance in patients and the tumor's potential to metastasize, impose limitations on treatment options [5]. Beyond these side effects, a prominent challenge in treatment lies in late diagnosis, which, along with economic costs and disease progression limitations, curtails the application of available therapeutic agents. Consequently, there is a

*Corresponding Author: bcol@mu.edu.tr

Received: 14.07.2023 Published: 28.03.2024

pressing need to uncover novel drugs and treatment modalities that can enhance treatment success and mitigate side effects [6].

Phenolic compounds, secondary metabolites found in fruits, vegetables, grains, and legumes [7], have garnered interest due to their use in diets and minimal side effects [8]. These compounds play roles in plant defense mechanisms against ecological and physiological stress factors, synthesized in response to stressors such as pathogenic microorganisms, insects, and UV radiation [9]. Phenolic compounds are classified into various groups, including lignin, tannins, and simple phenols -primarily phenolic acids containing benzoic acid and cinnamic acid derivatives- based on the number of phenol groups in their structure and their substitution position [10-11-12]. Benzoic acid (BA), a natural compound in the hydroxybenzoic acid group, is widely available and utilized [13].

Benzoic acid is synthesized through natural and synthetic pathways. For instance, it is synthetically produced by the oxidation of toluene at high pressure and temperature [14]. Plants synthesize benzoic acid from phenylalanine or shikimate [15]. Several benzoic acid derivatives, such as ubiquinone (Coenzyme Q) and folic acid, are vital for plant metabolism. Ubiquinone is a benzoquinone involved in the mitochondria and electron transport system of some bacteria [16]. Salicylic acid is an herbal hormone found in the defense mechanism of plants. At the same time, some volatile benzoic acid derivatives found in plants are involved in pollination and protection of reproductive organs from bacterial infections [17]. Benzoic acid is naturally formed by the oxidation of benzaldehyde because of microbial degradation of hippuric acid and phenylalanine during the formation of fermented milk products [18]. *Streptomyces maritimus*, an aquatic microorganism, synthesizes benzoic acid by β -oxidation of L-phenylalanine while producing enterocin [19].

The fact that benzoic acid is a natural compound and can be produced synthetically makes it versatile to be used in many fields ranging from cosmetics to food industry. Studies have shown that benzoic acid has antibacterial, antioxidant, antifungal, and anticancer activities. One of the biggest problems encountered in livestock is gastrointestinal diseases. Intestinal flora in small cattle can be improved by using benzoic acid [20]. In another study with benzoic acid, the antibacterial effect against Enterohemorrhagic *Escherichia coli* (EHEC) bacteria, which causes hemorrhagic uremic syndrome and is transmitted from contaminated food and water, was investigated. The inclusion of benzoic acid in the diet has been shown to improve the intestinal microbiota [21]. In addition to all these activities, benzoic acid (E210) is used as a preservative in acidic or slightly acidic foods because it has antimicrobial activity [22].

In addition to the inhibitory effect observed on microbial organisms, benzoic acid is also recognized for its anticancer activity in cancer cells. The literature contains relatively limited number of studies examining the cytotoxic effect of benzoic acid specific to different cancer types. Phenolic compounds, which are an integral part of the daily human diet and are absorbed by the colon, have been studied in the context of colorectal cancer. In experiments where CaCo-2 colorectal cancer cells were exposed to benzoic acid and caffeic acid, the induction of apoptosis in cancerous cells was observed. Apoptosis induction occurred independently of mitochondrial DNA (mtDNA) [23]. This finding is promising, considering another study that established a relationship between changes in mtDNA levels in cells and resistance to anticancer drugs [24].

In some studies, aiming to determine the mechanism of the cytotoxic effect of benzoic acid, it has been suggested that benzoic acid and its derivatives may possess histone deacetyltransferase inhibitor (HDACi) activity. Acetylation of histones by the histone acetyltransferase (HAT) and deacetylation by the histone deacetyltransferase (HDAC) are the most well-known epigenetic mechanisms in the regulation of transcription [25]. An increase in the level of the HDAC enzyme may lead to the silencing of tumor regulator genes and contribute to the pathogenesis of cancer [26]. Benzoic acid, hydroxy benzoic acid, dihydroxy benzoic acid, and methylated forms of benzoic acid, as well as HDAC inhibition effects on breast (HeLa), cervical (SiHa), colon (HCT-116), and rectal (HCT-15) cancer types were

studied. Dihydroxy benzoic acid has been found to have a 50% HDAC inhibition activity [27]. In another study, it was reported that hydroxybenzoic acid inhibits the HDAC3 enzyme in breast cancer cells (MCF-7) and promotes apoptosis [28].

As a result of studies, it has been established that benzoic acid exhibits a cytotoxic effect on cancer cells. However, the literature indicates a shortage of studies focusing on different types within a cancer group (e.g., Colon cancer - CaCO₂, HT29, SW48). In our conducted study, we investigated the cytotoxic effect of benzoic acid using 10 different cancer cell lines and 1 control one. The study aimed to determine the concentration of benzoic acid (IC₅₀), which inhibits half of the population in the target cancer types. This study was conducted to unveil the anticancer effect of benzoic acid specific to various types of cancer.

2. MATERIALS and METHODS

2.1. Chemicals and Cell Lines

DMEM (Dulbecco's Modified Eagle's Medium) (Capricorn Scientific #DMEM-HA), RPMI (Roswell Park Memorial Institute) (Sigma #R8758), Trypsin/EDTA (Pan Biotech #P10-019100), Penicillin/Streptomycin (Capricorn #PS-B), FBS (Fetal Bovine Serum) (Gibco #A4766801), DMSO (Dimethyl sulphoxide) (Biofroxx #67-68-5), Trypan blue (Sigma #T8154), DPBS (Dulbecco's Phosphate Buffered Saline) (Sigma #D8537), MTT (Thiazoyl Blue Tetrazolium Bromide) (Sigma #M2128), Benzoic acid (Sigma #242381) were purchased from the indicated suppliers shown in parentheses.

The cell lines used in this study are prostate cancer (PC3), cervical cancer (HeLA), liver cancer (HUH7), colon cancer (CaCO₂, HT29, SW48), bone cancer (MG63 and A673), pharyngeal cancer (2A3), lung cancer (CRM612) and kidney epithelial control cell line (Phoenix). HUH7 cancer cell line was obtained from Sigma Aldrich, CRM612 cancer cell line was obtained from Aydın Adnan Menderes University, Department of Medical Biology, and other cell lines were obtained from ATCC.

2.2. Cell Culture

Cells were grown at 37°C in a humidified environment with 5% CO₂. RPMI medium containing L-glutamine and sodium bicarbonate was used for the propagation of the PC3 cell line, and DMEM medium containing L-glutamine was used for the propagation of other cell lines. 10% FBS and 1.5% penicillin/streptomycin were added to the media. Cells were taken from flasks by trypsinization. Cells were seeded in 96-well cell culture plates at 10⁵ cells per well. For the cells to adhere to the wells, they were incubated for 24 hours at 37°C in a 5% CO₂ incubator. The benzoic acid was prepared with Ethyl alcohol (EtOH) at a stock concentration of 125 mg/ml. In the experiments, 0, 23.44 µg/ml, 46.88 µg/ml, 93.75 µg/ml, 187.5 µg/ml, 375 µg/ml and 750 µg/ml benzoic acid were used. The experiment was replicated 3 times at each concentration tested.

2.3. MTT Test to Determine the Cytotoxicity of Benzoic Acid

After the cells were exposed to benzoic acid at given concentrations for 48 hours and 72 hours, the medium containing benzoic acid was removed and 0.5 final volume of MTT solution was added to each well and incubated for 4 hours in the dark. After 4 hours, the MTT solution in the wells was removed from the wells and 100 µl of DMSO was added to each well to dissolve the formed formazan crystals. It was incubated for 15 minutes for the formation of purple color and absorbance values were measured at 570 nm in the spectrophotometer. Concentrations (IC₅₀) at which benzoic acid inhibited each cell line by 50% were calculated [29].

2.4. Statistical Analysis

Statistical analyses were performed using the GraphPad Prism 8.0.1 statistics program. Benzoic acid concentrations that inhibited the growth by 50% (IC₅₀) were calculated. The MTT assay of each cell group was performed in triplicate. A t-test was performed following one-way ANOVA, and the statistically significant levels of IC₅₀ values taken from two different time points were calculated. A p-value of less than 0.05 was considered significant. The calculations were carried out separately for each cell line for the 48- and 72-hour results.

3. RESULTS

The MTT test was conducted to assess the effect of benzoic acid on cell viability in various cancer cell lines. Cells were exposed to benzoic acid at concentrations of 0, 23.44 µg/ml, 46.88 µg/ml, 93.75 µg/ml, 187.5 µg/ml, 375 µg/ml, and 750 µg/ml for 48 and 72 hours. The Phoenix kidney epithelium-like cell line was included as a control.

As the concentration of benzoic acid increased, cell viability decreased depending on the dose and incubation time. Percentage cell viability (%) graphs were generated for each cell line separately based on increasing benzoic acid concentrations, with the no-treatment group normalized to 100. Figure 1 illustrates the cell viability graphs for HeLa, Huh7, CaCO₂, and MG63 cells upon exposure to benzoic acid for 48 and 72 hours. Cell viability ratios for HT29, A673, SW48, and PC3 cells are presented in Figure 2. The effect of benzoic acid on the control cell line Phoenix- kidney epithelial-like cells, as well as the other two cancer lines, 2A3 and CRM612, is illustrated in Figure 3.

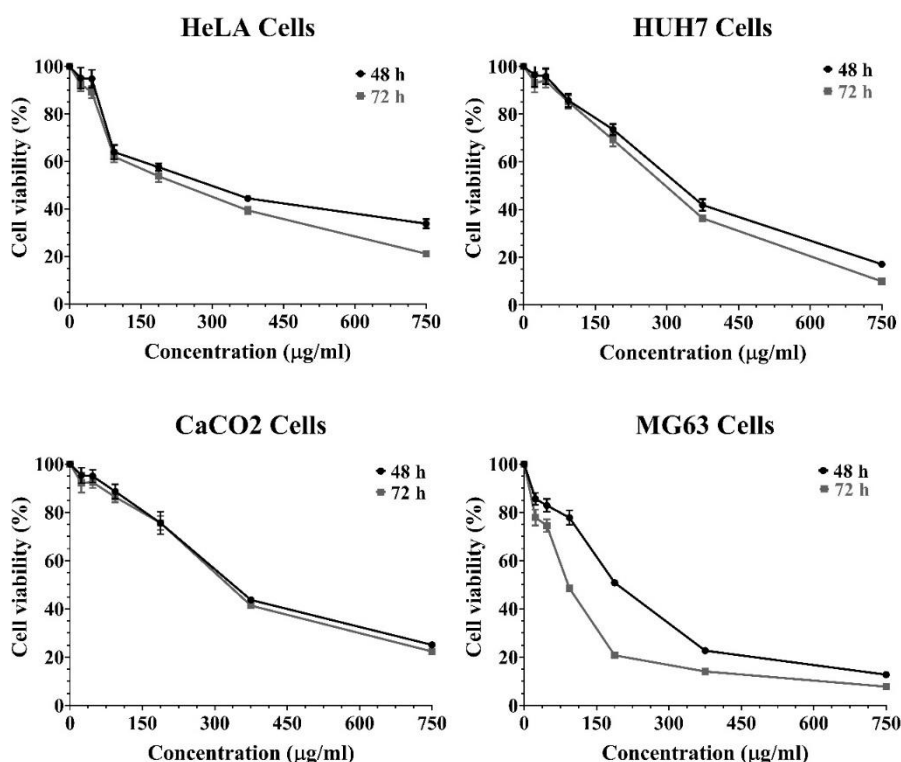


Figure 1. The cytotoxic effect of benzoic acid on HeLa, HUH7, CaCO₂, and MG63 cancer cells. Percentage cell viability graphs are displayed for 48 and 72 hours of incubation. Benzoic acid concentrations are shown in µg/ml

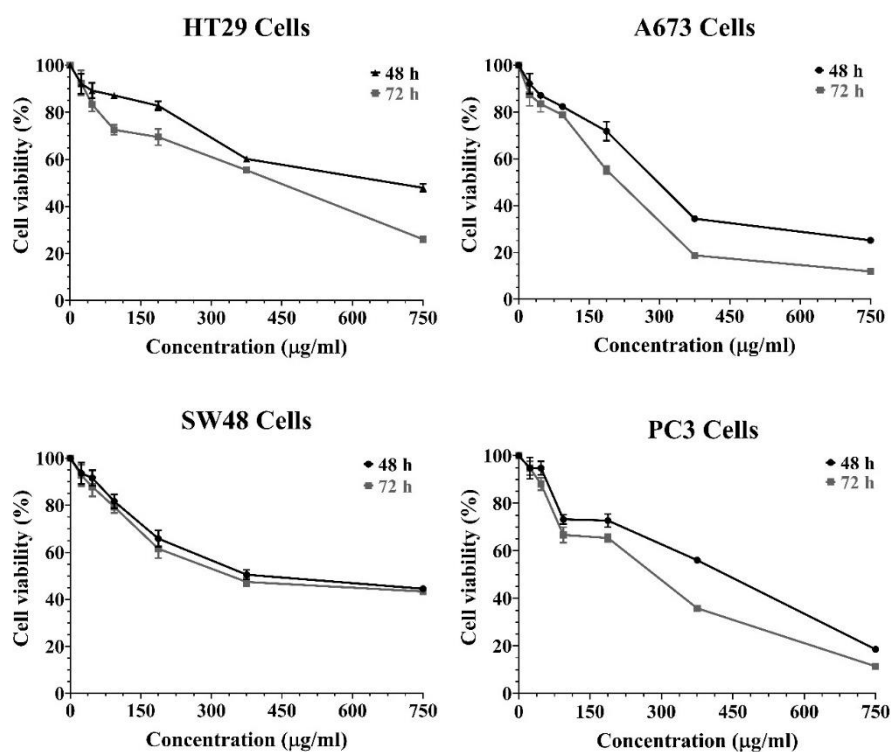


Figure 2. The cytotoxic effect of benzoic acid on HT29, A673, SW48 and PC3 cancer cells.

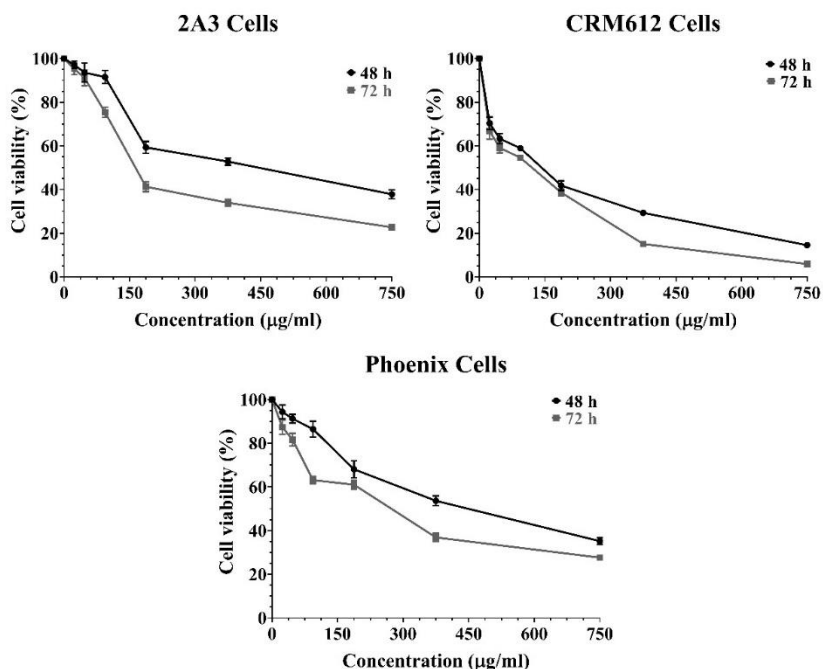


Figure 3. The cytotoxic effect of benzoic acid on 2A3, CRM612 cancer cells and Phoenix control cells.

IC₅₀ values were calculated for each cell line from the cell viability graphs to determine the benzoic acid concentration that inhibited 50% of the cell population for both 48 and 72-hour exposure times.

These IC50 values are presented in Table 1. The range of IC50 values was observed to be from $85.54 \pm 3.17 \mu\text{g/ml}$ to $670.6 \pm 43.26 \mu\text{g/ml}$, suggesting significant variation in the response of different cancer cells to BA, possibly attributable to various intrinsic tolerance mechanisms within the cells.

Statistical analysis of the findings from the 48-hour benzoic acid exposure revealed that HeLa, HUH7, MG63, A673, and CRM612 cells were significantly more affected ($p < 0.05$) (Figure 4) compared to the results obtained with the control cell line Phoenix. Subsequent statistical analyses performed after 72 hours of benzoic acid exposure revealed that MG63 and CRM612 cells were significantly more affected ($p < 0.05$) (Figure 5).

Among the cell lines affected by benzoic acid, CRM612 and MG63 stand out, particularly because these cell lines are inhibited by relatively low levels of BA compared to the control and other cell lines.

Table 1. IC50 values of the cancer cell lines used in this study and the Phoenix control cell line following exposure to benzoic acid for 48 and 72 hours

Cell line	IC50 ($\mu\text{g/ml}$)	
	48 hour	72 hour
HeLa	270.84 ± 14.22	219.61 ± 28.13
HUH7	317.83 ± 17.32	282.77 ± 7.62
CaCO2	331.07 ± 16.57	320.08 ± 12.22
MG63	195.21 ± 6.93	85.54 ± 3.17
HT29	670.6 ± 43.26	472.15 ± 10.09
A673	274.51 ± 14.11	199.31 ± 3.90
SW48	374.55 ± 33.11	321.58 ± 28.67
PC3	449.54 ± 13.12	260.84 ± 5.70
2A3	355.39 ± 16.95	193.06 ± 11.12
CRM612	108.18 ± 9.78	93.76 ± 7.49
Phoenix	410.54 ± 32.29	231.16 ± 25.25

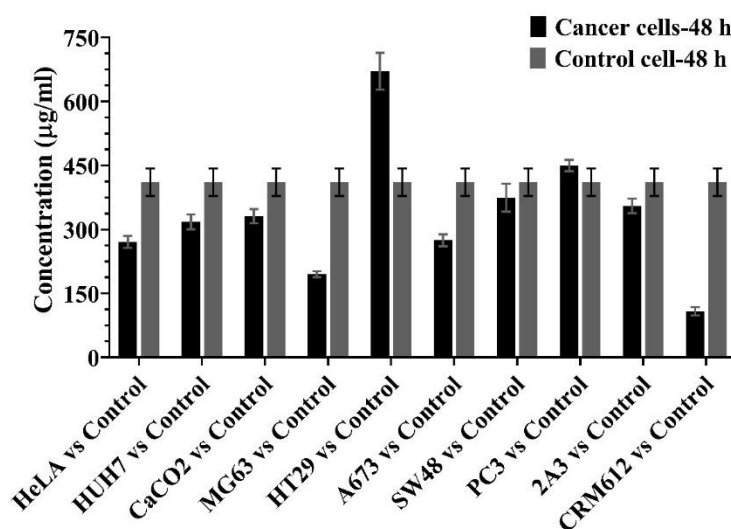


Figure 4. Comparison of IC50 values for the cancer cell lines and the control cell line following 48-hour exposure to benzoic acid

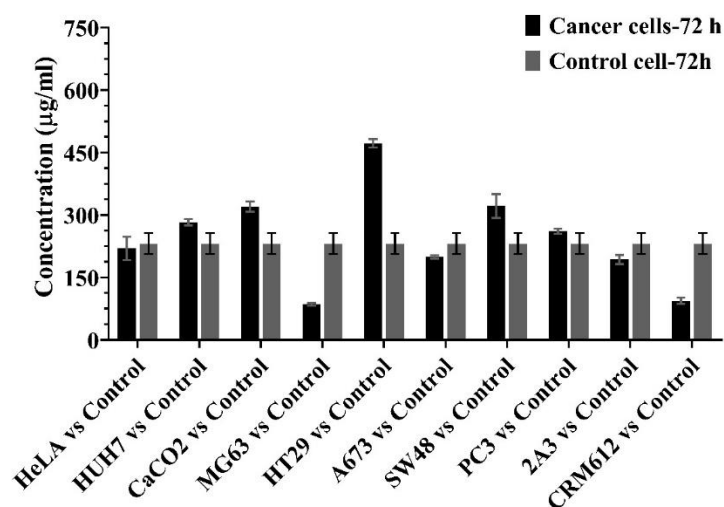


Figure 5. Comparison of IC50 values for the cancer cell lines and the control cell line following 72-hour exposure to benzoic acid

4. DISCUSSION AND CONCLUSION

Cancer is one of the leading causes of disease-related deaths globally, with its onset potentially triggered by lifestyle and dietary factors. Among the pivotal factors influencing cancer formation, along with genetic predisposition, is the escalation of Reactive Oxygen Species (ROS) within the cell due to environmental and physiological stress [30]. ROS instigates DNA damage by inducing mutations, causing structural alterations in DNA that result in aberrant cell proliferation and a decrease in apoptosis [31]. Furthermore, anomalies in post-translational epigenetic modifications in mammalian cells play a crucial role in the pathogenesis of cancer [26].

Epidemiological studies demonstrate that the consumption of foods rich in phenolic compounds is associated with a reduced risk of cancer [32]. The protective effects of these secondary metabolites may stem from their antioxidant and anti-inflammatory activities [33]. The antioxidant activity of phenolic acids is attributed to their capacity to inhibit reactive oxygen species and act as chelators of metal ions [34].

In the context of this study, we investigated the cytotoxic effects of increasing benzoic acid concentrations on 10 different cancer types and a control group cell line. We evaluated the decrease in cell viability resulting from 48- and 72-hour exposures to benzoic acid. Statistical analyses revealed that, especially at both time points, MG63 and CRM612 cancer cell lines were more sensitive to benzoic acid at lower concentrations compared to the control group ($p < 0.05$). Notably, both A673 and MG63, the two analyzed bone cancer cell lines, exhibited sensitivity to benzoic acid for both 48 and 72 hours. However, the proliferation of MG63, in particular, was inhibited at lower concentrations (48 h - 195.21 $\mu\text{g/ml}$, 72 h - 85.54 $\mu\text{g/ml}$). Hence, there appears to be a mechanism in these bone cancer cell lines that is affected by benzoic acid. We suggest that further investigation into the effect of BA on A673 and MG63 may yield potentially useful information.

Osteosarcoma, a cancer originating in the bones, is an aggressive type that can manifest throughout the entire skeletal system in individuals of various ages. Its development is notably faster during adolescence [35]. Common treatments for this cancer involve chemotherapy and surgical intervention [6]. In cases where metastasis has not occurred, the patient's survival rate increases with the removal of the tumor area through surgical intervention [36]. Osteosarcoma typically metastasizes to the lungs,

exacerbating the clinical outcomes for patients [37]. The primary factors contributing to the lung metastasis rate of 80-90% in osteosarcoma include tumor-host signaling pathways, the structure of lung epithelial tissue, and innate adaptive immunity [38-39]. Investigations are underway for new drugs aimed at curing this type of cancer. We propose that the molecular structures associated with benzoic acid could serve as a promising starting point for the development of new candidates in anti-cancer drug design.

Based on the findings of our study, the cell line most affected by benzoic acid (BA) was the CRM612 cell line, associated with lung cancer. This discovery is intriguing and calls for further investigation, especially considering that lung cancer-related deaths rank highest among cancer types. Lung cancer is linked to factors such as the consumption of tobacco products, air pollution, and economic inadequacy [40]. Additionally, lung cancer can occur due to the propensity of bone cancer to metastasize to the lung [37].

Within the scope of the study, we included three colon cancer cell lines namely CaCO2, SW48 and HT29 cell lines and found the change in cell viability of three different colorectal cancer cells exposed to benzoic acid. Colorectal cancer (CRC) accounted for 1.93 million reported cases worldwide in 2020 [41]. There is believed to be a relationship between the development of colorectal cancer and nutrition. The occurrence of CRC differs between individuals consuming fiber-rich diets and those consuming diets high in animal protein and fat [42]. The development of CRC is hindered by the high consumption of meat products, affecting intestinal flora and structure. On the other hand, butyrate, released in the intestine because of fibrous food consumption, protects the intestinal structure [43].

The Epithelial Growth Factor Receptor (EGFR) is a tyrosine kinase receptor found in major synthesis pathways involved in cell proliferation, survival, and motility. This receptor is expressed in 25-80% of advanced colorectal cancer patients [44]. Cetuximab, an antibody inhibiting the EGFR signaling pathway, is employed in the treatment of colorectal cancer [45]. While SW48 and CaCO2 colorectal cancer cells exhibit sensitivity to cetuximab, HT29 cancer cells display resistance [46]. Our cytotoxicity studies with benzoic acid yielded similar findings to cetuximab. An analysis of cell viability changes in CaCO2, SW48, and HT29 colorectal cancer cell lines revealed an observed alteration in the viability of CaCO2 and SW48 cell lines following a 48-hour benzoic acid exposure ($p < 0.05$).

The findings from cytotoxicity studies revealed variations in the inhibition concentration of benzoic acid among different types within the same cancer group. Literature studies suggest the existence of diverse inhibition mechanisms between cancer groups and types, with acetylation standing out as a particularly notable post-translational modification. Changes in the expression of HDAC, an enzyme involved in acetylation mechanisms, may contribute to the development of cancer pathogenesis. Research has demonstrated that benzoic acid and its derivatives exhibit HDAC inhibition activity in specific cancer types [27]. The intriguing aspect of benzoic acid being an inherent and natural component of the human diet, coupled with its observed cytotoxic activity in many of the analyzed cancer types within the study, further emphasizes the compound's significance.

As a result, the impact of benzoic acid on cancer cells should be further investigated, particularly to identify the biomolecules involved in the anticancer mechanism of the compound. This is especially pertinent for cervical, lung, colon, and bone cancer cell lines. In the present era, omics studies illuminate the mechanisms of action of various compounds on cells. Studies involving natural compounds with phenolic structures provide crucial examples of this [47-48]. More comprehensive studies using molecular genetics and omics approaches could be employed to decipher the genes, proteins, and metabolites associated with the effects of benzoic acid and its derivatives on cancer cells. Determining mRNA expression levels of target genes in specified cell lines or conducting proteomic analyses may lay the groundwork for future experiments. Focusing on the specific types of cancer, such as lung, colon, and bone cancers presented by this study, can offer valuable insights into the anticancer properties of

benzoic acid. In-depth studies in these areas may contribute to the development of potential therapeutic strategies or the identification of biomarkers associated with the anticancer activity of benzoic acid.

CONFLICT OF INTEREST

The authors stated that there are no conflicts of interest regarding the publication of this article.

AUTHORSHIP CONTRUBUTIONS

The author(s) contributed equally and stated that there are no conflicts of interest regarding the publication of this article.

REFERENCES

- [1] Hanahan D, Weinberg RA. The hallmarks of cancer. Cell 2000; 100(1), 57-70.
[https://doi.org/10.1016/S0092-8674\(00\)81683-9](https://doi.org/10.1016/S0092-8674(00)81683-9)
- [2] Lund AH, van Lohuizen M. Epigenetics and cancer. Genes Dev 2004; 18(19), 2315-2335
- [3] Sung H, Ferlay J, Siege RL, Laversanne M, et al. Global cancer statistics 2020: GLOBOCAN estimates of incidence and mortality worldwide for 36 cancers in 185 countries. CA-Cancer J Clin 2021; 71(3), 209-249.
- [4] Oto Murat. Osteosarkom ve varyantlarına tanısal yaklaşım modaliteleri. Pamukkale Tıp Dergisi 2008; (1), 59-64.
- [5] Cho WH, Lee HJ, Choi YJ, Oh JH, Kim HS, Cho HS. Capsaicin induces apoptosis in MG63 human osteosarcoma cells via the caspase cascade and the antioxidant enzyme system. Mol Med Rep 2013; 8(6), 1655-1662.
- [6] Wang M, Yin B, Wang HY, Wang RF. Current advances in T-cell-based cancer immunotherapy. Immunotherapy 2014; 6(12), 1265-1278.
- [7] Anantharaju PG, Gowda PC, Vimalambike MG, Madhunapantula SV. An overview on the role of dietary phenolics for the treatment of cancers. Nutr J 2016; 15(1), 1-16.
- [8] Devi KP, Rajavel T, Habtemariam S, Nabavi SF, Nabavi SM. Molecular mechanisms underlying anticancer effects of myricetin. Life Sci 2015; 142, 19-25.
- [9] Kennedy DO, Wightman EL. Herbal extracts and phytochemicals: plant secondary metabolites and the enhancement of human brain function. Adv Nutr 2011; 2(1), 32-50.
- [10] Soto-Vaca A, Gutierrez A, Losso JN, Xu Z, Finley JW. Evolution of phenolic compounds from color and flavor problems to health benefits. J Agr Food Chem 2012; 60(27), 6658-6677.
- [11] Onat KA, Kürkçü-Sezer M, Çöl B. Some biological activities of phenolic compounds cinnamic acid, caffeic acid and p-coumaric acid. J Ins Sci Tech 2021; 11 (4), 2587-2598.
- [12] Onat-Taşdelen, KA, Öztürkel-Kabakaş H, Yüksektepe E, et al. Functional groups matter: metabolomics analysis of *Escherichia coli* exposed to trans-cinnamic acid, and its derivatives unveils common and unique targets. World J Microbiol Biotechnol 2024; 40(2), 47.

- [13] Öztürkel-Kabakaş H, Taşdelen-Onat KA, Kürkçü-Sezer M, Çöl B. Investigation of the food protective activities of benzoic acid and derivatives occurring naturally in foods. Ege 7th International Conference on Applied Sciences 2022; 803-810.
- [14] Maki T, Takeda K. Benzoic acid, and derivatives. Ullmann's encyclopedia of industrial chemistry 2000; 3. https://doi.org/10.1002/14356007.a03_555
- [15] Wildermuth MC. Variations on a theme: synthesis and modification of plant benzoic acids. Curr Opin Plant Biol 2006; 9(3), 288-296.
- [16] Block A, Widhalm JR, Fatihi A, et al. The origin and biosynthesis of the benzenoid moiety of ubiquinone (coenzyme Q) in Arabidopsis. Plant Cell 2014; 26(5), 1938-1948.
- [17] Widhalm JR, Dudareva N. A familiar ring to it: biosynthesis of plant benzoic acids. Mol Plant 2015; 8(1), 83-97.
- [18] Davidson PM, Sofos, JN, Branen AL. Antimicrobials in food. CRC press 2005.
- [19] Xiang L, Moore BS. Biochemical characterization of a prokaryotic phenylalanine ammonia lyase. J Bacteriol 2005; 187(12), 4286-4289.
- [20] Torrallardona D, Badiola I, Broz J. Effects of benzoic acid on performance and ecology of gastrointestinal microbiota in weanling piglets. Livest Sci 2007; 108(1-3), 210-213.
- [21] Benjamin MM, Datta AR. Acid tolerance of enterohemorrhagic *Escherichia coli*. Appl Environ Microbiol 1995; 61(4), 1669-1672.
- [22] Leth T, Christensen T, Larsen IK. Estimated intake of benzoic and sorbic acids in Denmark. Food Addit Contam A 2010; 27(6), 783-792.
- [23] Sadeghi-Ekbatan S, Li XQ, Ghorbani M, Azadi B, Kubow S. Chlorogenic acid and its microbial metabolites exert anti-proliferative effects, S-phase cell-cycle arrest and apoptosis in human colon cancer Caco-2 cells. Int J Mol Sci 2018; 19(3), 723.
- [24] Koochekpour S, Marlowe T, Singh KK, Attwood K, Chandra D. Reduced mitochondrial DNA content associates with poor prognosis of prostate cancer in African American men. PloS one 2013; 8(9), e74688.
- [25] Roth SY, Denu JM, Allis CD. Histone acetyltransferases. Annu Rev Biochem 2001; 70(1), 81-120.
- [26] Marks PA, Richon VM, Rifkind RA. Histone deacetylase inhibitors: inducers of differentiation or apoptosis of transformed cells. J Natl Cancer Ins 2000; 92(15), 1210-1216.
- [27] Anantharaju PG, Reddy BD, Padukudru MA, Kumari-Chitturi CM, Vimalambike MG, Madhunapantula SV. Naturally occurring benzoic acid derivatives retard cancer cell growth by inhibiting histone deacetylases (HDAC). Cancer Biol Ther 2017; 18(7), 492-504.
- [28] Seidel C, Schneidenburger M, Dicato M, Diederich M. Antiproliferative and proapoptotic activities of 4-hydroxybenzoic acid-based inhibitors of histone deacetylases. Cancer Lett 2014; 343(1), 134-146.

- [29] Çöl B, Kürkçü-Sezer M, Sorucu A. Okaliptüs balının PC3, CaCO₂, HeLa ve HuH7 kanser hücre hatları üzerinde sitotoksitesinin değerlendirilmesi. *International Journal of Innovative Approaches in Science Research* 2021; 5 (4), 195-206.
- [30] Güner A, Nalbantsoy A, Sukatar A, Karabay-Yavaşoğlu NÜ. Apoptosis-inducing activities of *Halopteris scoparia* L. Sauvageau (Brown algae) on cancer cells and its biosafety and antioxidant properties. *Cytotechnology* 2019; 71(3), 687-704.
- [31] Reuter S, Gupta SC, Chaturvedi MM, Aggarwal BB. Oxidative stress, inflammation, and cancer: How are they linked. *Free Radic Biol Med* 2010; 49(11), 1603-1616.
- [32] Chiva-Blanch G, Badimon L. Effects of polyphenol intake on metabolic syndrome: current evidence from human trials. *Oxid Med Cell Longev* 2017; 1-17.
- [33] Zakłos-Szyda M, Nowak A, Pietrzyk N, Podsędek A. *Viburnum opulus* L. juice phenolic compounds influence osteogenic differentiation in human osteosarcoma Saos-2 cells. *Int J Mol Sci* 2020; 21(14), 4909.
- [34] Kandaswami C, Middleton E, Free radical scavenging, and antioxidant activity of plant flavonoids. *Adv Exp Med Biol* 1994; 351-376.
- [35] Zhang B, Wu D, Hu L, et al. Ligustilide inhibits the proliferation of human osteoblastoma MG63 cells through the TLR4-ERK pathway. *Life Sci* 2022; 288, 118993.
- [36] Dorfman HD, Czerniak B. Bone cancers. *Cancer* 1995; 75(S1), 203-210.
- [37] Hosseini F, Shanehbandi D, Soleimanpour J, Yousefi B, Alemi F. Melatonin increases the sensitivity of osteosarcoma cells to chemotherapy drug Cisplatin. *Drug Res* 2022; 312-318.
- [38] Reinecke JB, Roberts RD. Targetable intercellular signaling pathways facilitate lung colonization in osteosarcoma. *Adv Exp Med Biol* 2020; 111-123.
- [39] Meazza C, Scanagatta P, Metastatic osteosarcoma: a challenging multidisciplinary treatment. *Expert Rev Anticancer Ther* 2016; 16(5), 543-556.
- [40] Bade BC, Cruz CSD. Lung cancer 2020: epidemiology, etiology, and prevention. *Clin Chest Med* 2020; 41(1), 1-24.
- [41] Illian DN, Hafiz I, Meila O, et al. Distribution, and future directions of natural products against colorectal cancer in Indonesia: A systematic review. *Molecules* 2021; 26(16), 4984.
- [42] O'Keefe SJ, Li JV, Lahti L, et al. Fat, fibre and cancer risk in African Americans and rural Africans. *Nat Commun* 2015; 6(1), 1-14.
- [43] O'Keefe SJ. Diet, microorganisms and their metabolites, and colon cancer. *Nat Rev Gastroenterol Hepatol* 2016; 13(12), 691-706.
- [44] Reynolds NA, Wagstaff AJ. Cetuximab. *Drugs* 2004; 64 (1), 109-118.
- [45] Kuş S, Uygur T, Candan İ. Kolorektal kanser tedavisinde kullanılan Setuksimab'a bağlı akneiform erüpsiyon. *TÜRKDERM-Deri Hastalıkları ve Frengi Arşivi* 2006; 40(Supp: B), 85-87.

- [46] Graziani V, Potenza N, D'Abrosca B, Troiani T. NMR Profiling of *Ononis diffusa* Identifies Cytotoxic Compounds against Cetuximab-Resistant Colon Cancer Cell Lines. *Molecules* 2021; 26(11), 3266.
- [47] Elgin ES, Çatav ŞS., Babayeva A, et al. NMR metabolomics analysis of *Escherichia coli* cells treated with Turkish propolis water extract reveals nucleic acid metabolism as the major target. *J. Appl Microbiol* 2023; 134(1), lxac031.
- [48] Canbek U, Dibek E, Akgün U, et al. Analysis of the fluid Biochemistry in patients with prolonged wound drainage after hip hemiarthroplasty. *Injury* 2021; 5 (2), 918-925.



RESEARCH ARTICLE

PERFORMANCE EVALUATIONS OF THE MANTA RAY FORAGING OPTIMIZATION
ALGORITHM IN REAL-WORLD CONSTRAINED OPTIMIZATION PROBLEMS

Gülnur YILDIZDAN ^{1,*} 

¹ Kulu Vocational School, Selcuk University, Konya, Turkey

ABSTRACT

Metaheuristic algorithms are often preferred for solving constrained engineering design optimization problems. The most important reason for choosing these algorithms is that they guarantee a satisfactory response within a reasonable time. The swarm intelligence-based manta ray foraging optimization algorithm (MRFO) is a metaheuristic algorithm proposed to solve engineering applications. In this study, the performance of MRFO is evaluated on 19 mechanical engineering optimization problems in the CEC2020 real-world constrained optimization problem suite. In order to increase the MRFO performance, three modifications are made to the algorithm; in this way, the enhanced manta ray foraging optimization (EMRFO) algorithm is proposed. The effects of the modifications made are analyzed and interpreted separately. Its performance has been compared with the algorithms in the literature, and it has been shown that EMRFO is a successful and preferable algorithm for this problem suite.

Keywords: Constrained optimization problems, Manta ray foraging optimization algorithm, Real-world optimization problems

1. INTRODUCTION

Exact and metaheuristic methods can be used to solve constrained engineering design optimization problems. However, exact methods are not preferred because of local optima, computational complexity, and time requirements. Metaheuristic algorithms generally use random number search techniques to obtain a satisfactory answer within a reasonable period of time [1, 2]. In recent years, meta-heuristic algorithms have become increasingly popular for tackling challenging optimization problems in all engineering fields due to their cheap, efficient, and easy implementation. Figure 1 categorizes meta-heuristics into five groups based on their natural inspirations. These categories include evolution-based (Genetic algorithm [3] (GA), differential evolution [4] (DE), and biogeography-based optimization [5] (BBO), etc.), swarm-based, physics/chemistry-based (Gravitational search algorithm [6] (GSA), Artificial chemical reaction optimization algorithm [7] (ACROA), atom search optimization [8] (ASO), etc.), human-based algorithms (teaching-learning-based optimization [9] (TLBO), poor and rich optimization [10] (PRO), society and civilization algorithm [11] (SCA), etc.), and others (supply-demand-based optimization [12] (SDO), backtracking optimization search algorithm [13] (BSA), differential search algorithm [14] (DSA), etc.) [15].

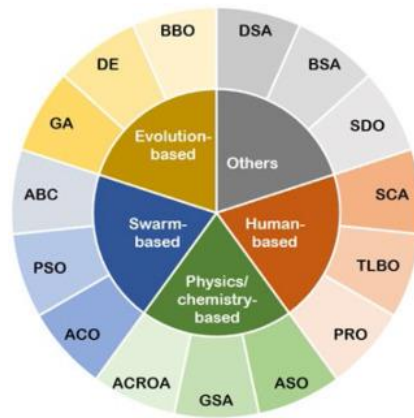


Figure 1. Meta-heuristic method classification[15]

Swarm-based algorithms, one of these classification categories, are algorithms inspired by the herd consciousness of living things in nature. The most well-known of these are algorithms such as the particle swarm optimization algorithm (PSO) [16], the artificial bee colony algorithm (ABC) [17], and the ant colony algorithm (ACO) [18], and their numbers are increasing rapidly day by day. One of the recently proposed swarm intelligence-based algorithms is manta ray foraging optimization (MRFO) [19]. This algorithm models three different strategies that manta rays use in foraging. Compared to other traditional optimization algorithms, it has a clearer mechanism, does not require additional parameter tuning, has a better balance between exploration and exploitation search ability, and has improved solution performance [20]. These features are the reason for the preference for MRFO. In this study, the performance of MRFO, which has been used in different optimization problems, on CEC2020 real-world constrained engineering problems has been evaluated. An enhanced algorithm (EMRFO) has been proposed by making three modifications to increase the performance of the algorithm. The performance increase provided by EMRFO is presented and discussed. The rest of the study is organized as follows: The literature review for MRFO is presented in the second section. The third section explains the steps of the MRFO algorithm and introduces the proposed EMRFO algorithm. The experimental study results are showcased in the fourth section. The fifth section covers the conclusions drawn from the study and suggests future work.

2. LITERATURE REVIEW

MRFO is a preferred algorithm in many different research fields. Houssein et al. developed a novel feature selection and electrocardiogram arrhythmia classification approach based on MRFO and support vector machines [21]. Houssein et al. used their proposed improved MRFO using opposition-based learning to solve the image segmentation problem in COVID-19 computed tomography images [22]. Hemeida et al. implemented the MRFO to reduce power loss by determining the optimal size and placement of distributed generators within the radial distribution network [23]. Tang et al. developed MRFO using adaptive control parameter strategies, an elite search pool, and a distribution estimation strategy to overcome the shortcomings of MRFO. They tested it on different test suites and three engineering design problems [24]. Gokulkumari developed a method for classifying brain tumors using the MRFO-based deep convolutional neural network algorithm [25]. Hassan et al. proposed the MRFO algorithm integrated with the gradient-based optimizer to solve the single and multi-purpose economic emission distribution problem [26]. Micev et al. proposed a new method based on the hybrid use of MRFO and a simulated annealing algorithm to solve the problem of setting the proportional-integral-derivative controller type for an automatic voltage regulator system [27]. Kahraman et al. used the MRFO algorithm, which they developed with the crowd-distance-based Pareto archiving strategy, to solve the CEC 2020 benchmarking functions and the multi-objective optimal power flow problem [28]. Got et al. proposed MRFO, which they developed with external archive and grid mechanisms, for multi-

purpose problems [29]. Elaziz et al. developed the algorithm by integrating the triangle mutation operator and orthogonal learning strategies into MRFO and tested it on CEC functions and engineering problems [30]. Zouache and Abdelaziz extended MRFO so that it can be applied to multi-objective problems [31]. The algorithm was created by integrating strategies such as population archive, crowding distance, and ϵ -dominance, which contribute to diversity and convergence. The proposed algorithm was applied to structural design problems such as four-bar truss design, speed-reduced design, welded beam design, and disk brake design, and compared with the literature. Ekinici et al. proposed the MRFO algorithm with improved diversification and intensification features [32]. The MRFO algorithm was developed with a generalized opposition-based learning technique and the Nelder-Mead simplex search method. The proposed algorithm was tested for solving unimodal and multimodal benchmark functions. It was also used to find the optimum values of a real PID plus a second-order derivative controller used in the magnetic object suspension system. Yousri et al. proposed an improved MRFO that adopts the Caputo fractional differ-sum operator to increase the utilization of past optimal solutions in MRFO and adaptively uses the somersault factor to avoid premature convergence [33]. The proposed algorithm was used for global optimization problems, engineering design optimization problems, and multi-threshold segmentation. Daqaq et al. presented an improved MRFO algorithm based on an elitist non-dominated sorting strategy to solve multi-objective optimization problems [34]. The algorithm's performance was tested on multimodal optimization problems, four engineering optimization problems, the CEC2020 test suite, and the modified real-world issue of IEEE 30-bus optimal power flow involving the wind/solar/small-hydro power generations. Liu et al. proposed an effective MRFO algorithm by integrating a nonlinear adjustment parameter based on the cosine factor, random individuals' information interaction, and fractional derivative mutation strategy into the standard algorithm [20]. The proposed algorithm was used to solve CEC2017 benchmark functions and seven engineering design optimization problems. Zhu et al. proposed a new MRFO based on variable spiral factors, matching games, and progressive learning that enables the dynamic adjustment of internal parameters [35]. The performance of the algorithm was validated on classical benchmark functions, the CEC2022 test suite, and three engineering optimization problems. Yang et al. proposed a new elite chaotic MRFO in which the population is initialized chaotic and integrated with an opposition-based learning strategy [36]. This algorithm was tested on the classical benchmark function, CEC2020 test functions, and three engineering optimization problems. Ghosh et al. obtained a binary version of the MRFO by applying the transfer functions, which are S-shaped and V-shaped. The resulting binary algorithm was applied to eighteen feature selection problems [37]. Yıldızdan proposed MRFO's binary version with the help of transfer functions and tested the binary algorithm on classical and CEC2005 benchmark functions [38]. Wang et al. discretized the MRFO algorithm with the sigmoid function, improved it with the XOR operator and velocity adjustment factor, and applied it to the spectrum allocation problem [39].

When the literature review was examined, it was seen that there were many improved or hybrid versions of MRFO proposed for many different continuous or discrete problems. The results obtained in the literature are also quite successful. The motivation for this study is that MRFO has become a frequently preferred algorithm recently, and there has been no significant study on its performance on CEC2020 real-world engineering problems. The contributions of the study to the literature are as follows:

- To preserve diversity and ensure the balance between foraging processes, three modifications are made to MRFO, and a new manta ray foraging optimizer (EMRFO) is proposed.
- The effectiveness of EMRFO was demonstrated on 19 mechanical engineering optimization problems in the CEC2020 real-world constrained optimization problem suite.
- Although the performance of MRFO has been examined on a few well-known engineering optimization problems, thanks to this study, its performance on a larger number of engineering

problems has been examined. A guiding resource has been created for researchers who are considering working in this field.

- The results obtained within the scope of this study revealed that EMRFO was more successful compared to the literature. Thus, a new version of MRFO that is promising for different problems was introduced to the literature.

3. MATERIAL AND METHOD

3.1. Manta Ray Foraging Optimization Algorithm (MRFO)

MRFO is a bio-inspired optimization algorithm proposed by Zhao et al. [19] in 2020, inspired by the feeding behavior of manta rays. The algorithm is based on three foraging techniques: chain, spiral, and somersault. The steps of the algorithm are as follows:

3.1.1. Initialization

The MRFO algorithm, similar to other meta-heuristic algorithms, begins by creating a random population using Equation 1.

$$X_i^d = Lb_i^d + rand \times (Ub_i^d - Lb_i^d) \quad i = 1, \dots, N \quad d = 1, \dots, D \quad (1)$$

In the equation, D is the number of dimensions and N is the population size (the number of individuals in the population). Lb and Ub are the lower and upper limits of the dimensions.

3.1.2. Chain foraging

Manta rays that feed on plankton can sense the position of food. Manta rays tend to gravitate toward places with high nutrient density. For this, they align and form a foraging chain. Except for the first manta ray at the beginning of the chain, they search according to the food source and the individual in front of it. That is, each individual is updated after each iteration using both the solution before it and the best solution so far. Chain foraging behavior in MRFO is formulated as in Equation 2.

$$X_{i,d}^{t+1} = \begin{cases} X_{i,d}^t + r \times (X_{best,d}^t - X_{i,d}^t) + \alpha \times (X_{best,d}^t - X_{i,d}^t) & i = 1 \\ X_{i,d}^t + r \times (X_{i-1,d}^t - X_{i,d}^t) + \alpha \times (X_{best,d}^t - X_{i,d}^t) & i = 2, \dots, N \end{cases} \quad (2)$$

$$\alpha = 2 \times r \times \sqrt{|\log(r)|} \quad (3)$$

In Equation 2, r is a vector of random numbers in the range [0,1]. α is the weight coefficient whose formula is given in Equation 3. $X_{i,d}^t$ is the position of the i th individual at time t of the d th dimension, and $X_{best,d}^t$ is the the position with the highest nutrient density.

3.1.3. Cyclone foraging

When manta rays see a piece of plankton in deep water, they both spiral toward the plankton piece and swim toward the manta rays in front of them. This behavior, called cyclone foraging, is formulated in the MRFO as given in Equation 4. β given in Equation 5 is the weight coefficient, T is the maximum number of iterations, and r is also a random number between 0 and 1.

$$X_{i,d}^{t+1} = \begin{cases} X_{best,d}^t + r \times (X_{best,d}^t - X_{i,d}^t) + \beta \times (X_{best,d}^t - X_{i,d}^t) & i = 1 \\ X_{best,d}^t + r \times (X_{i-1,d}^t - X_{i,d}^t) + \beta \times (X_{best,d}^t - X_{i,d}^t) & i = 2, \dots, N \end{cases} \quad (4)$$

$$\beta = 2e^{r \frac{T-t+1}{T}} \times \sin(2\pi r) \quad (5)$$

MRFO is an algorithm with comprehensive global search capability. To achieve this, a random position is created in the optimization process, and a spiral search is performed around this position. In the algorithm, this behavior is formulated as in Equations 6 and 7. In Equation 6, $X_{r,d}^t$ denotes a random location in the search space. Ub^d and Lb^d are also the upper and lower limit values for the d th dimension, respectively.

$$X_{r,d}^t = Lb^d + r \times (Ub^d - Lb^d) \quad (6)$$

$$X_{i,d}^{t+1} = \begin{cases} X_{r,d}^t + r \times (X_{r,d}^t - X_{i,d}^t) + \beta \times (X_{r,d}^t - X_{i,d}^t) & i = 1 \\ X_{r,d}^t + r \times (X_{i-1,d}^t - X_{i,d}^t) + \beta \times (X_{r,d}^t - X_{i,d}^t) & i = 2, \dots, N \end{cases} \quad (7)$$

3.1.4. Somersault foraging

Each manta ray swims back and forth around a food location, seen as a pivot, and somersaults to a new position. Thus, individuals update their location according to the best location found so far. In MRFO, this behavior is formulated according to Equation 8. In Equation 8, $r1$ and $r2$ are two random numbers between 0 and 1. The value of S is the somersault factor, which determines the distance covered during a somersault. The pseudocode and flowchart of MRFO are given in Figure 2 and Figure 3, respectively.

$$X_{i,d}^{t+1} = X_{i,d}^t + S \times (r1 \times X_{best,d}^t - r2 \times X_{i,d}^t), \quad i = 1, \dots, N \quad (8)$$

```

1. Determine  $T_{max}, N, Ub, Lb, t = 1$ 
2. Initialize population according to Equation 1.
3. Compute the fitness of each individual  $f(X_i)$ 
4. Obtain best individual ( $X_{best}$ )
5. While stop criterion is not satisfied do
6.   For  $i=1$  to  $N$ 
7.     If  $rand < 0.5$  then // Cyclone foraging
8.       If  $t / T_{max} < rand$  then
9.         Generate a random individual( $X_r(t)$ ) according to Equation 6.
10.        Create a new candidate individual ( $X_i(t + 1)$ ) according to Equation 7.
11.       Else
12.         Create a new candidate individual ( $X_i(t + 1)$ ) according to Equation 4.
13.       End If
14.     Else //Chain foraging
15.       Create a new candidate individual ( $X_i(t + 1)$ ) according to Equation 2.
16.     End If
17.   Compute the fitness of each individual  $f(X_i(t + 1))$ 
18.   If  $f(X_i(t + 1)) < f(X_{best})$  then
19.      $f(X_{best}) = f(X_i(t + 1))$ 
20.   End If
21. //Somersault foraging
22.   Create a new candidate individual ( $X_i(t + 1)$ ) according to Equation 8.
23.   Compute the fitness of the individual  $f(X_i(t + 1))$ 
24.   If  $f(X_i(t + 1)) < f(X_{best})$  then
25.      $f(X_{best}) = f(X_i(t + 1))$ 
26.   End If
27. End For
28. End While
    
```

Figure 2. The pseudocode of MRFO

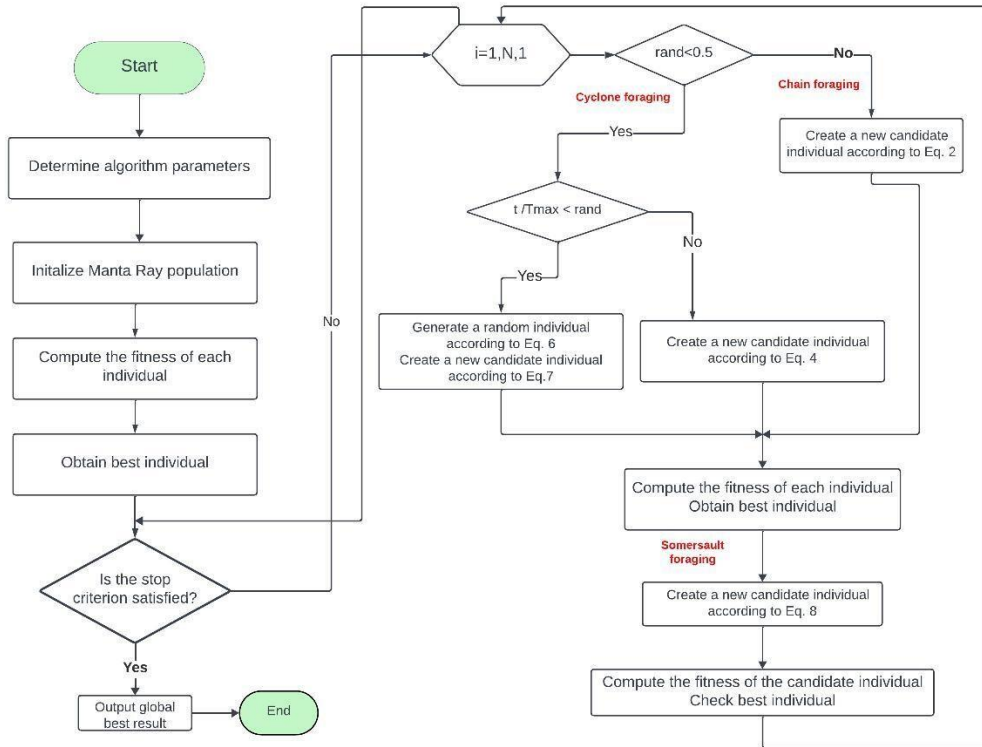


Figure 3. The flowchart of MRFO

3.2. Enhanced Manta Ray Foraging Optimization Algorithm (EMRFO)

MRFO is a swarm intelligence-based metaheuristic algorithm proposed for engineering applications. In general, MRFO, which has a good performance, has some drawbacks when analyzed in detail. These can be listed as follows: especially in the early iterations, the selection of random reference points weakens the exploitation ability, the chain foraging tends to bring the solutions to the local optimum, and the population diversity decreases in the late iterations [24]. This study proposes an enhanced algorithm called EMRFO to address the drawbacks of MRFO. Three modifications have been made to the MRFO to achieve this goal.

- As can be seen from Figure 2, the balance between exploration and exploitation in MRFO is determined by whether the result (C) of the linearly increasing iteration/maximum iteration (i.e., $t/Tmax$) operation is less than a random number. Here, choosing the C parameter with nonlinearly increasing characteristics is beneficial for the search process to be more balanced. Thus, one of the disadvantages of MRFOA, which is the weakening of the ability to benefit due to random reference location selection in early iterations, is prevented. For this reason, different studies have been carried out on the nonlinear use of this parameter in the literature [24, 40]. This study proposes the use of the simulated annealing inertia weight strategy [41] for parameter C . The mathematical formulation of this strategy is given in Equation 9. In Equation 9, t represents the number of iterations, and w_{start} and w_{end} represent the start and end values for the parameter, respectively.

$$C_t = w_{start} + (w_{end} - w_{start}) \times 0.95^{t-1} \tag{9}$$

Figure 4 shows the change of the C parameter in MRFO and EMRFO. When the graphic is examined, when the nonlinear C parameter is used as in EMRFO, foraging behavior in random

locations is dominant in the first 20% of the total iteration. In the remaining part, searches are made around locations with high nutritional value. Thus, the disadvantage of weakening the ability of MRFO to provide benefits due to random reference location selection in early iterations is eliminated.

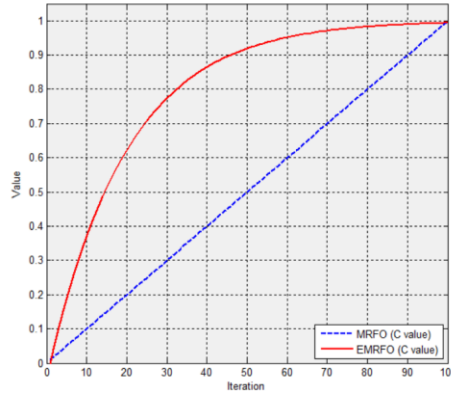


Figure 4. Change of C values

- The second modification was made to the S parameter used in somersault foraging (Equation 8). The value of S is the somersault factor that determines the distance covered during a somersault around the food location chosen as the pivot. In MRFO, the S parameter is a fixed value ($S = 2$). There are different studies in the literature on the selection of the S value [24, 42]. In this study, the S value is used by decreasing it within a certain interval. To determine these interval values, tests are performed for different values. At the end of this testing process, the interval $[5, 2]$ is chosen, which yields the most successful results. In this way, exploration is supported by using a larger somersault distance initially. Over time, decreasing the S value supports exploitation by conducting a more focused search with smaller somersault distances. Thus, by changing the distance during the somersault foraging, diversity is contributed and premature convergence is prevented. In order to achieve this, the S value is used by decreasing in a certain interval nonlinearly according to Equation 10, which is obtained by editing Equation 9.

$$S_t = w_{end} + (w_{start} - w_{end}) \times 0.95^{t-1} \quad (10)$$

Figure 5 shows the change of the S parameter in MRFO and EMRFO. The graphic shows that the non-linear change of the S parameter in EMRFO supports the ability to exploration first, then exploitation, using different somersault distances.

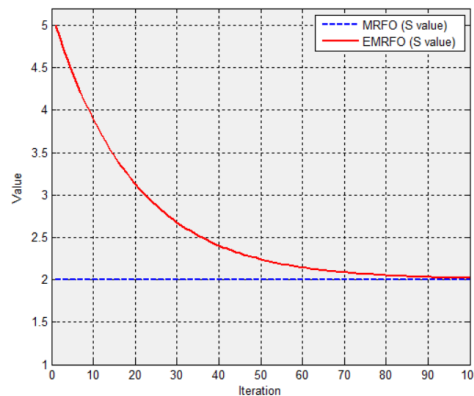


Figure 5. Change of S values

- Finally, an update strategy was integrated into somersault foraging to prevent the drawback of MRFO losing diversity towards the last iterations and to contribute to avoiding local minima by preserving diversity for longer periods of time. For this, an update rate (UR) is first determined. Then, as shown in Figure 6, each individual in the population and the candidate individual obtained after applying the algorithm steps to that individual are exchanged at the determined UR rate [43].

UR=0.3	Selected dimensions={1, 5, 9}									
ith individual	0.21	0.45	0.11	0.54	0.43	0.7	0.98	0.23	0.87	0.12
candidate individual for ith individual	0.27	0.22	0.65	0.57	0.32	0.8	0.73	0.13	0.91	0.44
new candidate individual after the update strategy applied	0.21	0.22	0.65	0.57	0.43	0.8	0.73	0.13	0.87	0.44

Figure 6. Updating strategy

The pseudocode of the EMRFO algorithm obtained after the three modifications mentioned above in the MRFO algorithm is given in Figure 7. The flowchart of EMRFO is also presented in Figure 8.

```

1. Determine  $T_{max}, N, Ub, Lb, t = 1$ 
2. Initialize population according to Equation 1.
3. Compute the fitness of each individual  $f(X_i)$ 
4. Obtain best individual ( $X_{best}$ )
5. While stop criterion is not satisfied do
6.   For  $i=1$  to  $N$ 
7.     If  $rand < 0.5$  then // Cyclone foraging
8.       Calculate  $C_t$  value according to Equation 9.
9.       If  $C_t < rand$  then
10.        Generate a random individual( $X_r(t)$ ) according to Equation 6.
11.        Create a new candidate individual ( $X_i(t + 1)$ ) according to Equation 7.
12.      Else
13.        Create a new candidate individual ( $X_i(t + 1)$ ) according to Equation 4.
14.      End If
15.    Else //Chain foraging
16.      Create a new candidate individual ( $X_i(t + 1)$ ) according to Equation 2.
17.    End If
18.  Compute the fitness of each individual  $f(X_i(t + 1))$ 
19.  If  $f(X_i(t + 1)) < f(X_{best})$  then
20.     $f(X_{best}) = f(X_i(t + 1))$ 
21.  End If
22. //Somersault foraging
23. Calculate  $S_t$  value according to Equation 10.
24. Create a new candidate individual ( $X_i(t + 1)$ ) according to Equation 8.
25. Apply updating strategy.
26. Compute the fitness of the individual  $f(X_i(t + 1))$ 
27. If  $f(X_i(t + 1)) < f(X_{best})$  then
28.    $f(X_{best}) = f(X_i(t + 1))$ 
29. End If
30. End For
31. End While

```

Figure 7. The pseudocode of EMRFO

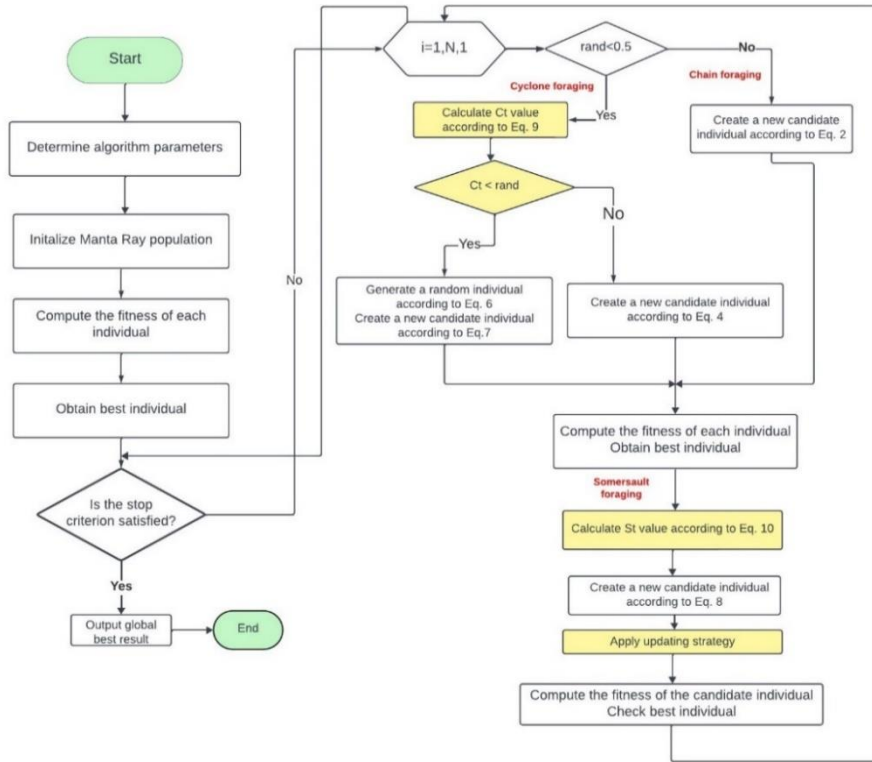


Figure 8. The flowchart of EMRFO

3.3. Nonparametric Friedman Test

In this study, the non-parametric Friedman test is used to reveal significant differences between metaheuristic algorithms. The steps of the test can be summarized as follows [44]:

The hypotheses are defined first.

Hypothesis 0 (H0): The results of the compared algorithms do not differ statistically significantly.
 Hypothesis 1 (H1): The results of the compared algorithms differ statistically significantly.

- During R_N runs, gather evaluation criteria for every metaheuristic algorithm (the run number is represented by R_N).
- Sort the metaheuristic algorithms that have been tested in order of best to worst, from 1 to k , which is denoted as r_{ij} .
- Calculate the mean of the obtained ranks over R_N runs for the j th algorithm according to Equation 11.

$$R_j = \frac{1}{R_N} \sum_i^j r_{ij} \quad (11)$$

- Using Equation 12, write the nonparametric Friedman statistic Ff .

$$Ff = \frac{12n}{(k+1)k} \left[\sum_j R_j^2 - \frac{k(k+1)^2}{4} \right] \quad (12)$$

To calculate the probability of rejecting the null hypothesis in this test, a p-value is used. The null hypothesis should be rejected if the p-value is less than 0.05. In other words, there is a significant difference in the results of the compared algorithms [45].

4. EXPERIMENTAL RESULTS

Solving real-world optimization problems can be challenging due to their complex objective functions and numerous constraints. To overcome these challenges, various metaheuristics and constraint-handling approaches have been proposed. In this section, the performance of the proposed EMRFO algorithm is evaluated on CEC2020 real-world constrained optimization problems [46]. The real-world constrained optimization problems are formulated as in Equation 13 [46].

$$\begin{aligned}
 & \text{Minimize : } f(\bar{x}), \bar{x} = (x_1, x_2, \dots, x_D) \\
 & \text{Subject to : } g_i(\bar{x}) \leq 0, \quad i = 1, 2, \dots, p \\
 & \quad \quad \quad h_j(\bar{x}) = 0, \quad j = p + 1, \dots, m
 \end{aligned} \tag{13}$$

where $f(\bar{x})$ is the objective function, \bar{x} is the D-dimensional solution vector, the $g_i(\bar{x})$ function is the i th inequality constraint, and $h_j(\bar{x})$ is the j th equality constraint. These constraints may or may not be linear. The CEC2020 real-world constrained optimization problem suite consists of 57 problems in total and six groups: industrial chemical processes, process synthesis and design problems, mechanical engineering problems, power system problems, power electronics problems, and livestock feed ration optimization. In this study, the performance of EMRFO is tested on mechanical engineering problems (RC15-RC33). This group consists of 19 problems, and their features are given in Table 1. In the table, D is the dimension of the problem, g is the number of inequality constraints, h is the number of equality constraints, and $f(\bar{x}^*)$ is the best-known feasible objective function value.

As it is known, in optimization, a fixed amount of function evaluations called maximum function evaluation numbers (*MaxFEs*) are allocated, and when the algorithm reaches this number, the optimization process is stopped. The MaxFEs for the problems in Table 1 are determined by Equation 14. The population size is also chosen as 100. In comparisons, the best (best fitness value), mean (mean of fitness values), and standard deviation (standard deviation of fitness values) values obtained from 25 independent studies are used. Also, in comparison tables, bold font shows a better value, italic font shows equal values, and gray background shows a better standard deviation value for equal mean values.

$$\text{MaxFEs} = \begin{cases} 1 \times 10^5 & \text{if } D \leq 10 \\ 2 \times 10^5 & \text{if } 10 \leq D \leq 30 \end{cases} \tag{14}$$

In this section, firstly, the effect of the modifications made in *MRFO* on performance is analyzed. Let *MRFO_C* be the improved algorithm obtained by adding the first modification that suggests the use of the parameter C, which exhibits nonlinearly increasing characteristics in *MRFO*, to the algorithm. Accordingly, Table 2 presents the comparison results of *MRFO* and *MRFO_C*. When the results are analyzed, it is seen that *MRFO_C* achieved a better mean in 11 out of 19 problems. In two of the remaining problems, *MRFO* finds a better mean value, while in the other five, the algorithms find the same mean value. But in these five problems, *MRFO_C* has a smaller standard deviation value. In the RC31 problem, both algorithms find 0.00E + 00. These results show that the first modification positively affects the MRFO's performance.

Table 1. Features of the mechanical engineering problems

Problem	Name	D	g	h	$f(\bar{x}^*)$
RC15	Weight Minimization of a Speed Reducer	7	11	0	2,9944244658E+03
RC16	Optimal Design of Industrial refrigeration System	14	15	0	3,2213000814E-02
RC17	Tension/compression spring design (case 1)	3	3	0	1,2665232788E-02
RC18	Pressure vessel design	4	4	0	5,8853327736E+03
RC19	Welded beam design	4	5	0	1,6702177263E+00
RC20	Three-bar truss design problem	2	3	0	2,6389584338E+02
RC21	Multiple disk clutch brake design problem	5	7	0	2,3524245790E-01
RC22	Planetary gear train design optimization problem	9	10	1	5,2576870748E-01
RC23	Step-cone pulley problem	5	8	3	1,6069868725E+01
RC24	Robot gripper problem	7	7	0	2,5287918415E+00
RC25	Hydro-static thrust bearing design problem	4	7	0	1,6254428092E+03
RC26	Four-stage gear box problem	22	86	0	3,5359231973E+01
RC27	10-bar truss design	10	3	0	5,2445076066E+02
RC28	Rolling element bearing	10	9	0	1,4614135715E+04
RC29	Gas Transmission Compressor Design (GTCD)	4	1	0	2,9648954173E+06
RC30	Tension/compression spring design (case 2)	3	8	0	2,6138840583E+00
RC31	Gear train design Problem	4	1	1	0,0000000000E+00
RC32	Himmelblau's Function	5	6	0	-3,0665538672E+04
RC33	Topology Optimization	30	30	0	2,6393464970E+00

Secondly, the effect of the second modification made in $MRFO$ is analyzed. Let $MRFO_S$ be the improved algorithm obtained by adding the second modification that suggests the use of the parameter S , which exhibits nonlinearly decreasing characteristics in $MRFO$, to the algorithm. Accordingly, Table 3 presents the comparison results of $MRFO$ and $MRFO_S$. When the results are analyzed, it is found that $MRFO_S$ finds a better mean value in 7 problems, while $MRFO$ finds a better mean value in 5 problems. In six of the remaining problems, the algorithms found the same mean value. In two of these problems, $MRFO$, and in the remaining four, the $MRFO_S$ algorithm obtained a better standard deviation value. In the RC31 problem, both algorithms find $0.00E + 00$. These results show that the second modification improves the $MRFO$'s performance.

Table 4 shows the comparison results of $MRFO_{CS}$, which is obtained by integrating the first and second modifications into the standard algorithm, and the $MRFO$ algorithm. When the results in the table are analyzed, $MRFO_{CS}$ finds the best mean value in 12 out of 19 problems, while $MRFO$ finds the best mean value in 1 problem. In five of the remaining problems, the algorithms find the same mean value, but in these problems, $MRFO_{CS}$ performs better by finding better standard deviation values. In the RC31 problem, both algorithms find $0.00E + 00$. These results show that integrating both modifications into $MRFO$ further improves $MRFO$'s performance. To see this effect more clearly, the results of the $MRFO_C$, $MRFO_S$, and $MRFO_{CS}$ algorithms are compared in Table 5. When the table is examined, the $MRFO_C$ algorithm finds a better mean value in 3 of the problems, while the $MRFO_S$ algorithm finds a better mean value in 2 of the problems. The $MRFO_{CS}$ algorithm achieves a better mean value in 8 of the remaining problems. Of the five problems where the algorithms find the same mean, $MRFO_C$ obtains a better standard deviation value in three of them and $MRFO_{CS}$ in the remaining two. Additionally, in the RC31 problem, it finds the value $0.00E + 00$ in three algorithms. According to the results of this comparison, it is proven that the use of the two modifications together contributes more to the performance.

Table 2. Comparison results of the *MRFO* and *MRFO_C* algorithms

	<i>MRFO</i>			<i>MRFO_C</i>		
	Best	Mean	Std	Best	Mean	Std
RC15	2,994424E+03	2,994425E+03	8,933243E-05	2,994424E+03	2,994424E+03	4,781112E-07
RC16	3,254210E-02	4,194690E-02	6,952061E-03	3,221305E-02	4,038194E-02	8,051717E-03
RC17	1,266675E-02	1,267320E-02	5,055811E-06	1,266576E-02	1,266873E-02	2,743722E-06
RC18	6,059714E+03	6,324653E+03	2,404949E+02	6,059714E+03	6,127095E+03	1,267901E+02
RC19	1,670218E+00	<i>1,670218E+00</i>	1,234202E-12	1,670218E+00	<i>1,670218E+00</i>	2,703950E-15
RC20	2,638958E+02	<i>2,638959E+02</i>	8,129818E-06	2,638958E+02	<i>2,638959E+02</i>	6,355131E-06
RC21	2,352425E-01	<i>2,352425E-01</i>	3,271315E-12	2,352425E-01	<i>2,352425E-01</i>	5,870076E-14
RC22	5,257687E-01	5,287543E-01	3,035527E-03	5,257687E-01	5,278581E-01	2,496295E-03
RC23	1,714135E+01	2,619215E+01	1,118297E+01	1,624213E+01	2,307006E+01	6,292782E+00
RC24	2,697086E+00	2,954188E+00	2,301767E-01	2,614242E+00	2,839908E+00	1,684963E-01
RC25	1,640789E+03	1,766357E+03	9,996301E+01	1,623517E+03	1,708607E+03	6,220753E+01
RC26	3,736598E+01	8,869061E+15	1,611897E+16	3,646089E+01	1,288893E+16	4,760657E+16
RC27	5,245301E+02	5,275083E+02	3,028573E+00	5,245136E+02	5,279593E+02	3,156006E+00
RC28	1,695820E+04	<i>1,695820E+04</i>	2,184191E-03	1,695820E+04	<i>1,695820E+04</i>	9,737234E-05
RC29	2,964896E+06	2,964902E+06	4,628019E+00	2,964895E+06	2,964899E+06	2,284177E+00
RC30	2,658559E+00	2,671626E+00	4,955796E-02	2,658559E+00	2,660319E+00	8,184043E-03
RC31	0,000000E+00	<i>0,000000E+00</i>	0,000000E+00	0,000000E+00	<i>0,000000E+00</i>	0,000000E+00
RC32	-3,066554E+04	<i>-3,066554E+04</i>	2,027150E-03	-3,066554E+04	<i>-3,066554E+04</i>	2,448015E-04
RC33	2,639352E+00	2,639400E+00	8,820392E-05	2,639347E+00	2,639348E+00	5,596236E-06

Table 3. Comparison results of the *MRFO* and *MRFO_S* algorithms

	<i>MRFO</i>			<i>MRFO_S</i>		
	Best	Mean	Std	Best	Mean	Std
RC15	2,994424E+03	<i>2,994425E+03</i>	8,933243E-05	2,994424E+03	<i>2,994425E+03</i>	4,928646E-05
RC16	3,254210E-02	4,194690E-02	6,952061E-03	3,249612E-02	4,267801E-02	7,982063E-03
RC17	1,266675E-02	1,267320E-02	5,055811E-06	1,266574E-02	1,268067E-02	1,033643E-05
RC18	6,059714E+03	6,324653E+03	2,404949E+02	6,059720E+03	6,244510E+03	2,431724E+02
RC19	1,670218E+00	<i>1,670218E+00</i>	1,234202E-12	1,670218E+00	<i>1,670218E+00</i>	9,856824E-13
RC20	2,638958E+02	<i>2,638959E+02</i>	8,129818E-06	2,638958E+02	2,638958E+02	7,175023E-06
RC21	2,352425E-01	<i>2,352425E-01</i>	3,271315E-12	2,352425E-01	<i>2,352425E-01</i>	7,432136E-12
RC22	5,257687E-01	5,287543E-01	3,035527E-03	5,257687E-01	5,283521E-01	2,244001E-03
RC23	1,714135E+01	2,619215E+01	1,118297E+01	1,632368E+01	4,634495E+01	6,675387E+01
RC24	2,697086E+00	2,954188E+00	2,301767E-01	2,705441E+00	2,915821E+00	2,119451E-01
RC25	1,640789E+03	1,766357E+03	9,996301E+01	1,647601E+03	1,747498E+03	8,257355E+01
RC26	3,736598E+01	8,869061E+15	1,611897E+16	3,647122E+01	4,404589E+14	1,081002E+15
RC27	5,245301E+02	5,275083E+02	3,028573E+00	5,245299E+02	5,297212E+02	2,717610E+00
RC28	1,695820E+04	<i>1,695820E+04</i>	2,184191E-03	1,695820E+04	<i>1,695820E+04</i>	5,237155E-04
RC29	2,964896E+06	<i>2,964902E+06</i>	4,628019E+00	2,964896E+06	<i>2,964902E+06</i>	5,143730E+00
RC30	2,658559E+00	2,671626E+00	4,955796E-02	2,658559E+00	2,662654E+00	1,294429E-02
RC31	0,000000E+00	<i>0,000000E+00</i>	0,000000E+00	0,000000E+00	<i>0,000000E+00</i>	0,000000E+00
RC32	-3,066554E+04	<i>-3,066554E+04</i>	2,027150E-03	-3,066554E+04	<i>-3,066554E+04</i>	1,383139E-03
RC33	2,639352E+00	2,639400E+00	8,820392E-05	2,639356E+00	2,639488E+00	3,840580E-04

Table 4. Comparison results of the *MRFO* and *MRFO_{CS}* algorithms

	<i>MRFO</i>			<i>MRFO_{CS}</i>		
	Best	Mean	Std	Best	Mean	Std
RC15	2,994424E+03	2,994425E+03	8,933243E-05	2,994424E+03	2,994424E+03	5,672839E-07
RC16	3,254210E-02	4,194690E-02	6,952061E-03	3,222404E-02	3,859848E-02	6,765000E-03
RC17	1,266675E-02	1,267320E-02	5,055811E-06	1,266555E-02	1,266943E-02	4,402280E-06
RC18	6,059714E+03	6,324653E+03	2,404949E+02	6,059714E+03	6,110158E+03	1,064905E+02
RC19	1,670218E+00	<i>1,670218E+00</i>	1,234202E-12	1,670218E+00	<i>1,670218E+00</i>	7,921320E-15
RC20	2,638958E+02	<i>2,638959E+02</i>	8,129818E-06	2,638958E+02	<i>2,638959E+02</i>	6,802541E-06
RC21	2,352425E-01	<i>2,352425E-01</i>	3,271315E-12	2,352425E-01	<i>2,352425E-01</i>	1,070512E-13
RC22	5,257687E-01	5,287543E-01	3,035527E-03	5,259674E-01	5,276695E-01	1,210525E-03
RC23	1,714135E+01	2,619215E+01	1,118297E+01	1,698765E+01	1,854255E+01	1,514401E+00
RC24	2,697086E+00	2,954188E+00	2,301767E-01	2,757983E+00	2,897183E+00	1,471321E-01
RC25	1,640789E+03	1,766357E+03	9,996301E+01	1,621391E+03	1,706032E+03	9,037795E+01
RC26	3,736598E+01	8,869061E+15	1,611897E+16	3,625376E+01	2,349845E+15	6,911838E+15
RC27	5,245301E+02	5,275083E+02	3,028573E+00	5,244839E+02	5,284012E+02	3,188696E+00
RC28	1,695820E+04	<i>1,695820E+04</i>	2,184191E-03	1,695820E+04	1,695820E+04	4,729283E-05
RC29	2,964896E+06	2,964902E+06	4,628019E+00	2,964896E+06	2,964899E+06	3,753715E+00
RC30	2,658559E+00	2,671626E+00	4,955796E-02	2,658559E+00	2,658587E+00	8,867289E-05
RC31	0,000000E+00	0,000000E+00	0,000000E+00	0,000000E+00	0,000000E+00	0,000000E+00
RC32	-3,066554E+04	<i>-3,066554E+04</i>	2,027150E-03	-3,066554E+04	<i>-3,066554E+04</i>	1,895641E-04
RC33	2,639352E+00	2,639400E+00	8,820392E-05	2,639347E+00	2,639347E+00	6,932692E-07

Table 5. Comparison results of the *MRFO_C*, *MRFO_S* and *MRFO_{CS}* algorithms

	<i>MRFO_C</i>		<i>MRFO_S</i>		<i>MRFO_{CS}</i>	
	Mean	Std	Mean	Std	Mean	Std
RC15	2,994424E+03	4,781112E-07	2,994425E+03	4,928646E-05	2,994424E+03	5,672839E-07
RC16	4,038194E-02	8,051717E-03	4,267801E-02	7,982063E-03	3,859848E-02	6,765000E-03
RC17	1,266873E-02	2,743722E-06	1,268067E-02	1,033643E-05	1,266943E-02	4,402280E-06
RC18	6,127095E+03	1,267901E+02	6,244510E+03	2,431724E+02	6,110158E+03	1,064905E+02
RC19	<i>1,670218E+00</i>	2,703950E-15	<i>1,670218E+00</i>	9,856824E-13	<i>1,670218E+00</i>	7,921320E-15
RC20	2,638959E+02	6,355131E-06	2,638958E+02	7,175023E-06	2,638959E+02	6,802541E-06
RC21	<i>2,352425E-01</i>	5,870076E-14	<i>2,352425E-01</i>	7,432136E-12	<i>2,352425E-01</i>	1,070512E-13
RC22	5,278581E-01	2,496295E-03	5,283521E-01	2,244001E-03	5,276695E-01	1,210525E-03
RC23	2,307006E+01	6,292782E+00	4,634495E+01	6,675387E+01	1,854255E+01	1,514401E+00
RC24	2,839908E+00	1,684963E-01	2,915821E+00	2,119451E-01	2,897183E+00	1,471321E-01
RC25	1,708607E+03	6,220753E+01	1,747498E+03	8,257355E+01	1,706032E+03	9,037795E+01
RC26	1,288893E+16	4,760657E+16	4,404589E+14	1,081002E+15	2,349845E+15	6,911838E+15
RC27	5,279593E+02	3,156006E+00	5,297212E+02	2,717610E+00	5,284012E+02	3,188696E+00
RC28	<i>1,695820E+04</i>	9,737234E-05	<i>1,695820E+04</i>	5,237155E-04	<i>1,695820E+04</i>	4,729283E-05
RC29	<i>2,964899E+06</i>	2,284177E+00	2,964902E+06	5,143730E+00	<i>2,964899E+06</i>	3,753715E+00
RC30	2,660319E+00	8,184043E-03	2,662654E+00	1,294429E-02	2,658587E+00	8,867289E-05
RC31	0,000000E+00	0,000000E+00	0,000000E+00	0,000000E+00	0,000000E+00	0,000000E+00
RC32	<i>-3,066554E+04</i>	2,448015E-04	<i>-3,066554E+04</i>	1,383139E-03	<i>-3,066554E+04</i>	1,895641E-04
RC33	2,639348E+00	5,596236E-06	2,639488E+00	3,840580E-04	2,639347E+00	6,932692E-07

Thirdly, the performance impact of the update strategy integrated into the somersault phase of the algorithm in order to preserve diversity for longer is analyzed. The optimal value for the UR value, indicating the update rate, is also determined. The results are given in Table 6 in comparison according to the mean value. The UR values are selected from a range between 0.1 and 0.5, with increments of 0.1. When the UR value is taken as 0.5, the best mean value is found in 4 problems. In two of the problems where the algorithms obtained the same mean value, it found the best standard deviation for $UR = 0.5$. According to these results, although 0.5 seems to be the most appropriate value, the nonparametric Friedman test [47] is applied for a more detailed evaluation. As mentioned before, in this study, the Friedman test is used to determine whether there is a significant difference between the algorithms, and the mean rank values obtained are given in Figure 9. The problems we study are minimization problems, and therefore, when evaluating Friedman test results, the algorithm with a smaller mean rank is considered to perform better. Accordingly, when Figure 9 is analyzed, it is seen that the algorithm with a UR value of 0.2 ranks first with a mean rank value of 2.89. Therefore, the UR value is chosen as 0.2 in the proposed EMRFO algorithm. Moreover, all EMRFO sub-versions with the update strategy obtained better mean rank values than the standard MRFO algorithm and ranked higher in the ranking. Figure 10 shows the convergence graphics of MRFO and EMRFO for four selected problems. Graphics are drawn according to the best values obtained by the algorithms. The convergence ability has been examined by selecting problems in which the algorithms find close values. In the RC15 problem, the algorithms find the same value. In the RC15 graphic, it can be seen that although EMRFO starts from a solution that is farther from the optimal, it converges faster than MRFO. The algorithms find the same value in the RC19 problem. According to the graphic, EMRFO starts to search from a solution closer to the optimal, but the two algorithms exhibit a similar convergence speed. Similar to RC19, in RC28, although the EMRFO starts searching from a better solution, EMRFO and MRFO converge at the same speed. When the RC33 graphic is examined, it is seen that EMRFO converges to a value closer to the optimal faster than MRFO.

Table 6. Comparison results of the *EMRFO* with different UR values

	UR	0.1	0.2	0.3	0.4	0.5
RC15	Mean	2,994424E+03	2,994424E+03	2,994424E+03	2,994424E+03	2,994424E+03
	Std	4,071313E-07	6,178244E-07	9,357967E-07	5,032104E-07	3,901230E-07
RC16	Mean	3,932953E-02	3,503066E-02	3,731769E-02	3,483386E-02	3,462827E-02
	Std	6,280985E-03	2,998453E-03	5,382151E-03	2,028029E-03	2,311009E-03
RC17	Mean	1,267058E-02	1,267062E-02	1,267238E-02	1,267158E-02	1,266951E-02
	Std	6,530173E-06	2,743085E-06	4,531782E-06	8,685000E-06	3,154004E-06
RC18	Mean	6,113323E+03	6,097922E+03	6,107582E+03	6,107154E+03	6,065886E+03
	Std	1,052608E+02	1,101071E+02	1,073265E+02	1,075247E+02	1,300511E+01
RC19	Mean	1,670218E+00	1,670218E+00	1,670218E+00	1,670218E+00	1,670218E+00
	Std	6,938080E-15	1,280029E-14	4,246029E-15	2,607383E-15	8,639472E-15
RC20	Mean	2,638959E+02	2,638959E+02	2,638959E+02	2,638959E+02	2,638959E+02
	Std	9,255367E-06	1,117208E-05	1,285150E-05	7,508691E-06	8,537156E-06
RC21	Mean	2,352425E-01	2,352425E-01	2,352425E-01	2,352425E-01	2,352425E-01
	Std	1,835236E-14	3,668458E-14	7,047372E-14	1,163729E-13	8,960553E-14
RC22	Mean	5,282837E-01	5,265442E-01	5,267592E-01	5,275840E-01	5,265863E-01
	Std	2,952660E-03	1,341955E-03	7,461250E-04	1,364557E-03	1,070154E-03
RC23	Mean	1,476827E+02	4,552499E+01	1,667919E+01	5,648618E+02	1,736887E+01
	Std	1,181553E+02	5,342818E+01	2,640131E-01	1,732807E+03	1,947398E+00
RC24	Mean	2,846105E+00	2,841463E+00	2,920189E+00	2,981002E+00	2,997555E+00
	Std	1,193459E-01	1,071138E-01	1,745038E-01	1,618122E-01	1,040719E-01
RC25	Mean	1,725546E+03	1,722699E+03	1,747194E+03	1,697705E+03	1,713279E+03
	Std	9,147076E+01	6,927179E+01	5,385686E+01	3,039111E+01	5,802935E+01
RC26	Mean	2,923076E+15	5,425705E+01	4,819498E+01	1,034750E+14	4,557533E+01
	Std	9,243577E+15	1,514599E+01	1,538641E+01	3,272166E+14	7,277022E+00
RC27	Mean	5,271598E+02	5,271363E+02	5,271166E+02	5,271591E+02	5,289394E+02
	Std	3,188783E+00	3,091667E+00	3,129993E+00	3,066334E+00	2,810040E+00
RC28	Mean	1,695820E+04	1,695820E+04	1,695820E+04	1,695820E+04	1,695820E+04
	Std	1,008211E-04	6,555526E-05	1,165918E-04	7,306640E-05	1,162785E-04
RC29	Mean	2,964898E+06	2,964898E+06	2,964898E+06	2,964899E+06	2,964900E+06
	Std	1,500307E+00	1,415458E+00	2,514889E+00	2,798226E+00	2,903451E+00
RC30	Mean	2,658559E+00	2,658559E+00	2,658565E+00	2,658559E+00	2,658559E+00
	Std	1,311500E-09	9,747018E-13	1,750382E-05	1,670440E-10	0,000000E+00
RC31	Mean	0,000000E+00	4,435135E-14	1,687493E-13	3,234578E-14	2,772378E-13
	Std	0,000000E+00	6,419820E-14	2,304124E-13	4,757450E-14	7,406385E-13
RC32	Mean	-3,066554E+04	-3,066554E+04	-3,066554E+04	-3,066554E+04	-3,066554E+04
	Std	1,451593E-04	3,579815E-04	8,693618E-05	7,873023E-04	9,772617E-05
RC33	Mean	2,639347E+00	2,639348E+00	2,639347E+00	2,639347E+00	2,639349E+00
	Std	9,732917E-08	3,714109E-06	3,301452E-07	3,685461E-07	6,480390E-06

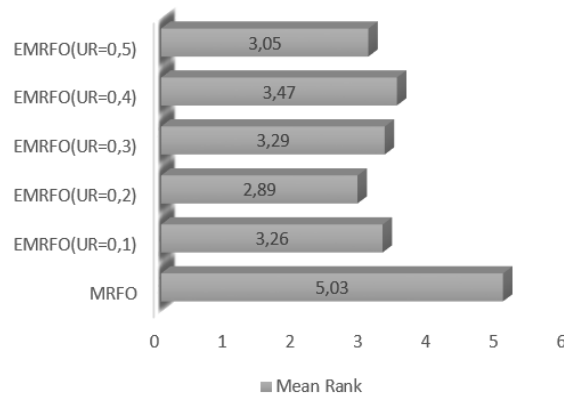


Figure 9. Friedman test results

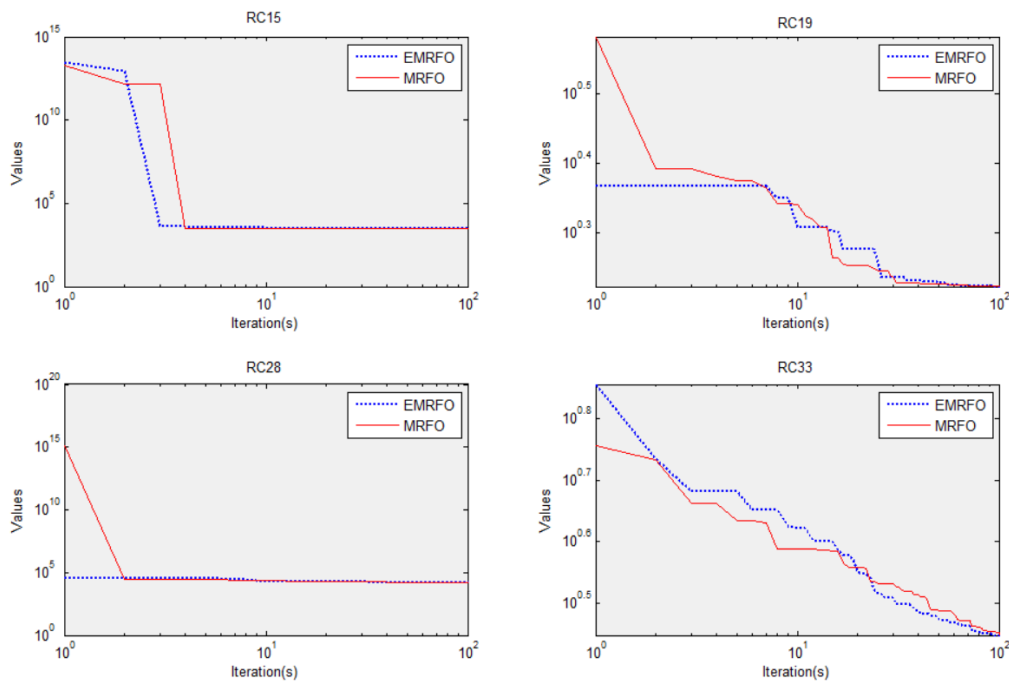


Figure 10. Convergence graphics of MRFO and EMRFO

Finally, the proposed EMRFO algorithm is compared with the algorithms in the literature, and the obtained results are given in Table 7. In this table, MVPA (Most Valuable Player Algorithm) results are taken from [48], ABC (Artificial Bee Colony Algorithm), SSA (Salp Swarm Algorithm), and GWO (Grey Wolf Optimizer) results are taken from [49]. When Table 7 is analyzed, it is observed that EMRFO finds the best mean value alone in 5 problems, and in 7 problems, it finds the same best mean value with some other algorithms. According to the pairwise comparison results with other algorithms given at the end of Table 7, the proposed algorithm obtains better mean values in more problems than the other algorithms except for ABC. In addition, Friedman test results based on the mean values given in Table 7 are presented in Figure 11. According to the ranking result, EMRFO ranks first with a mean rank value of 3.11. In addition, the ABC algorithm ranks second, while the MRFO and GWO algorithms rank third. In light of all the evaluations given in this section, it can be concluded that the modifications made in MRFO contribute to the performance of the algorithm, and the proposed EMRFO is an algorithm that produces preferable successful results compared to the literature.

Table 7. Comparison results of the EMRFO with other algorithms in the literature

Problems	EMRFO	MRFO	MVPA	ABC	SSA	GWO
RC15	2,994E+03	2,994E+03	2,994E+03	2,994E+03	3,002E+03	2,998E+03
RC16	3,503E-02	4,195E-02	4,936E-02	6,360E-02	4,916E+00	3,878E-02
RC17	1,267E-02	1,267E-02	1,277E-02	1,284E-02	1,272E-02	1,268E-02
RC18	6,098E+03	6,325E+03	6,371E+03	5,774E+03	6,108E+03	5,906E+03
RC19	1,670E+00	1,670E+00	1,670E+00	1,889E+00	1,696E+00	1,688E+00
RC20	2,639E+02	2,639E+02	2,639E+02	2,639E+02	2,639E+02	2,639E+02
RC21	2,352E-01	2,352E-01	2,352E-01	2,352E-01	2,352E-01	2,353E-01
RC22	5,265E-01	5,288E-01	7,484E-01	5,34E+00	5,358E-01	5,34E+00
RC23	4,552E+01	2,619E+01	1,628E+01	1,605E+01	1,604E+01	1,605E+01
RC24	2,841E+00	2,954E+00	2,810E+00	4,071E+00	2,945E+00	3,907E+00
RC25	1,723E+03	1,766E+03	2,284E+03	6,573E+02	4,346E+02	3,665E+02
RC26	5,426E+01	8,869E+15	1,218E+02	1,293E+06	3,500E+06	1,631E+07
RC27	5,271E+02	5,275E+02	5,281E+02	5,231E+02	5,247E+02	5,241E+02
RC28	1,696E+04	1,696E+04	1,696E+04	1,695E+04	1,698E+04	1,700E+04
RC29	2,965E+06	2,965E+06	2,965E+06	3,005E+06	3,059E+06	2,967E+06
RC30	2,659E+00	2,672E+00	2,903E+00	2,767E+00	2,675E+00	2,702E+00
RC31	4,435E-14	0,000E+00	0,000E+00	4,377E-15	9,281E-22	2,443E-14
RC32	-3,067E+04	-3,067E+04	-3,067E+04	-3,044E+04	-3,067E+04	-3,066E+04
RC33	2,639E+00	2,639E+00	2,639E+00	2,639E+00	2,713E+00	2,790E+00
Better		8	8	7	11	10
Worst		2	3	9	7	8
Equal		9	8	3	1	1

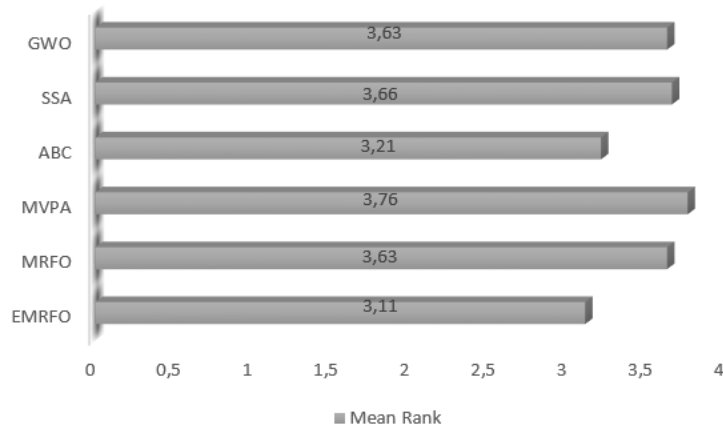


Figure 11. Friedman test results

5. CONCLUSIONS AND FUTURE WORK

In this study, the performance of the proposed MRFO algorithm for engineering applications is tested on mechanical engineering optimization problems in the CEC2020 real-world constrained optimization problems suite. In order to overcome the drawbacks of the MRFO algorithm and increase its performance, the algorithm has been developed with three modifications, and EMRFO has been

proposed. The modifications made are integrated into the algorithm separately, and their effect on performance is shown. When the results of EMRFO are analyzed, it is determined that the algorithm found more successful values and converged faster than the standard algorithm. In addition, in the comparisons made with the algorithms in the literature, EMRFO took first place and proved that it is a competitive, successful, and preferable algorithm for this problem suite. In future studies, EMRFO can be applied to different problem suites. In addition, it can be discretized for solving discrete optimization problems.

CONFLICT OF INTEREST

The author stated that there are no conflicts of interest regarding the publication of this article.

REFERENCES

- [1] Ezugwu AE, Shukla AK, Nath R, Akinyelu AA, Agushaka JO, Chiroma H, Muhuri PK. Metaheuristics: a comprehensive overview and classification along with bibliometric analysis. *Artificial Intelligence Review* 2021; 54(6): p. 4237-4316.
- [2] Pan JS, Zhang LG, Wang RB, Snášel V, Chu SC. Gannet optimization algorithm : A new metaheuristic algorithm for solving engineering optimization problems. *Mathematics and Computers in Simulation* 2022; 202: p. 343-373.
- [3] Tang KS, Man KF, Kwong S, He Q. Genetic algorithms and their applications. *IEEE signal processing magazine* 1996; 13(6): p. 22-37.
- [4] Price KV. Differential evolution in *Handbook of optimization: From classical to modern approach*. Springer, p. 187-214, 2013.
- [5] Simon D. Biogeography-based optimization. *IEEE transactions on evolutionary computation* 2008; 12(6): p. 702-713.
- [6] Rashedi E, Nezamabadi-Pour H, Saryazdi S. GSA: a gravitational search algorithm. *Information sciences* 2009; 179(13): p. 2232-2248.
- [7] Alatas B. ACROA: artificial chemical reaction optimization algorithm for global optimization. *Expert Systems with Applications* 2011; 38(10): p. 13170-13180.
- [8] Zhao W, Wang L, Zhang Z. Atom search optimization and its application to solve a hydrogeologic parameter estimation problem. *Knowledge-Based Systems* 2019; 163: p. 283-304.
- [9] Rao RV, VSavsani VJ, Vakharia D. Teaching-learning-based optimization: a novel method for constrained mechanical design optimization problems. *Computer-aided design* 2011; 43(3): p. 303-315.
- [10] Moosavi SHS, Bardsiri VK. Poor and rich optimization algorithm: A new human-based and multi populations algorithm. *Engineering Applications of Artificial Intelligence* 2019; 86: p. 165-181.
- [11] Ray T, Liew KM. Society and civilization: an optimization algorithm based on the simulation of social behavior. *IEEE Transactions on Evolutionary Computation* 2003; 7(4): p. 386-396.

- [12] Zhao W, Wang L, Zhang Z. Supply-demand-based optimization: A novel economics-inspired algorithm for global optimization. *IEEE Access* 2019; 7: p. 73182-73206.
- [13] Civicioglu P. Backtracking search optimization algorithm for numerical optimization problems. *Applied Mathematics and computation* 2013; 219(15): p. 8121-8144.
- [14] Liu J, Wu C, Wu G, Wang X. A novel differential search algorithm and applications for structure design. *Applied Mathematics and Computation* 2015; 268: p. 246-269.
- [15] Wang L, Cao Q, Zhang Z, Mirjalili S, Zhao W. Artificial rabbits optimization: A new bio-inspired meta-heuristic algorithm for solving engineering optimization problems. *Engineering Applications of Artificial Intelligence* 2022; 114: p. 105082.
- [16] Kennedy J, Eberhart R. Particle swarm optimization. in *Proceedings of ICNN'95-international conference on neural networks 1995*: IEEE.
- [17] Karaboga D, Akay B. A comparative study of artificial bee colony algorithm. *Applied mathematics and computation* 2009; 214(1): p. 108-132.
- [18] Dorigo M, Birattari M, Stutzle T. Ant colony optimization. *IEEE computational intelligence magazine* 2006; 1(4): p. 28-39.
- [19] Zhao W, Zhang Z, Wang L. Manta ray foraging optimization: An effective bio-inspired optimizer for engineering applications. *Engineering Applications of Artificial Intelligence* 2020; 87: p. 103300.
- [20] Liu J, Chen Y, Liu X, Zuo F, Zhou H. An efficient manta ray foraging optimization algorithm with individual information interaction and fractional derivative mutation for solving complex function extremum and engineering design problems. *Applied Soft Computing* 2024; 150: p. 111042.
- [21] Houssein EH, Ibrahim IE, Neggaz N, Hassaballah M, Wazery YM. An efficient ECG arrhythmia classification method based on Manta ray foraging optimization. *Expert Systems with Applications* 2021; 181: p. 115131.
- [22] Houssein EH, Emam MM, Ali AA. Improved manta ray foraging optimization for multi-level thresholding using COVID-19 CT images. *Neural Computing and Applications* 2021; 33(24): p. 16899-16919.
- [23] Hemeida MG, Ibrahim AA, Mohamed AAA, Alkhalaf S, El-Dine AMB. Optimal allocation of distributed generators DG based Manta Ray Foraging Optimization algorithm (MRFO). *Ain Shams Engineering Journal* 2021; 12(1): p. 609-619.
- [24] Tang A, Zhou H, Han T, Xie L. A Modified Manta Ray Foraging Optimization for Global Optimization Problems. *IEEE Access* 2021; 9: p. 128702-128721.
- [25] Gokulkumari G. Classification of brain tumor using manta ray foraging optimization-based DeepCNN classifier. *Multimedia Research* 2020; 3(4): p. 32-42.
- [26] Hassan MH, Houssein EH, Mahdy MA, Kamel S. An improved manta ray foraging optimizer for cost-effective emission dispatch problems. *Engineering Applications of Artificial Intelligence* 2021; 100: p. 104155.

- [27] Micev M, Čalasan M, Ali ZM, Hasanien HM, Abdel Aleem SHE. Optimal design of automatic voltage regulation controller using hybrid simulated annealing – Manta ray foraging optimization algorithm. *Ain Shams Engineering Journal* 2021; 12(1): p. 641-657.
- [28] Kahraman HT, Akbel M, Duman S. Optimization of Optimal Power Flow Problem Using Multi-Objective Manta Ray Foraging Optimizer. *Applied Soft Computing* 2022; 116: p. 108334.
- [29] Got A, Zouache D, Moussaoui A. MOMRFO: Multi-objective Manta ray foraging optimizer for handling engineering design problems. *Knowledge-Based Systems* 2022; 237: p. 107880.
- [30] Elaziz MA, Abualigah L, Ewees AA, Al-qaness MAA, Mostafa RR, Yousri D, Ibrahim RA. Triangular mutation-based manta-ray foraging optimization and orthogonal learning for global optimization and engineering problems. *Applied Intelligence* 2023; 53(7): p. 7788-7817.
- [31] Zouache D, Abdelaziz FB. Guided Manta Ray foraging optimization using epsilon dominance for multi-objective optimization in engineering design. *Expert Systems with Applications* 2022; 189: p. 116126.
- [32] Ekinci S, Izi D, Kayri M. An Effective Controller Design Approach for Magnetic Levitation System Using Novel Improved Manta Ray Foraging Optimization. *Arabian Journal for Science and Engineering* 2022; 47(8): p. 9673-9694.
- [33] Yousri D, AbdelAty AM, Al-qaness MAA, Ewees AA, Radwan AG, Abd Elaziz M. Discrete fractional-order Caputo method to overcome trapping in local optima: Manta Ray Foraging Optimizer as a case study. *Expert Systems with Applications* 2022; 192: p. 116355.
- [34] Daqaq F, Kamel S, Ouassaid M, Ellaia R, Agwa AM. Non-Dominated Sorting Manta Ray Foraging Optimization for Multi-Objective Optimal Power Flow with Wind/Solar/Small- Hydro Energy Sources. *Fractal and Fractional* 2022; 6(4):194.
- [35] Zhu D, Wang S, Zhou C, Yan S. Manta ray foraging optimization based on mechanics game and progressive learning for multiple optimization problems. *Applied Soft Computing* 2023; 145: p. 110561.
- [36] Yang J, Liu Z, Zhang X, Hu G. Elite Chaotic Manta Ray Algorithm Integrated with Chaotic Initialization and Opposition-Based Learning. *Mathematics* 2022; 10(16):2960.
- [37] Ghosh KK, Guha R, Bera SK, Kumar N, Sarkar R. S-shaped versus V-shaped transfer functions for binary Manta ray foraging optimization in feature selection problem. *Neural Computing and Applications* 2021; 33(17): p. 11027-11041.
- [38] Yıldızdan G. Bin_MRFOA: A Novel manta ray foraging optimization algorithm for binary optimization. *Konya Journal Of Engineering Sciences* 2023; 11(2): p. 449-467.
- [39] Wang D, Liu X, Li Z, Lu B, Guo A, Chai G. Discrete Manta Ray Foraging Optimization Algorithm And Its Application In Spectrum Allocation. *Journal Of Computer Applications* 2022; 42(1): p. 215.
- [40] Özsoydan FB, Baykasoglu A. Analysing the effects of various switching probability characteristics in flower pollination algorithm for solving unconstrained function minimization problems. *Neural Computing and Applications* 2019; 31(11): p. 7805-7819.

- [41] Bansal JC, Singh PK, Saraswat M, Verma A, Jadon SS, Abraham A. Inertia Weight strategies in Particle Swarm Optimization. in 2011 Third World Congress on Nature and Biologically Inspired Computing 2011.
- [42] Jusof MFM, Nasir ANK, Razak AAA, Rizal NAM, Ahmad MA, Muhamad IH. Adaptive-Somersault MRFO for Global Optimization with an Application to Optimize PD Control. in Proceedings of the 12th National Technical Seminar on Unmanned System Technology 2020: NUSYS'20 2022:Springer.
- [43] Hakli H. BinEHO: a new binary variant based on elephant herding optimization algorithm. *Neural Computing and Applications* 2020; 32: p. 16971-16991.
- [44] Ma J, Xia D, Guo H, Wang Y, Niu X, Liu Z, Jiang S. Metaheuristic-based support vector regression for landslide displacement prediction: A comparative study. *Landslides* 2022; 19(10): p. 2489-2511.
- [45] Korkmaz S, Şahman MA, Cinar AC, Kaya E. Boosting the oversampling methods based on differential evolution strategies for imbalanced learning. *Applied Soft Computing* 2021; 112: p.107787.
- [46] Kumar A, Wu G, Ali MZ, Mallipeddi R, Suganthan PN, Das S. A test-suite of non-convex constrained optimization problems from the real-world and some baseline results. *Swarm and Evolutionary Computation* 2020; 56: p. 100693.
- [47] Friedman M. The use of ranks to avoid the assumption of normality implicit in the analysis of variance. *Journal of the american statistical association* 1937; 32(2012): p. 675-701.
- [48] Uymaz SA. Evaluation of the Most Valuable Player Algorithm for Solving Real-World Constrained Optimization Problems. *Bilişim Teknolojileri Dergisi* 2021.
- [49] Wansasueb K, Panmanee S, Panagant N, Pholdee N, Bureerat S, Yıldız AR. Hybridised differential evolution and equilibrium optimiser with learning parameters for mechanical and aircraft wing design. *Knowledge-Based Systems* 2022; 239: p. 107955.



RESEARCH ARTICLE

NOVEL APPROACH FOR ONE-POT SELF-ASSEMBLED MONOLAYER PREPARATION
OF GOLD TIPPED CdSe/CdS NANORODS

Zeynep DİKMEN 

Faculty of Engineering, Department of Biomedical Engineering, Eskişehir Osmangazi University, 26040 Eskişehir, Turkey

ABSTRACT

In this study, CdSe/CdS nanorods (NRs) were synthesized via hot injection method to perform simultaneous self-assembly studies with gold tip formation on the nanorods. In this new approach, we propose and demonstrate reductant chemical and gold organosol-free synthesis of gold-tipped nanocrystals on the subphase. Instead of gold organosol usage, gold precursor was prepared by addition of gold source into subphase, and photocatalytic reduction of gold on the tip of nanorods was achieved by exciting the samples under UV-light excitation. Reduction of gold nanoparticles on the tip of NRs was also tried by heating effect, which results in smaller gold tip formation. The optical properties of these nanorods were determined by spectrophotometric measurements, and gold-tipped nanorods were imaged by TEM analysis. This method enables self-assembly of nanorods and following gold tip formation on the subphase, and it can pave the way to prepare well-defined metal-tipped oriented surfaces that can be used for optical and photocatalysis applications.

Keywords: Gold-tipped nanorod, Self-assembly, CdSe/CdS nanorod

1. INTRODUCTION

Nanocrystals (NCs) with a size regime between 1-10 nm constitute a major class of nanomaterials since they have remarkable properties that can be tuned by controlling their size and shape. Quantum confinement occurs when the size of the material is comparable to exciton Bohr radius and differs in nanocrystal physical properties from bulk materials. Since the size of NCs decreases, the number of atoms also decreases from a few thousand to a few hundred. This results in an increase in the surface/volume ratio. The high surface-to-volume ratio of NCs affects their structural and optical properties significantly. So, the properties of the nanocrystal can be adjusted by changing their sizes [1-4]. New optoelectronic properties can be created by using heteronanocrystals (HNCs) by changing their composition, size, and shape. CdSe/CdS HNC is a significant model since it presents the appealing characteristics of strong, tunable and polarized light emission that can be manipulated by external electric fields [5]. Band alignment of the heteronanocrystals is strongly dependent on the quantum confinement of charge carriers (i.e., electrons and holes) that can be adjusted by changing the size of the CdSe quantum dot (QD) core and the geometry of the CdS shell [6]. In such NRs, CdSe is a spherical core, and CdS is rod shaped shell. This structure presents useful properties for many applications because of the separation of charge carriers. The hole is located in the core while electrons can move through the CdS rod body, as a good example of type I^{1/2} heteronano structures [6]. CdSe/CdS HNRs can be used for emerging applications such as photovoltaics, photodetectors, LEDs, lasers, and single photon sources. They also got great attention for optical labeling, photocatalytic solar fuel production, and photoconductive films because of their high quantum yield and low full width half maximum values of PL.

Diverse combinations of semiconductor/metal hybrid nanostructures have been reported in the literature, such as PbSe/Au, Ag or Pd, CdSe/Au, and CdS/Au or CdSe/CdZnS/Au [7]. Metal tips of such

multicomponent heterostructures can act both as an electrical contact [8-10] and as an anchor point for self-assembly [11], while the core-shell structure of NRs is responsible for the unique optical properties [10, 12, 13]. Metal-tipped, seeded core-shell semiconductor nanorods exemplify to multifarious functionalized nano structures [14]. An example of metal-tipped heteronanorods is Pt-tipped CdSe/CdS HNRs, which have been used effectively for photocatalytic hydrogen production [15]. The system is composed of a platinum-tipped CdS nanorod with an embedded CdSe seed. In such structures, holes are three-dimensionally confined to the core, whereas the electrons are delocalized through the rod body and can be transferred to the metal tip. Consequently, the separation of the electrons from the holes within a tunable physical length and efficient, long-lasting charge carrier separation can be achieved over three different components. This feature makes the metal-tipped heteronanocrystals crucial for solar energy harvesting, photocatalysts, or as building blocks in solar cells.

Understanding and mastering both the synthesis and the self-assembly phenomena has been recently made for various nanocrystals [16, 17]. The self assembly process can be controlled by external fields, by interparticle interactions as well as solvent, subphase or capping ligand choice. Binary solvent/nonsolvent usage also affects the self assembly tendency of the nanocrystals [18]. Ordered assemblies and orientation control of nanorods and their metal tipped counterparts are important for investigation their chemical and physical interactions among nanocrystals. It is also emerging research area for practical applications, as it results in the engineering of new materials and the fabrication of devices [10]. Synthesis of gold-tipped nanocrystals as emerging material for many application reported in the literature [7, 19]. Nevertheless, there is a need for enhancement in the preparation of in-situ self-assembled films of metal tipped nanocrystals.

Herein, a hot injection method with a seeded growth approach was used to synthesize CdSe/CdS nanorods. The optical, morphological and composition characterization of the nanocrystals was performed. This red emissive nanorods were used for self-assembly experiments. The main aim was one-pot formation of gold tipped nanorods without using any reducing, stabilizing agent and simultaneous self assembly of the sample. This new method can be used to prepare all-the same-oriented Au tipped nanorods self assembled monolayer films for further photocatalysis applications, lasing, and surface enhanced Raman spectroscopy. It also paves the way for conducting the method to other nanocrystals (i.e. nanoplatelets) or other metal precursors (i.e. platinum, silver, and palladium) for improved applications.

2. EXPERIMENTAL

2.1. Materials and Characterization

Cadmium oxide (CdO, Sigma-Aldrich, 99.9%), trioctyl phosphine oxide (TOPO, Alfa Aesar, 98%), trioctyl phosphine (TOP, abcr, 97%), octadecylphosphonic acid (ODPA, abcr, 97%), selenium (Se, Sigma-Aldrich, 99.99%), sulphur (S, Sigma-Aldrich, 90%), ethanol (EtOH, Sigma-Aldrich, 99.8%), methanol (MeOH, Alfa Aesar, 99.9%), tetrahydrofuran (THF, Sigma-Aldrich, 99.9%), hexane (Honeywell), toluene (TOL, Merck, anhydrous), potassium tetrachloroaurate(III) (KAuCl₄, CHEMPUR, 99.95%), ethylene glycol (EG, Sigma-Aldrich, 99%) diethylene glycol (DEG, Sigma-Aldrich, 99%) were used.

Transmission electron microscopy (TEM) analysis was conducted using a Hitachi HT7800 T at an accelerating voltage of 100 kV. Spectrophotometric analysis at 25 °C across the wavelength range of 200–700 nm was carried out using UV–VIS spectrophotometry (Perkin Elmer Lambda 35). The Au-NRs sample underwent X-ray diffraction (XRD) measurements using a powder diffractometer (Empyrean, Panalytical) with CuK α irradiation, scanning through 2 θ angles ranging from 20 to 90°. Perkin-Elmer LS-55 spectrophotometer was employed to get the photoluminescence (PL) spectra.

2.2. Methods

Preparation of Se precursor

0.058 g of Se powder is weighed and placed in a 2 ml vial, then 1.2 g of TOP is added. A magnetic stirrer is placed to vial and mixed for 1 hour at 80 °C to ensure that all Se powder dissolved. A colorless homogeneous solution formation indicates that interaction between Se powder and TOP has occurred.

Synthesis of CdSe seed

CdSe quantum dots were synthesized by hot injection method, which is performed by injecting a cold chalcogenide precursor into a high-temperature metal precursor. 3 g of TOPO is weighed and placed in a 3-necked flask with a round bottom. While the Vigreux column is attached to it, the other two outlets are closed with a high temperature-resistant rubber septa. The Vigreux column is closed with a t-adaptor for nitrogen and vacuum output. In this way, the system is placed in the glove box. 0.06 g CdO and 0.28 g ODPa are added inside the glove box. The taps of the flask and Vigreux column are closed, and the flask is taken out of the box for further attachment to the Schenk line. The mixture is kept in N₂(g) atmosphere until it melts, the oxygen and water in the environment and the chemicals that will disrupt the reaction are removed by stirring for 1 hour under vacuum ($4 \cdot 10^{-2}$ Torr) at 170 °C. Then, Cd and TOPO-ODPA molecules are allowed to interact at 300 °C. A color change in the solution from brown to colorless indicates that the reaction has occurred. As soon as the solution becomes colorless, the temperature of the environment is increased to 385 °C. The heater is lowered to 380 °C, and when the temperature reach at this value, 1.5 g TOP and then Se-TOP precursor is injected. When the color of the solution in the reaction flask turns brownish red, the heating jacket is quickly removed, the flask is rapidly cooled, and 5 mL of anhydrous toluene is injected. Then, the quantum dot colloidal solution in the flask is transferred to the vial closed with a septum. It is placed in a glove box and the quantum dot is precipitated by adding 2 mL of anhydrous methanol twice. The solution is centrifuged at 3000 rpm for 10 minutes. The remaining supernatant is removed, and 4 mL of TOP is added as a solvent. For nanocrystal characterization, 5 mL QD is taken into a vial, TOP is removed by evaporation at 60 °C, and 3 mL of toluene is added, and absorption and fluorescence spectra are recorded. Using absorption spectroscopy, first the diameter of the synthesized nanocrystal is calculated, and then the concentration of the stock solution.

Preparation of S precursor

0.12 g of S powder was weighed and placed in a 2 ml vial, and 1.5 g of TOP was added and stirred at 80 °C for 1 hour to ensure the interaction of S and TOP ligands. The discoloration of the solution indicated the interaction between S and TOP molecules.

Synthesis of CdSe/CdS NRs

CdSe/CdS NRs synthesized via seeded growth were weighed in a 0.06 g CdO, 3 g TOPO, 0.34 g ODPa glove cabinet and added to a three-necked flask. The water was removed under vacuum for approximately 1 hour at 170 °C. It was heated to 350-380 °C, which is the temperature of the reaction environment. When it reached the injection temperature, 1.5 g of TOP was injected, after which it was heated to the required temperature for the injection of S-TOP and CdSe quantum dot precursors. When it reached 350–380 °C, 200 µL of CdSe core (400 µM) and S-TOP reagent were quickly injected. The temperature drops suddenly but rises again. At this temperature, crystals were allowed to grow for 6 minutes. Rapid cooling of the reaction flask was achieved. When the temperature dropped to 60 °C, 10 mL of toluene was injected and transferred to vials prepared in a nitrogen atmosphere using a syringe. Purification was achieved by centrifugation at 3000 rpm by adding methanol solution [17].

One-pot self assembly and gold tip formation on the NRs

NRs solution (27 mg/mL) in toluene/heptane mixture was prepared. 5 mg of KAuCl_4 was dissolved in 20 mL subphase (EG or DEG). The mixture was put into the Petri dish followed by addition of hydrophobic NR solution on top of subphase. The toluene/heptane solvents are allowed to evaporate for the self-assembled layer formation. Then, the self assembled layer was placed under UV-light for 20 minutes for photocatalytic reduction of gold ions into gold tips.

3. RESULTS AND DISCUSSION

Here synthesis of CdSe/CdS core/shell nanorod was performed via hot injection method modified by seeded growth approach using CdSe QD as seed. Narrow size distributions of CdSe/CdS nanorods with strong and tunable light emission from green to red can be performed by this method [17]. Orange-red emissive CdSe/CdS NRs with narrow size distribution were synthesized by using well-defined CdSe QDs as seed. TEM images of the CdSe QDs and NRs are given in Figure 1-a,b, respectively. The mean size of the CdSe seeds was measured as 2.87 nm, while the mean thickness of NRs was 3.52 nm, and the mean length was 71.80 nm.

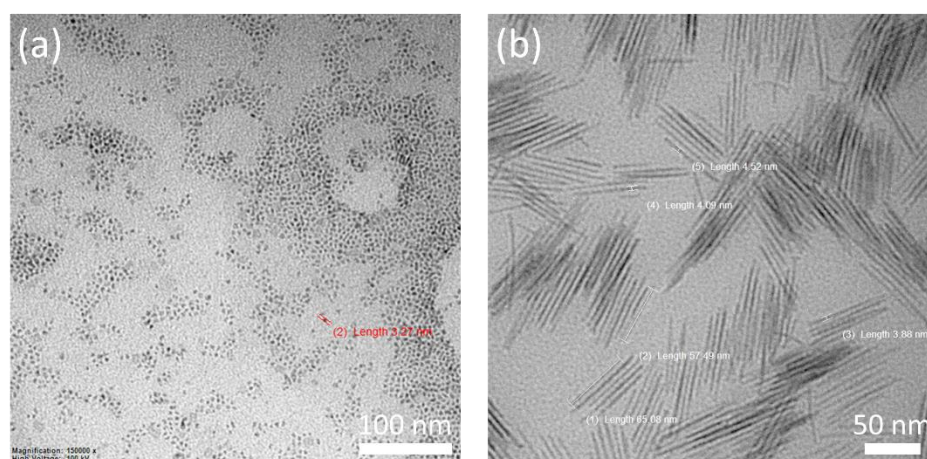


Figure 1. TEM images of CdSe quantum dots (a), and NRs (b).

The absorption from CdS shell as the high-energy peaks and the lowest energy peak originated from electronic transitions from holes confined in the CdSe seed can be seen in the absorption spectrum (Figure 2a). Photoluminescence (PL) peak is at 610 nm as shown in Figure 2b [17, 20]. Digital images of the NRs under daylight and UV-light excitation are given in Figure 2c with an orange-red emission.

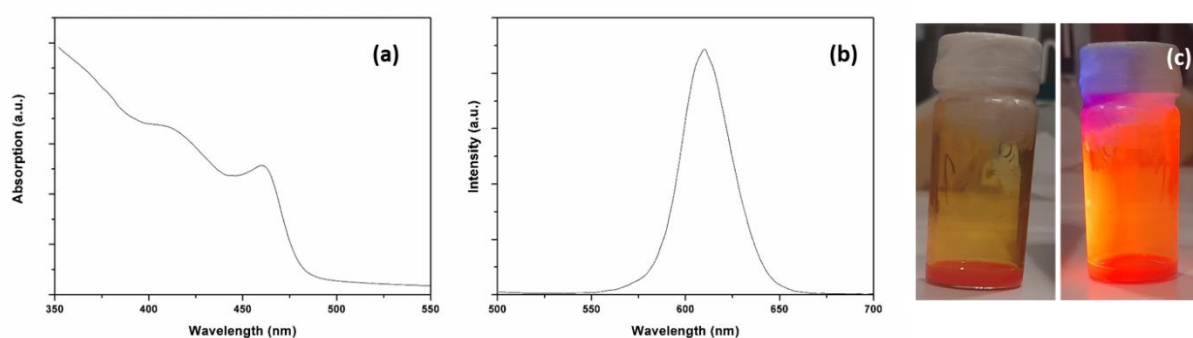


Figure 2. Absorption (a) and photoluminescent (b) spectra of NRs. Digital images of synthesized NRs under daylight (left) and UV-light excitation (right) (c).

The NRs were characterized by X-Ray diffraction pattern as given in Figure 3. The major reflections of hexagonal close-packed cadmium chalcogenide structure are observed at $2\theta = 24.86^\circ, 26.45^\circ, 28.21^\circ, 36.61^\circ, 43.78^\circ, \text{ and } 51.88^\circ, 71.03^\circ, 83.354^\circ$ which can be assigned to the, (010), (002), (011), (012), (110), (112), (121), (123) reflections, respectively [21].

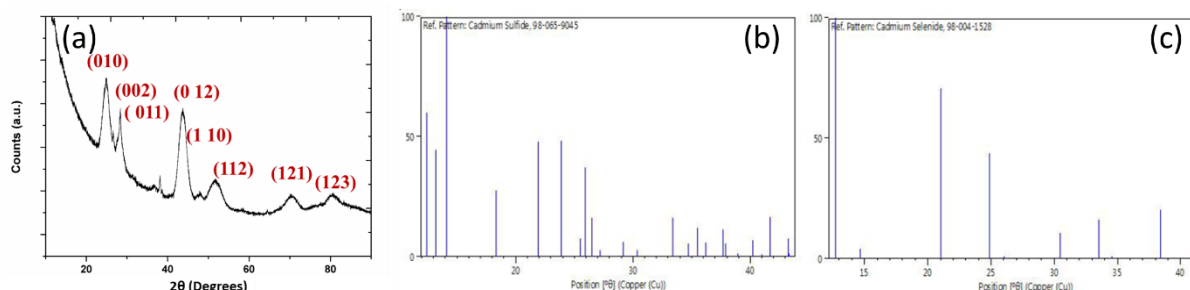


Figure 3. XRD pattern of synthesized NRs (a), reference peak positions of CdS (b), reference peak positions of CdSe (c).

These NRs have a tendency to self-assemble by easily organizing in close-packed ordered arrays on substrates over large areas [16]. Self assembly of NRs were performed on the EG and DEG subphases by dissolving gold source in it. Self-assembly of nanorods is a well-known phenomena for decades however self assembly of metal tipped NRs by orienting the metal tips on the same direction is challenging [17, 22–28]. In our approach, self assembly of NRs is followed by metal tip formation. Thanks to gold precursor containing subphase, gold ions are contacted to one side of NRs and tip formation can be controlled by this approach. The self assembly process on the gold precursor containing subphase is depicted in Figure 4.

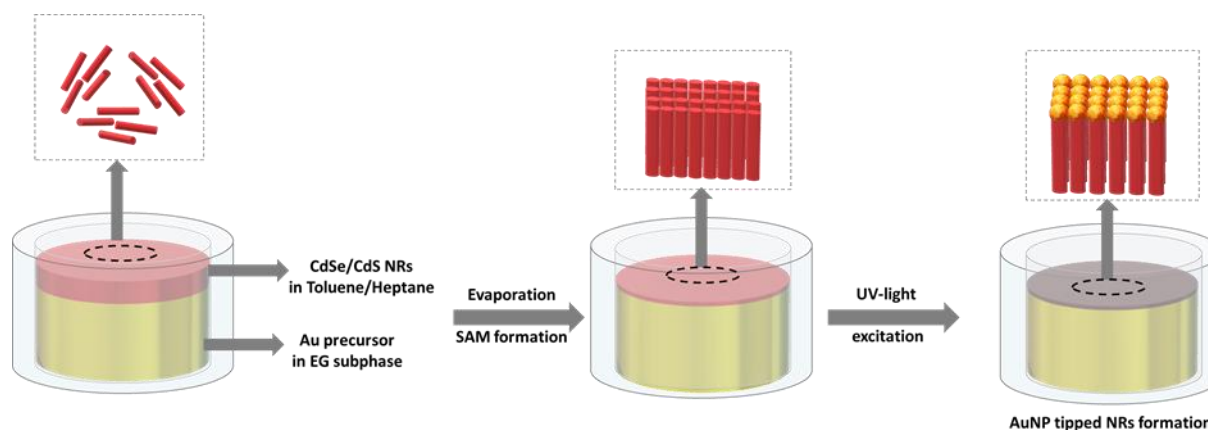


Figure 4. Preparation steps of Au-tipped CdSe/CdS NRs on the subphase

TEM images of self assembled NRs and gold tipped NRs are given in Figure 5a and b-c, respectively. The reduction of gold ions on the NRs was also tried by heat treatment which resulted in smaller gold nanoparticles formation around NRs as given in Figure 5d. If self assembly procedure is carried out in low concentration or on the more hydrophobic subphase (i.e. diethylene glycol), lateral assembly occurs while more hydrophilic (i.e. ethylene glycol) subphase usage or increased concentration results with the vertical orientation of NRs.

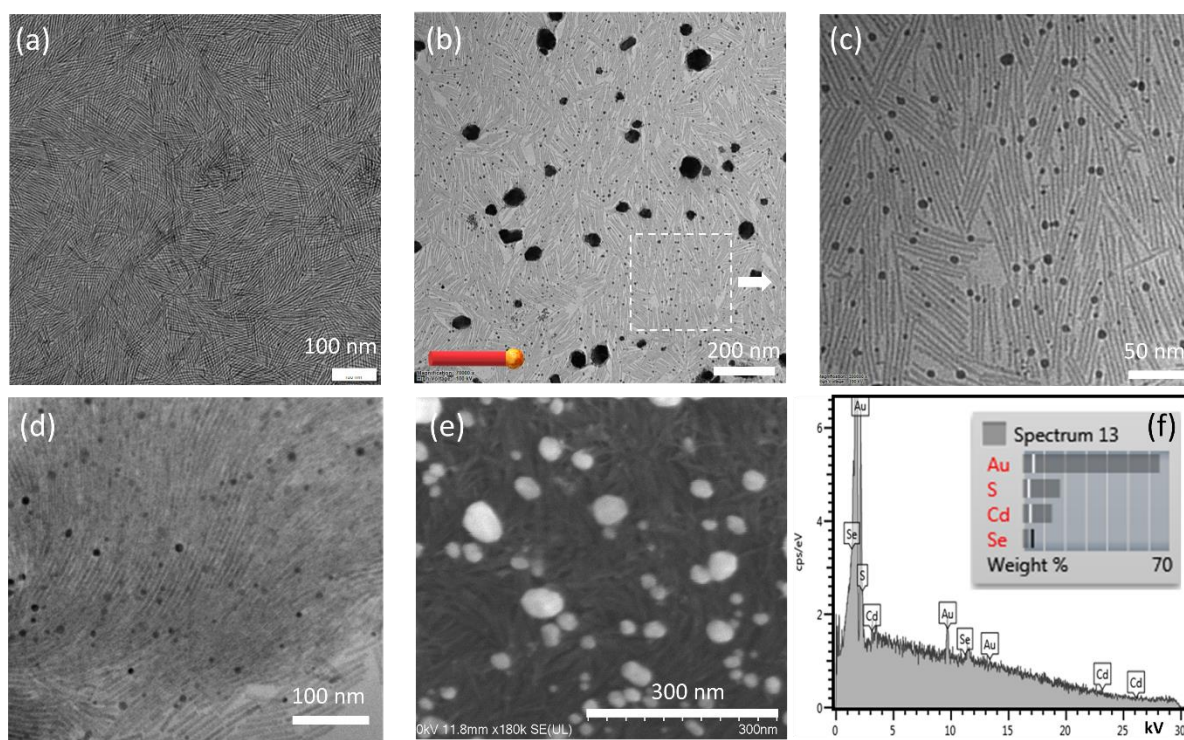


Figure 5. TEM images of self-assembled NRs (a), gold-tipped NRs (b,c) and smaller gold tipped NRs (d). SEM image of gold tipped NRs (e) and EDS analysis of the gold-tipped NRs film on silicon wafer (f).

Thicker film of gold tipped nanorods were prepared for EDS analysis by top picking method onto a silicon wafer as we reported before [18].

Self assembly of such emerging hybrid nanocrystals can be used for efficient charge carrier separation [29] which is crucial for photocatalytic hydrogen production [15] or such surfaces can be used to form cavity for lasing applications [24].

4. CONCLUSION

In conclusion, synthesis of colloidal semiconductor quantum dots and nanorods and characterization of the nanocrystals by electron microscopy, X-ray diffraction pattern and spectrophotometric methods were performed. Such NRs were used for self assembly studies to improve a novel method for metal tipped NR preparation. This new method for one-pot self assembly of metal tipped NRs was demonstrated successfully. In contrast to reported studies in the literature, gold organosol usage or any reductant, stabilizer chemical was not used to prepare gold tipped NRs. Moreover, orientation control over metal tip formation is possible with this approach. Such self assembled layers of gold tipped NRs can be used as surface enhanced Raman spectroscopy (SERS), catalyst for hydrogen production, solar energy conversion and lasing applications.

CONFLICT OF INTEREST

The author stated that there are no conflicts of interest regarding the publication of this article.

ACKNOWLEDGEMENT

This study was supported by the Scientific Research Projects Coordination Unit of Eskişehir Osmangazi University (ESOGU BAP) within the scope of the project numbered FCD-2023-2764.

REFERENCES

- [1] de Mello Donegá C, Liljeroth P, Vanmaekelbergh D. Physicochemical Evaluation of the Hot-Injection Method, a Synthesis Route for Monodisperse Nanocrystals. *Small* 2005; 1: 1152-1162.
- [2] Hadar I, Hitin GB, Sitt A, Faust A, Banin U. Polarization Properties of Semiconductor Nanorod Heterostructures: From Single Particles to the Ensemble. *J. Phys. Chem. Lett.* 2013; 4: 502-507.
- [3] Alivisatos AP. Semiconductor Clusters, Nanocrystals, and Quantum Dots. *Science* (New York, N.Y.) 1996; 271: 933-937.
- [4] Murray CB, Norris DJ, Bawendi MG. Synthesis and characterization of nearly monodisperse CdE (E = sulfur, selenium, tellurium) semiconductor nanocrystallites. *J Am Chem Soc* 1993; 115: 8706-8715.
- [5] Planelles J, Rajadell F, Climente JJ. Electronic Origin of Linearly Polarized Emission in CdSe/CdS Dot-in-Rod Heterostructures. *J Phys Chem Lett C* 2016; 120: 27724-27730.
- [6] Donegá CdM. Synthesis and properties of colloidal heteronanocrystals. *Chem Soc Rev* 2011; 40: 1512-1546.
- [7] Dikmen Z. Gold-tipped CdSe/CdZnS colloidal quantum wells as non-quenching plasmonic particles for optical applications. *Opt Mater* 2024; 147: 114761.
- [8] Sheldon MT, Trudeau P-E, Mokari T, Wang L-W, Alivisatos AP. Enhanced Semiconductor Nanocrystal Conductance via Solution Grown Contacts. *Nano Lett* 2009; 9: 3676-3682.
- [9] Deka S, Falqui A, Bertoni G, Sangregorio C, Poneti G, Morello G, Giorgi MD, Giannini C, Cingolani R, Manna L, Cozzoli PD. Fluorescent Asymmetrically Cobalt-Tipped CdSe@CdS Core@Shell Nanorod Heterostructures Exhibiting Room-Temperature Ferromagnetic Behavior. *J Am Chem Soc* 2009; 131: 12817-12828.
- [10] Chakraborty S, Xing G, Xu Y, Ngiam SW, Mishra N, Sum TC, Chan Y. Engineering Fluorescence in Au-Tipped, CdSe-Seeded CdS Nanoheterostructures. *Small* 2011; 7: 2847-2852.
- [11] Figuerola A, Franchini IR, Fiore A, Mastria R, Falqui A, Bertoni G, Bals S, Van Tendeloo G, Kudera S, Cingolani R, Manna L. End-to-End Assembly of Shape-Controlled Nanocrystals via a Nanowelding Approach Mediated by Gold Domains. *Adv Mater* 2009; 21: 550-554.
- [12] Müller J, Lupton JM, Lagoudakis PG, Schindler F, Koeppe R, Rogach AL, Feldmann J, Talapin DV, Weller H. Wave Function Engineering in Elongated Semiconductor Nanocrystals with Heterogeneous Carrier Confinement. *Nano Lett* 2005; 5: 2044-2049.
- [13] Kraus RM, Lagoudakis PG, Rogach AL, Talapin DV, Weller H, Lupton JM, Feldmann J. Room-Temperature Exciton Storage in Elongated Semiconductor Nanocrystals. *Phys Rev Lett* 2007; 98: 017401.
- [14] Menagen G, Macdonald JE, Shemesh Y, Popov I, Banin U. Au Growth on Semiconductor Nanorods: Photoinduced versus Thermal Growth Mechanisms. *J Am Chem Soc* 2009; 131: 17406-17411.

- [15] Amirav LA, Alivisatos AP. Photocatalytic Hydrogen Production with Tunable Nanorod Heterostructures. *J. Phys. Chem. Lett.* 2010; 1: 1051-1054.
- [16] Talapin DV, Shevchenko EV, Murray CB, Kornowski A, Förster S, Weller H. CdSe and CdSe/CdS Nanorod Solids. *J Am Chem Soc* 2004; 126: 12984-12988.
- [17] Carbone L, Nobile C, De Giorgi M, Sala FD, Morello G, Pompa P, Hych M, Snoeck E, Fiore A, Franchini IR, et al. Synthesis and Micrometer-Scale Assembly of Colloidal CdSe/CdS Nanorods Prepared by a Seeded Growth Approach. *Nano Lett* 2007; 7: 2942-2950.
- [18] Dikmen Z, Işık AT, Bozkaya İ, Dehghanpour Baruj H, Canım kurbey B, Shabani F, Ahmad M, Demir HV. Vertically oriented self-assembly of colloidal CdSe/CdZnS quantum wells controlled via hydrophilicity/lipophilicity balance: optical gain of quantum well stacks for amplified spontaneous emission and random lasing. *Nanoscale* 2023; 15: 9745-9751.
- [19] Hao J, Liu H, Wang K, Sun XW, Delville J-P, Delville M-H. Hole Scavenging and Electron–Hole Pair Photoproduction Rate: Two Mandatory Key Factors to Control Single-Tip Au–CdSe/CdS Nanoheterodimers. *ACS Nano* 2021; 15: 15328-15341.
- [20] Peng X, Schlamp MC, Kadavanich AV, Alivisatos AP. Epitaxial Growth of Highly Luminescent CdSe/CdS Core/Shell Nanocrystals with Photostability and Electronic Accessibility. *J Am Chem Soc* 1997; 119: 7019-7029.
- [21] Duan T, Ai J, Cui X, Feng X, Duan Y, Han L, Jiang J, Che S. Spontaneous chiral self-assembly of CdSe@CdS nanorods. *Chem* 2021; 7: 2695-2707.
- [22] Pietra F, Rabouw FT, van Rhee PG, van Rijssel J, Petukhov AV, Ern  BH, Christianen PCM, de Mello Doneg  C, Vanmaekelbergh D. Self-Assembled CdSe/CdS Nanorod Sheets Studied in the Bulk Suspension by Magnetic Alignment. *ACS Nano* 2014; 8: 10486-10495.
- [23] Wang T, Zhuang J, Lynch J, Chen O, Wang Z, Wang X, LaMontagne D, Wu H, Wang Z, Cao YC. Self-Assembled Colloidal Superparticles from Nanorods. *Science (New York, N.Y.)* 2012; 338: 358-363.
- [24] Zavelani-Rossi M, Krahne R, Della Valle G, Longhi S, Franchini IR, Girardo S, Scotognella F, Pisignano D, Manna L, Lanzani G, Tassone F. Self-assembled CdSe/CdS nanorod micro-lasers fabricated from solution by capillary jet deposition. *Laser & Photonics Rev* 2012; 6: 678-683.
- [25] Salant A, Amitay-Sadovsky E, Banin U. Directed Self-Assembly of Gold-Tipped CdSe Nanorods. *J Am Chem Soc* 2006; 128: 10006-10007.
- [26] Zhao N, Liu K, Greener J, Nie Z, Kumacheva E. Close-Packed Superlattices of Side-by-Side Assembled Au-CdSe Nanorods. *Nano Lett* 2009; 9: 3077-3081.
- [27] Zhao N, Vickery J, Guerin G, Park JI, Winnik MA, Kumacheva E. Self-Assembly of Single-Tip Metal–Semiconductor Nanorods in Selective Solvents. *Angew Chem Int Ed Engl* 2011; 50: 4606-4610.
- [28] Mokari T, Rothenberg E, Popov I, Costi R, Banin U. Selective Growth of Metal Tips onto Semiconductor Quantum Rods and Tetrapods. *Science* 2004; 304: 1787-1790.

- [29] Mokari T, Sztrum CG, Salant A, Rabani E, Banin U. Formation of asymmetric one-sided metal-tipped semiconductor nanocrystal dots and rods. *Nat Mat* 2005; 4: 855-863.



RESEARCH ARTICLE

THE TRAVELING WAVE SOLUTIONS OF THE CONFORMABLE TIME-FRACTIONAL
ZOOMERON EQUATION BY USING THE MODIFIED EXPONENTIAL FUNCTION
METHOD

Ashlı ALKAN^{1,*} , Tolga AKTÜRK² , Hasan BULUT³ 

¹ Department of Mathematics, Faculty of Science, Fırat University, Elazığ, Turkey

² Department of Mathematics and Science Education, Faculty of Education, Ordu University, Ordu, Turkey

³ Department of Mathematics, Faculty of Science, Fırat University, Elazığ, Turkey

ABSTRACT

The present study focuses on the acquisition of traveling wave solutions associated with the conformable time-fractional Zoomeron equation through the utilization of the modified exponential function method (MEFM). The solution functions derived from mathematical computations encompass hyperbolic, trigonometric, and rational functions. Various graphical representations, such as 2D, 3D, contour graphs, and density graphs, are utilized to visually depict the distinct features of the solution functions derived from the determination of suitable parameters.

Keywords: The wave solution, Zoomeron equation, The conformable derivative

1. INTRODUCTION

Nonlinear partial differential equations (NPDEs) have a significant role in various scientific disciplines, such as optics, hydrodynamics, economics, meteorology, plasma physics, and engineering. The existing body of literature presents a range of approaches for acquiring solutions to these equations. Several approaches have been proposed in the literature for solving various types of differential equations. These methods include the (G'/G) expansion method, the new function methods, the generalized Kudryashov method, the sine-Gordon expansion method, the ∂ – dressing method, the homotopy perturbation method. In the present investigation, the modified exponential function method (MEFM) is implemented to address the problem of solving a nonlinear conformable time-fractional Zoomeron equation (CTFZE). New interactions between traveling wave solutions have been identified [1-11].

CTFZE can be defined as follows [9, 13-15]:

$$\frac{\partial^{2\alpha} u}{\partial t^{2\alpha}} \left[\frac{u_{xy}}{u} \right] - \frac{\partial^2 u}{\partial x^2} \left[\frac{u_{xy}}{u} \right] + 2 \frac{\partial^\alpha u}{\partial t^\alpha} [u^2]_x = 0, 0 < \alpha \leq 1, \quad (1)$$

where $u = u(x, y, t)$.

The organization of the article is as follows: In Section 2, the methodology of modified expansion function method has been provided. In Section 4, an application about the conformable time-fractional Zoomeron equation is presented. Section 5 presents the final remarks of the study.

*Corresponding Author: alkanasli47@gmail.com

Received:03.10.2023

Published:28.03.2024

2. THE METHODOLOGY OF MODIFIED EXPONENTIAL FUNCTION METHOD

This section presents an overview of MEFM.

Handle the subsequent NPDE

$$P(u, u_x, u_t, u_{xx}, u_{xxx}, u_{tt}, u_{tx}, \dots) = 0, \quad (2)$$

where, the function $u(x, y, t)$ is of unknown nature, while P represents a polynomial that involves $u(x, y, t)$ as well as its derivatives.

Step 1: The subsequent transformation of the traveling wave is characterized by the

$$u(x, y, t) = u(\xi), \xi = k(x + y - ct), \quad (3)$$

where k, c are nonzero constants and can be computed at a later stage.

By substituting Equation (3) into Equation (2), we obtain the subsequent nonlinear ordinary differential equation (NODE).

$$N(u, u', u'', u''', \dots) = 0. \quad (4)$$

Step 2: According to the MEFM, it is assumed that the desired solution can be described as follows:

$$u(\xi) = \frac{\sum_{i=0}^n A_i [\exp(-\Omega(\xi))]^i}{\sum_{j=0}^m B_j [\exp(-\Omega(\xi))]^j} = \frac{A_0 + A_1 e^{-\Omega} + \dots + A_m e^{-n\Omega}}{B_0 + B_1 e^{-\Omega} + \dots + B_n e^{-m\Omega}}, \quad (5)$$

where A_i ($0 \leq i \leq m$) and B_j ($0 \leq j \leq n$).

The balance principle is employed to derive positive integer values for the variables m and n

$$\Omega' = e^{-\Omega(\xi)} + \mu e^{\Omega(\xi)} + \lambda. \quad (6)$$

Equation (6) exhibits the subsequent families of solutions as described in [12].

Family 1: For $\mu \neq 0, \lambda^2 - 4\mu > 0$, then we have the solution

$$\Omega(\xi) = \ln \left(\frac{-\sqrt{\lambda^2 - 4\mu}}{2\mu} \tanh \left(\frac{\sqrt{\lambda^2 - 4\mu}}{2} (\xi + EE) - \frac{\lambda}{2\mu} \right) \right). \quad (7)$$

Family 2: For $\mu \neq 0, \lambda^2 - 4\mu < 0$, then we get the solution

$$\Omega(\xi) = \ln \left(\frac{-\sqrt{\lambda^2 + 4\mu}}{2\mu} \tan \left(\frac{\sqrt{-\lambda^2 + 4\mu}}{2} (\xi + EE) - \frac{\lambda}{2\mu} \right) \right). \quad (8)$$

Family 3: For $\mu = 0, \lambda \neq 0, \lambda^2 - 4\mu > 0$, then we have the solution

$$\Omega(\xi) = -\ln \left(\frac{\lambda}{e^{\lambda(\xi + EE)} - 1} \right). \quad (9)$$

Family 4: For $\mu \neq 0, \lambda \neq 0, \lambda^2 - 4\mu = 0$, then we get the solution

$$\Omega(\xi) = \ln\left(-\frac{2\lambda(\xi + EE) + 4}{\lambda^2(\xi + EE)}\right). \quad (10)$$

Family 5: For $\mu = 0, \lambda = 0, \lambda^2 - 4\mu = 0$, then we have the solution

$$\Omega(\xi) = \ln(\xi + EE), \quad (11)$$

where, EE is a integral constant.

Step 3: Substituting Equation (5) and its derivatives in Equation (4), we acquire the algebraic equation system. The system has been solved using the Mathematica software package, resulting in the acquisition of solutions for the CTFZE.

3. APPLICATION

In this part, we will employ the MEFM to acquire solutions for the CTFZE. Let us contemplate the subsequent traveling wave transform:

$$u(x, y, t) = u(\xi), \xi = \left(kx + ry - c\frac{t^\alpha}{\alpha}\right). \quad (12)$$

The subsequent NODE is derived as

$$krc^2 \left(\frac{u''}{u}\right)'' - rk^3 \left(\frac{u''}{u}\right)'' - 2ck(u^2)'' = 0. \quad (13)$$

When the balancing procedure is implemented on Equation (12), it results in the establishment of the subsequent connection.

$$n = m + 1.$$

By selecting $m = 1$, then we get $n = 2$. Hence, Equation (5) is acquired for m and n values in the following.

$$u(\xi) = \frac{A_0 + A_1 e^{-\Omega} + A_2 e^{-2\Omega}}{B_0 + B_1 e^{-\Omega}}. \quad (14)$$

By rearranging Equation (14) according to the corresponding term in Equation (13), a set of algebraic equations is obtained. This set consists of the coefficients of the exponential function $e^{-\Omega(\xi)}$.

The Mathematica software tool yielded the following coefficients that are deemed appropriate.

Case:

$$A_0 = -\frac{\sqrt{r}\sqrt{S}\lambda B_0}{\sqrt{2}(-2S + k^3 r(\lambda^2 - 4\mu))^{1/4}(kr(\lambda^2 - 4\mu))^{1/4}},$$

$$A_1 = -\frac{\sqrt{r}\sqrt{S}(2B_0 + \lambda B_1)}{\sqrt{2}(-2S + k^3 r(\lambda^2 - 4\mu))^{1/4}(kr(\lambda^2 - 4\mu))^{1/4}},$$

$$A_2 = -\frac{\sqrt{2}\sqrt{r}\sqrt{S}B_1}{(-2S + k^3r(\lambda^2 - 4\mu))^{1/4}(kr(\lambda^2 - 4\mu))^{1/4}},$$

$$c = -\frac{\sqrt{-2S + k^3r(\lambda^2 - 4\mu)}}{\sqrt{kr(\lambda^2 - 4\mu)}}.$$

By substituting the given coefficients into Equation (13), the resulting solutions are as follows:

Family 1: For $\mu \neq 0, \lambda^2 - 4\mu > 0$, then we obtain the solution,

$$u_1(x, y, t) = \left(-\frac{\sqrt{r}\sqrt{S} \left(\varpi + \lambda\sqrt{\varpi} \operatorname{Tanh} \left[\frac{1}{2}(\zeta)\sqrt{\varpi} \right] \right)}{\sqrt{2}(-2S + k^3r\varpi)^{1/4}(kr(\varpi))^{1/4} \left(\lambda + \sqrt{\varpi} \operatorname{Tanh} \left[\frac{1}{2}(\zeta)\sqrt{\varpi} \right] \right)} \right). \quad (15)$$

where, $\zeta = EE + kx + ry - \frac{ct^\alpha}{\alpha}, \varpi = \lambda^2 - 4\mu$.

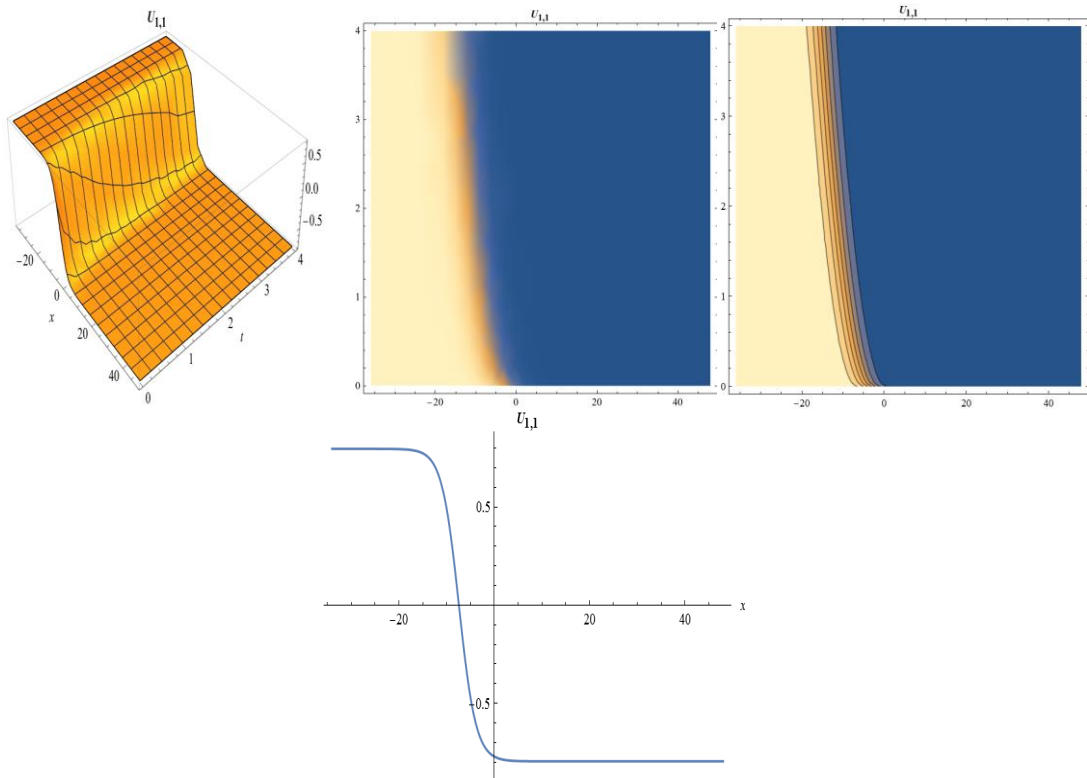


Figure 1: The 2D, 3D, density, contour graphs of Eq. (15) for $k = 0.25, \lambda = 3, \mu = 1, B_0 = 1.2, B_1 = 0.55, r = -0.75, S = 0.24, A_0 = -1.2812, A_1 = -1.44135, A_2 = 0.391477, c = -0.757958, \alpha = 0.5, EE = 0.82, y = 1.2, t = 0.5$.

Family 2: When $\mu \neq 0, \lambda^2 - 4\mu < 0$, then we have the solution,

$$u_2(x, y, t) = \left(\frac{\sqrt{r}\sqrt{S} \left(-\varpi + \lambda\sqrt{-\varpi} \operatorname{Tan} \left[\frac{1}{2}\zeta\sqrt{-\varpi} \right] \right)}{\sqrt{2}(-2S + k^3r(\varpi))^{1/4}(kr(\varpi))^{1/4} \left(\lambda - \sqrt{-\varpi} \operatorname{Tan} \left[\frac{1}{2}\zeta\sqrt{-\varpi} \right] \right)} \right), \quad (16)$$

where, $\zeta = EE + kx + ry - \frac{ct^\alpha}{\alpha}$, $\varpi = \lambda^2 - 4\mu$.

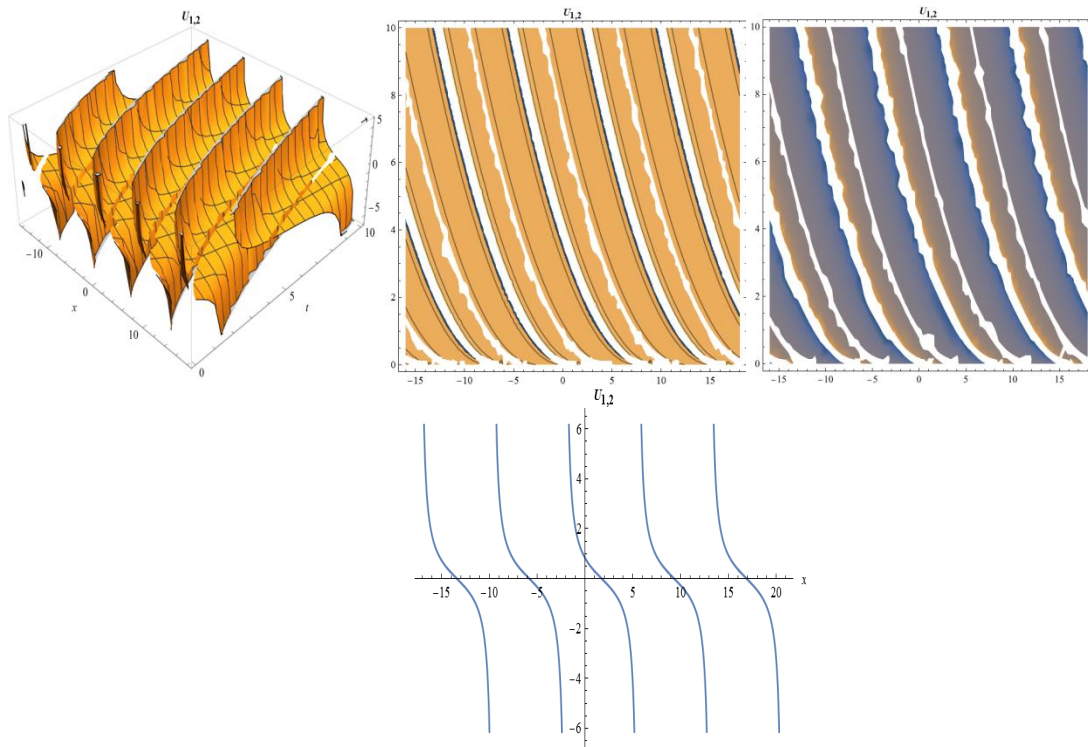
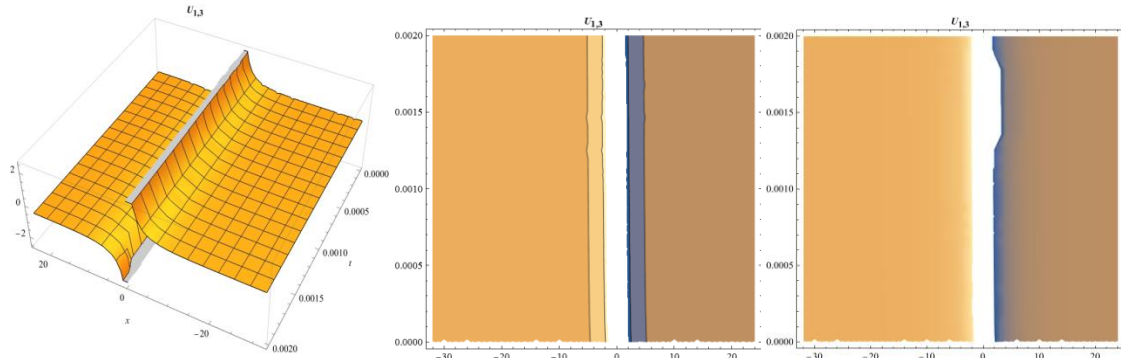


Figure 2: The 2D, 3D, density, contour graphs of Eq. (15) for $k = 0.25, \lambda = 1, \mu = 3, B_0 = 1.2, B_1 = 0.55, r = -0.75, S = -0.24, A_0 = 0.340068, A_1 = 0.836002, A_2 = 0.311729, c = -0.543348, \alpha = 0.5, EE = 0.82, y = 1.2, t = 0.5$.

Family 3: For $\mu = 0, \lambda \neq 0, \lambda^2 - 4\mu < 0$, the solution of Eq. (1) is obtained as,

$$u_3(x, y, t) = \left(-\frac{\sqrt{r}\sqrt{S}\lambda\text{Coth}\left[\frac{1}{2}\zeta\lambda\right]}{\sqrt{2}(kr\lambda^2)^{1/4}(-2S + k^3r\lambda^2)^{1/4}} \right), \tag{17}$$

where, $\zeta = EE + kx + ry - \frac{ct^\alpha}{\alpha}$.



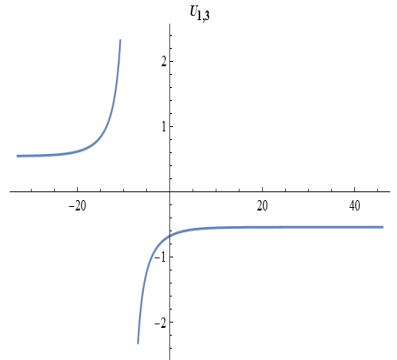


Figure 3: The 2D, 3D, density, contour graphs of Eq. (15) for $k = 0.25, \lambda = 1, \mu = 0, B_0 = 1.2, B_1 = 0.55, r = -0.75, S = 0.24, A_0 = -0.653316, A_1 = -1.60607, A_2 = -0.598873, c = -1.61941, \alpha = 0.5, EE = 0.82, \gamma = 1.2, t = 0.5$.

4. CONCLUSION

In this article, traveling wave solutions of CTFZE are effectively obtained using MEFM. The outcomes indicate that the MEFM is a highly efficient mathematical approach for solving NPDEs. The solutions acquired were verified using the Mathematica program, and visual representations in the form of two-dimensional and three-dimensional graphs, as well as density and contour plots, were generated using proper parameters.

ACKNOWLEDGEMENTS

We would like to thank the referees for their contributions.

CONFLICT OF INTEREST

The authors stated that there are no conflicts of interest regarding the publication of this article.

AUTHORSHIP CONTRIBUTIONS

Autors' contributions are equal.

REFERENCES

- [1] Hossain AKS, Akbar MA. Closed form solutions of two nonlinear equation via the enhanced (G'/G) expansion method. Cogent Mathematics and Statistics, 2017, 4(1), 1355958.
- [2] Akturk T, Bulut H, Gurefe Y. An application of the new function method to the Zhiber-Shabat equation. An International Journal of Optimization and Control: Theories & Applications, 2017, 7(3), 271-274.
- [3] Baskonus HM, Bulut H. New hyperbolic function solutions for some nonlinear partial differential equation arising in mathematical physics. Entropy, 2015, 17(2015), 4255-4270.
- [4] Chen Y, Yan Z. New exact solutions of $(2+ 1)$ -dimensional Gardner equation via the new sine-

- Gordon equation expansion method. *Chaos, Solitons & Fractals*, 2005, 26(2), 399-406.
- [5] Dubrovsky VG, Lisitsyn YV. The construction of exact solutions of two-dimensional integrable generalizations of Kaup–Kuperschmidt and Sawada–Kotera equations via ∂^{-} -dressing method. *Physics Letters A*, 2002, 295(4), 198-207.
- [6] Mohiud-Din ST. Homotopy perturbation method for solving fourth-order boundary value problems, *Math. Prob. Engr.*, 2007, 2007, 1-15. doi:10.1155/2007/98602.
- [7] Baskonus HM, Bulut H, Atangana A. On the complex and hyperbolic structures of the longitudinal wave equation in a magneto-electro-elastic circular rod. *Smart Materials and Structures*, 2016, 25(3), 035022.
- [8] Xu F. Application of Exp-function method to symmetric regularized long wave (SRLW) equation. *Physics Letters A*, 2008, 372(3), 252-257.
- [9] Kumar D, Kaplan M. New analytical solutions of (2+1) dimensional conformable time-fractional Zoomeron equation via two distinct techniques, *Chinese J. Phys.*, 2018, 53, 2173-2185.
- [10] Baskonus HM, Bulut H, Sulaiman TA. Investigation of various travelling wave solutions to the extended (2+1)-dimensional quantum ZK equation. *The European Physical Journal Plus*, 2017, 132(11), 482.
- [11] Shen G, Sun Y, Xiong Y. New travelling-wave solutions for Dodd-Bullough equation. *Journal of Applied Mathematics*, 2013, 2013, 1-5.
- [12] Naher H, Abdullah FA. New approach of (G'/G)-expansion method and new approach of generalized (G'/G)-expansion method for nonlinear evolution equation. *American Institute of Physics Advances*, 2013, 3(3), 032116.
- [13] Gao W., Rezazadeh H, Pinar Z, Baskonus HM, Sarwar, Yel G. Novel explicit solutions for the nonlinear Zoomeron equation by using newly extended direct algebraic technique. *Optical and Quantum Electronics*, 2020, 52, 1-13.
- [14] Hosseini K, Korkmaz A, Bekir A, Samadani F, Zabihi A, Topsakal M. New wave form solutions of nonlinear conformable time-fractional Zoomeron equation in (2+ 1)-dimensions. *Waves in Random and Complex Media*, 2021, 31(2), 228-238.
- [15] Demirbilek U, Ala V, Mamedov KR. Exact solutions of conformable time fractional Zoomeron equation via IBSEFM. *Applied Mathematics-A Journal of Chinese Universities*, 2021, 36, 554-563.



RESEARCH ARTICLE

SYNTHESIS OF ALUMINA FROM KAOLIN FOUND IN AJEBO, OGUN STATE, NIGERIA

Henry Ekene MGBEMERE ¹ and Chiedozi Valentine OLUIGBO ^{2,*} 

¹Department of Metallurgical and Materials Engineering, School of Engineering, University of Lagos, Lagos State, Nigeria

²Department of Welding and Fabrication Engineering Technology, School of Engineering, Federal Polytechnic Ilaro, Ogun State, Nigeria

ABSTRACT

This study proposes the utilization of kaolin as an alternate resource for alumina production due to the decreasing availability of bauxite ores in Nigeria. This project covers the procedures and operations required to produce a high surface area γ -alumina using kaolin, a refractory material. The kaolin used in this study was sourced from Ajebo in Ogun State, Nigeria. The mineral processing of kaolin was the initial step involving removing inherent impurities from the clay. Subsequently, calcination was performed to eliminate crystallised water and impurities and activate the kaolin's limited alumina content. This activation process facilitated the subsequent acid-leaching reactions. At 90°C, 5M HCl acid was used to leach meta-kaolin, which was then filtered. The filtrate was mixed with 5M NaOH at 90°C and was transformed into sodium aluminate. This reaction also facilitated the removal of magnesium and iron hydroxides. Subsequently, HCl was introduced to adjust the pH of the solution. The resulting aluminium hydroxide was then calcinated at temperatures of 700°C and 900°C for 2 hours each to produce γ -alumina. Ultimately, the calcined material was cooled to ambient temperature inside the furnace. The produced γ -alumina was further characterised using X-ray Fluorescence (XRF), Fourier Transform Infrared spectrometer (FTIR), and Scanning Electron Microscopy (SEM).

Keywords: Alumina, Calcination, Kaolin, Leaching, Synthesis

1. INTRODUCTION

The growing global demand for alumina has raised interest in exploring alternate technologies for its production from low-grade ores. Certain low-cost minerals have been identified as viable and economically feasible resources for aluminium, making them suitable for alumina production by synthesis. Several minerals in this category include kaolin, mica, bauxite, sillimanite, fly ash, andalusite, alunite, and kyanite. Among the several minerals examined, it is worth noting that bauxite emerges as a notable source of alumina, albeit with a marked scarcity [1]. Bauxite, the primary raw material used in the Bayer process to produce alumina, is found in limited quantities globally, including Nigeria. The scarcity of bauxite implies a significant demand for kaolin as a viable substitute for the manufacturing of alumina [2]. Kaolin emerges as a particularly appealing option for the manufacture of alumina compared to other types of clays, primarily owing to its higher aluminum concentration. Kaolin is mainly composed of kaolinite, which has a chemical composition of $\text{Al}_2\text{O}_3 \cdot 2\text{SiO}_2 \cdot 2\text{H}_2\text{O}$ and is characterised by its two-layer silicate structure [3]. Kaolin is a low-cost, naturally occurring substance with a high silica and alumina concentration, making it a suitable substitute for bauxite ore. However, because kaolin is inert and inactive, it must be activated to become active kaolin, which is accomplished by calcination [4].

Aluminium oxide, or alumina (Al_2O_3), can occur in several intermediate phases, contingent upon the specific precursor and procedures employed during processing [5]. The most thermodynamically stable form of alumina is known as α -alumina, which is commonly utilized as a ceramic material. The term "transitional aluminas" is used to refer to other phases of alumina, of which gamma(γ)-alumina is a

*Corresponding Author: olu7wonders@yahoo.com

Received: 13.10.2023 Published: 28.03.2024

crucial example [6]. Gamma-alumina has exceptional characteristics such as high purity, excellent dispersion, and a specific surface area. It possesses resilience to elevated temperatures and inert properties, making it highly suitable for many applications [7]. Wang *et al.* [8] conducted a study that found γ -alumina to have more excellent thermodynamic stability than α -alumina, mainly when a critical surface area is achieved. Due to its porous nature and remarkable activity, γ -alumina is commonly employed as an adsorbent and catalyst support [9].

Kaolin has been used to synthesize alumina in various studies. Ibrahim *et al.* [10] used a low-cost kaolin to extract γ -alumina by employing a combination approach for producing alumina particles from local kaolin. The method consisted of a two-step process: calcination at 700°C using sodium chloride and leaching using sulfuric and hydrochloric acids, yielding 79.28% pure alumina. In a study conducted by Hosseini *et al.* [11], synthesizing γ -alumina from kaolin was achieved by subjecting kaolin to a calcination process at 800°C for 2 hours, resulting in the transformation of kaolin into meta-kaolin. The synthesis of γ -alumina powder then involved the extraction of alumina from meta-kaolin via a reaction with H_2SO_4 . Subsequently, the resulting aluminium sulfate precipitated in ethanol. The aluminium sulfate was dried and subsequently subjected to calcination at 900°C for 2 hours, which led to the formation of γ -alumina. A similar procedure was reported by Kshash and Baha'a [12]. Bawa *et al.* [13] and Salahudeen *et al.* [14] described the synthesis of γ -alumina from Kankara kaolin. The hydrothermal process was used by Bawa *et al.* [13] to synthesize γ -alumina from kaolin. The alumina was obtained through the thermal processing of ammonium alum produced from the filtrate of dealuminated metakaolin. At 800°C calcination temperature and 3 hours soaking, crystalline aluminium sulfate with 39 wt. % Al_2O_3 was produced, while γ -alumina was produced after 3 hours of soaking at 850°C. However, Salahudeen *et al.* [14] used a simple three-step dealumination, precipitation, and calcination method. The kaolin underwent a wet beneficiation process, followed by metakaolinization and dealumination. The precipitation of amorphous aluminium hydroxide from aluminium sulfate was achieved by utilizing a sodium hydroxide solution. The generated aluminum hydroxide underwent thermal processing at various calcination temperatures ranging from 300°C to 900°C. Subsequently, at 900°C, a complete formation of the γ -alumina phase was identified.

Tantawy and Alomari [15] describe using hydrochloric and sulfuric acids to produce alumina from kaolin through acid leaching. The kaolin sample underwent calcination at 850°C. Subsequently, it was subjected to leaching using a 6 M acid solution at 90°C. This was followed by adding 5.0 M NaOH and HCl solutions to the leaching solution. The resulting precipitated aluminium hydroxide was then transformed into alumina through calcination at a temperature of 900°C. However, Yang *et al.* [16] describe synthesizing nanosized γ - Al_2O_3 using acid-leachates from calcined kaolin. The precipitation of Aluminium (hydro)oxide occurred with the addition of ammonia to the leachate, facilitated by its inclusion of polyethylene glycol. After calcination, a fine white powder consisting of nanosized γ - Al_2O_3 particles was successfully produced. On the other hand, Park *et al.* [17] synthesized alumina powders from kaolin with 1.0 M H_2SO_4 solution via alumina extraction processes with and without ultrasound and found that the utilization of ultrasound during the synthesis of Al_2O_3 powders proved to be an effective method for reducing the required synthesis time.

This current study utilized kaolin, a readily available and cost-effective mineral in Nigeria, as the primary material for the synthesis of alumina. This study aims to synthesize γ -alumina with a high surface area using kaolin sourced from Ajebo in Ogun State, Nigeria.

2. MATERIALS AND METHODS

Figure 1 describes the methodology involved in the production of alumina from kaolin.

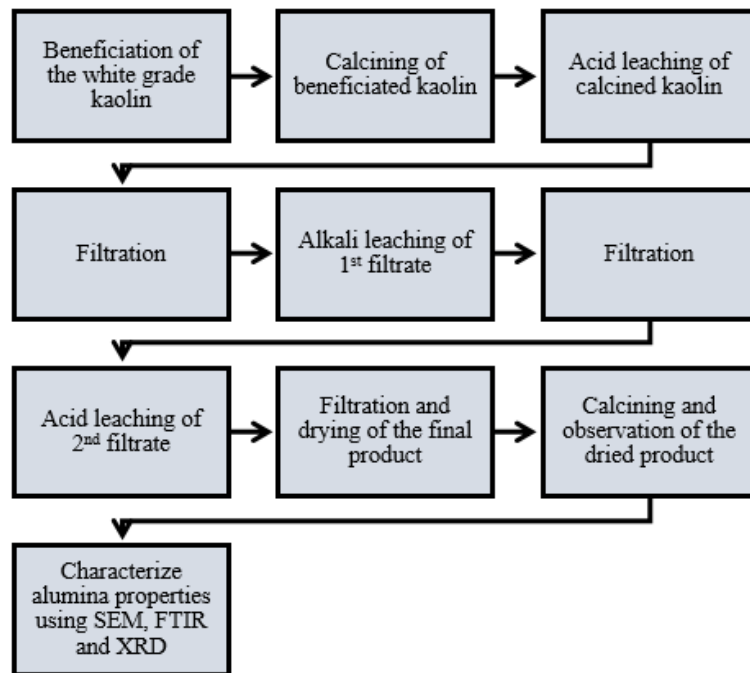


Figure 1. A schematic representation illustrating the sequential steps involved in the production of alumina from kaolin.

2.1. Sample Preparation and Characterisation

The kaolin clay was collected in lumps from Ajebo in Ogun State, Nigeria. Afterward, it was crushed and pulverised to smaller sizes using a milling machine. The powdered clay was soaked in water for forty-eight hours. This enabled easy separation of the fine clay particles that are physically bonded and may not disintegrate by mere vibration. The decantation process was carried out to reduce water content before wet sieving. Wet sieving was done to optimize the properties with a sieve of finer mesh size (100 μm) to avoid near misses of impurities in the clay. Wet sieving aims to separate fine clay particles still bonded to the surfaces of sand particles and other impurities in the batch. A suspension of clay and water was the result of wet sieving. The clay particles, which were initially dispersed, were allowed to settle, after which the water left above was decanted. After the decantation of water, the leftover clay slurry was dried and pulverised. The dried kaolin was calcined in the Vecstar heat treatment furnace, Model LF3, at a temperature of 750°C for 2 hours. It was cooled to room temperature in the furnace to obtain the metakaolin phase. Calcination was performed to eliminate the presence of crystallized water and impurities and to activate the small amount of alumina in the kaolin, activating this layer for the leaching with acid reactions.

The calcined kaolin 20 g was mixed with 200 ml of 5M hydrochloric acid in a 250 ml round bottom flask. The mixture in a round bottom flask attached to a reflux condenser was heated to 90°C and stirred at 500 rpm for 3 hours using a Stuart Hot Plate and Stirrer Model No. UC152. The reflux condenser was used to minimize the acid loss; stirring was done to have a homogenous mixture and speed up the kaolin bond's breaking. The slurry produced was diluted with 200 ml distilled water and filtered using a funnel and Whatman filter paper of Cat No. 1001125. The filtrate was a golden yellow solution, while the residue was cream-like powder. Distilled water was used to wash the dealuminated residue and dried at 100°C in the laboratory oven. A second leaching stage was done by heating the filtrate to 90°C in an Electrotherm EM 250 heating mantle. Afterward, the filtrate was mixed with an excess 5M Sodium hydroxide solution at 90°C. It was transformed into sodium aluminate to aid the separation of the hydroxides of magnesium and iron. A cloudy solution was formed with the addition of excess sodium hydroxide. The resulting mixture, when filtered, yielded a colourless solution, and the residue was

brownish. After filtration, 5M HCl was mixed with the sodium aluminate while stirring to bring the pH to 7 using pH Meter Model PHS – 25. The aluminium hydroxide produced was filtered and dried at 120°C in the laboratory oven for 24 hours. The aluminium hydroxide produced was divided into two portions, calcined at temperatures of 700°C and 900°C for 2 hours, and cooled to room temperature inside the furnace to obtain alumina. The samples were characterised using Scanning Electron Microscope (SEM), X-ray Fluorescence (XRF), X-ray Diffractometry (XRD), and Fourier Transform Infrared (FTIR).

3. RESULTS AND DISCUSSION

3.1. Compositional Analysis

Table 1 presents the chemical analysis by XRF of raw kaolin and processed alumina at temperatures of 700°C and 900°C, illustrating the amounts and types of constituents. Based on the data presented in the table, a substantial amount of the gangue in the kaolin sample was eliminated during the calcination process and subsequent acid leaching. This resulted in the production of the final alumina product, which underwent calcination at temperatures of 700°C and 900°C. Alumina had a purity of 82.32% and 82.91% after the final calcination at 700°C and 900°C, respectively. These values are roughly comparable to the chemical composition of commercial gamma-alumina, which is 89.80% [7]. However, they are higher than the 79.28% alumina extraction observed by Ibrahim *et al.* [10] and comparable to the 85.02% value obtained by Bawa *et al.* [12] for alumina synthesized from kankara kaolin.

Table 1. Chemical composition of kaolin, processed alumina at 700°C and 900°C.

Compound	Concentration Weight %		
	kaolin	alumina (700°C)	alumina (900°C)
Al ₂ O ₃	36.11	82.32	82.91
SiO ₂	57.492	15.63	15.07
CaO	2.043	0.24	0.29
TiO ₂	2.246	0.09	0.09
Fe ₂ O ₃	0.519	0.21	0.13
P ₂ O ₅	0.385	1.07	1.39
LOI	1.040		

3.2. X-Ray Diffraction

XRD analysis was conducted to characterise the sample's phase and crystal structure. Different peaks at various crystallite sizes indicate alumina phases or crystal shape anisotropy (e.g., preferred development in particular directions). Using the Debye-Scherrer formula, the average crystallite size (D, nm) of the alumina sample was calculated;

$$D = \frac{0.9\lambda}{\beta \cos \theta} \quad (1)$$

Where 0.9 is Scherrer's constant, λ is the wavelength of X-ray radiation, β is the full width at half maximum (FWHM) of the diffraction peak, and θ is the Bragg diffraction angle.

At 700°C, the average crystallite size of calcined alumina is estimated to be 1.18 nm, while at 900°C, it is estimated to be 1.46 nm. This may be attributed to a high temperature of calcination, which increased atomic mobility, causing grain growth and consequently yielding improved crystallinity.

The XRD patterns for alumina powder made by calcination at 700°C and 900°C are displayed in Figure 2. As the calcination temperature increased, it was observed that the diffraction patterns became slightly

clearer and had higher peak intensities. Additionally, the diffraction pattern of the alumina powder at 900°C shows narrow peaks, indicating a high degree of crystallinity. An increase in calcination temperature would also cause a change in some diffraction peaks from γ - to α -alumina. The XRD pattern seen below reveals the presence of several amorphous phases that are distinguished by low peaks.

The JCPDS file exhibited a congruence with the X-ray diffractogram provided by [11], confirming the presence of γ -alumina at low and high calcination temperatures. The characteristic peaks of γ -alumina are $2\theta = 716.67^\circ$, $2\theta = 550^\circ$, $2\theta = 433.33^\circ$, $2\theta = 400^\circ$, and $2\theta = 283.33^\circ$. The findings of the analysis are depicted in Figure 2.

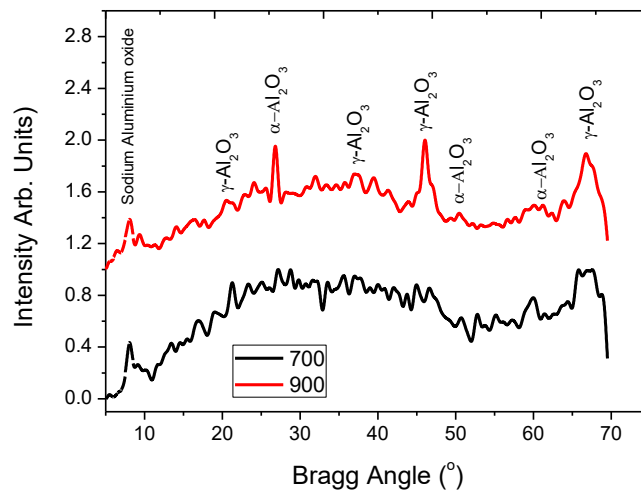


Figure 2. The XRD patterns for the gamma-alumina processed at 700°C and 900°C.

3.3. Fourier Transform Infrared Spectroscopy (FTIR)

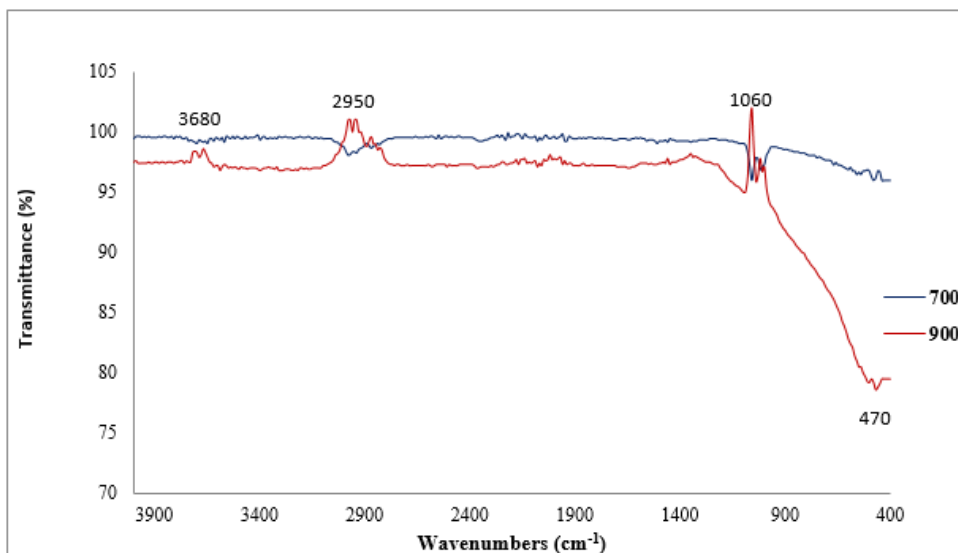


Figure 3. The FTIR spectra of gamma-alumina processed at 700°C and 900°C.

The observed result demonstrates the presence of an absorption peak within the mid-infrared (mid-IR) region spanning from 400 cm⁻¹ to 4000 cm⁻¹. This peak identifies the chemical bonds and functional

groups within the compound. The spectra region involves a lot of essential stretch modes. An FTIR spectrum alumina's Figure 3 showed the distinctive peak at 470 cm^{-1} wavenumber, which can be attributed to the stretching vibration of the Al-O band in alumina. The absorption peak within the 1060 cm^{-1} wavenumber increased when the calcination temperature was raised from 700°C to 900°C , as can be seen. This wavenumber corresponds to the symmetric bending of the Al-O-H bond [18]. The wavenumber around 2950 cm^{-1} could be associated with C-H bonds from organic remains observed in the calcined samples. The O-H vibrational mode is found around 3680 cm^{-1} . This could be ascribed to the rapid adsorption of water molecules in the environment. Generally, it was observed that raising the calcination temperature from 700°C to 900°C decreases the absorption peak except for the peaks at 1060 cm^{-1} and 2950 cm^{-1} corresponding to the alumina produced at the calcination temperature of 900°C .

3.4. Scanning Electron Microscopy (SEM)

The SEM micrographs for the 700°C and 900°C processed alumina is shown in Figure 4.

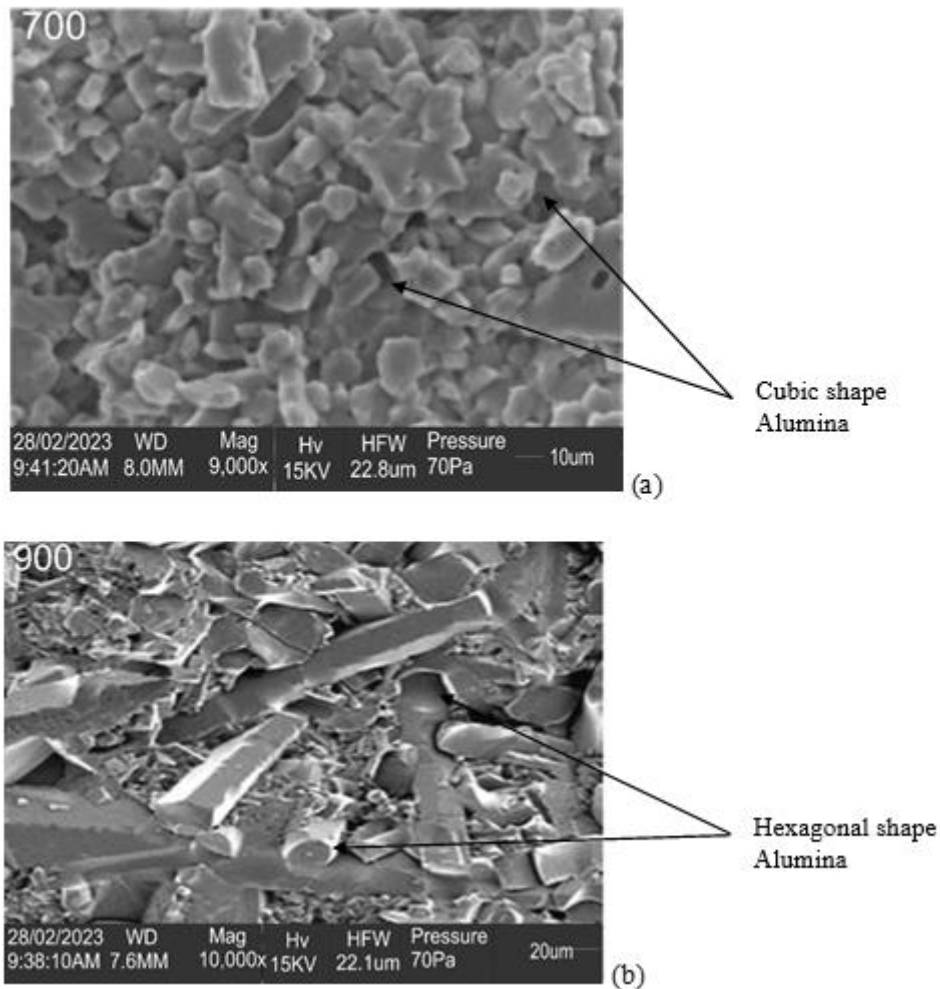


Figure 4. SEM images of gamma-alumina (a) calcined at 700°C (b) calcined at 900°C .

The SEM was employed to analyze and characterise the morphology of the material. The morphology of the alumina changes as the temperature increases from 700°C to 900°C during calcination. The Figure 4(b) micrograph of processed γ -alumina reveals the presence of rod-like hexagonal structures in the sample that underwent calcination at 900°C . This is in contrast to Figure 4(a), which shows the cubic-

shaped γ -alumina sample that was calcined at 700°C. A lesser fraction of tubular crystals is also observed at 700°C. The SEM image further indicates the presence of tiny amorphous particles alongside the crystalline ones in Figure 4(b).

4. CONCLUSION

This study extracted alumina from kaolin by leaching with hydrochloric acid and sodium hydroxide. The alumina hydroxide produced underwent calcination at temperatures of 700°C and 900°C, and the final γ -alumina produced was characterised using FTIR, XRD, and SEM. Based on the findings above and analysis, it can be established that:

- There is a considerable increase in the proportion of the alumina obtained from 36.11 wt. % to 82.32 wt. % and 82.91 wt. % at temperatures of 700°C and 900°C, respectively, which are suitable for the production of aluminum metal.
- The morphology of the alumina changes as the calcination temperature changes from 700°C to 900°C with a small number of amorphous particles alongside the crystalline ones.
- As displayed in the FTIR, the absorption peak decreases except for the peaks at 1060 cm^{-1} and 2950 cm^{-1} corresponding to the alumina produced during the calcination process at a temperature of 900°C when the calcination temperature is increased from 700°C to 900°C.
- At higher temperatures, the crystallite sizes were bigger, indicating a higher degree of crystallinity.

CONFLICT OF INTEREST

The authors stated that there are no conflicts of interest regarding the publication of this article.

AUTHORSHIP CONTRIBUTIONS

Henry Ekene Mgbemere: Conceptualization, Original draft data analysis, Graphing and Review.

Chiedozie Valentine Oluigbo: Investigation, Formal analysis, Graphing, Writing – review and editing.

REFERENCES

- [1] Kianinia Y, Darban AK, Taheri-Nassaj E, Rahnama B, Fotoutan A. Synthesis of nano-size mesoporous γ - Al_2O_3 powder from domestic Hamedan kaolin. *Iranian Journal of Materials Science & Engineering* 2015;12(1).
- [2] Aderemi BO, Ajayi OA. Sourcing Aluminium from Kaolin Clay for Metallurgical Industry. In *Proceedings of Nigerian Materials Congress 2009*; 104-107.
- [3] Rahayu ES, Subiyanto G, Imanuddin A, Nadina S, Ristiani R, Yuniarti E. Kaolin as a source of silica and alumina for synthesis of zeolite γ and amorphous silica alumina. In *MATEC Web of conferences 2018 (Vol. 156, p. 05002)*. EDP Sciences.
- [4] Bagherzadeh Y, Golmakani MH, Karimi EZ. Straight synthesis of α and γ alumina from kaolin by HCl acid leaching. *Journal of Mining and Metallurgy, Section B: Metallurgy*. 2023(00):17-.
- [5] Bhattacharyya S, Behera PS. Synthesis and characterization of nano-sized α -alumina powder from kaolin by acid leaching process. *Applied Clay Science*. 2017;146:286-90.

- [6] Bawa SG, Ahmed AS, Okonkwo PC. The Study of Thermal Effect on the Surface Properties of Gamma-Alumina Synthesized from Kankara Kaolin. *Nigerian Journal of Technology*. 2016;35(1):66-70.
- [7] Paranjpe KY. Alpha, Beta and Gamma Alumina as a catalyst - A Review. *The Pharma Innovation Journal*. 2017; 6(11): 236-238.
- [8] Wang Y, Wang J, Shen M, Wang W. Synthesis and properties of thermostable γ -alumina prepared by hydrolysis of phosphide aluminium. *Journal of Alloys and Compounds*. 2009;467(1-2):405-12.
- [9] Said S, Mikhail S, Riad M. Recent processes for the production of alumina nano-particles. *Materials Science for Energy Technologies*. 2020;3:344-63.
- [10] Ibrahim KM, Moumani MK, Mohammad SK. Extraction of γ -alumina from low-cost kaolin. *Resources*. 2018;7(4):63.
- [11] Hosseini SA, Niaei A, Salari D. Production of γ -Al₂O₃ from kaolin. *Open Journal of Physical Chemistry*. 2011; 25;1(02):23-7.
- [12] Kshash JM, Baha'a AS. Preparation of nanogama alumina from Iraqi kaolin. *Iraqi Bulletin of Geology and Mining*. 2018;14(1):121-30.
- [13] Bawa SG, Ahmed AS, Okonkwo PC. Synthesis of gamma-alumina from Kankara kaolin as potential zeolite active matrix. *Nigerian Journal of Basic and Applied Sciences*. 2016;24(2):66-72.
- [14] Salahudeen N, Ahmed AS, Ala'a H, Dauda M, Waziri SM, Jibril BY. Synthesis of gamma alumina from Kankara kaolin using a novel technique. *Applied Clay Science*. 2014;105:170-7.
- [15] Tantawy MA, Alomari AA. Extraction of alumina from Nawan kaolin by acid leaching. *Oriental Journal of Chemistry*. 2019;35(3):1013.
- [16] Yang H, Liu M, Ouyang J. Novel synthesis and characterization of nanosized γ -Al₂O₃ from kaolin. *Applied Clay Science*. 2010;47(3-4):438-43.
- [17] Park JH, Kim SW, Lee SH, Kim HS, Park SS, Park HC. Synthesis of Alumina Powders from Kaolin with and without Ultrasounds. *Journal of Materials Synthesis and Processing*. 2002;10:289-93.
- [18] Farahmandjou M, Golabiyan N. Synthesis and characterisation of Al₂O₃ nanoparticles as catalyst prepared by polymer co-precipitation method. *Materials Engineering Research*. 2019;1(2):40–44.



RESEACRH ARTICLE

THE NOVEL CONFORMABLE METHODS TO SOLVE CONFORMABLE TIME-FRACTIONAL COUPLED JAULENT-MIODEK SYSTEM

Özkan AVİT¹ , Halil ANAÇ^{2,*} 

¹ Graduate Education Institute, Gumushane University, Gumushane, Turkey

² Torul Vocational School, Gumushane University, Gumushane, Turkey

ABSTRACT

This research utilizes two novel methods, specifically the conformable q-homotopy analysis transform method (Cq-HATM) and the conformable Elzaki Adomian decomposition method (CEADM), to examine the numerical solutions for the conformable time-fractional coupled Jaulent-Miodek system. One of the two unique methods proposed is the Cq-HATM, which is a hybrid approach that combines the q-homotopy analysis transform method with the Laplace transform, employing the concept of conformable derivative. The CEADM method, similar to the aforementioned approach, is a hybrid technique that combines the Adomian decomposition method with Elzaki transform using the concept of conformable derivative. The computer simulations were performed to offer validation for the effectiveness and dependability of the recommended approaches. After conducting a comparison between the exact solutions and the solutions acquired using the unique methods, it is apparent that both of these approaches demonstrate simplicity, effectiveness in tackling nonlinear conformable time-fractional coupled systems.

Keywords: Conformable time-fractional coupled Jaulent-Miodek system, Conformable Elzaki Adomian decomposition method, Conformable Elzaki transform

1. INTRODUCTION

The field of fractional calculus has been subject to substantial research and has been rigorously defined by a multitude of eminent scientists [1-3]. Scientists have established the essential framework for the discipline of fractional analysis. Then, the innovative conceptualizations of fractional calculus have been developed. Fractional partial differential equations are commonly utilized to develop nonlinear models and to analyse of dynamical system [4-6]. The application of fractional calculus has been employed to examine and investigate various domains, including chaos theory, financial models, disordered environments, and optics. The identification and analysis of nonlinear phenomena in the natural world are strongly dependent on the utilization of solutions derived from fractional differential equations [7-9]. A wide array of analytical and numerical approaches are utilized to get exact solutions for fractional differential equations that encompass nonlinear phenomena, owing to their intrinsic complexity [10-11].

In a recent scholarly paper, the innovative of fractional derivative and fractional integral have been presented. The authors have effectively shown that the recently introduced definition possesses the inherent attributes of the classical derivative as defined in classical analysis, while also incorporating a limit form that closely resembles the definition of the classical derivative. The author presents a new conceptualization of the fractional derivative in his scholarly contribution. The provided definition encompasses a range of mathematical ideas, such as the product rule, quotient rule, chain rule, fractional Rolle's theorem, and fractional mean value theorems. The application of the conformable fractional derivative is considered to be a fundamental and highly beneficial methodology. Moreover, it enhances our capacity to express the behavior demonstrated by concrete entities. The application of the conformable

*Corresponding Author: halilanac0638@gmail.com

Received: 23.10.2023

Published: 28.03.2024

fractional derivative represents a novel methodology for tackling complex problem domains. Fractional order models are frequently utilized in the domain of engineering and applied sciences owing to their capacity to provide a more accurate depiction of real-world occurrences. Conformable fractional derivatives have been utilized by numerous scholars from diverse academic disciplines. The application of the conformable fractional operator functions as a strategy to address certain constraints inherent in current fractional operators. The issue under consideration encompasses a collection of mathematical topics, including the mean value theorem, the chain rule, the product rule for differentiating two functions, the derivative of the quotient of two functions, and Rolle's theorem [12].

The Elzaki transform method (ETM), first proposed by Elzaki, has been employed for the resolution of linear ordinary differential equations featuring constant coefficients [13]. Elzaki utilized the differential transform method in combination with the Elzaki transform (ET) to tackle various nonlinear differential equations [14]. The Homotopy Perturbation Elzaki Transform Method (HPETM) was originally proposed by Elzaki and Hilal. In addition, HPETM has effectively resolved three nonlinear partial differential equations (PDEs) [15]. In their study, Elzaki and Kim utilized an innovative hybrid method that integrates the ET with the modified variational iteration method in order to address the radial diffusivity and shock wave equations [16-17]. In [13], Aggarwal et al. utilized ET in order to derive the solutions for linear Volterra integral equations of the first kind. However, HPETM was employed by Jena and Chakraverty in order to derive a solution for the system of time-fractional Navier-Stokes equations [18].

Nevertheless, it is crucial to acknowledge that the fractional order possesses the capacity to manifest both time and space [19-23]. The subject matter at hand concerns the progressive domain of fractional partial differential equations (FPDEs), which contain variable order fractional operators [30-31, 33]. A plethora of rigorous numerical approaches have been developed and recorded in academic literature, with significant contributions from respected scholars in the field. Numerous methods have been put up in scholarly works to address mathematical quandaries. The methods encompassed in this set of techniques consist of the Adomian Decomposition Method (ADM) [37], the Homotopy Analysis Method (HAM) [35], the Homotopy Perturbation Method (HPM) [27-29], the Collocation Method [38], the Sumudu Transform Method (STM) [36], the Differential Transformation Method (DTM) [24-25, 32, 34], and the Variational Iteration Method (VIM) [26].

The main aim of this study is to obtain novel numerical solutions for the conformable time-fractional coupled Jaulent-Miodek system using the conformable q-homotopy analysis transform method (Cq-HATM). The secondary aim of the research is to obtain novel numerical solutions for the conformable time-fractional coupled Jaulent-Miodek system with using the conformable Elzaki Adomian decomposition method (CEADM).

The following is a comprehensive list of the remaining components of the study. The fundamental principles that form the basis of conformable fractional calculus and the Elzaki transform is presented in Section 2. In Section 3, new conformable numerical methods are presented. In Section 4, an illustrated example of the conformable time-fractional coupled Jaulent-Miodek system is shown. The results are given in Section 5.

2. MATERIAL AND METHOD

This section provides some fundamental definitions.

Definition 2.1. [12, 39-41] Let a function $g: [0, \infty) \rightarrow \mathbb{R}$. Then, the conformable fractional derivative of g order α is defined as

$$T_{\alpha}(g)(x) = \lim_{\varepsilon \rightarrow 0} \frac{g(x + \varepsilon x^{1-\alpha}) - g(x)}{\varepsilon}, \alpha \in (0, 1]. \quad (2)$$

for all $x > 0$.

Theorem 2.1. [12, 39-41] Let $\alpha \in (0, 1]$ and g, h be α -differentiable at a point $x > 0$. Then

$$(i) T_\alpha(ag + bh) = aT_\alpha(g) + bT_\alpha(h), \text{ for all } a, b \in \mathbb{R}, \tag{3}$$

$$(ii) T_\alpha(x^p) = px^{p-1}, \text{ for all } p \in \mathbb{R}, \tag{4}$$

$$(iii) T_\alpha(\lambda) = 0, \text{ for all constant functions, } f(t) = \lambda, \tag{5}$$

$$(iv) T_\alpha(gh) = gT_\alpha(h) + hT_\alpha(g), \tag{6}$$

$$(v) T_\alpha\left(\frac{g}{h}\right) = \frac{hT_\alpha(g) - gT_\alpha(h)}{h^2}. \tag{7}$$

Definition 2.2. [42] Let $0 < \alpha \leq 1$, $g: [0, \infty) \rightarrow \mathbb{R}$ be function. Then, the conformable fractional Elzaki transform (CFET) of order α of g is described as

$${}_cE_\alpha[g(t)] = T_\alpha(v) = \int_0^\infty pK_\alpha(-p, t)g(t)d_\alpha t, \tag{8}$$

where $K_\alpha(-p, t) = E_\alpha\left(-\frac{1}{p}, t\right), p > 0$.

Definition 2.3. [42] Let $0 < \alpha \leq 1$, $g: [0, \infty) \rightarrow \mathbb{R}$ be real function. The CFET for the conformable fractional derivative of the function $g(t)$ is defined as

$${}_cE_\alpha[T_\alpha g(t)](p) = \frac{1}{p} {}_cE_\alpha[g(t)](p) - pg(0). \tag{9}$$

Definition 2.4. [45] Assume that $0 < \alpha \leq 1$, $g: [0, \infty) \rightarrow \mathbb{R}$ be real function. The conformable fractional Laplace transform of order α of g is defined by

$$\mathcal{L}_\alpha[g(t)](s) = F_\alpha(s) = \int_0^\infty E_\alpha(-s, t)g(t)d_\alpha t,$$

where E_α is Mittag-Leffler function.

2.1. The Novel Numerical Techniques

The part provides an introduction to Cq-HATM and CEADM.

2.1.1. Conformable q-homotopy analysis transform method

Now, we will present a new method. Consider the conformable time-fractional order nonlinear partial differential equation (CTFNPDE) to give the main idea of Cq-HATM:

$${}_tT_\alpha u(x, t) + Au(x, t) + Hu(x, t) = h(x, t), t > 0, n - 1 < \alpha \leq n, \tag{10}$$

where A is a linear operator, H is a nonlinear operator, $h(x, t)$ is a source term, and ${}_tT_\alpha$ is a conformable fractional derivative of order α .

Now, by performing conformable Laplace transform (CLT) on Eq. (10) and using initial condition, then we get

$$s\mathcal{L}_\alpha[u(x, t)] - u(x, 0) + \mathcal{L}_\alpha[Au(x, t)] + \mathcal{L}_\alpha[Hu(x, t)] = \mathcal{L}_\alpha[h(x, t)]. \tag{11}$$

If we simplify the Eq. (11), then we have

$$\mathcal{L}_\alpha[u(x, t)] - \frac{1}{s}u(x, 0) + \frac{1}{s}\mathcal{L}_\alpha[Au(x, t)] + \frac{1}{s}\mathcal{L}_\alpha[Hu(x, t)] - \frac{1}{s}\mathcal{L}_\alpha[h(x, t)] = 0. \tag{12}$$

We define the nonlinear operator by the assist of HAM for real function $\varphi(x, t; q)$ as follows

$$N[\varphi(x, t; q)] = \mathcal{L}_\alpha[\varphi(x, t; q)] - \frac{1}{s}\varphi(x, t; q)(0^+) + \frac{1}{s}(\mathcal{L}_\alpha[A\varphi(x, t; q)] + \mathcal{L}_\alpha[H\varphi(x, t; q)] - \mathcal{L}_\alpha[h(x, t)]), \tag{13}$$

where $q \in [0, \frac{1}{n}]$.

We establish a homotopy in the following:

$$(1 - nq)\mathcal{L}_\alpha[\varphi(x, t; q) - u_0(x, t)] = hqH^+(x, t)H[\varphi(x, t; q)], \tag{14}$$

where, $h \neq 0$ is an auxiliary parameter and \mathcal{L}_α represents conformable Laplace transform. For $q = 0$ and $q = \frac{1}{n}$, the results in Eq. (14) are respectively provided:

$$\varphi(x, t; 0) = u_0(x, t), \varphi(x, t; \frac{1}{n}) = u(x, t). \tag{15}$$

Therefore, by amplifying q from 0 to $\frac{1}{n}$, then the solution $\varphi(x, t; q)$ converges from $u_0(x, t)$ to the solution $u(x, t)$. Employing the Taylor theorem around q and expanding $\varphi(x, t; q)$ and then, we obtain

$$\varphi(x, t; q) = u_0(x, t) + \sum_{m=1}^{\infty} u_m(x, t)q^m, \tag{16}$$

where

$$u_m(x, t) = \frac{1}{m!} \frac{\partial^m \varphi(x, t; q)}{\partial q^m} \Big|_{q=0}. \tag{17}$$

Eq. (16) converges at $q = \frac{1}{n}$ for the appropriate $w_0(x, t)$, n and h . Then, we have

$$u(x, t) = u_0(x, t) + \sum_{m=1}^{\infty} u_m(x, t) \left(\frac{1}{n}\right)^m. \tag{18}$$

If we differentiate the zeroth order deformation of Eq. (14) m –times with respect to q and we divide by $m!$, respectively, then for $q = 0$, we obtain

$$\mathcal{L}_\alpha[u_m(x, t) - k_m u_{m-1}(x, t)] = hH^+(x, t)\mathcal{R}_m(\vec{u}_{m-1}), \tag{19}$$

where the vectors are defined by

$$\vec{u}_m = \{u_0(x, t), u_1(x, t), \dots, u_m(x, t)\}. \tag{20}$$

When we apply to the inverse CLT to Eq. (19), then we obtain

$$u_m(x, t) = k_m u_{m-1}(x, t) + h\mathcal{L}_\alpha^{-1}[H^+(x, t)\mathcal{R}_m(\vec{u}_{m-1})], \tag{21}$$

where

$$\begin{aligned} \mathcal{R}_m(\vec{u}_{m-1}) = \mathcal{L}_\alpha[u_{m-1}(x, t)] - \left(1 - \frac{k_m}{n}\right)\frac{1}{s}u_0(x, t) + \frac{1}{s}\mathcal{L}_\alpha[Au_{m-1}(x, t) + H_{m-1}(x, t) \\ - h(x, t)], \end{aligned} \tag{22}$$

and

$$k_m = \begin{cases} 0, & m \leq 1, \\ n, & m > 1. \end{cases} \tag{23}$$

where, H_m^+ is homotopy polynomial and presented as

$$H_m^+ = \frac{1}{m!} \frac{\partial^m \varphi(x, t; q)}{\partial q^m} \Big|_{q=0} \text{ and } \varphi(x, t; q) = \varphi_0 + q\varphi_1 + q^2\varphi_2 + \dots. \tag{24}$$

By utilizing Eqs. (21)-(22), then we obtain

$$\begin{aligned} u_m(x, t) = (k_m + h)u_{m-1}(x, t) - \left(1 - \frac{k_m}{n}\right)\frac{1}{s}u_0(x, t) + h\mathcal{L}_\alpha^{-1} \left[\left(\frac{1}{s}\mathcal{L}_\alpha[Au_{m-1}(x, t) \right. \right. \\ \left. \left. + H_{m-1}(x, t) - f(x, t)]\right) \right]. \end{aligned} \tag{25}$$

By using q-HATM, the series solution is

$$u(x, t) = \sum_{m=0}^{\infty} u_m(x, t) \left(\frac{1}{n}\right)^m. \tag{26}$$

2.1.2. Conformable Elzaki Adomian decomposition method

The examination of CTFNPDE in Eq. (10) is conducted:

Now, by performing CFET on Eq. (10) and using initial condition, then we have

$$\frac{1}{v} {}_c E_\alpha[u(x, t)] - v u(x, 0) + {}_c E_\alpha[Au(x, t) + Hu(x, t)] = {}_c E_\alpha[h(x, t)]. \tag{27}$$

If we simplify the Eq. (27), then we get

$${}_c E_\alpha[u(x, t)] = v^2 u(x, 0) + v {}_c E_\alpha[h(x, t)] - v {}_c E_\alpha[Au(x, t) + Hu(x, t)]. \tag{28}$$

On applying inverse CFET to Eq. (28), then we have

$$u(x, t) = C(x, t) - ({}_c E_\alpha)^{-1} \{v {}_c E_\alpha [Au(x, t) + Hu(x, t)]\}, \tag{29}$$

where $C(x, t)$ is obtained from initial condition and non-homogeneous term. Now, assume that, the infinite series solution is of the form:

$$u(x, t) = \sum_{m=0}^{\infty} u_m(x, t). \tag{30}$$

By employing Eqs. (29) and (30), then we have

$$\sum_{m=0}^{\infty} u_m(x, t) = C(x, t) - ({}_c E_\alpha)^{-1} \left\{ v {}_c E_\alpha \left[A \sum_{m=0}^{\infty} u_m(x, t) + \sum_{m=0}^{\infty} B_m(u_m(x, t)) \right] \right\}, \tag{31}$$

where $B_m(u_m)$ is Adomian polynomial and that denotes the nonlinear term $Hu(x, t)$. By comparing both of sides of Eq. (31), we have

$$u_0(x, t) = C(x, t), \tag{32}$$

$$u_1(x, t) = -({}_c E_\alpha)^{-1} \{v {}_c E_\alpha [u_0(x, t) + B_0]\}, \tag{33}$$

$$u_2(x, t) = -({}_c E_\alpha)^{-1} \{v {}_c E_\alpha [u_1(x, t) + B_1]\}, \tag{34}$$

⋮

In a similar manner, the general recursive relation is derived by

$$u_{m+1}(x, t) = -({}_c E_\alpha)^{-1} \{v {}_c E_\alpha [u_m(x, t) + B_m]\}, m \geq 1, \tag{35}$$

Ultimately, the solution $u(x, t)$ is approximated as follows.

$$u(x, t) = \sum_{m=0}^{\infty} u_m(x, t) \tag{36}$$

3. RESULTS

The part aims to present visual representations of the conformable time-fractional coupled Jaulent-Miodek system..

Example 3.1. [43-44] Consider the conformable time-fractional coupled Jaulent-Miodek system (CTFCJMS)

$$\begin{cases} u_t^\alpha + u_{xxx} + \frac{3}{2} w w_{xxx} + \frac{9}{2} w_x w_{xx} - 6u u_x - 6u w w_x - \frac{3}{2} u_x w^2 = 0, \\ w_t^\alpha + w_{xxx} - 6w u_x - 6u w_x - \frac{15}{2} w_x w^2 = 0, \\ 0 < \alpha \leq 1, 0 < t \leq 1, -10 \leq x \leq 10, \end{cases} \tag{37}$$

with the initial conditions

$$\begin{aligned}
 u(x, 0) &= \frac{1}{8} \lambda^2 \left(1 - 4 \operatorname{sech}^2 \left(\frac{\lambda x}{2} \right) \right), \\
 w(x, 0) &= \lambda \operatorname{sech} \left(\frac{\lambda x}{2} \right).
 \end{aligned}
 \tag{38}$$

Case (i) Cq-HATM solution

CLT is employed to Eq. (37), and by applying Eq. (38), the resulting expression is produced as

$$\begin{aligned}
 \mathcal{L}_\alpha[u(x, t)] - \frac{u(x, 0)}{s} + \frac{1}{s} \mathcal{L}_\alpha(u_{xxx} + \frac{3}{2} w w_{xxx} + \frac{9}{2} w_x \cdot w_{xx} - 6 u u_x - 6 u w w_x - \frac{3}{2} u_x w^2) &= 0, \\
 \mathcal{L}_\alpha[w] - \frac{1}{s} w(x, 0) + \frac{1}{s} \mathcal{L}_\alpha \left[w_{xxx} - 6 w u_x - 6 u w_x - \frac{15}{2} w_x w^2 \right] &= 0.
 \end{aligned}
 \tag{39}$$

The nonlinear operators are defined by employing Eq. (39):

$$\begin{aligned}
 N^1[\varphi(x, t; q), \psi(x, t; q)] &= \mathcal{L}_\alpha[\varphi(x, t; q)] - \frac{1}{s} \left(\frac{1}{8} \lambda^2 \left(1 - 4 \operatorname{sech}^2 \left(\frac{\lambda x}{2} \right) \right) \right) \\
 + \frac{1}{s} \mathcal{L}_\alpha \left[\frac{\partial^3 \varphi}{\partial x^3} + \frac{3}{2} \psi \frac{\partial^3 \psi}{\partial x^3} + \frac{9}{2} \frac{\partial \psi}{\partial x} \cdot \frac{\partial^2 \psi}{\partial x^2} - 6 \varphi \frac{\partial \varphi}{\partial x} - 6 \varphi \psi \frac{\partial \psi}{\partial x} - \frac{3}{2} \frac{\partial \varphi}{\partial x} \psi^2 \right]
 \end{aligned}
 \tag{40}$$

$$\begin{aligned}
 N^2[\varphi(x, t; q), \psi(x, t; q)] &= \mathcal{L}_\alpha[\psi(x, t; q)] - \frac{1}{s} \left(\lambda \operatorname{sech} \left(\frac{\lambda x}{2} \right) \right) \\
 + \frac{1}{s} \mathcal{L}_\alpha \left[\frac{\partial^3 \psi}{\partial x^3} - 6 \psi \frac{\partial \varphi}{\partial x} - 6 \varphi \frac{\partial \psi}{\partial x} - \frac{15}{2} \psi^2 \frac{\partial \psi}{\partial x} \right].
 \end{aligned}
 \tag{41}$$

The $m - th$ order deformation equations are defined by the application of the proposed algorithm:

$$\mathcal{L}_\alpha[u_m(x, t) - k_m u_{m-1}(x, t)] = h \mathcal{R}_{1,m}[\vec{u}_{m-1}, \vec{w}_{m-1}],
 \tag{42}$$

$$\mathcal{L}_\alpha[w_m(x, t) - k_m w_{m-1}(x, t)] = h \mathcal{R}_{2,m}[\vec{u}_{m-1}, \vec{w}_{m-1}],
 \tag{43}$$

where

$$\begin{aligned}
 \mathcal{R}_{1,m}[\vec{u}_{m-1}, \vec{w}_{m-1}] &= \mathcal{L}_\alpha[u_{m-1}] - \frac{1}{s} \left(1 - \frac{km}{n} \right) \left(\frac{1}{8} \lambda^2 \left(1 - 4 \operatorname{sech}^2 \left(\frac{\lambda x}{2} \right) \right) \right) \\
 + \frac{1}{s} \mathcal{L}_\alpha \left[\frac{\partial^3 u_{m-1}}{\partial x^3} + \frac{3}{2} \sum_{r=0}^{m-1} w_r \frac{\partial^3 w_{m-1-r}}{\partial x^3} + \frac{9}{2} \sum_{r=0}^{m-1} \frac{\partial w_r}{\partial x} \frac{\partial^2 w_{m-1-r}}{\partial x^2} - 6 \sum_{r=0}^{m-1} u_r \frac{\partial u_{m-1-r}}{\partial x} \right. \\
 \left. - 6 \sum_{r=0}^{m-1} \left(\sum_{j=0}^r u_j w_{r-j} \right) \frac{\partial w_{m-1-r}}{\partial x} - \frac{3}{2} \sum_{r=0}^{m-1} \left(\sum_{j=0}^r w_j w_{r-j} \right) \frac{\partial w_{m-1-r}}{\partial x} \right],
 \end{aligned}
 \tag{44}$$

$$\begin{aligned} \mathcal{R}_{2,m}[\vec{u}_{m-1}, \vec{w}_{m-1}] &= \mathcal{L}_\alpha[w_{m-1}] - \frac{1}{s} \left(1 - \frac{km}{n}\right) \left(\lambda \operatorname{sech}\left(\frac{\lambda x}{2}\right)\right) \\ &+ \frac{1}{s} \mathcal{L}_\alpha \left[\frac{\partial^3 u_{m-r}}{\partial x^3} - 6 \sum_{r=0}^{m-1} w_r \frac{\partial u_{m-1-r}}{\partial x} \right. \\ &\quad \left. - 6 \sum_{r=0}^{m-1} u_r \frac{\partial w_{m-1-r}}{\partial x} - \frac{15}{2} \sum_{r=0}^{m-1} \left(\sum_{j=0}^r w_j w_{r-j} \right) \frac{\partial w_{m-1-r}}{\partial x} \right]. \end{aligned} \tag{45}$$

By utilizing the inverse CLT to Eqs. (42)-(43), we obtain

$$u_m(x, t) = k_m u_{m-1}(x, t) + h \mathcal{L}_\alpha^{-1} \{ \mathcal{R}_{1,m}[\vec{u}_{m-1}, \vec{w}_{m-1}] \}, \tag{46}$$

$$w_m(x, t) = k_m w_{m-1}(x, t) + h \mathcal{L}_\alpha^{-1} \{ \mathcal{R}_{2,m}[\vec{u}_{m-1}, \vec{w}_{m-1}] \}. \tag{47}$$

By employing initial conditions, we are able to drive

$$u_0(x, t) = \frac{1}{8} \lambda^2 \left(1 - 4 \operatorname{sech}^2 \left(\frac{\lambda x}{2} \right) \right), \tag{48}$$

$$w_0(x, t) = \lambda \operatorname{sech} \left(\frac{\lambda x}{2} \right). \tag{49}$$

To get the values of $u_1(x, t)$ and $w_1(x, t)$, we substitute $m = 1$ into Eqs. (46)-(47), resulting in the following expressions:

$$u_1(x, t) = -h \frac{\sinh\left(\frac{\lambda x}{2}\right) \lambda^5 t^\alpha}{4\alpha \cosh^3\left(\frac{\lambda x}{2}\right)}, \tag{50}$$

$$w_1(x, t) = h \frac{t^\alpha \lambda^4 \sinh\left(\frac{\lambda x}{2}\right)}{4\alpha \cosh^2\left(\frac{\lambda x}{2}\right)}. \tag{51}$$

In a similar vein, by substituting $m = 2$ into Eqs. (46)-(47), the resulting values for $u_2(x, t)$ and $w_2(x, t)$ can be obtained:

$$u_2(x, t) = -(n+h)h \frac{t^\alpha \lambda^5 \sinh\left(\frac{\lambda x}{2}\right)}{4\alpha \cosh^3\left(\frac{\lambda x}{2}\right)} - h^2 \left(\frac{t^{2\alpha} \lambda^8 \left(\cosh^2\left(\frac{\lambda x}{2}\right) - \frac{3}{2} \right)}{16\alpha^2 \cosh^4\left(\frac{\lambda x}{2}\right)} \right), \tag{52}$$

$$w_2(x, t) = (n+h)h \frac{t^\alpha \lambda^4 \sinh\left(\frac{\lambda x}{2}\right)}{4\alpha \cosh^2\left(\frac{\lambda x}{2}\right)} + h^2 \left(\frac{t^{2\alpha} \lambda^7 \left(\cosh^2\left(\frac{\lambda x}{2}\right) - 2 \right)}{32\alpha^2 \cosh^3\left(\frac{\lambda x}{2}\right)} \right). \tag{53}$$

By employing this approach, it is possible to identify the remaining terms. The solutions of the CTFCJMS are determined through the Cq-HATM:

$$u(x, t) = u_0(x, t) + \sum_{m=1}^{\infty} u_m(x, t) \left(\frac{1}{n}\right)^m, \tag{54}$$

$$w(x, t) = w_0(x, t) + \sum_{m=1}^{\infty} w_m(x, t) \left(\frac{1}{n}\right)^m. \tag{55}$$

By substituting $\alpha = 1, n = 1, h = -1$ into Eqs. (54)-(55), we have that the resulting outcomes, denoted as $\sum_{m=1}^M u_m(x, t) \left(\frac{1}{n}\right)^m$ and $\sum_{m=1}^M w_m(x, t) \left(\frac{1}{n}\right)^m$, respectively, converge to the exact solutions $u(x, t) = \xi - \kappa \coth[\kappa(x + \theta - \xi t)]$ and $w(x, t) = -\kappa^2 \operatorname{cosech}^2[\kappa(x + \theta - \xi t)]$ of the CTFCJMS when $M \rightarrow \infty$.

Case (ii) CEADM solution

By employing the CFET to Eq. (37) and utilizing Eq. (38), the resulting expression is obtained.

$$\begin{aligned} & \frac{1}{v} E_{\alpha}^c \{u(x, t)\} - vu(x, 0) \\ & + E_{\alpha}^c \left[\frac{\partial^3 u}{\partial x^3} + \frac{3}{2} w \frac{\partial^3 w}{\partial x^3} + \frac{9}{2} \frac{\partial w}{\partial x} \frac{\partial^2 w}{\partial x^2} - 6u \frac{\partial u}{\partial x} - 6uw \frac{\partial w}{\partial x} - \frac{3}{2} \frac{\partial u}{\partial x} w^2 \right] = 0, \end{aligned} \tag{56}$$

$$\frac{1}{v} E_{\alpha}^c \{w(x, t)\} - vw(x, 0) + E_{\alpha}^c \left[\frac{\partial^3 w}{\partial x^3} - 6w \frac{\partial u}{\partial x} - 6u \frac{\partial w}{\partial x} - \frac{15}{2} \frac{\partial w}{\partial x} w^2 \right] = 0. \tag{57}$$

Rearranging Eqs. (56)-(57), then we obtain

$$\begin{aligned} E_{\alpha}^c \{u(x, t)\} &= v^2 u(x, 0) \\ &- v E_{\alpha}^c \left[\frac{\partial^3 u}{\partial x^3} + \frac{3}{2} w \frac{\partial^3 w}{\partial x^3} + \frac{9}{2} \frac{\partial w}{\partial x} \frac{\partial^2 w}{\partial x^2} - 6u \frac{\partial u}{\partial x} - 6uw \frac{\partial w}{\partial x} - \frac{3}{2} \frac{\partial u}{\partial x} w^2 \right], \end{aligned} \tag{58}$$

$$E_{\alpha}^c \{w(x, t)\} = v^2 w(x, 0) - v E_{\alpha}^c \left[\frac{\partial^3 w}{\partial x^3} - 6w \frac{\partial u}{\partial x} - 6u \frac{\partial w}{\partial x} - \frac{15}{2} \frac{\partial w}{\partial x} w^2 \right]. \tag{59}$$

By utilizing the inverse CFET on Eqs. (58)-(59), we are able to derive the following result:

$$\begin{aligned} u(x, t) &= \frac{1}{8} \lambda^2 \left(1 - 4 \operatorname{sech}^2 \left[\frac{\lambda x}{2} \right] \right) - (E_{\alpha}^c)^{-1} \left\{ v E_{\alpha}^c \left[\frac{\partial^3 u}{\partial x^3} + \frac{3}{2} w \frac{\partial^3 w}{\partial x^3} + \frac{9}{2} \frac{\partial w}{\partial x} \frac{\partial^2 w}{\partial x^2} - 6u \frac{\partial u}{\partial x} \right. \right. \\ &\left. \left. - 6uw \frac{\partial w}{\partial x} - \frac{3}{2} \frac{\partial u}{\partial x} w^2 \right] \right\}, \end{aligned} \tag{60}$$

$$w(x, t) = \lambda \operatorname{sech} \left[\frac{\lambda x}{2} \right] - (E_{\alpha}^c)^{-1} \left\{ v E_{\alpha}^c \left[\frac{\partial^3 w}{\partial x^3} - 6w \frac{\partial u}{\partial x} - 6u \frac{\partial w}{\partial x} - \frac{15}{2} \frac{\partial w}{\partial x} w^2 \right] \right\}. \tag{61}$$

Let us consider the assumption that the answer to the infinite series can be expressed in the following form:

$$u(x, t) = \sum_{m=0}^{\infty} u_m(x, t), \tag{62}$$

$$w(x, t) = \sum_{m=0}^{\infty} w_m(x, t). \tag{63}$$

Utilizing Adomian decomposition method, if we rewrite Eqs. (62)-(63), then it is obtained as

$$\sum_{m=0}^{\infty} u_m(x, t) = \frac{1}{8} \lambda^2 \left(1 - 4 \operatorname{sech}^2 \left[\frac{\lambda x}{2} \right] \right) - (E_{\alpha}^c)^{-1} \left\{ v E_{\alpha}^c \left[\frac{\partial^3 u_{m-1}(x, t)}{\partial x^3} \right] + \frac{3}{2} \sum_{m=0}^{\infty} A_m + \frac{9}{2} \sum_{m=0}^{\infty} B_m - 6 \sum_{m=0}^{\infty} C_m - 6 \sum_{m=0}^{\infty} E_m - \frac{3}{2} \sum_{m=0}^{\infty} F_m \right\}, \tag{64}$$

$$\sum_{m=0}^{\infty} w_m(x, t) = \lambda \operatorname{sech} \left[\frac{\lambda x}{2} \right] - (E_{\alpha}^c)^{-1} \left\{ v E_{\alpha}^c \left[\frac{\partial^3 w_{m-1}(x, t)}{\partial x^3} \right] - 6 \sum_{m=0}^{\infty} G_m - 6 \sum_{m=0}^{\infty} H_m - \frac{15}{2} \sum_{m=0}^{\infty} K_m \right\}, \tag{65}$$

where $A_m, B_m, C_m, E_m, F_m, G_m, H_m, K_m$ are Adomian polynomials of the form $w \frac{\partial^3 w}{\partial x^3} = \sum_{m=0}^{\infty} A_m$, $\frac{\partial w}{\partial x} \frac{\partial^2 w}{\partial x^2} = \sum_{m=0}^{\infty} B_m$, $u \frac{\partial u}{\partial x} = \sum_{m=0}^{\infty} C_m$, $uw \frac{\partial w}{\partial x} = \sum_{m=0}^{\infty} E_m$, $w^2 \frac{\partial w}{\partial x} = \sum_{m=0}^{\infty} F_m$, $w \frac{\partial w}{\partial x} = \sum_{m=0}^{\infty} G_m$, $u \frac{\partial w}{\partial x} = \sum_{m=0}^{\infty} H_m$, $w^2 \frac{\partial w}{\partial x} = \sum_{m=0}^{\infty} K_m$.

By taking both sides of Eqs. (64)-(65) and making use of the initial condition (38) and Eqs. (64)-(65), we simply obtain the following iterations:

$$u_0(x, t) = \frac{1}{8} \lambda^2 \left(1 - 4 \operatorname{sech}^2 \left[\frac{\lambda x}{2} \right] \right), \tag{66}$$

$$w_0(x, t) = \lambda \operatorname{sech} \left[\frac{\lambda x}{2} \right], \tag{67}$$

$$u_1(x, t) = \frac{t^{\alpha} \lambda^5 \sinh \left(\frac{\lambda x}{2} \right)}{4 \alpha \cosh^3 \left(\frac{\lambda x}{2} \right)}, \tag{68}$$

$$w_1(x, t) = - \frac{t^{\alpha} \lambda^4 \sinh \left(\frac{\lambda x}{2} \right)}{4 \alpha \cosh^2 \left(\frac{\lambda x}{2} \right)}, \tag{69}$$

$$u_2(x, t) = - \left(\frac{t^{2\alpha} \lambda^8 \left(2 \cosh^2 \left(\frac{\lambda x}{2} \right) - 3 \right)}{32 \alpha^2 \cosh^4 \left(\frac{\lambda x}{2} \right)} \right), \tag{68}$$

$$w_2(x, t) = \left(\frac{t^{2\alpha} \lambda^7 \left(\cosh^2 \left(\frac{\lambda x}{2} \right) - 2 \right)}{32 \alpha^2 \cosh^3 \left(\frac{\lambda x}{2} \right)} \right). \tag{69}$$

By continuing in a similar manner, the outcomes for CTFCJMS can be derived.

$$\begin{aligned}
 u(x, t) &= \sum_{m=0}^{\infty} u_m(x, t) = u_0(x, t) + u_1(x, t) + u_2(x, t) + \dots \\
 &= \frac{1}{8} \lambda^2 \left(1 - 4 \operatorname{sech}^2 \left[\frac{\lambda x}{2} \right] \right) + \frac{t^\alpha \lambda^5 \sinh \left(\frac{\lambda x}{2} \right)}{4\alpha \cosh^3 \left(\frac{\lambda x}{2} \right)} - \left(\frac{t^{2\alpha} \lambda^8 \left(2 \cosh^2 \left(\frac{\lambda x}{2} \right) - 3 \right)}{32\alpha^2 \cosh^4 \left(\frac{\lambda x}{2} \right)} \right), \tag{70}
 \end{aligned}$$

$$\begin{aligned}
 w(x, t) &= \sum_{m=0}^{\infty} w_m(x, t) = w_0(x, t) + w_1(x, t) + w_2(x, t) + \dots \\
 &= \lambda \operatorname{sech} \left[\frac{\lambda x}{2} \right] - \frac{t^\alpha \lambda^4 \sinh \left(\frac{\lambda x}{2} \right)}{4\alpha \cosh^2 \left(\frac{\lambda x}{2} \right)} + \left(\frac{t^{2\alpha} \lambda^7 \left(\cosh^2 \left(\frac{\lambda x}{2} \right) - 2 \right)}{32\alpha^2 \cosh^3 \left(\frac{\lambda x}{2} \right)} \right). \tag{71}
 \end{aligned}$$

Figure 1 displays the 3D graphical representations of Cq-HATM, the exact solution, and the absolute error for $u(x, t)$ and $w(x, t)$.

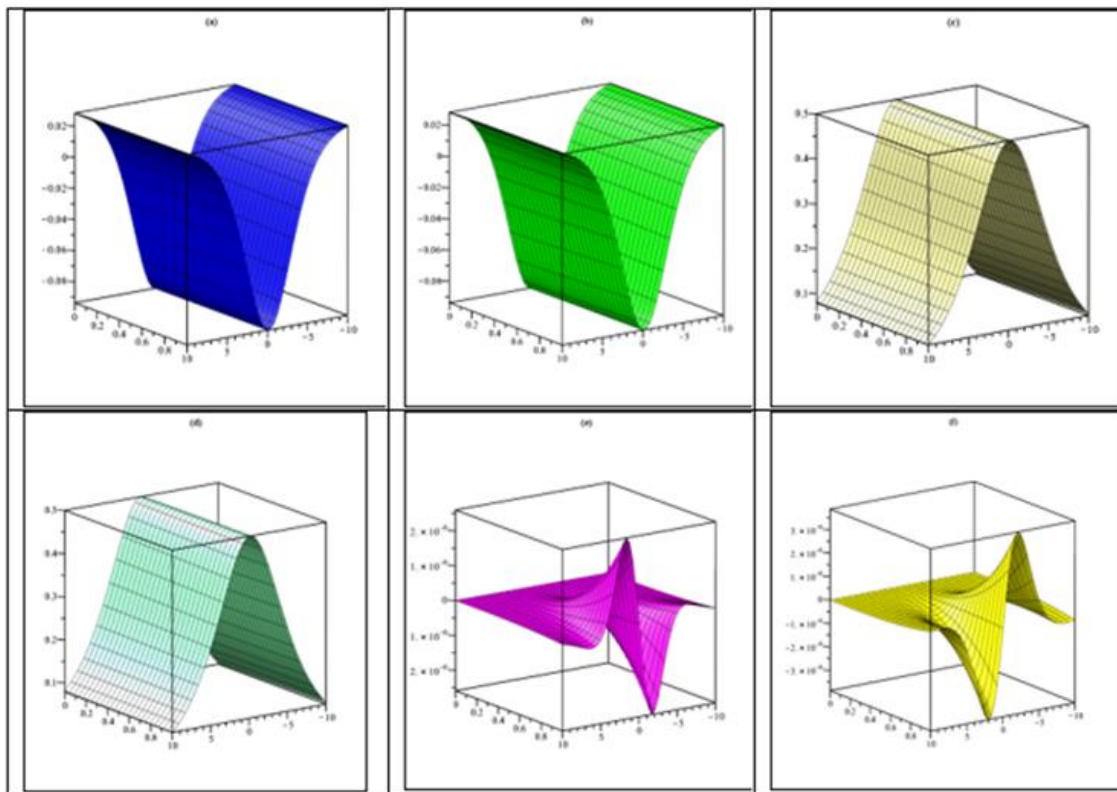


Figure 1. (a) Nature of Cq-HATM solution $u(x, t)$ (b) Nature of exact solution $u(x, t)$ (c) Nature of Cq-HATM solution $w(x, t)$ (d) Nature of exact solution $w(x, t)$ (e) Nature of absolute error= $|u_{exact} - u_{Cq-HATM}|$ (f) Nature of absolute error= $|w_{exact} - w_{Cq-HATM}|$ at $\lambda = 0.5, h = -1, n = 1, \alpha = 1$ for Ex. 3.1.

Figure 2 presents the three-dimensional graphical depictions of CEADM, the exact solution, and the absolute error for $u(x, t)$ and $w(x, t)$.

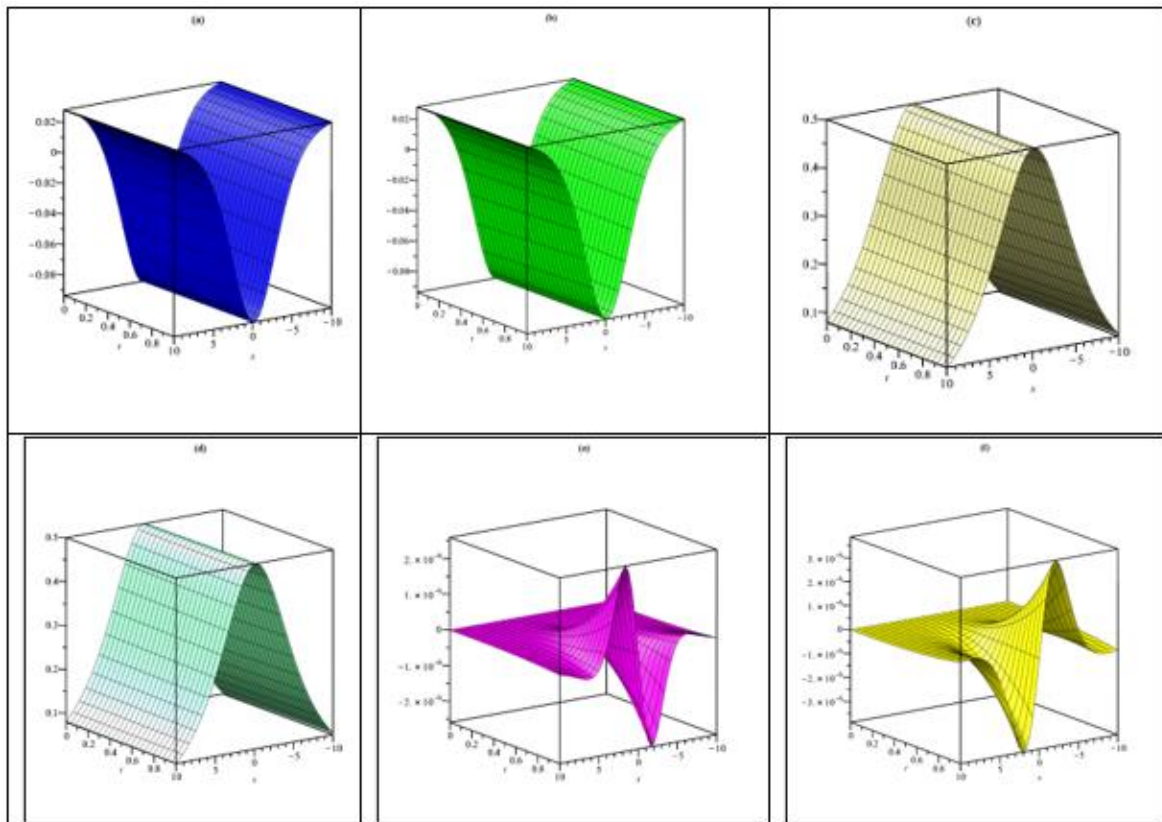


Figure 2. (a) Nature of CEADM solution $u(x, t)$ (b) Nature of exact solution $u(x, t)$ (c) Nature of CEADM solution $w(x, t)$ (d) Nature of exact solution $w(x, t)$ (e) Nature of absolute error= $|u_{exact} - u_{CEADM}|$ (f) Nature of absolute error= $|w_{exact} - w_{CEADM}|$ at $\lambda = 0.5, \alpha = 1$ for Ex. 3.1.

Figure 3 shows the two-dimensional graphical representations of Cq-HATM for $u(x, t), w(x, t)$ solutions and the exact solution for different α values.

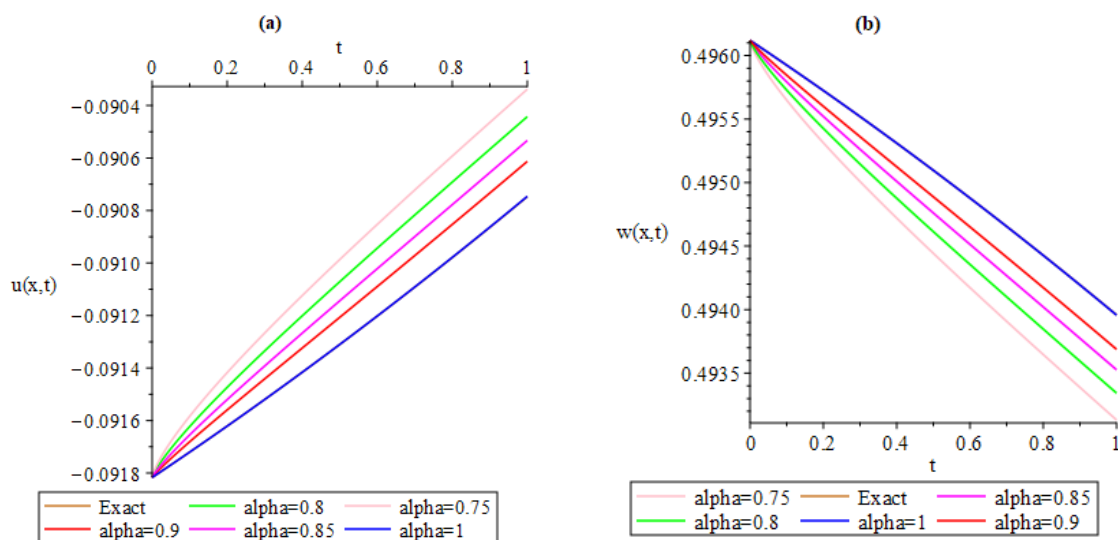


Figure 3. The comparison of the Cq-HATM solutions for $u(x, t)$ and exact solution (b) The comparison of the Cq-HATM solutions for $w(x, t)$ and exact solution at $\lambda = 0.5, h = -1, n = 1, x = 0.5$ with different α .

Figure 4 displays the graphical depictions of CEADM for the solutions $u(x, t)$ and $w(x, t)$, as well as the exact solution, in a two-dimensional format. These representations vary based on the different α values.

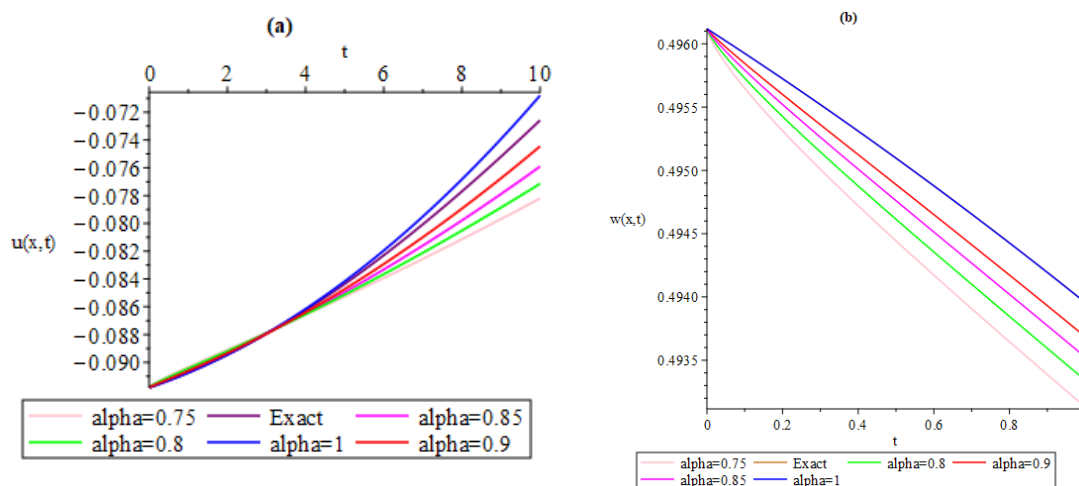


Figure 4. The comparison of the CEADM solutions for $u(x, t)$ and exact solution (b) The comparison of the CEADM solutions for $w(x, t)$ and exact solution at $\lambda = 0.5, x = 0.5$ with different α .

Table 1 shows the numerical solution of $u(x, t)$ obtained from the solution of CTFCJMS with Cq-HATM for different x, t and α values.

Table 1. Numerical solution of $u(x, t)$ by Cq-HATM for CTFCJMS with different x, t and α at $\lambda = 0.5, n = 1, h = -1$.

x	t	$\alpha = 0.75$	$\alpha = 0.80$	$\alpha = 0.85$	$\alpha = 0.90$	$\alpha = 1$
0.1	0.001	1.2×10^{-6}	7.7×10^{-7}	4.5×10^{-7}	2.3×10^{-7}	2.5×10^{-16}
	0.002	2.0×10^{-6}	1.3×10^{-6}	7.7×10^{-7}	4.1×10^{-7}	2.0×10^{-15}
	0.003	2.7×10^{-6}	1.7×10^{-6}	1.0×10^{-6}	5.8×10^{-7}	6.8×10^{-15}
	0.004	3.4×10^{-6}	2.1×10^{-6}	1.3×10^{-6}	7.3×10^{-7}	1.6×10^{-14}
	0.005	3.9×10^{-6}	2.5×10^{-6}	1.5×10^{-6}	8.7×10^{-7}	3.1×10^{-14}
0.2	0.001	2.5×10^{-6}	1.5×10^{-6}	9.0×10^{-7}	4.7×10^{-7}	5.0×10^{-16}
	0.002	4.1×10^{-6}	2.6×10^{-6}	1.5×10^{-6}	8.3×10^{-7}	4.0×10^{-15}
	0.003	5.5×10^{-6}	3.5×10^{-6}	2.1×10^{-6}	1.1×10^{-6}	1.3×10^{-14}
	0.004	6.7×10^{-6}	4.3×10^{-6}	2.6×10^{-6}	1.4×10^{-6}	3.2×10^{-14}
	0.005	7.8×10^{-6}	5.1×10^{-6}	3.1×10^{-6}	1.7×10^{-6}	6.3×10^{-14}
0.3	0.001	3.7×10^{-6}	2.3×10^{-6}	1.3×10^{-6}	7.0×10^{-7}	7.5×10^{-16}
	0.002	6.1×10^{-6}	3.8×10^{-6}	2.3×10^{-6}	1.2×10^{-6}	6.0×10^{-15}
	0.003	8.2×10^{-6}	5.2×10^{-6}	3.1×10^{-6}	1.7×10^{-6}	2.0×10^{-14}
	0.004	1.0×10^{-5}	6.4×10^{-6}	3.9×10^{-6}	2.1×10^{-6}	4.8×10^{-14}
	0.005	1.1×10^{-5}	7.6×10^{-6}	4.6×10^{-6}	2.5×10^{-6}	9.3×10^{-14}
0.4	0.001	5.0×10^{-6}	3.0×10^{-6}	1.7×10^{-6}	9.3×10^{-7}	9.8×10^{-16}
	0.002	8.1×10^{-6}	5.1×10^{-6}	3.0×10^{-6}	1.6×10^{-6}	7.9×10^{-15}
	0.003	1.0×10^{-5}	6.9×10^{-6}	4.1×10^{-6}	2.2×10^{-6}	2.6×10^{-14}
	0.004	1.3×10^{-5}	8.5×10^{-6}	5.2×10^{-6}	2.8×10^{-6}	6.3×10^{-14}
	0.005	1.5×10^{-5}	1.0×10^{-5}	6.2×10^{-6}	3.4×10^{-6}	1.2×10^{-13}
0.5	0.001	6.2×10^{-6}	3.8×10^{-6}	2.2×10^{-6}	1.1×10^{-6}	1.2×10^{-15}
	0.002	1.0×10^{-5}	6.3×10^{-6}	3.8×10^{-6}	2.0×10^{-6}	9.7×10^{-15}
	0.003	1.3×10^{-5}	8.6×10^{-6}	5.2×10^{-6}	2.8×10^{-6}	3.2×10^{-14}
	0.004	1.6×10^{-5}	1.0×10^{-5}	6.4×10^{-6}	3.5×10^{-6}	7.7×10^{-14}
	0.005	1.9×10^{-5}	1.2×10^{-5}	7.6×10^{-6}	4.2×10^{-6}	1.5×10^{-13}

Table 2 presents the numerical solution of the function $w(x, t)$, which was derived from the solution of the CTFCJMS using the Cq-HATM. The table displays the results for various values of x, t , and α .

Table 2. Numerical solution of $w(x, t)$ by Cq-HATM for CTFCJMS with different x, t and α at $\lambda = 0.5, n = 1, h = -1$.

x	t	$\alpha = 0.75$	$\alpha = 0.80$	$\alpha = 0.85$	$\alpha = 0.90$	$\alpha = 1$
0.1	0.001	2.5×10^{-6}	1.5×10^{-6}	9.0×10^{-7}	4.7×10^{-7}	3.1×10^{-16}
	0.002	4.1×10^{-6}	2.6×10^{-6}	1.5×10^{-6}	8.3×10^{-7}	2.5×10^{-15}
	0.003	5.5×10^{-6}	3.5×10^{-6}	2.1×10^{-6}	1.1×10^{-6}	8.5×10^{-15}
	0.004	6.8×10^{-6}	4.3×10^{-6}	2.6×10^{-6}	1.4×10^{-6}	2.0×10^{-14}
	0.005	7.9×10^{-6}	5.1×10^{-6}	3.1×10^{-6}	1.7×10^{-6}	3.9×10^{-14}
0.2	0.001	5.0×10^{-6}	3.1×10^{-6}	1.8×10^{-6}	9.4×10^{-7}	6.3×10^{-16}
	0.002	8.3×10^{-6}	5.2×10^{-6}	3.1×10^{-6}	1.6×10^{-6}	5.0×10^{-15}
	0.003	1.1×10^{-5}	7.0×10^{-6}	4.2×10^{-6}	2.3×10^{-6}	1.7×10^{-14}
	0.004	1.3×10^{-5}	8.6×10^{-6}	5.3×10^{-6}	2.9×10^{-6}	4.0×10^{-14}
	0.005	1.5×10^{-5}	1.0×10^{-5}	6.2×10^{-6}	3.4×10^{-6}	7.9×10^{-14}
0.3	0.001	7.5×10^{-6}	4.6×10^{-6}	2.7×10^{-6}	1.4×10^{-6}	9.4×10^{-16}
	0.002	1.2×10^{-5}	7.7×10^{-6}	4.6×10^{-6}	2.4×10^{-6}	7.5×10^{-15}
	0.003	1.6×10^{-5}	1.0×10^{-5}	6.3×10^{-6}	3.4×10^{-6}	2.5×10^{-14}
	0.004	2.0×10^{-5}	1.2×10^{-5}	7.9×10^{-6}	4.3×10^{-6}	6.0×10^{-14}
	0.005	2.3×10^{-5}	1.5×10^{-5}	9.3×10^{-6}	5.1×10^{-6}	1.1×10^{-13}
0.4	0.001	1.0×10^{-5}	6.1×10^{-6}	3.5×10^{-6}	1.8×10^{-6}	1.2×10^{-15}
	0.002	1.6×10^{-5}	1.0×10^{-5}	6.1×10^{-6}	3.3×10^{-6}	9.9×10^{-15}
	0.003	2.1×10^{-5}	1.3×10^{-5}	8.4×10^{-6}	4.5×10^{-6}	3.3×10^{-14}
	0.004	2.6×10^{-5}	1.7×10^{-5}	1.0×10^{-5}	5.7×10^{-6}	7.9×10^{-14}
	0.005	3.1×10^{-5}	2.0×10^{-5}	1.2×10^{-5}	6.8×10^{-6}	1.5×10^{-13}
0.5	0.001	1.2×10^{-5}	7.6×10^{-6}	4.4×10^{-6}	2.3×10^{-6}	1.5×10^{-15}
	0.002	2.0×10^{-5}	1.2×10^{-5}	7.6×10^{-6}	4.1×10^{-6}	1.2×10^{-14}
	0.003	2.7×10^{-5}	1.7×10^{-5}	1.0×10^{-5}	5.7×10^{-6}	4.1×10^{-14}
	0.004	3.3×10^{-5}	2.1×10^{-5}	1.3×10^{-5}	7.1×10^{-6}	9.8×10^{-14}
	0.005	3.8×10^{-5}	2.5×10^{-5}	1.5×10^{-5}	8.5×10^{-6}	1.9×10^{-13}

Table 3 demonstrates the numerical solution of $u(x, t)$ obtained from the solution of CTFCJMS with CEADM for distinct x, t and α values.

Table 3. Numerical solution of $u(x, t)$ by CEADM for CTFCJMS with different x, t and α at $\lambda = 0.5$.

x	t	$\alpha = 0.75$	$\alpha = 0.80$	$\alpha = 0.85$	$\alpha = 0.90$	$\alpha = 1$
0.1	0.001	1.2×10^{-6}	7.7×10^{-7}	4.5×10^{-7}	2.3×10^{-7}	2.5×10^{-16}
	0.002	2.0×10^{-6}	1.3×10^{-6}	7.7×10^{-7}	4.1×10^{-7}	2.0×10^{-15}
	0.003	2.7×10^{-6}	1.7×10^{-6}	1.0×10^{-6}	5.8×10^{-7}	6.8×10^{-15}
	0.004	3.4×10^{-6}	2.1×10^{-6}	1.3×10^{-6}	7.3×10^{-7}	1.6×10^{-14}
	0.005	3.9×10^{-6}	2.5×10^{-6}	1.5×10^{-6}	8.7×10^{-7}	3.1×10^{-14}
0.2	0.001	2.5×10^{-6}	1.5×10^{-6}	9.0×10^{-7}	4.7×10^{-7}	5.0×10^{-16}
	0.002	4.1×10^{-6}	2.6×10^{-6}	1.5×10^{-6}	8.3×10^{-7}	4.0×10^{-15}
	0.003	5.5×10^{-6}	3.5×10^{-6}	2.1×10^{-6}	1.1×10^{-6}	1.3×10^{-14}
	0.004	6.7×10^{-6}	4.3×10^{-6}	2.6×10^{-6}	1.4×10^{-6}	3.2×10^{-14}
	0.005	7.8×10^{-6}	5.1×10^{-6}	3.1×10^{-6}	1.7×10^{-6}	6.3×10^{-14}
0.3	0.001	3.7×10^{-6}	2.3×10^{-6}	1.3×10^{-6}	7.0×10^{-7}	7.5×10^{-16}
	0.002	6.1×10^{-6}	3.8×10^{-6}	2.3×10^{-6}	1.2×10^{-6}	6.0×10^{-15}
	0.003	8.2×10^{-6}	5.2×10^{-6}	3.1×10^{-6}	1.7×10^{-6}	2.0×10^{-14}
	0.004	1.0×10^{-5}	6.4×10^{-6}	3.9×10^{-6}	2.1×10^{-6}	4.8×10^{-14}
	0.005	1.1×10^{-5}	7.6×10^{-6}	4.6×10^{-6}	2.5×10^{-6}	9.3×10^{-14}
0.4	0.001	5.0×10^{-6}	3.0×10^{-6}	1.7×10^{-6}	9.3×10^{-7}	9.8×10^{-16}
	0.002	8.1×10^{-6}	5.1×10^{-6}	3.0×10^{-6}	1.6×10^{-6}	7.9×10^{-15}
	0.003	1.0×10^{-5}	6.9×10^{-6}	4.1×10^{-6}	2.2×10^{-6}	2.6×10^{-14}
	0.004	1.3×10^{-5}	8.5×10^{-6}	5.2×10^{-6}	2.8×10^{-6}	6.3×10^{-14}
	0.005	1.5×10^{-5}	1.0×10^{-5}	6.2×10^{-6}	3.4×10^{-6}	1.2×10^{-13}
0.5	0.001	6.2×10^{-6}	3.8×10^{-6}	2.2×10^{-6}	1.1×10^{-6}	1.2×10^{-15}
	0.002	1.0×10^{-5}	6.3×10^{-6}	3.8×10^{-6}	2.0×10^{-6}	9.7×10^{-15}
	0.003	1.3×10^{-5}	8.6×10^{-6}	5.2×10^{-6}	2.8×10^{-6}	3.2×10^{-14}
	0.004	1.6×10^{-5}	1.0×10^{-5}	6.4×10^{-6}	3.5×10^{-6}	7.7×10^{-14}
	0.005	1.9×10^{-5}	1.2×10^{-5}	7.6×10^{-6}	4.2×10^{-6}	1.5×10^{-13}

Table 4 shows the numerical solution of the function $w(x, t)$, which was derived from the solution of the CTFCJMS using the CEADM. The table displays the results for various values of x, t , and α .

Table 4. Numerical solution of $w(x, t)$ by CEADM for CTFCJMS with different x, t and α at $\lambda = 0.5$.

x	t	$\alpha = 0.75$	$\alpha = 0.80$	$\alpha = 0.85$	$\alpha = 0.90$	$\alpha = 1$
0.1	0.001	2.5×10^{-6}	1.5×10^{-6}	9.0×10^{-7}	4.7×10^{-7}	3.1×10^{-16}
	0.002	4.1×10^{-6}	2.6×10^{-6}	1.5×10^{-6}	8.3×10^{-7}	2.5×10^{-15}
	0.003	5.5×10^{-6}	3.5×10^{-6}	2.1×10^{-6}	1.1×10^{-6}	8.5×10^{-15}
	0.004	6.8×10^{-6}	4.3×10^{-6}	2.6×10^{-6}	1.4×10^{-6}	2.0×10^{-14}
	0.005	7.9×10^{-6}	5.1×10^{-6}	3.1×10^{-6}	1.7×10^{-6}	3.9×10^{-14}
0.2	0.001	5.0×10^{-6}	3.1×10^{-6}	1.8×10^{-6}	9.4×10^{-7}	6.3×10^{-16}
	0.002	8.3×10^{-6}	5.2×10^{-6}	3.1×10^{-6}	1.6×10^{-6}	5.0×10^{-15}
	0.003	1.1×10^{-5}	7.0×10^{-6}	4.2×10^{-6}	2.3×10^{-6}	1.7×10^{-14}
	0.004	1.3×10^{-5}	8.6×10^{-6}	5.3×10^{-6}	2.9×10^{-6}	4.0×10^{-14}
	0.005	1.5×10^{-5}	1.0×10^{-5}	6.2×10^{-6}	3.4×10^{-6}	7.9×10^{-14}
0.3	0.001	7.5×10^{-6}	4.6×10^{-6}	2.7×10^{-6}	1.4×10^{-6}	9.4×10^{-16}
	0.002	1.2×10^{-5}	7.7×10^{-6}	4.6×10^{-6}	2.4×10^{-6}	7.5×10^{-15}
	0.003	1.6×10^{-5}	1.0×10^{-5}	6.3×10^{-6}	3.4×10^{-6}	2.5×10^{-14}
	0.004	2.0×10^{-5}	1.2×10^{-5}	7.9×10^{-6}	4.3×10^{-6}	6.0×10^{-14}
	0.005	2.3×10^{-5}	1.5×10^{-5}	9.3×10^{-6}	5.1×10^{-6}	1.1×10^{-13}
0.4	0.001	1.0×10^{-5}	6.1×10^{-6}	3.5×10^{-6}	1.8×10^{-6}	1.2×10^{-15}
	0.002	1.6×10^{-5}	1.0×10^{-5}	6.1×10^{-6}	3.3×10^{-6}	9.9×10^{-15}
	0.003	2.1×10^{-5}	1.3×10^{-5}	8.4×10^{-6}	4.5×10^{-6}	3.3×10^{-14}
	0.004	2.6×10^{-5}	1.7×10^{-5}	1.0×10^{-5}	5.7×10^{-6}	7.9×10^{-14}
	0.005	3.1×10^{-5}	2.0×10^{-5}	1.2×10^{-5}	6.8×10^{-6}	1.5×10^{-13}
0.5	0.001	1.2×10^{-5}	7.6×10^{-6}	4.4×10^{-6}	2.3×10^{-6}	1.5×10^{-15}
	0.002	2.0×10^{-5}	1.2×10^{-5}	7.6×10^{-6}	4.1×10^{-6}	1.2×10^{-14}
	0.003	2.7×10^{-5}	1.7×10^{-5}	1.0×10^{-5}	5.7×10^{-6}	4.1×10^{-14}
	0.004	3.3×10^{-5}	2.1×10^{-5}	1.3×10^{-5}	7.1×10^{-6}	9.8×10^{-14}
	0.005	3.8×10^{-5}	2.5×10^{-5}	1.5×10^{-5}	8.5×10^{-6}	1.9×10^{-13}

4. DISCUSSION AND CONCLUSION

Figure 1 displays the three-dimensional graphs of the numerical solutions obtained by the Cq-HATM, as well as the exact solutions and the absolute errors between the Cq-HATM solutions and the exact solutions for the CTFCJMS. The three-dimensional graphs depicting the numerical solutions obtained by the CEADM for the CTFCJMS are shown in Figure 2. Additionally, the exact solutions and the absolute errors between the CEADM solutions and the exact solutions are also illustrated in the same figure. Figure 3 depicts the two-dimensional graphs of the solutions $u(x, t)$ and $w(x, t)$ of the CTFCJMS, obtained using the Cq-HATM, for various alpha values. The two-dimensional graphical representations of the solutions $u(x, t)$ and $w(x, t)$ of the CTFCJMS are shown in Figure 4, which have been derived by the utilization of the CEADM, while considering different values of α . The numerical solutions of $u(x, t)$ and $w(x, t)$ found using Cq-HATM for the values of $\alpha = 0.75, \alpha = 0.8, \alpha = 0.85, \alpha = 0.9$, and $\alpha = 1$ for CTFCJMS are presented in Tables 1-2. Also, the numerical solutions of $u(x, t)$ and $w(x, t)$ found using CEADM for various values of $\alpha = 0.75, \alpha = 0.8, \alpha = 0.85, \alpha = 0.9$, and $\alpha = 1$ for CTFCJMS are presented in Tables 3-4.

In this study, CTFCJMS has been examined by the new numerical methods, namely, Cq-HATM and CEADM. The reliability of these new methods has been confirmed by numerical results. The new methods presented to solve such coupled fractional systems have been determined to possess notable advantages and demonstrate effectiveness.

CONFLICT OF INTEREST

The authors stated that there are no conflicts of interest regarding the publication of this article.

AUTHORSHIP CONTRIBUTIONS

Autors' contributions are equal.

REFERENCES

- [1] Liouville J. 1832. Mémoire sur quelques questions de géométrie et de mécanique, et sur un nouveau genre de calcul pour résoudre ces questions. *J Ecole Polytech* 1832; 13(21): 1-69.
- [2] Miller KS, Ross B. An introduction to the fractional calculus and fractional differential equations. Wiley, New York, 1993.
- [3] Podlubny I. Fractional Differential Equations. Academic Press, New York, 1999.
- [4] Baleanu D, Diethelm K, Scalas E, Trujillo JJ. Fractional calculus: models and numerical methods. World Scientific, London, 2012.
- [5] Povstenko Y. 2015. Linear fractional diffusion-wave equation for scientists and engineers. Birkhäuser, Switzerland, 2015.
- [6] Baleanu D, Wu GC, Zeng SD. Chaos analysis and asymptotic stability of generalized Caputo fractional differential equations. *Chaos Solit Fractals* 2017; 102: 99–105.
- [7] Sweilam NH, Abou Hasan MM, Baleanu D. New studies for general fractional financial models of awareness and trial advertising decisions. *Chaos Solit Fractals* 2017; 104: 772-784.
- [8] Liu DY, Gibaru O, Perruquetti W, Laleg-Kirati TM. Fractional order differentiation by integration and error analysis in noisy environment. *IEEE Trans Automat* 2015; 60: 2945–2960.
- [9] Esen A, Sulaiman TA, Bulut H, Baskonus HM. Optical solitons to the space-time fractional (1+1)-dimensional coupled nonlinear Schrödinger equation. *Optik* 2018; 167: 150–156.
- [10] Caponetto R, Dongola G, Fortuna L, Gallo A. New results on the synthesis of FO-PID controllers. *Commun Nonlinear Sci Numer Simul* 2010; 15: 997–1007.
- [11] Veerasha P, Prakasha DG, Baskonus HM. Novel simulations to the time-fractional Fisher's equation. *Math Sci* 2019; 13(1): 33-42.
- [12] Khalil R, Al Horani M, Yousef A, Sababheh M. A new definition of fractional derivative. *J Comput Appl Math* 2014; 264: 65-70.
- [13] Aggarwal S, Chauhan R, Sharma N. 2018. Application of Elzaki transform for solving linear Volterra integral equations of first kind. *Int J Res Advent Technol* 2018; 6(12): 3687-3692.
- [14] Elzaki TM. Applications of new transform “Elzaki transform” to partial differential equations. *Glob J Pure Appl Math* 2011; 7(1): 65-70.

- [15] Elzaki TM. Solution of nonlinear differential equations using mixture of Elzaki transform and differential transform method. In *International Mathematical Forum*, 2012; 7(13): 631-638.
- [16] Elzaki TM, Hilal EMA. Homotopy perturbation and Elzaki transform for solving nonlinear partial differential equations. *Math Theory Model* 2012; 2(3): 33-42.
- [17] Elzaki TM, Kim H. The solution of radial diffusivity and shock wave equations by Elzaki variational iteration method. *Int J Math Anal* 2015; 9(22): 1065-1071.
- [18] Jena RM, Chakraverty S. Solving time-fractional Navier–Stokes equations using homotopy perturbation Elzaki transform. *SN Appl Sci* 2019; 1: 1-16.
- [19] Abu-Gdairi R, Al-Smadi M, Gumah G. An expansion iterative technique for handling fractional differential equations using fractional power series scheme. *J Math Stat* 2015; 11(2), 29–38.
- [20] Baleanu D, Golmankhaneh AK, Baleanu MC. Fractional electromagnetic equations using fractional forms. *Int J Theor Phys* 2009; 48(11): 3114–3123.
- [21] Baleanu D, Jajarmi A, Hajipour M. On the nonlinear dynamical systems within the generalized fractional derivatives with Mittag–Leffler kernel. *Nonlinear Dyn* 2018; 2018(1): 1–18.
- [22] Baleanu, D., Asad, J. H., Jajarmi, A. 2018. New aspects of the motion of a particle in a circular cavity. *Proc Rom Acad Ser A*, 2018; 19(2): 143–149.
- [23] Baleanu D, Jajarmi A, Bonyah E, Hajipour M. New aspects of poor nutrition in the life cycle within the fractional calculus. *Adv Differ Equ* 2018; 2018(1): 1-14.
- [24] Anaç H, Merdan M, Bekiryazıcı Z, Kesemen T. Bazı Rastgele Kısmi Diferansiyel Denklemlerin Diferansiyel Dönüşüm Metodu ve Laplace-Padé Metodu Kullanarak Çözümü. *Gümüşhane Üniversitesi Fen Bilimleri Enstitüsü Dergisi* 2019; 9(1): 108-118.
- [25] Ayaz F. Solutions of the system of differential equations by differential transform method. *Appl Math Comput* 2004; 147(2): 547-567.
- [26] He JH. Variational iteration method-a kind of non-linear analytical technique: some examples. *Int J Non Linear Mech* 1999; 34(4): 699-708.
- [27] He JH. Homotopy perturbation method: a new nonlinear analytical technique. *Appl Math Comput* 2003; 135(1): 73-79.
- [28] He JH. Homotopy perturbation method for solving boundary value problems. *Phys Lett* 2006; 350(1-2): 87-88.
- [29] He JH. Addendum: new interpretation of homotopy perturbation method. *Int J Mod Phys B* 2006; 20(18): 2561-2568.
- [30] Jajarmi A, Baleanu D. Suboptimal control of fractional-order dynamic systems with delay argument. *J Vib Control* 2018; 24(12): 2430-2446.
- [31] Jajarmi A, Baleanu D. A new fractional analysis on the interaction of HIV with CD4+ T-cells. *Chaos Solitons Fractals* 2018; 113: 221-229.

- [32] Kangalgil F, Ayaz F. Solitary wave solutions for the KdV and mKdV equations by differential transform method. *Chaos Solitons Fractals* 2009; 41(1): 464-472.
- [33] Klimek M. Fractional sequential mechanics-models with symmetric fractional derivative. *Czech J Phys* 2001; 51(12): 1348-1354.
- [34] Merdan M. A new applicaiton of modified differential transformation method for modeling the pollution of a system of lakes. *Selçuk J Appl Math* 2010; 11(2): 27-40.
- [35] Alkan A. Improving homotopy analysis method with an optimal parameter for time-fractional Burgers equation. *Karamanoğlu Mehmetbey Üniversitesi Mühendislik ve Doğa Bilimleri Dergisi*, 2022; 4(2): 117-134.
- [36] Wang K, Liu S. A new Sumudu transform iterative method for time-fractional Cauchy reaction-diffusion equation. *Springer Plus* 2016; 5(1): 865.
- [37] Wazwaz AM. A reliable modification of Adomian decomposition method. *Appl Math Comput* 1999; 102(1): 77-86.
- [38] Aslefallah M, Abbasbandy S, Yüzbaşı Ş. (2023). Numerical Solution for a Class of Nonlinear Emden-Fowler Equations by Exponential Collocation Method. *Appl Appl Math* 2023; 18(1): 1-13.
- [39] Abdeljawad, T. 2015. On conformable fractional calculus. *J Comput Appl Math* 2015; 279: 57-66.
- [40] Ala V, Demirbilek U, Mamedov KR. An application of improved Bernoulli sub-equation function method to the nonlinear conformable time-fractional SRLW equation. *AIMS Math* 2020; 5(4): 3751-3761.
- [41] Gözütok U, Çoban H, Sağıroğlu Y. Frenet frame with respect to conformable derivative. *Filomat* 2019; 33(6): 1541-1550.
- [42] Shrinath M, Bhadane A. New conformable fractional Elzaki transformation: Theory and applications. *Malaya J Mat* 2019; 1: 619-625.
- [43] Kaya D, El-Sayed SM. A numerical method for solving Jaulent-Miodek equation. *Phys Lett A*, 2003; 318(4-5): 345-353.
- [44] Cinar M, Onder I, Secer A, Bayram M, Abdulkadir Sulaiman T, Yusuf A. Solving the fractional Jaulent–Miodek system via a modified Laplace decomposition method. *Waves Random Complex Media* 2022; 1-14.
- [45] Silva FS, Moreira DM, Moret MA. Conformable Laplace transform of fractional differential equations. *Axioms*, 2018; 7(3): 55.



RESEARCH ARTICLE

EXACT TRAVELING WAVE SOLUTIONS FOR THE NON-LINEAR COUPLE DRINFEL'D-SOKOLOV-WILSON (DSW) DYNAMICAL SYSTEM USING EXTENDED JACOBI ELLIPTIC FUNCTION EXPANSION METHOD

Nisa ÇELİK¹

Department of Mathematics, Faculty of Arts and Sciences, Bursa Uludag University, 16059 Bursa, Türkiye

ABSTRACT

The study of water waves is significant for researchers working in many branches of science. The behaviour of waves can be studied by observation or experimental means, but theoretically, mathematical modeling provides solutions to many problems in physics and engineering. Progress in this field is inevitable, with those who work in mathematics, physics, and engineering putting forth interdisciplinary studies.

Jacobi elliptic functions are valuable mathematical tools that can be applied to various aspects of mathematics, physics, and ocean engineering. In this study, traveling wave solutions of the general Drinfel'd-Sokolov-Wilson (DSW) system, introduced as a model of water waves, were obtained by using Jacobi elliptic functions and the wave dynamics were examined. The extended Jacobi elliptic function expansion method is an effective method for generating periodic solutions. It has been observed that the periodic solutions obtained by using Jacobi elliptic function expansions containing different Jacobi elliptic functions may be different and some new periodic solutions can be obtained. 3D simulations were made using Maple™ to see the behaviour of the solutions obtained for different appropriate values of the parameters. 2D simulations are presented for easy observation of wave motion. In addition, we transformed the one of the exact solutions found by the extended Jacobi elliptic function expansion method into the new solution under the symmetry transformation.

Keywords: DSW system, Exact solutions, Extended Jacobi elliptic function expansion method

1. INTRODUCTION

Installation of heavy and complex submarine equipment, submarine pipelines and submarine cables has been studied extensively in recent years due to their importance in ocean engineering. Various mathematical models for submarine installation have been obtained and different dynamic behaviours have been studied in various ways. Submarine installations are in the splash zone, completely submerged or close to the seafloor. If the structure is in the splash zone, shallow water waves, if the structure is completely underwater or close to the seabed, seabed waves are effective in the installation [1].

Autonomous underwater vehicles (AUVs) have an indispensable role in the exploration of the deep-sea, marine surveillance, and underwater rescue operations. Due to the intricate nature of the AUV system and the unpredictable underwater environment, controlling them is a challenging task. The control design faces some challenges like high precision multivariate, strong couplings, nonlinearities, and unknown distortions. To overcome these challenges, various control strategies have been developed to create trajectory-tracking controllers for AUVs, such as back step control, pattern predictive control, fuzzy control, and sliding mode control. However, all of these control schemes

require calculations based on the underwater and surface wave strength, highlighting the importance of wave theory in this field [2].

When studying equations that describe wave phenomena, it is necessary to analyse travelling wave solutions. These solutions are permanent forms that move at a constant velocity. To obtain travelling wave solutions, the nonlinear evolution equations are usually reduced to associated ordinary differential equations. Solitary wave theory, which is rapidly advancing in several scientific fields, from shallow water waves to plasma physics, places particular interest in different types of travelling wave solutions [3].

The study of water waves is significant for researchers working in many branches of science. The behaviour of waves can be studied by observation or experimental means, but theoretically, mathematical modeling provides solutions to many problems in physics and engineering. Progress in this field is inevitable, with those who work in mathematics, physics, and engineering putting forth interdisciplinary studies.

Partial differential equations have an important place in the theory of waves. Solutions of a nonlinear partial differential equation can be explained by the concept of waves, which helps us to understand many physical phenomena. If the obtained solutions of the equation can be expressed with the time-dependent motion of a wave, the physical event that occurs can be explained more meaningfully. There are many methods in the literature to obtain wave solutions of partial differential equations. Some of these are the F-expansion method [4], the Jacobi elliptic function expansion method [5,6], (G'/G)-expansion method [7], Lie symmetry approach [8], and so on [9-12].

In modeling multiple events, partial differential equation systems consisting of at least two partial differential equations have an important place in the literature. Partial differential equation systems are also systems whose solutions can be obtained by the methods mentioned above.

The DSW system in dispersive water wave was introduced in 1981 by Drinfel'd and Sokolov [13] and Wilson [14] which resulted in the discovery of wave phenomena that have significant applications in fluid dynamics, ocean engineering, and science. This system serves as the fundamental integrable nonlinear system that describes surface gravitational waves propagating over a horizontal seabed. The DSW equation is expressed in the following form:

$$u_t + \alpha v v_x = 0 \tag{1}$$

$$v_t + \beta u v_x + s u_x v + \eta v_{xxx} = 0$$

The discovery of the DSW system and its wave phenomena has opened new avenues of research in various scientific fields and continues to pave the way for advancements in fluid dynamics and ocean engineering. Some researchers with various methods have studied this system: Shen et al. produced lump, soliton, and lump off solutions [15], Bashar et al. used the new auxiliary equation (NAE) method [16], Khan et al. used the enhanced (G'/G)-expansion method [17], with a special selection Ren et al. used the consistent Riccati expansion method (CRE) [18], etc.

This article is organized as follows: In Chapter 2, we introduced the Jacobi elliptic functions and extended Jacobi elliptic function expansion method [19]. In Chapter 3, we apply these methods to the DSW system and present many solutions. In addition, we transformed the one of the exact solutions found by the new extended direct algebra method into a new solution under the symmetry transformation. We gave numerical simulations of the solutions obtained for different values of the parameters in 3D in Chapter 4. We also gave 2D plots to see how the wave motion changes as time changes. We have given a 2D drawing to see how the wave motion can be realized as time changes. In the last chapter, the results obtained in this study are given.

2. MATERIAL AND METHODS

In this section, information about Jacobi elliptic functions will be given and the extended Jacobi elliptic function expansion method will be introduced.

2.1. Jacobi Elliptic Function

Legendre, who worked for decades on elliptic integrals, first introduced by John Wallis between 1655 and 1659, introduced the normal forms of elliptic integrals that are still in use. Later, in 1828, Jacobi defined the elliptic functions as inverses of the elliptic integrals. Jacobi elliptic functions are obtained by inverting the elliptic integrals of the first kind. For a given constant m , the function snu is defined with the help of the integral

$$u = \int_0^x \frac{dt}{\sqrt{(1-t^2)(1-m^2t^2)}}.$$

When this integral is reversed, then the Jacobi elliptic function snu is defined as $x = snu$. Similarly, cnu and dnu functions can be defined with the help of following identities:

$$sn^2\xi + cn^2\xi = 1, \quad dn^2\xi + m^2 sn^2\xi = 1. \quad (2)$$

where $dn(\xi)$ is a third kind Jacobian elliptic function.

With these definitions, $sn0 = 0$, $cn0 = 1$ and $dn0 = 1$ are obtained clearly. Each Jacobi elliptic function depends on a parameter m and this parameter is called the modulus of the Jacobi elliptical function. The aforementioned double periodic functions have the following properties:

$$\frac{d}{d\xi} sn(\xi) = cn(\xi)dn(\xi), \quad \frac{d}{d\xi} cn(\xi) = -sn(\xi)dn(\xi), \quad \frac{d}{d\xi} dn(\xi) = -m^2cn(\xi)sn(\xi) \quad (3)$$

Other Jacobi functions which is denoted by Glaisher's symbols and are generated by these three kinds of functions, namely.

$$ns\xi = \frac{1}{sn\xi}, \quad nc\xi = \frac{1}{cn\xi}, \quad nd\xi = \frac{1}{dn\xi}, \quad sc\xi = \frac{cn\xi}{sn\xi}, \quad cs\xi = \frac{sn\xi}{cn\xi}, \quad ds\xi = \frac{dn\xi}{sn\xi}, \quad sd\xi = \frac{sn\xi}{dn\xi} \quad (4)$$

that have the relations

$$ns^2\xi - cs^2\xi = 1, \quad ns^2\xi = m^2 + ds^2\xi, \quad sc^2\xi + 1 = nc^2\xi, \quad m^2sd^2\xi + 1 = nd^2\xi$$

with the modals m ($0 < m < 1$).

2.2. Extended Jacobi Elliptic Function Expansion Method

This section presents the extended Jacobi elliptic function expansion method for solving nonlinear evolution equations. Consider a nonlinear evolution equation of the form:

$$P(u, u_x, u_t, u_{xx}, u_{tt}, \dots) = 0 \quad (5)$$

By using the transformation $\xi = k(x - wt)$ and $u(x, t) = U(\xi)$, the Eq(5) can be transformed into an ordinary differential equation of the form

$$B(U, U', U'', \dots) = 0 \tag{6}$$

where $U = U(\xi), U' = \frac{dU}{d\xi}, U'' = \frac{d^2U}{d\xi^2}, \dots$. To find periodic and solitary wave solutions of Eq (5), we assume that $u = u(\xi)$ can be expressed as a finite series of Jacobi elliptic sine and cosine functions.

Using ten different Jacobi elliptic functions, we assume that the solutions of Eq (6) will be in the following forms:

$$u(\xi) = a_0 + \sum_{j=1}^n f_i^{j-1}(\xi) [a_j f_i(\xi) + b_j g_i(\xi)], \quad i = 1, 2, 3, \dots \tag{7}$$

with

$$\begin{aligned} f_1(\xi) &= sn(\xi) \text{ and } g_1(\xi) = cn(\xi) \\ f_2(\xi) &= sn(\xi) \text{ and } g_2(\xi) = dn(\xi) \\ f_3(\xi) &= ns(\xi) \text{ and } g_3(\xi) = cs(\xi) \\ f_4(\xi) &= ns(\xi) \text{ and } g_4(\xi) = ds(\xi) \\ f_5(\xi) &= sc(\xi) \text{ and } g_5(\xi) = nc(\xi) \\ f_6(\xi) &= sd(\xi) \text{ and } g_6(\xi) = nd(\xi) \end{aligned} \tag{8}$$

where n, a_j, b_j ($j = 0, 1, 2, 3, \dots$) are constants.

To determine the value of n , we balance the highest power nonlinear term with the highest order derivative. Thus, the highest degree of $\frac{d^p U}{d\xi^p}$ is taken as:

$$O\left(\frac{d^p U}{d\xi^p}\right) = n + p, \quad p = 1, 2, 3, \dots$$

and the nonlinear term as

$$O\left(U^q \frac{d^p U}{d\xi^p}\right) = (q + 1)n + p, \quad q = 0, 1, 2, 3, \dots$$

Replacing each f_i, g_i in (8) to corresponding f_i, g_i in (7) we get the new ansatz. Then selecting one of these outcomes and substituting it into (6) and equating to zero the coefficients of all powers of elliptic functions, we obtain a system of algebraic equations for a_j, b_j ($j = 0, 1, 2, \dots$). By substituting a_j, b_j in (6), the solution of Eq.(6) is obtained. In this solution of Eq.(6), the solution of Eq.(5) is obtained by taking $\xi = k(x - wt)$ [18].

3. APPLYING THE METHODS TO DSW-SYSTEM

3.1. Extended Jacobi Elliptic Function Expansion Method to DSW System

To apply the extended Jacobi elliptic function expansion method to solve Eq.(1), we substitute the following transformation:

$$u(x, t) = u(\xi), \quad v(x, t) = v(\xi), \quad \xi = k(x - wt)$$

Thus, Eq. (1) can be written in the following form:

$$-kwu' + \alpha kvv' = 0$$

$$-wv' + \beta uv' + su'v + \eta k^2 v''' = 0 \tag{9}$$

From the 1st equation in (9) we have

$$u = \frac{\alpha}{2w} v^2. \tag{10}$$

Using (10) in the 2nd equation in (9) and then integrating, we get undermentioned ODE:

$$-6w^2v + \alpha(\beta + 2s)v^3 + 6\eta wk^2v'' = 0 \tag{11}$$

Balancing the highest power nonlinear term and the highest order derivative yields $n=1$. Since $n = 1$, if (7) is used and $f_1(\xi) = sn(\xi)$ and $g_1(\xi) = cn(\xi)$ are selected from (8), we get

$$v(\xi) = a_0 + a_1 sn(\xi) + b_1 cn(\xi). \tag{12}$$

Using (12) in (11) and collecting all the different powers of $sn^i(\xi)cn^j(\xi), i = 0,1, j = 0..3$, and setting the coefficients of $sn^i(\xi)cn^j(\xi)$ to zero, we obtain a system of nonlinear algebraic equations with respect to a_0, a_1, b_1, k, w which is over-determined system. Solving these equations by the help of Maple™, we get

Set 1:

$$\left\{ a_0 = 0, a_1 = \sqrt{-\frac{3m^2-6}{2\alpha(2s+\beta)}} mk^2\eta, b_1 = \sqrt{-\frac{6-3m^2}{2\alpha(2s+\beta)}} mk^2\eta, w = \frac{\eta k^2(m^2-2)}{2} \right\}. \tag{13}$$

Substituting (13) into (12), we have

$$v_{1,m}(\xi) = \sqrt{-\frac{3m^2-6}{2\alpha(2s+\beta)}} mk^2\eta sn(\xi) + \sqrt{-\frac{6-3m^2}{2\alpha(2s+\beta)}} mk^2\eta cn(\xi)$$

and using (10) we obtain

$$u_{1,m}(\xi) = -\frac{\alpha}{k^2\eta} \left(\sqrt{-\frac{3m^2-6}{2\alpha(2s+\beta)}} mk^2\eta sn(\xi) + \sqrt{-\frac{6-3m^2}{2\alpha(2s+\beta)}} mk^2\eta cn(\xi) \right)^2.$$

If we calculate the limits of $v_{1,m}(\xi), u_{1,m}(\xi)$ for $m \rightarrow 1$, we get $cn(\xi, m) \rightarrow sech(\xi), sn(\xi, m) \rightarrow tanh(\xi)$ and therefore the equations above degenerates into a solution of the DSW equation that is both periodic and exact. It can be written as

$$v_1(\xi) = \frac{\sqrt{6}}{2} \sqrt{\frac{1}{\alpha(2s+\beta)}} k^2\eta tanh(\xi) + \frac{\sqrt{6}}{2} \sqrt{-\frac{1}{\alpha(2s+\beta)}} k^2\eta sech(\xi)$$

$$u_1(\xi) = -\frac{\alpha}{k^2\eta} \left(\frac{\sqrt{6}}{2} \sqrt{\frac{1}{\alpha(2s+\beta)}} k^2\eta tanh(\xi) + \frac{\sqrt{6}}{2} \sqrt{-\frac{1}{\alpha(2s+\beta)}} k^2\eta sech(\xi) \right)^2$$

where $\xi = k(x - wt)$. Therefore the solution of the system (1) is found as

$$\left\{ \begin{aligned} v_1(x, t) &= \frac{\sqrt{6}}{2} \sqrt{\frac{1}{\alpha(2s+\beta)}} k^2\eta tanh(k(x - wt)) + \frac{\sqrt{6}}{2} \sqrt{-\frac{1}{\alpha(2s+\beta)}} k^2\eta sech(k(x - wt)) \\ u_1(x, t) &= -\frac{\alpha}{k^2\eta} \left(\frac{\sqrt{6}}{2} \sqrt{\frac{1}{\alpha(2s+\beta)}} k^2\eta tanh(k(x - wt)) + \frac{\sqrt{6}}{2} \sqrt{-\frac{1}{\alpha(2s+\beta)}} k^2\eta sech(k(x - wt)) \right)^2 \end{aligned} \right\} \tag{14}$$

Set 2:

$$\left\{ a_0 = 0, a_1 = 0, b_1 = \sqrt{-\frac{12-24m^2}{\alpha(2s+\beta)}} mk^2\eta, w = 2\eta k^2 m^2 - \eta k^2 \right\} \quad (15)$$

Substituting (15) into (12), we have

$$v_{2,m}(\xi) = \sqrt{-\frac{12-24m^2}{\alpha(2s+\beta)}} mk^2\eta \operatorname{cn}(\xi)$$

and using (10) we obtain

$$u_{2,m}(\xi) = \frac{(12-24m^2)m^2 k^4 \eta^2}{2(2\eta k^2 m^2 - \eta k^2)(2s+\beta)} \operatorname{cn}^2(\xi, m)$$

If we calculate the limits of $v_{2,m}(\xi), u_{2,m}(\xi)$ for $m \rightarrow 1$, we get $\operatorname{cn}(\xi, m) \rightarrow \operatorname{sech}(\xi)$ and therefore the equations above degenerates into a solution of the DSW equation that is both periodic and exact. It can be written as

$$v_2(\xi) = \frac{2\sqrt{3}k^2\eta}{\sqrt{\alpha(2s+\beta)}} \operatorname{sech}(\xi)$$

$$u_2(\xi) = \frac{6\eta k^2}{2s+\beta} \operatorname{sech}^2(\xi)$$

since $\xi = k(x - wt)$. Therefore, the solution of the system (1) is found as

$$\left\{ v_2(x, t) = \frac{2\sqrt{3}k^2\eta}{\sqrt{\alpha(2s+\beta)}} \operatorname{sech}(k(x - wt)), u_2(x, t) = \frac{6\eta k^2}{2s+\beta} \operatorname{sech}^2(k(x - wt)) \right\}. \quad (16)$$

Set 3:

$$\left\{ a_0 = 0, a_1 = \sqrt{\frac{12m^2+12}{\alpha(2s+\beta)}} mk^2\eta, b_1 = 0, w = -\eta k^2(m^2 + 1), k = k \right\} \quad (17)$$

Substituting (17) into (12), we have

$$v_{3,m}(\xi) = \sqrt{\frac{12m^2+12}{\alpha(2s+\beta)}} mk^2\eta \operatorname{sn}(\xi, m)$$

and using (10) we have

$$u_{3,m}(\xi) = -\frac{6m^2 k^2 \eta}{2s+\beta} \operatorname{sn}^2(\xi, m).$$

If we calculate the limits of $v_{3,m}(\xi), u_{3,m}(\xi)$ for $m \rightarrow 1$, we get $\operatorname{sn}(\xi, m) \rightarrow \tanh(\xi)$ and therefore the equations above degenerates into a solution of the DSW equation that is both periodic and exact. It can be written as

$$v_3(\xi) = 2\sqrt{6}k^2\eta \sqrt{\frac{1}{\alpha(2s+\beta)}} \tanh(\xi)$$

$$u_3(\xi) = -\frac{6\eta k^2 \tanh^2(\xi)}{2s+\beta},$$

since $\xi = k(x - wt)$. Then the solution of the system (1)

$$\left\{ v_3(x, t) = 2\sqrt{6}k^2\eta \sqrt{\frac{1}{\alpha(2s+\beta)}} \tanh(k(x-wt)), u_3(x, t) = -\frac{6\eta k^2 \tanh^2(k(x-wt))}{2s+\beta} \right\}. \quad (18)$$

Now since $n = 1$, if (7) is used and $f_3(\xi) = ns(\xi)$ and $g_3(\xi) = cs(\xi)$ are selected from (8), we get

$$v(\xi) = a_0 + a_1 ns(\xi) + b_1 cs(\xi). \quad (19)$$

Using (18) in (11) and collecting all the different powers of $ns^i(\xi)cs^j(\xi), i = 0,1, \dots, 6, j = 0,1$, and setting the coefficients of $ns^i(\xi)cs^j(\xi)$ to zero, we obtain a system of nonlinear algebraic equations with respect to k, w, a_0, a_1, b_1 which is over-determined system. Solving these equations by the help of the Maple™, we get

Set 1:

$$\left\{ a_0 = 0, a_1 = \sqrt{\frac{12m^2+12}{\alpha(2s+\beta)}} k^2\eta, b_1 = 0, w = -\eta k^2(1+m^2) \right\} \quad (20)$$

Substituting (20) into (19), we have

$$v_{4,m}(\xi) = \sqrt{\frac{12m^2+12}{\alpha(2s+\beta)}} k^2\eta ns(\xi)$$

and using (10) we obtain

$$u_{4,m}(\xi) = -\frac{12m^2+12}{4(2s+\beta)} k^2\eta ns^2(\xi).$$

If we calculate the limits of $v_{4,m}(\xi), u_{4,m}(\xi)$ for $m \rightarrow 1$, we get $ns(\xi, m) \rightarrow coth(\xi)$ and therefore the equations above degenerates into a solution of the DSW equation that is both periodic and exact. It can be written as

$$v_4(\xi) = 2\sqrt{6} \sqrt{\frac{1}{\alpha(2s+\beta)}} k^2\eta coth(\xi)$$

$$u_4(\xi) = -\frac{6k^2\eta}{2s+\beta} coth^2(\xi)$$

where $\xi = k(x-wt)$. Then the solution of the system (1) is found as

$$\left\{ v_4(x, t) = 2\sqrt{6} \sqrt{\frac{1}{\alpha(2s+\beta)}} k^2\eta coth(k(x-wt)), u_4(x, t) = -\frac{6\eta k^2 coth^2(k(x-wt))}{2s+\beta} \right\}. \quad (21)$$

Now since $n = 1$, if (7) is used and $f_4(\xi) = ns(\xi)$ and $g_4(\xi) = ds(\xi)$ are selected from (8), we get

$$v(\xi) = a_0 + a_1 ns(\xi) + b_1 ds(\xi) \quad (22)$$

Using (22) in (11) and collecting all the different powers of $sn^i(\xi)dn^j(\xi), i = 0,1, j = 0..3$, and setting the coefficients of $sn^i(\xi)dn^j(\xi)$ to zero, we obtain a system of nonlinear algebraic equations with respect to a_0, a_1, b_1, k, w which is over-determined. Solving these equations by the help of the Maple™, we get

Set 1:

$$\left\{ a_0 = 0, \quad a_1 = \sqrt{\frac{12(1+m^2)}{\alpha(2s+\beta)}} k^2 \eta, \quad b_1 = 0, \quad k = k, \quad w = -\eta k^2 (m^2 + 1) \right\}. \quad (23)$$

Substituting (23) into (22), we have

$$v_{5,m}(\xi) = \sqrt{\frac{12(1+m^2)}{\alpha(2s+\beta)}} k^2 \eta \operatorname{ns}(\xi)$$

and using (10) we obtain

$$u_{5,m}(\xi) = -3 \frac{k^2 \eta (m^2 + 1)}{2s + \beta} \operatorname{ns}^2(\xi).$$

If we calculate the limits of $v_{5,m}(\xi), u_{5,m}(\xi)$ for $m \rightarrow 1$, we get $\operatorname{ns}(\xi, m) \rightarrow 1/\tanh(\xi)$ and therefore the equations above degenerates into a solution of the DSW equation that is both periodic and exact. It can be written as

$$v_5(\xi) = 2 \sqrt{\frac{6}{\alpha(2s+\beta)}} k^2 \eta \frac{1}{\tanh(\xi)}$$

$$u_5(\xi) = -\frac{6k^2 \eta}{(2s+\beta)} \frac{1}{\tanh^2(\xi)}$$

where $\xi = k(x - wt)$. Then the solution of the system (1) is found as

$$\left\{ v_5(x, t) = 2 \sqrt{\frac{6}{\alpha(2s+\beta)}} k^2 \eta \frac{1}{\tanh(k(x-wt))}, \quad u_5(x, t) = -\frac{6k^2 \eta}{(2s+\beta)} \frac{1}{\tanh^2(k(x-wt))} \right\}. \quad (24)$$

Set 2:

$$\left\{ a_0 = 0, \quad a_1 = 0, \quad b_1 = \sqrt{\frac{12(1-2m^2)}{\alpha(2s+\beta)}} k^2 \eta, \quad k = k, \quad w = -\eta k^2 (m^2 + 1) \right\} \quad (25)$$

Substituting (25) into (22), we have

$$v_{6,m}(\xi) = \sqrt{\frac{12(1-2m^2)}{\alpha(2s+\beta)}} k^2 \eta \operatorname{ds}(\xi)$$

and using (10) we obtain

$$u_{6,m}(\xi) = -\frac{k^2 \eta (2m^2 - 1)}{2s + \beta} \operatorname{ds}^2(\xi).$$

If we calculate the limits of $v_{6,m}(\xi), u_{6,m}(\xi)$ for $m \rightarrow 1$, we get $\operatorname{ds}(\xi, m) \rightarrow \operatorname{sech}(\xi)/\tanh(\xi)$ and therefore the equations above degenerates into a solution of the DSW equation that is both periodic and exact. It can be written as

$$v_6(\xi) = 2 \sqrt{\frac{-3}{\alpha(2s+\beta)}} k^2 \eta \frac{\operatorname{sech}(\xi)}{\tanh(\xi)}$$

$$u_6(\xi) = -\frac{6k^2 \eta}{(2s+\beta)} \frac{\operatorname{sech}^2(\xi)}{\tanh^2(\xi)}$$

where $\xi = k(x - wt)$. Then the solution of the system (1) is found as

$$\left\{ v_6(x, t) = 2 \sqrt{\frac{-3}{\alpha(2s+\beta)}} k^2 \eta \frac{\operatorname{sech}(\xi)}{\tanh(\xi)}, \quad u_6(x, t) = -\frac{6k^2 \eta}{(2s+\beta)} \frac{\operatorname{sech}^2(\xi)}{\tanh^2(\xi)} \right\}. \quad (26)$$

Set 3:

$$\left\{ a_0 = 0, a_1 = \sqrt{-\frac{3m^2-6}{2\alpha(2s+\beta)}} k^2 \eta, b_1 = \sqrt{-\frac{3m^2-6}{2\alpha(2s+\beta)}} k^2 \eta, w = \frac{\eta k^2 (m^2-2)}{2} \right\}. \tag{27}$$

Substituting (27) into (21), we have

$$v_{7,m}(\xi) = \sqrt{-\frac{3m^2-6}{2\alpha(2s+\beta)}} k^2 \eta ns(\xi) + \sqrt{-\frac{3m^2-6}{2\alpha(2s+\beta)}} k^2 \eta ds(\xi)$$

and using (10) we obtain

$$u_{7,m}(\xi) = -\frac{\alpha}{k^2 \eta} \left(\sqrt{-\frac{3m^2-6}{2\alpha(2s+\beta)}} k^2 \eta ns(\xi) + \sqrt{-\frac{3m^2-6}{2\alpha(2s+\beta)}} k^2 \eta ds(\xi) \right)^2.$$

If we calculate the limits of $v_{7,m}(\xi), u_{7,m}(\xi)$ for $m \rightarrow 1$, we get $ns(\xi, m) \rightarrow \frac{1}{\tanh(\xi)}, ds(\xi, m) \rightarrow \frac{\operatorname{sech}(\xi)}{\tanh(\xi)}$ and therefore the equations above degenerates into a solution of the DSW equation that is both periodic and exact. It can be written as

$$v_7(\xi) = \sqrt{\frac{6}{\alpha(2s+\beta)}} k^2 \eta \frac{(1+\operatorname{sech}(\xi))}{2 \tanh(\xi)}$$

$$u_7(\xi) = -\frac{3k^2 \eta (1+\operatorname{sech}(\xi))^2}{2(2s+\beta) \tanh^2(\xi)}$$

where $\xi = k(x - wt)$. Then the solution of the system (1) is found as

$$\left\{ v_7(x, t) = \sqrt{\frac{6}{\alpha(2s+\beta)}} k^2 \eta \frac{(1+\operatorname{sech}(\xi))}{2 \tanh(\xi)}, u_7(x, t) = -\frac{3k^2 \eta (1+\operatorname{sech}(\xi))^2}{2(2s+\beta) \tanh^2(\xi)} \right\}. \tag{28}$$

3.2. New Exact Solution by Lie Transformation Groups

Lie symmetry analysis is one of the most general and effective methods for obtaining exact solutions of nonlinear partial differential equations. In the last few decades, Lie’s method has been applied to a number of physical and engineering models. Solutions of partial differential equations can be transformed into another solution under the act of any symmetry group. Solutions that do not change under a symmetry transformation are called invariant solutions.

In this section, we will transform the exact solution (26) of the system (1) obtained by the extended Jacobi elliptic function method into a new solution under the symmetry transformation.

Essential aim is to yield one new exact solution by the transformation groups of which makes the Eq. (1) invariant.

Equation (1) accepts a three dimensional Lie algebra having the generators given below:

$$X_1 = \frac{\partial}{\partial t}, X_2 = \frac{\partial}{\partial x}, X_3 = 3t \frac{\partial}{\partial t} + x \frac{\partial}{\partial x} - 2u \frac{\partial}{\partial u} - 2v \frac{\partial}{\partial v}.$$

Thus, one parameter $G_i, (i = 1,2,3)$ groups produced by $X_i, (i = 1,2,3)$ can be obtained in the following form:

$$G_1: (t, x, u, v) \rightarrow (t + \varepsilon, x, u, v),$$

$$G_2: (t, x, u, v) \rightarrow (t, x + \varepsilon, u, v),$$

$$G_3: (t, x, u, v) \rightarrow (te^{3\varepsilon}, xe^\varepsilon, ue^{-2\varepsilon}, ve^{-2\varepsilon}).$$

Let us consider the nontrivial generator X_3 , then the transformation $\{\bar{u} = f_1(\bar{x}, \bar{t}), \bar{v} = f_2(\bar{x}, \bar{t}), \{u(z, t) = f(xe^\varepsilon, te^{3\varepsilon})e^{2\varepsilon}, v(z, t) = f(xe^\varepsilon, te^{3\varepsilon})e^{2\varepsilon}\}$ is obtained as corresponding transformation where

$$\begin{aligned} \bar{x} &= xe^\varepsilon & \bar{x} &= xe^\varepsilon \\ \bar{t} &= te^{3\varepsilon} & \bar{t} &= te^{3\varepsilon} \\ \bar{v} &= ve^{-2\varepsilon} & \bar{v} &= ve^{-2\varepsilon} \end{aligned}$$

We know from the theory of Lie groups that using these variables the solution $\{u(x, t), v(x, t)\}$ of the Eq. (1) transforms into another solution of the Eq. (1). Under this symmetry transformation, using solution (26) of the DSW system obtained by the extended Jacobi elliptic function expansion method we reach to the following solution

$$\begin{aligned} u_{new} &= -\frac{6\eta k^2 \operatorname{sech}(k(-wte^{3\varepsilon} + xe^\varepsilon))^2}{(2s + \beta) \tanh(k(-wte^{3\varepsilon} + xe^\varepsilon))^2} \\ v_{new} &= -\frac{6\eta k^2 \operatorname{sech}(k(-wte^{3\varepsilon} + xe^\varepsilon))^2 e^{2\varepsilon}}{(2s + \beta) \tanh(k(-wte^{3\varepsilon} + xe^\varepsilon))^2}. \end{aligned}$$

Then the solution of the system (1) is found as

$$\left\{ v_{new}(x, t) = -\frac{6\eta k^2 \operatorname{sech}(k(-wte^{3\varepsilon} + xe^\varepsilon))^2 e^{2\varepsilon}}{(2s + \beta) \tanh(k(-wte^{3\varepsilon} + xe^\varepsilon))^2}, u_{new}(x, t) = -\frac{6\eta k^2 \operatorname{sech}(k(-wte^{3\varepsilon} + xe^\varepsilon))^2}{(2s + \beta) \tanh(k(-wte^{3\varepsilon} + xe^\varepsilon))^2} \right\}. \quad (29)$$

New solutions can be obtained in the same way by using other solutions.

4. GRAPHICAL REPRESENTATIONS OF THE RESULT

Graphs are a powerful tool commonly used to visually represent and communicate data and information. The purpose of graphics is to make data more meaningful and accessible. They are also used to reduce complexity, facilitate focus, and provide quick understanding. In this section, we visualized the exact solutions we obtained using the extended Jacobi elliptic method with specific parameter values in 2D and 3D graphs. These graphs were intended to assist readers in better understanding and interpreting the solutions.

Figure 1 given below is given for to show the behaviour of (14) by using the parameters $\{\alpha = -1, \beta = 3, s = 1, \eta = 3, k = 1, w = -\frac{3}{2}\}$ (in complex plane)

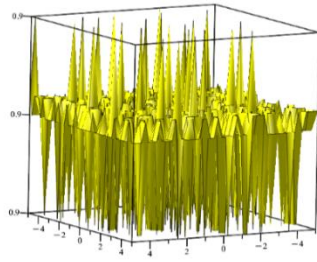
Figure 2 given below is given for to show the behaviour of (14) by using the parameters $\{\alpha = -1, \beta = 3, s = 1, \eta = 3, k = 1, w = -\frac{3}{2}\}$ (in real plane)

Figure 3 given below is given for to show the behaviour of (21) by using the parameters $\{\alpha = 1, \beta = 1, s = 1, \eta = -2, k = \frac{1}{2}, w = 1\}$

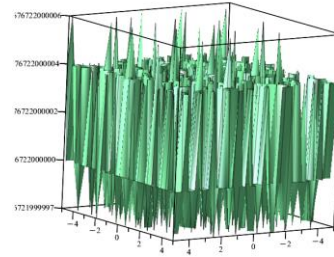
Figure 4 given below is given for to show the behaviour of (24) by using the parameters $\{\alpha = 1, \beta = 1, s = 1, \eta = -2, k = 1, w = 4\}$

Figure 5 given below is given for to show the behaviour of (28) by using the parameters $\{\alpha = 1, \beta = 1, s = 1, \eta = 1, k = 1, w = -\frac{1}{2}\}$

Figure 6 given below is given for to show the behaviour of (29) by using the parameters $\{\alpha = 1, \beta = 1, s = 1, \eta = 1, k = 1, \varepsilon = \frac{1}{3}, w = -\frac{1}{2}\}$

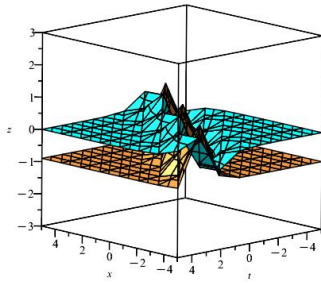


$u_1(x, t)$

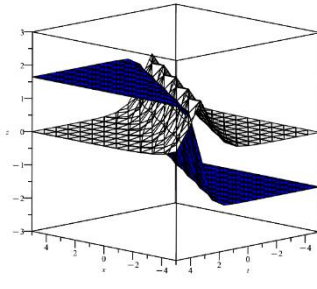


$v_1(x, t)$

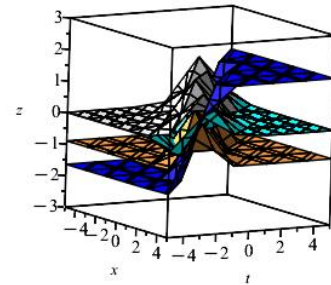
Figure 1. Profile of solution (14)



$\{Re(u_1(x, t)), Im(u_1(x, t))\}$

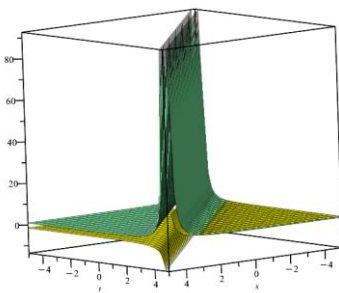


$\{Re(v_1(x, t)), Im(v(x, t))\}$

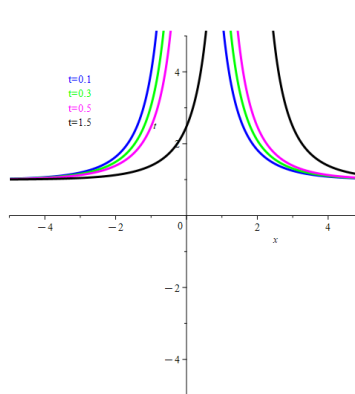


$\{Re(u_1(x, t)), Im(u_1(x, t)), Re(v_1(x, t)), Im(v(x, t))\}$

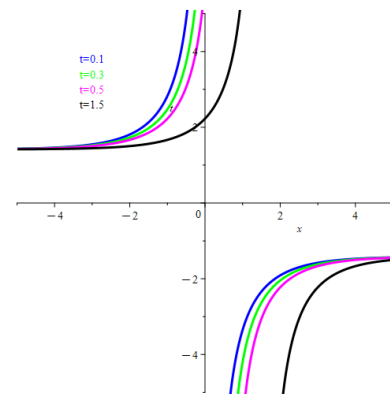
Figure 2. Profile of solution (14)



$\{u_4(x, t), v_4(x, t)\}$



$u_4(x, t_i)$



$v_4(x, t_i)$

Figure 3. Profile of solution (21)

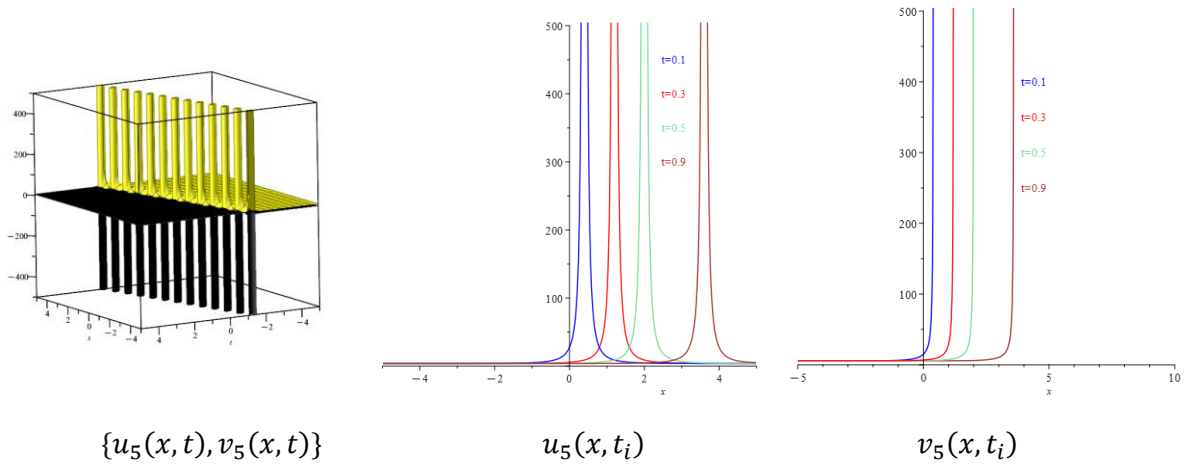


Figure 4. Profile of solution (24)

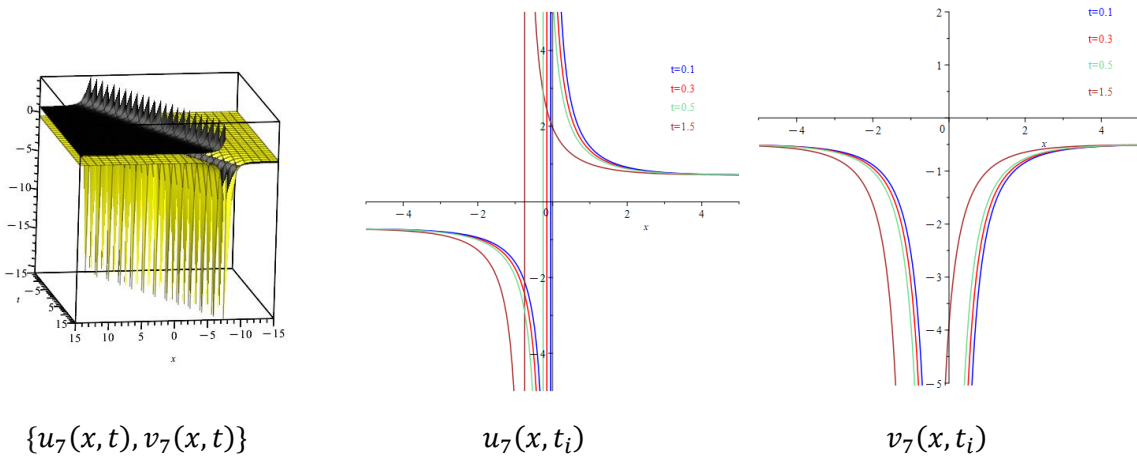


Figure 5. Profile of solution (28)

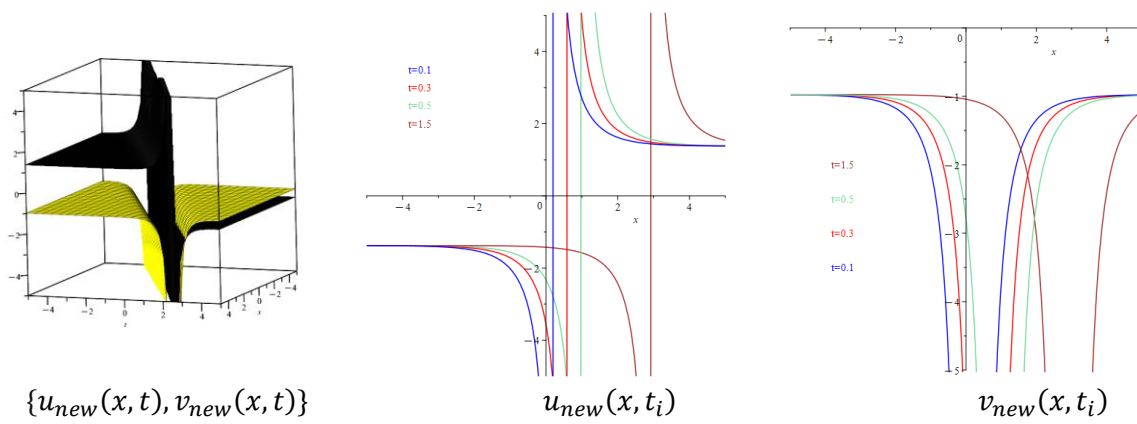


Figure 6. Profile of solution (29)

5. CONCLUSIONS

In this study, the extended Jacobi elliptic function expansion method was applied to the DSW system and the exact solutions of this system were obtained. Research has demonstrated that the periodic wave solutions derived from the Jacobi elliptic function expansion may vary depending on the choice of the Jacobi elliptic function used. Consequently, this approach can lead to the discovery of a multitude of novel periodic solutions as well as shock wave or solitary wave solutions. The physical characterization of some solutions obtained in our study is depicted in two- and three-dimensional graphics. We produced new solutions with the help of Lie symmetry groups previously given in the literature. The new solution is graphed in Figure 6.

When we reviewed the literature, we noticed that some of the solutions obtained in [17] structurally resemble the solutions we obtained in (14), (16), (18), and (21). However, the enhanced (G'/G) -expansion method used in [17] includes parameters associated with hyperbolic function variables due to the auxiliary equation used in the application of the method. On the other hand, the extended Jacobi elliptic function expansion method we used does not require an auxiliary equation. Therefore, although the solutions we obtained structurally resemble each other, it is observed that different solutions emerge when looking at the hyperbolic function variables they contain. Additionally it is seen that the solutions (16) and (18) obtained in this study coincide with the solutions obtained using the Jacobi elliptic function expansion method of the same system [20]. According to our research, other solutions obtained are not available in the literature.

Figure 1 shows the multi soliton solution of (14) at special parameter values in the complex space. In Figure 2, a kink shape soliton and a bell shape soliton together represent the solution. Figure 3 shows a bright soliton and singular kink shape soliton. Figure 4 shows the periodic wave solution. The multi soliton solution is also seen in Figure 5. In Figure 6, we see that a singular kink wave and a kink wave together represent the solution.

From the open literature, we notice that Lie symmetry analysis of system (1) is carried out with special coefficient selection. Zhang and Zhao made a special case Lie symmetry analysis of the system by choosing $\alpha=2, \beta=3k, s=3b, \eta=-a$ [21]. They systematically constructed the Lie symmetries together with some symmetry reductions and group invariant solutions corresponding to this reduction. In their study, we saw that the symmetry generators obtained in the special case of the DSW-system and the generators we obtained for the general DSW-system are the same. Therefore, with the new solution generation method we use, an even richer solution set of the system can be obtained.

The obtained solutions were checked one by one by substituting them in the equations of the system with Maple. Numerical simulations of the solutions obtained from the method discussed were performed for specific parameter values.

We think that the new wave solutions obtained by applying extended Jacobi elliptic expansion method from the DSW system, resulting from the interaction between water waves and long waves, will have a significant impact on the field of ocean engineering. Furthermore, this research has the potential to provide novel perspectives on the behaviour of various scientific phenomena.

The solutions obtained can be used as an auxiliary function in the modeling of autonomous underwater vehicles, in the installation of heavy and complex submarine equipment, in the placement of submarine pipelines and submarine cables. We also believe that it will be useful for those working in the fields of physics and engineering in interpreting ocean waves, the physics of underwater sound and how to make sense of sounds underwater.

CONFLICT OF INTEREST

The researcher declared that she had no conflicts of concern relating to the publication of this research.

REFERENCES

- [1] Andre EM, Costa DO, Fernandes AC, Junior JSS. A review on the modelling of subsea lifting operations, *Ocean Engineering*, 2023; 268: 113293.
- [2] Sun H, Zong G, Cui J, Shi K. Fixed-time sliding mode output feedback tracking control for autonomous underwater vehicle with prescribed performance constraint. *Ocean Engineering*, 2022 ; 247: 110673.
- [3] Wazwaz AM. *Partial Differential Equations and Solitary Waves Theory*, Nonlinear Physical Science. Saint Xavier University, 2009; Chicago, IL 60655.
- [4] Çelik N, Seadawy AR., Sağlam Y, Yaşar E. A model of solitary waves in a nonlinear elastic circular rod: Abundant different type exact solutions and conservation laws. *Chaos, Solitons and Fractals*, 2021; 143: 1-19, 110486.
- [5] Sait S. Extended Jacobi elliptic function solutions for general boussinesq systems. *Revista Mexicana de Física*, 2023; 69.2 Mar-Apr: 021401-1.
- [6] Sait S, Altunay R. Abundant travelling wave solutions of 3+ 1 dimensional Boussinesq equation with dual dispersion. *Revista Mexicana de Física*, E 2022; 19 (2 Jul-Dec): 020203-1.
- [7] Rezazadeh H, Davadi AG, Gholami D. Combined formal periodic wave-like and soliton-like solutions of the conformable Schrödinger-KdV equation using the G'/G -expansion technique. *Results in Physics*, 2023; 47-106352.
- [8] San S, Yaşar E. On the Lie symmetry analysis, analytic series solutions, and conservation laws of the time fractional Belousov–Zhabotinskii system. *Nonlinear Dynamics*, 2022; 109(4): 2997-3008.
- [9] Jhangeer A, Seadawy A.R, Ali F, Ahmed Abbirah. New complex waves of perturbed Schrödinger equation with Kerr law nonlinearity and Kundu-Mukherjee-Naskar equation. *Result in Physics*, 2020; 16-102816.
- [10] Rehman UH, Ullah N, Imran MA. Optical solitons of Biswas-Arshed equation in birefringent fibers using extended direct algebraic. method. *International Journal for Light and Electron Optics-Optik*, 2021; 226: 1-15, 165378.
- [11] Günhan AN, Yaşar E. A new (3+ 1) dimensional Hirota bilinear equation: Painlavé integrability, Lie symmetry analysis, and conservation laws. *Journal of Taibah University for Science*, 2022; 16(1): 1287-1297.
- [12] Rabie WB, Ahmed HM, Mirzazadeh M, Akbulut A, Hashemi MS. Investigation of solitons and conservation laws in an inhomogeneous optical fiber through a generalized derivative nonlinear Schrödinger equation with quintic nonlinearity. *Optical and Quantum Electronics*, 2023; 55(9): 825.

- [13] Drinfel'd VG, Sokolov VV. Equations of Korteweg–de Vries type, and simple Lie algebras Sov. Math. Dokl., 1981; 23: 457–462.
- [14] Wilson G. The affine Lie algebra $C(1, 2)$ and an equation of Hirota and Satsuma. Physics Letters A, 1982; 89.7: 332-334.
- [15] Shen S, Ding X, Zhang R, Hu X. Intereaction solutions to the (1+1)-dimensional generalized Drinfel'd-Sokolov-Wilson equation. Modern Physics Letters B, 2019; 33(27) :1950329.
- [16] Bashar MdH, Yiasir SMA, Islam SMR, Rahman MM. Wave solutions of the couple Drinfel'd-Sokolov-Wilson equation: New wave solutions and free parameters effect. Journal of Ocean Engineering and Science, 2022.
- [17] Khan K, Akbar M A, Koppelaar H. Study of coupled nonlinear partial differential equations for finding exact analytical solutions. Royal Society open science, 2015: 2(7); 140406.
- [18] Ren B, Lin J, Lou ZM. Consistent Riccati expansion and rational solutions of the Drinfel'd Sokolov-Wilson equation. Applied Mathematics Letter, 2020: 105; 106326.
- [19] Emad HM, Zahran, Mostafa MA Khater. Exact Traveling Wave Solutions for the System of Shallow Water Wavw Equations and Modified Liouville Equation Using Extended Jacobian Elliptic Function Expansion Method. American Journal of Computational Mathematics, 2014: 4; 455-463.
- [20] Çelik N. Nonlinear models in Ocean Engineering: Exact solutions, 3D and 2D simulations of the General Drinfel'd-Sokolov-Wilson system with Jacobi Elliptic Functions. MAS 18th International European Conference on Mathematics, Engineering, Natural&Medical Sciences, 2023; 112-119.
- [21] Zhang Y, Zhao Z. Lie symmetry analysis, Lie Backlund symmetries, explicit solutions, and conservation laws of Drinfeld-Sokolov-Wilson system. Boundry Value Problems, 2017: 154; 2-7.



MEMORY-BASED SELF-ORDERING FFT FOR EFFICIENT I/O SCHEDULING

Zeynep KAYA ¹ , Erol SEKE ^{2*} 

¹ Dept. of Electrical-Electronics Eng., Engineering, Şeyh Edebalı University, Bilecik, Turkey

² Dept. of Electrical-Electronics Eng., Engineering and Architecture, Osmangazi University, Eskişehir, Turkey

ABSTRACT

A complex-valued self-ordering radix-2 memory-based Fast Fourier Transform (FFT) architecture suitable for low end Field Programmable Gate Arrays (FPGA) is presented. Employing a self-ordering algorithm within the data flow, both input and output data are kept in normal sequential order, not in digit-reversed-order. This way, with an appropriate scheduling, last stage of the FFT and I/O operations are performed in parallel with no wait states. Self-ordering FFT algorithms are generally designed for software implementations. We designed and implemented one on FPGA (hardware), showing that considerable number of clock cycle savings can be obtained compared to unordered FFT counterparts. The approach is implemented on various FPGAs. The results are compared with similar radix-2 architectures in terms of required clock cycles and resource usage, confirming the advantage of the approach.

Keywords: FFT, DFT, memory-based FFT, self-ordering, FPGA, radix-2

1. INTRODUCTION

Discrete Fourier Transform (DFT) is almost always implemented as FFT (Fast Fourier Transform) and used in wide range of signal processing applications like high performance communications and image processing. Since it is computationally intensive, hardware implementations find a valuable place when real-time applications require it. Some researchers prefer pipeline FFT architectures to perform continuous data flow and high speed [1,3-5,15]. Other researchers employ memory-based FFT architectures because of the lower resource requirements and lesser occupied chip area [6,12,14,19]. Low resource and low power usage is especially important for hand-held battery powered devices. Figure 1 illustrates the recursive structure of the FFT, which enables designers create various software and hardware implementations depending on the applications' requirements and availability of the resources.

The term memory-based refers to the hardware design that continuously reads relatively small chunks of data from memory for intermediate FFT operations and writes the results back to the memory, repeating this until the complete FFT result appears in the memory. This is similar to software approach but done with hardware with higher parallelism and speed. Many researchers use memories with a capacity of $2N$ [8,18] or greater $2N+$ [14] for N -point FFT, in order to improve speed and/or to avoid memory conflicts. It should be noted that aiming minimum memory (size N) gains importance when N is large and posing problems in small FPGAs. However, it is possible to reduce memory down to N with the efficient addressing algorithms [6,10,12].

Researchers try to improve performance by improving parallelism (reading/writing larger chunks, higher radix FFT) by proposing various memory addressing schemas, by efficient data feed-in/out to/from this structure and/or by reducing the resource (memory, chip area etc.) requirements [11,17,19]. The studies of Xiao *et al.* [20,21] improved the address generation logic that has critical path independent of the transform size, hence suggested for large transforms by the authors. In the study of Ma *et al.* [12], researchers used two processing elements (PEs) working in parallel for radix-2 FFT on

*Corresponding Author: eseke@ogu.edu.tr

Received: 06.12.2023 Published: 28.03.2024

real-valued input data. Garrido *et al.* [6] proposed a radix-4 algorithm on 4 blocks of memory of size $N/4$ each. FFT results are inherently in bit-reversed order and may require reordering at the end. However, using high-radix FFT increase the amount of the hardware and parallel PEs complicates the addressing algorithm. In our study, we achieve radix-2 FFT with self-ordering addressing algorithm without any conflict by using simple counters and one PE, in order to show that obtaining already-ordered output reduces both the total number of required clock cycles and memory.

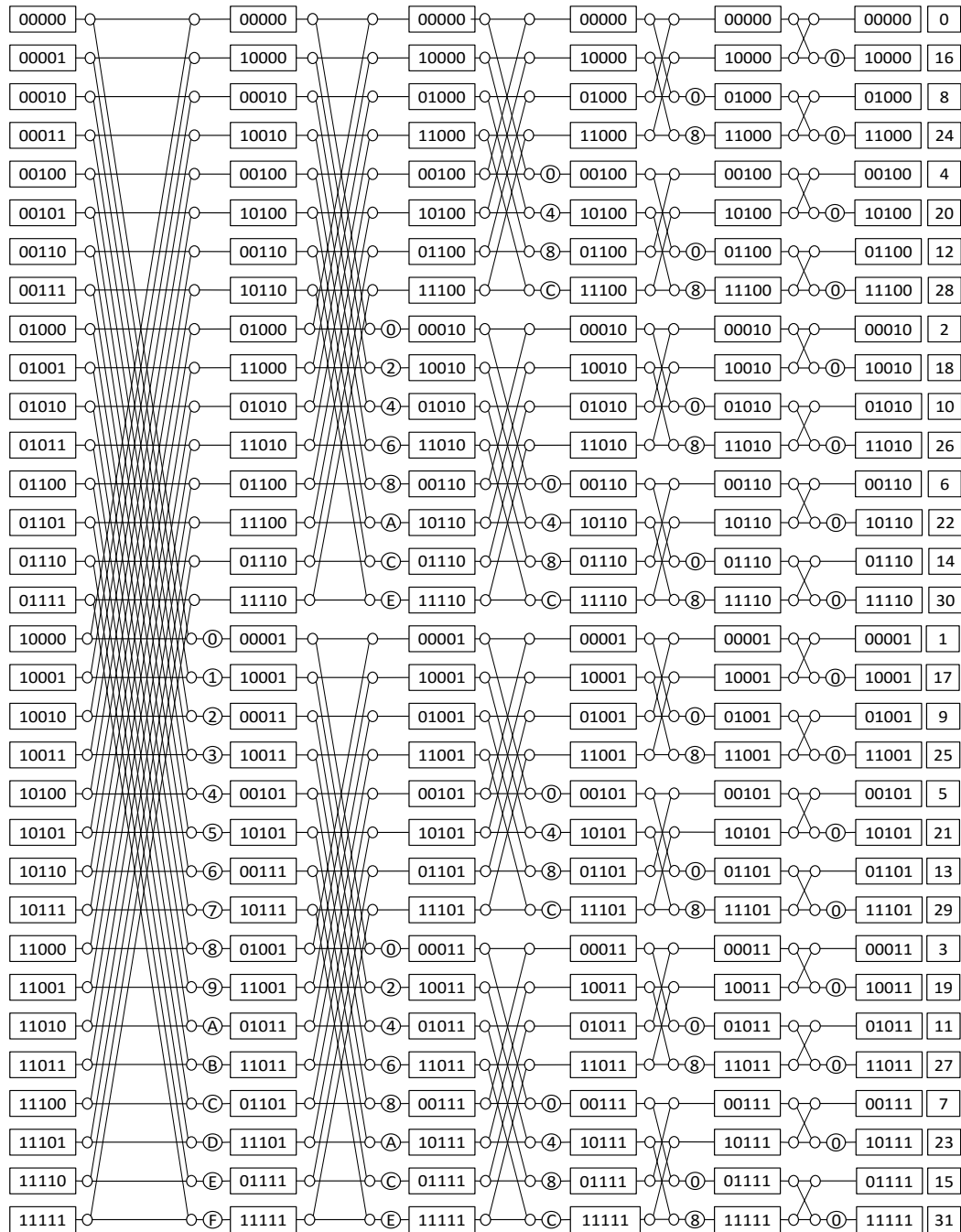


Figure 1. Radix-2 $N=32$ DIF FFT process tree showing actual memory addresses in binary to expose the self-ordering process

Memory addressing schemes are available for general memory-based FFT architectures which facilitate normal ordered FFT outputs [7,14,16]. There exist normal ordered input/output designs [7] implemented

in ASIC for special high throughput requirements. The radix-16 512-point FFT chip in the work of Huang and Chen [7] uses 16 blocks of memory and is not customized for FPGA implementations for different needs. Each memory block has only 32 locations, hardly holding the “memory-based FFT” title. It requires 16 complex floating-point multipliers, not suitable for small FPGAs.

Two methods for self-sorting FFT algorithm are presented in the works of Chu and George [2] and Johnson and Burrus [9]. The work of Chu and George [2] requires in-place swapping of data after each stage, whereas swapping in the latter [9] is performed on the write-addresses. However, both methods are designed for software implementations and is not restricted by resource count limitations faced by hardware implementations. For example, there can never be a memory access conflict in a software implementation.

Currently, all practical FFT implementations on hardware platforms reorder the output data after FFT processing is finished, either by transferring the unordered data to the ordering circuit or performing the sorting in place and preventing the new data loading during the sort. Since the output data is in bit-reversed order, it is not possible to start a new in-place FFT cycle during these operations.

In this study, we aim for re-configurable low-capacity FPGA needs and ordered input/output capability. For ordered input/output, we implemented the methods of [2,9] in hardware by performing stage operations in a special order that prevents memory access conflicts while doing one PE calculation per clock cycle. We took the advantage of ordered i/o and used it for further parallelism by parallelizing input, output and last stage processing.

In the following subsections, basics of memory based FFT and self-sorting algorithm are given briefly. Section 2 details the implemented FFT hardware where each subsection describes a specific part (problems in and solutions developed for) of the circuit. Since the rotator (twiddle factors) generation can be handled as a separate part of the problem, we did not spare a specific section for that as the purpose of this paper is to develop an addressing method for self-ordering and scheduling. However, in implementations we used a quarter cycle look-up table for providing real and imaginary parts of the twiddle factors. Clock cycle comparisons are given with similar FFT hardware implementations in Section 3.

1.1. Memory-Based FFT

Assuming that the data to be processed is already loaded into memory of size- N where N is an integer power of r , radix- r memory based FFT algorithm with single processing element reads r memory locations, performs radix- r FFT on them, and writes the r sub-results back into the memory. Data flow from/to memory for $N = 2^5=32$ radix-2 FFT is given in Figure 1, as an example. Connections within stages show the memory locations read (from left) and written (to right). When radix-2 FFT results are written back to the locations originally occupied by the two-input data of the elementary 2in-2out computation, the final FFT results are normally in bit-reversed order and can be ordered with additional processing and possibly with additional hardware resources. With the implementation of self-sorting, the memory addresses are swapped at each stage as shown in binary in Figure 1. Note that, although the FFT tree shown in Figure 1 remains the same, the output data memory locations are in the same order with the output data index (normal ordered data indexes).

We claim that, in this paper, by applying a self-ordering algorithm within stage processing to obtain the results in normal order, reading the final results out and writing in new data for the next round of FFT can also be done in parallel. That is, data from the last stage calculations need not be written back into memory, instead the ordered data can be sent to output. Simultaneously, since the intermediate data in these memory locations will no longer be needed, new data can be loaded. This means, clock cycles required for data read-in/read-out are completely eliminated from the total clock count. Therefore, we

claim that the benefits of applying a self-ordering algorithm are; ordered data at the output, considerable savings on total clock cycles. It should be noted that, without self-ordered outputs, reading in new input data could not have been performed simultaneously with reading out FFT data as the memory locations to write would have been busy until the end of read-out.

Clock cycle savings can be seen by comparing Figure 2a and Figure 2d. The total clock cycles required for radix-2 N -point FFT is $N/2 \log_2(N)$. In the usual approach, it would have been $N/2 \log_2(N) + N_{load} + N_{unload} + N_{sort}$, where N_{load} and N_{unload} are clock cycles required to load in unprocessed data and unload processed data respectively. N_{load} and N_{unload} are usually equal to the the number of input samples, N . However, by parallelizing flows to/from memory blocks, they can be made equal to N/N_B where N_B is the number of independently accessible memory blocks. N_{sort} is the number of clock cycles to order the output data when the application requires.

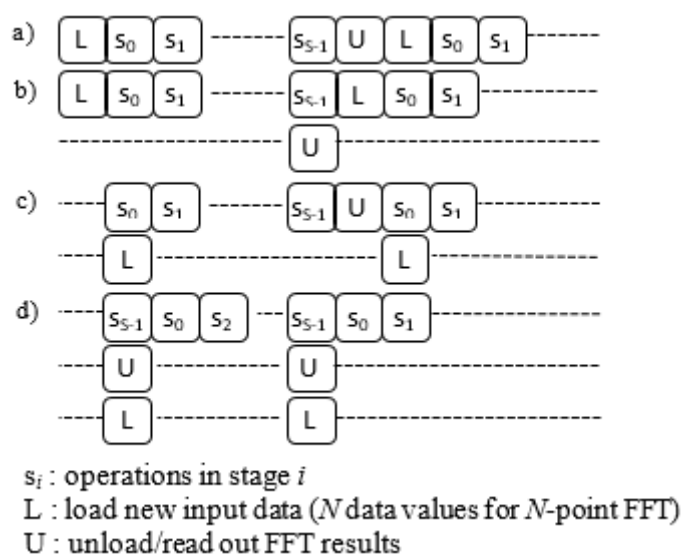


Figure 2. Possible timing diagrams of Memory-Based FFTs, (a) Conceptual timing for basic Load-process-Unload case, (b) Unloading is performed in parallel with the last stage, (c) Loading is performed in parallel with the first stage, (d) Loading, Unloading and the last stages are performed in parallel

1.2. Self-Ordering Algorithm

The method proposed in this paper adapts the “self-sorting in-place” algorithm, described for software FFT implementations [2,9] like Stockham FFT, to limited FPGA (hardware) resources. A difficulty/confusion arouses when the word "cycle" in software implementations is tried to be mapped to "clock cycle" in hardware. In a software cycle, both memory access count and number of calculations are virtually unlimited, whereas FPGA counterpart is limited by the design of the memory component and other resources. For dual-port block memory components in FPGAs, only two addresses can be accessed for reading and/or writing on a single clock pulse.

In this self-sorting schema, $S = \log_2(N)$ being the number of address bits and the number of stages in a radix-2 FFT at the same time, two inputs of the radix-2 PE are read from

$$\begin{aligned} R_0 &= a_{S-1}a_{S-2} \cdots a_1a_0 \\ R_1 &= b_{S-1}b_{S-2} \cdots b_1b_0 \end{aligned} \quad (1)$$

addresses where R_0 and R_1 differs only in one bit whose position is determined by the stage number $s = 0 \dots S - 1$. For example, in first stage of a DIF (Decimation in Frequency) FFT implementation

these addresses would be $0a_{S-2} \dots a_1 a_0$ and $1a_{S-2} \dots a_1 a_0$. In the second stage the addresses would be $a_{S-1}0 \dots a_1 a_0$ and $a_{S-1}1 \dots a_1 a_0$, and so on. However, while writing the PE results back into memory, this differing bit is swapped with its symmetric LSB bit in both R_0 and R_1 . For example, the write addresses for the first stage would be $a_0 a_{S-2} \dots a_1 0$ and $a_0 a_{S-2} \dots a_1 1$. In the second stage, they would be $a_{S-1} a_1 \dots 0 a_0$ and $a_{S-1} a_1 \dots 1 a_0$ and so on for stages up to $S_h = \text{int}(S/2)$. After stage S_h , since all permutations/relocations are completed, the rest of the stages can be performed by “write where it is read from” approach.

When a complete PE cycle per clock pulse is aimed for radix- r FFT, $2r$ memory accesses are required in a single clock cycle; r reads and r writes. For a radix-2 in-place algorithm, this minimally calls for two dual port memory blocks in which a total of 4 ports can be independently read or written provided that no more than two accesses are required for each. Self-ordering introduces additional addressing problems, on the other hand. We have proven that, with a simple example in appendix A, “self-sorting in-place” algorithm as given by [2,9] for radix-2 FFT aiming one PE per clock cycle cannot be generalized efficiently for hardware implementations with less than four dual port memory-blocks. This is because, at some points of the algorithm, it becomes necessary to access 3 address locations of a dual port memory at the same time, which is not possible. We have discussed this in section "Multi-Block Memory Access".

The following sections describe the proposed solutions to problems in hardware (FPGA) implementation of self-sorting radix-2 FFT.

2. HARDWARE DESIGN OF PROPOSED APPROACH

Widely used illustration of a memory-based FFT architecture diagram that uses dual-port memory blocks is shown in Figure 3. Address generator circuit is the main controller of the operation flow. It generates the physical access addresses for the memory blocks, physical memory block selection/activation signals, multiplexer selection signals to route the appropriate memory output data to PE and proper signals for the twiddle factor generation. It is also necessary to generate input-ready (Ird) and data-ready (Ord) signals to indicate the circuit is ready to receive new input data and ready to spit out the calculated FFT data respectively.

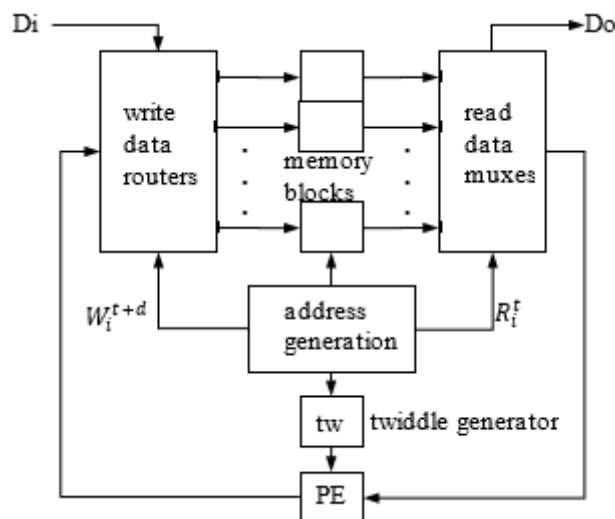


Figure 3. General block diagram of a memory-based FFT circuit. d represents an appropriate delay for feeding write addresses to memory blocks after read addresses

The following subsections describe in detail how these signals are generated for the proposed method. We skipped the description of twiddle factor generation as it is optimization-goal dependent. However, in the actual tests, we employed quarter wave look-up table method for practical reasons. That is, sine samples for $1/4^{\text{th}}$ of a full period are stored in a memory look-up table, and the real and imaginary parts of the twiddle factors are generated using symmetry of sine wave.

2.1. Address Generation

The earliest time the PE results can be written back into the memory is the next clock cycle that follows the read operation of its input data. That is, when the memory read and write addresses are (R_0^t, R_1^t) and (W_0^t, W_1^t) where $t = 0, 1, 2 \dots$ indicating clock cycle number, (W_0^t, W_1^t) are the write addresses of the PE data calculated using the data obtained by reading addresses (R_0^{t-1}, R_1^{t-1}) . It is obvious that the data in the (W_0^t, W_1^t) must have already been read, otherwise they will be overwritten and lost. Since we opted to use a set of data pipeline registers between the complex adders and the multiplier within PE circuit, as shown in Figure 4, a delay of two clock cycles on PE outputs is obtained.

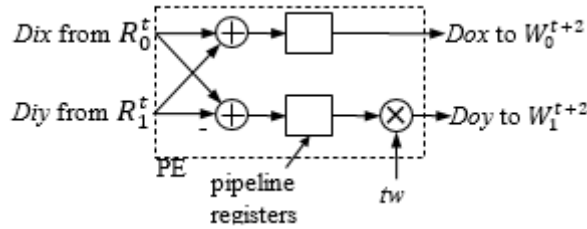


Figure 4. General design of radix-2 PE circuit. W_i^{t+2} addresses are generated two clocks after R_i^t addresses

Consequently, write addresses are also delayed by two clock cycles using address pipeline registers. Let us now analyze the first stage read/write addresses;

$$\begin{aligned} R_0^t &= 0a_{s-2} \dots a_1 a_0, R_1^t = 1a_{s-2} \dots a_1 a_0, \\ W_0^t &= a_0 a_{s-2} \dots a_1 0, W_1^t = a_0 a_{s-2} \dots a_1 1 \end{aligned} \quad (2)$$

Since the only differing bits are lsb and msb bits (a_0), consecutively performing PE pairs for which only the values of these bits differ, such that;

$$\begin{aligned} R_0^t &= 0a_{s-2} \dots a_1 0, R_1^t = 1a_{s-2} \dots a_1 0, \\ W_0^t &= 0a_{s-2} \dots a_1 0, W_1^t = 0a_{s-2} \dots a_1 1, \\ R_0^{t+1} &= 0a_{s-2} \dots a_1 0, R_1^{t+1} = 1a_{s-2} \dots a_1 1, \\ W_0^{t+1} &= 1a_{s-2} \dots a_1 0, W_1^{t+1} = 1a_{s-2} \dots a_1 1 \end{aligned} \quad (3)$$

completes the access requirements for these four addresses for the current stage. For the first PE pair in the first stage of $N=32$ for example, these addresses would be 00000, 10000, 00001 and 10001. By pairwise processing of PEs, entire first stage can be completed without any need for additional large temporary storage and the stage can be completed in-place.

Logically, we assumed that $a_{s-2} \dots a_1 a_0$ bits are generated by a binary counter with $S - 1$ bits. In that case, for the first stage, the a_0 bit automatically handles the consecutive pairing. For other stages up to S_h , a_0 should be swapped with s^{th} bit, so that pairings described above will occur.

2.2. Multi-Block Memory Access

One or more of the address bits should be assigned as memory-block-selection bits. For example, in a 4 block-memory design, 2 address lines are to be used for that purpose.

We are forced to handle pairwise processing of PEs as explained in the previous section. Write addresses delayed by two clock cycles will not conflict with the current read addresses when a_1 of the counter with the one at the center of address bits. This bit and one of its neighbors (selection is arbitrary) are used as two selection signals for 4 memory blocks. For $N=32$ for example, a_0 and a_1 are used from counter bits $a_3a_2a_1a_0$. However, when a_1 is one of the swapped bits for self-ordering, it is swapped with a_2 first and used as one of the block selection signals. With an additional bit that identifies one of R_0 or R_1 , the final address lines would be $R_0 = 0a_3a_1a_2a_0$ and $R_1 = 1a_3a_1a_2a_0$. The pair a_1a_2 will be used as block selection signals. Write addresses are then, $W_0 = a_0a_3a_1a_20$ and $W_1 = a_0a_3a_1a_21$. Since this approach will work only for odd number of address bits, the proposed schema will handle FFTs with $N = 2^b$ where b is odd ($N=32,128,512,2048\dots$). But it will handle FFTs with even b if additional write-only clock cycles are inserted before starting and after finishing the stage $s = S_h$. It adds some complexity in the control circuit, hence we kept this option out of this paper. Complete flow of the address generation circuit is given Figure 5 with one additional bit inversion which will be described in the Section 2.3.

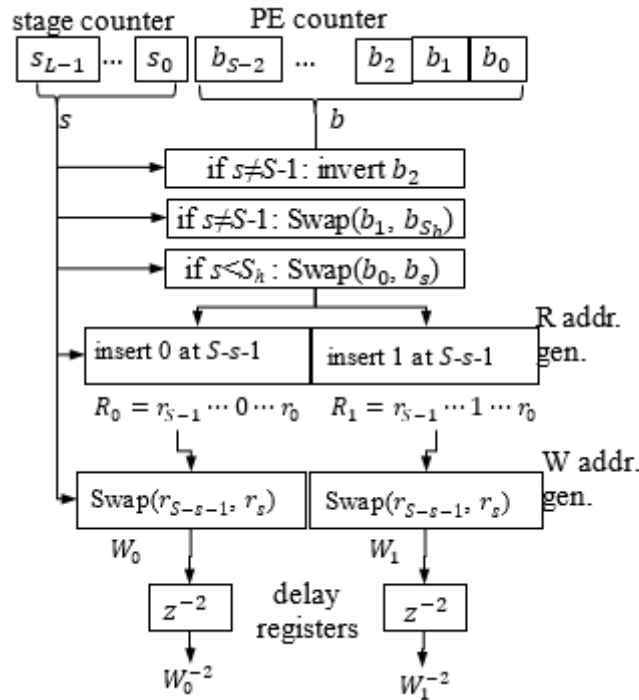


Figure 5. Generation of read/write addresses. Swap and insert functions are implemented as multiplexers (combinatorial logic)

2.3. Address Routing Circuits

With the address bit arrangements described in the previous section, no more than 2 internal address locations are required to be accessed for each dual-port memory block. Accesses to each of 8 ports could be managed by using 4-to-1 multiplexers on each port. Further circuit simplification can be achieved by managing the order of processing at each stage. It is possible to have any single port to see only two of $\dot{R}_0, \dot{R}_1, \dot{W}_0, \dot{W}_1$ at any given cycle, where dotted address notations ($\dot{R}_0, \dot{R}_1, \dot{W}_0, \dot{W}_1$) indicate the physical

addresses (two block selection bits excluded) and necessary delays are applied for write addresses. For example, port A of all memory blocks will see either one of \dot{R}_0 or \dot{W}_1 , or the port is not used in the current cycle. Similarly, the other port (B) will see either \dot{R}_1 or \dot{W}_0 . This arrangement suggests the circuit illustrated in Figure 6, per memory block.

In Figure 6, M_p is one of the four memory blocks where p is either 0, 1, 2 or 3. A and B indicates the two ports of the dual-port memory. mR_0 , mR_1 , mW_0 and mW_1 are S_h^{th} and 1^{st} bits of the respective addresses. The routers simply multiplexes \dot{R} or \dot{W} inputs to the address lines depending on these bits. Since, with the described address generation algorithm, only one of them is allowed at any time, the routers will allow \dot{W} to pass if its mW bits equal to p (and activate WE -write enable- output), otherwise it will let \dot{R} pass through. The routers will also activate CE (memory enable) signal if any of its address inputs point to p .

Stage transitions (when a new stage is started) pose a problem in managing multiplexer-friendly (use of 2 input mux instead of 4) addressing of block memories. Since consecutive pairings are managed by a_1 counter bit, pair ordering in consecutive stages is handled by just inverting one of the higher counter bits, for example a_2 . This is shown in Figure 5 as a first step after generating counter values. These inversion and bit swapping are not performed in the last stage since the last stage must be performed in normal order. Outputs of the last stage will not be written back to memory anyway, instead new data will be loaded in normal order, and no conflict will occur.

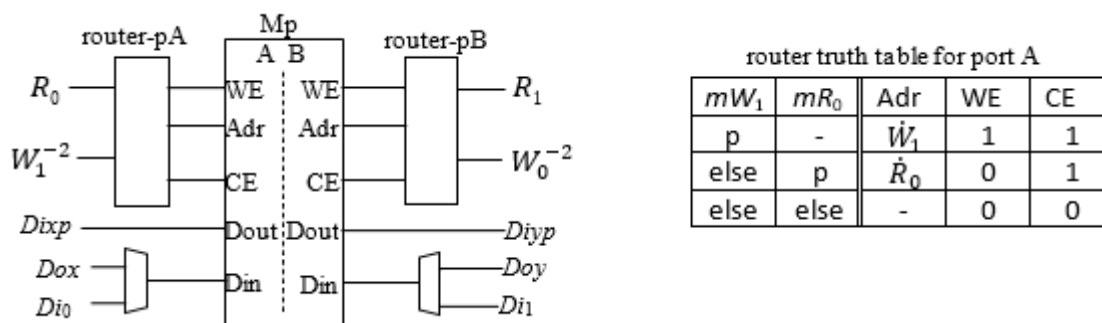


Figure 6. Address routing circuits for p th dual-port memory block. Truth table shows signal routing for port A. All routers are identical except that address inputs of B ports receive R_1 and W_0 . p is a two bits value for selecting p^{th} memory block. mW and mR are S_h^{th} and S_{h-1}^{th} bits of W and R inputs of the router. The remaining bits are \dot{W}_1 and \dot{R}_0 . '-' indicate don't-care, therefore PE outputs (Dox , Doy) can directly be routed to the Din inputs except when new data are being filled into memories

Memory output data ($Dixp$ and $Diyp$, where p is one of 0, 1, 2 or 3) shall also be multiplexed into PE inputs Dix and Diy using mR_0 and mR_1 two bit selectors, respectively. However, since data comes out from memories after a clock cycle, mR_0 and mR_1 selectors should also be delayed by 1 clock cycle.

Two additional signals (Ird , Ord) are generated by the address generation circuit given in Figure 5 (these signals are not shown) indicating that the FFT operation is in the last stage so that the calculated results should be taken out from PE outputs and new data for FFT should be provided. Input data multiplexers controlled with this signal are shown in Figure 6.

This completes the general design of the radix-2 self-ordered in-place FFT with the total clock cycles of

$$N_{clk} = N/2 \log_2(N) \tag{4}$$

and no additional clock cycles are required for re-ordering and data inputs & outputs.

3. RESULTS AND COMPARISONS

A general radix-2 complex-valued FFT schema contains $N/2$ PE in each of $\log_2 N$ stages, making minimal clock count of $\frac{N}{2} \log_2 N$, assuming that one PE calculation is performed in each clock cycle. This excludes clock cycles required for loading new data and unloading calculated FFT output. Since our proposed self-ordering method does loading, unloading and the last FFT stage all in parallel, the number of overhead clock cycles is zero. That is, requiring no overhead clock cycles, the number of clock cycles between new data loadings is $\frac{N}{2} \log_2 N$. Clock cycles given in Table 1 does not include overhead clock cycles (but marked as T_{lu}) as referenced methods do not provide such numbers.

In Table 1, the work of Ma and Wanhammar [13] exhibits the minimum clock cycles, but do not include overhead cycles and the output data is in bit-reversed order. The method in [8] has the lowest cycles, however again, it does not include additional clock cycles and uses mixed radix. It also uses $2N$ memory. The method of Ma *et al.* [12] on the other hand uses N memory locations but designed for real-valued inputs. It is naturally expected to achieve half the required clock cycles for complex-valued FFTs anyway. Our proposed method requires lowest possible clock cycles in its category. It can be easily implemented on FPGAs with low resource counts.

Since the main target is low resource small FPGAs, the proposed schema is designed in VHDL for $N=32, 128, 512$ and 2048 and tested on Spartan 3E and Virtex-6 FPGAs, feeding it with stored data samples and real-time sampled data and observing the output. Input and output data were 18 bit fixed-point. This wordlength selection is arbitrary and has no effect on number of clock cycles. In tests/experiments on Spartan 3E, design has achieved 115 MHz clock frequency for $N=512$ with 116 FFs, 754 4-input LUTs. On Virtex-6, the clock frequency was 186 MHz for $N=2048$ with 174 slice registers and 607 LUTs. Obviously, clock speeds are not impressive but accepted as reasonable since no clock speed improvement measures (like pipelining combinatorial circuits) were taken in the design and the devices are low end. It was notable that $N=2048$ fixed-point FFT comfortably fits in a Spartan XC3S100E device. Since the initial target was low end FPGAs, the choice of radix-2 was appropriate as they have limited number of DSP-slices/multipliers. Therefore, we compared the method with the radix-2 methods found in the literature.

Table 1. Comparison with previous radix-2 memory-based methods

method	radix, #banks,M	#clock cycles	#clock cycles for $N=2048$	#cycles with parallel loading/unloading to 4 memory blocks
Ma and Wanhammar [13]	2,4, N	$\frac{N}{2} \log(N) + T_{lu}$	$11264 + T_{lu}$	12288
Jo and Sunwoo [8] ¹	2-4,4,2 N	$\frac{N}{8} \log(N) + T_{lu}$	$3840 + T_{lu}$	4864
Ma <i>et al.</i> [12] ²	2,4, N	$\frac{N}{4} \log(N) - \frac{N}{4} + 1 + T_{lu}$	$6145 + T_{lu}$	7169
proposed ³ .	2,4, N	$\frac{N}{2} \log(N)$	11264	11264

T_{lu} : clock cycles required for i/o and possible re-ordering

$T_{lu} = N/N_B, N_B$: number of memory blocks

¹: radix-2 and radix-4 mixed (large PE), $2N$ memory

²: real-valued inputs

³: includes i/o clock cycles

All the methods given in Table 1 have similar/comparable resource utilization [8] uses twice the memory that of the others. It should be noted that the proposed method is not intended to reduce number of clock cycles spent in performing the actual FFT calculations. However it eliminates the clock cycles required

to load input data and unload the results after FFT. These clock cycles are shown as T_{lu} in Table 1. The numbers in the rightmost column of Table 1 gives the total number of clock cycles required for loading data, processing (FFT) them and reading out the processed data, assuming that all 4 memory blocks are loaded and unloaded in parallel. Even the state-of-the-art references do not discuss on these overhead cycles and assume that the input data is already loaded. It is generally $T_{lu} = 2N/N_B$ where N_B is the number of memory banks that can be read/written in parallel (assuming that no ordering is required). Proposed method requires load/unload processes too, but they are done in parallel to FFT calculation whereas in other methods parallel load/calculate/unload is not possible due to unordered placement of data in the memory.

In section 2.2, it is stated that for cases of $N = 2^b$ where b is even, additional clock cycles must be inserted between stages. For a particular case of $N = 1024$, there are 10 stages and therefore 20 additional write-only clock cycles are needed to prevent addressing conflicts. This will make the total number of clock cycles 5140, which is 492 clock cycles smaller than the required clock cycles for [13]. This means that, inserting additional clock cycles does not really affect the performance but slightly increase the chip area usage due to the needed management circuitry for write-only cycles. In our example implementation, the increase was less than 1%, not even making into synthesizer statistics.

4. CONCLUSION

A radix-2 memory-based FFT architecture with normal ordered input and output data and a novel application of a self-sorting algorithm is presented and experimented. Small FPGAs with low resource counts are targeted. With a single complex multiplier, it achieves minimum possible clock cycles ($\frac{N}{2} \log_2(N)$) between FFT cycles by eliminating clock cycles required for data feed-in and read-out. FFT processing circuit is never in a wait-for-data state. For comparisons with other memory-based radix-2 designs with minimum required memory of N and minimum number of clock cycles $\frac{N}{2} \log_2(N)$, it should be noted that it is not possible to do data feed-in and read-out simultaneously because of the digit-reversed ordering nature of the FFT algorithm. This is achieved with our proposed schema by embedding a self-ordering algorithm into the design. Although the proposed schema works for only FFTs with $N = 2^b$ where b is odd, it works for even b s with a few write cycles inserted between stages. It is obvious that this radix-2 FFT architecture with efficient self-sorting addressing method provides savings in total required clock cycles and reduction in hardware resources. It is also obvious that radix- 2^k and quite possible that higher radix FFTs can be implemented using the proposed approach, by increasing the number of memory blocks accordingly.

CONFLICT OF INTEREST

The authors declare that they have no known competing financial interests or personal relationships that could have appeared to influence the work reported in this paper.

AUTHORSHIP CONTRIBUTIONS

Authors have equal contribution in design of the system, HDL testing and manuscript preparation.

REFERENCES

- [1] Chang YN, Parhi KK. An efficient pipelined FFT architecture, IEEE Transactions on Circuits and Systems II: Analog and Digital Signal Processing 2003; 50-6: 322–325.

- [2] Chu E, George A. FFT algorithms and their adaptation to parallel processing, *Linear Algebra and its Applications* 1998; 284-1-3: 95–124.
- [3] Garrido M. A survey on pipelined FFT hardware architectures, *Journal of Signal Processing Systems* 2021; <https://doi.org/10.1007/s11265-021-01655-1>.
- [4] Garrido M, Grajal J, Sanchez MA, Gustafsson O, Pipelined radix-2k feedforward FFT architectures, *IEEE Transactions on Very Large Scale Integration (VLSI) Systems* 2013; 21: 23–32.
- [5] Garrido M, Moller K, Kumm M. World’s fastest FFT architectures: Breaking the barrier of 100 GS/s, *IEEE Transactions on Circuits and Systems I: Regular Papers* 2019; 66-4: 1507–1516.
- [6] Garrido M, Sanchez MA, Lopez-Vallejo ML, Grajal J. A 4096-point radix-4 memory-based FFT using DSP slices, *IEEE Transactions on Very Large Scale Integration (VLSI) Systems* 2016; 25: 375–379.
- [7] Huang SJ, Chen SG. A high-throughput radix-16 FFT processor with parallel and normal input/output ordering for IEEE 802.15.3C Systems, *IEEE Transactions on Circuits and Systems I: Regular Papers* 2012; 59-8: 1752–1765.
- [8] Jo BG, Sunwoo MH. New continuous-flow mixed-radix (CFMR) FFT processor using novel in-place strategy, *IEEE Transactions on Circuits and Systems I: Regular Papers* 2005; 52-5: 911–919.
- [9] Johnson H, Burrus C. An in-order, in-place radix-2 FFT, *ICASSP '84. IEEE International Conference on Acoustics, Speech, and Signal Processing* 1984.
- [10] Kaya Z, Seke E, A novel addressing algorithm of radix-2 FFT using single-bank dual-port memory, *Circuit World* 2020; 48: 64–70.
- [11] Luo HF, Liu Y-J, Shieh M-D. Efficient memory-addressing algorithms for FFT processor design, *IEEE Transactions on Very Large Scale Integration (VLSI) Systems* 2015; 23-10: 2162–2172.
- [12] Ma ZG, Yin XB, Yu F. A novel memory-based FFT architecture for real-valued signals based on a radix-2 decimation-in-frequency algorithm, *IEEE Transactions on Circuits and Systems II: Express Briefs* 2015; 62-9: 876–880.
- [13] Ma Y, Wanhammar L, A hardware efficient control of memory addressing for high-performance FFT processors, *IEEE Transactions on Signal Processing* 2000; 48-3: 917–921.
- [14] Mao XB, Ma ZG, Yu F, Xing QJ. A continuous-flow memory-based architecture for real-valued FFT, *IEEE Transactions on Circuits and Systems II: Express Briefs* 2017; 64-11; 1352–1356.
- [15] Nguyen NH, Khan SA, Kim CH, Kim JM. A high-performance, resource-efficient, reconfigurable parallel-pipelined FFT processor for FPGA platforms, *Microprocessors and Microsystems* 2018; 60: 96–106.
- [16] Sorokin H, Takala J. Conflict-free parallel access scheme for mixed-radix FFT supporting I/o permutations, *2011 IEEE International Conference on Acoustics, Speech and Signal Processing (ICASSP)* 2011.

- [17] Takala JH, Jarvinen TS, Sorokin HT. Conflict-free parallel memory access scheme for FFT processors, Proceedings of the 2003 International Symposium on Circuits and Systems, 2003.
- [18] Tsai PY, Lin CY. A generalized conflict-free memory addressing scheme for continuous-flow parallel-processing FFT processors with rescheduling, IEEE Transactions on Very Large Scale Integration (VLSI) Systems 2011; 19-12: 2290–2302.
- [19] Valencia D, Alimohammad A. Compact and high-throughput parameterisable architectures for memory-based FFT algorithms, IET Circuits, Devices and Systems 2019; 13-5: 696–703.
- [20] Xiao X, Oruklu E, Saniie J, An efficient FFT engine with reduced addressing logic, IEEE Transactions on Circuits and Systems II: Express Briefs 2008; 55-11: 1149–1153.
- [21] Xiao X, Oruklu E, Saniie J. Fast memory addressing scheme for radix-4 FFT implementation, IEEE International Conference on Electro/Information Technology 2009.

